
THE UNIVERSITY *of* EDINBURGH

# Non-linear Equalisation Techniques for High-Speed Step-Index Plastic Optical Fibre Communication

*Isaac N.O. Osahon*


A thesis submitted for the degree of Doctor of Philosophy.
**The University of Edinburgh**.
November 2020

# Abstract

Step-index plastic optical fibres (SI-POF) have become a promising candidate as the media for short-range in-home and automotive networks due to their low cost and their ease of installation. However, they have the smallest bandwidth compared to the other optical fibres. Therefore, high-speed communication over SI-POF results in inter-symbol interference (ISI) that linearly distorts the signal. Moreover, there are non-linearities from the optical front-end that further degrade the SI-POF performance.

A straightforward solution is to use non-linear equalisers (NLE) with the SI-POF system as they compensate for the non-linear distortions while mitigating the channel ISI. Three NLEs – transversal decision feedback equaliser (DFE), Volterra equaliser/DFE, and the multi-layer perceptron-based equaliser/DFE (MLPDFE) – have been introduced in the literature. High-order modulation formats – like pulse amplitude modulation (PAM), carrier-less amplitude and phase modulation (CAP), and discrete multi-tone (DMT) – can be used in combination with the NLE to overcome the bandwidth limitation further. Thus, the thesis deals with the performance of these NLEs for PAM, CAP, and DMT transmission in order to achieve high data rates (from several hundreds of megabits-per-second (Mbps) to gigabits-per-second (Gbps)) in SI-POF.

The contributions of this research work are in threefold: firstly, a simulation model is used to evaluate and compare the performance of the NLEs for PAM and CAP schemes. The study shows that for a highly non-linear SI-POF with higher PAM (or CAP) modulation order, the MLPDFE offers higher data rates than the Volterra DFE followed by the transversal DFE. This simulation study is further verified with various experiments. For instance, the MLPDFE offers an error-free bit rate of about 6.2 Gbps over a 30 m SI-POF while the transversal DFE offers about 5 Gbps at similar SI-POF length. A computational complexity comparison of each NLE shows that the transversal DFE requires the least computing requirement, and the VOLT2DFE has higher computational order than the MLPDFE.

Secondly, the work investigates a recently introduced frequency domain NLE (FD-NLE) for DMT transmission over SI-POF. It explores the performance of the FD-NLE for DMT with clipping distortion in a highly non-linear SI-POF system. The FD-NLE is shown in this case as the better choice than the conventional frequency domain equaliser. With insight from the FD-NLE for DMT, both Volterra and the MLP equalisers are translated to the frequency domain for PAM and CAP transmission over SI-POF. A computational complexity analysis shows that implementing the NLEs (with PAM and CAP) in the frequency domain reduces their complexity by at least 60% if there are more than 16 feedforward taps for the equaliser.

Finally, extensive experiments are carried out to evaluate and compare the bit error rate (BER) performances and the computational complexity of the modulation schemes with their respective NLEs. The comparisons show that for a short-length SI-POF of up to 30 m, representing benign channel conditions, bit-loaded DMT with FD-NLE offers the best performance requiring the least complexity and the least transmitted electrical power. However, at longer lengths, PAM with MLPDFE gives the best performance. CAP with the MLPDFE demands the highest computational complexity and the transmitted electrical power.

# Declaration of originality

I declare that this thesis has been composed solely by myself and that it has not been submitted, either in whole or in part, in any previous application for a degree. Except where otherwise acknowledged, the work presented is entirely my own.

Isaac Osahon

# Acknowledgements

I would like to take this opportunity to first and foremost thank God for being my strength and guide in the writing of this thesis. Without Him, I would not have had the wisdom or the physical ability to do so.

My most heartfelt gratitude goes to my family for their love and support; this thesis would have been impossible without them. I am indebted to my parents, Felix Osahon and Janet Osahon, for cheering me on in this academic journey. I want to also thank my siblings for always helping me keep it all together, even with us being far from each other.

I am also grateful to the Federal Government of Nigeria with the petroleum technology development fund (PTDF) for their financial support.

I offer my sincerest gratitude to my supervisor, Dr Wasiu Oyewole Popoola, for his assistance, patience, encouragement and advice throughout my PhD. His huge passion for research in many areas on optical communications has deeply inspired me. I fully appreciate his continuous support and encouragement. My sincere thanks also go to Dr Majid Safari for his insightful comments.

Last but not least, I would like to acknowledge Dr Sujan Rajbhandari for sharing his insight on the fundamentals of machine learning, and I want to thank Dr Evangelos Pikasis for his expertise on plastic optical fibre communications.

# Contents

# List of figures

# List of tables

# Acronyms and abbreviations

| | |
|---|---|
| **10GE-PON** | 10 Gigabit ethernet PON |
| **ADC** | Analogue-to-digital converter |
| **ADSL** | Asymmetrical DSL |
| **ANN** | Artificial neural network |
| **APD** | Avalanche PD |
| **BER** | Bit-error-rate |
| **BP** | Back-propagation |
| **CAP** | Carrier-less amplitude and phase modulation |
| **CAP-$M^2$** | CAP with QAM-$M^2$ format |
| **CCDF** | Complementary cumulative distribution function |
| **DAC** | Digital-to-analogue converter |
| **DC** | Direct current |
| **DFE** | Decision feedback equaliser/equalisation |
| **DFF** | Decision feedback filter |
| **DFT/IDFT** | Discrete Fourier transforms/Inverse DFT |
| **DMT** | Discrete multi-tone |
| **DMT_QAM-$M^2$** | DMT with QAM-$M^2$ format |
| **DSL** | Digital subscriber line |
| **DSP** | Digital signal processor/processing |
| **DVB-T** | Terrestrial digital video broadcasting |
| **DVI** | Digital-visual-interface |
| **E-PON** | Ethernet PON |
| **EB** | Exabyte(s) |
| **EMI** | Electromagnetic interference |
| **FD** | Frequency-domain |
| **FD-MLPDFE** | Frequency-domain based MLPDFE |
| **FD-NLE** | Frequency-domain based NLE |
| **FD-VOLT2DFE** | Frequency-domain based VOLT2DFE |
| **FEC** | Forward error correction |

| | |
|---|---|
| **FFT/IFFT** | Fast Fourier transforms/Inverse FFT |
| **FIR** | Finite impulse response |
| **FITH** | Fibre-in-the-home |
| **FPGA** | Field programmable gate array |
| **FTTB** | Fibre-to-the-building |
| **FTTC** | Fibre-to-the-cabinet |
| **FTTH** | Fibre-to-the-home |
| **G-PON** | Gigabit PON |
| **Gbps** | Gigabits-per-seconds |
| **GEPOF** | Gigabit ethernet POF |
| **GI-POF** | Graded index POF |
| **GOF** | Glass optical fibre |
| **HD** | high-definition |
| **I/Q** | In-phase and quadrature-phase |
| **IEEE** | Institute of electrical and electronics engineering |
| **IM/DD** | Intensity modulation and direct detection |
| **IoT** | Internet of Things |
| **ISI** | Inter-symbol interference |
| **LAN** | Local area network |
| **LD** | Laser diode |
| **LED** | Light emitting diode |
| **Li-Fi** | Light fidelity |
| **LMBP** | Leveberg Marquardart BP |
| **LMS** | Least mean squares |
| **LNA** | Low noise amplifier |
| **m-POF** | Microstructured POF |
| **Mbps** | Megabits-per-seconds |
| **MCM** | Multi-carrier modulation |
| **MLP/MLPDFE** | Multi-layer perceptron/ MLP based DFE |
| **MLSE** | Maximum likelihood sequence estimator |
| **MM-GOF** | Multimode GOF |
| **MMSE** | Minimum mean square error |
| **MOST** | Media oriented systems transport |

| | |
|---|---|
| **MSM-PD** | Metal-semiconductor-metal PD |
| **NA** | Numerical aperture |
| **NG-PON1** | First next-generation PON |
| **NG-PON2** | Second next-generation PON |
| **NLE** | Non-linear equaliser/equalisation |
| **NRZ** | Non-return-to-zero |
| **OFDM** | Orthogonal frequency division multiplexing |
| **OLT** | Optical line termination |
| **ONU** | Optical network unit |
| **P-I** | Optical power - Electrical current |
| **P/S** | Parallel-to-serial |
| **PAM** | Pulse amplitude modulation |
| **PAM-*M*** | PAM with $M$ levels |
| **PAPR** | Peak-to-average-power |
| **PD** | Photodiode |
| **PF-GI-POF** | Perfluorinated GI-POF |
| **PIN-PD** | pin PD |
| **PLC** | Power line communication |
| **PMMA** | Polymethylacrylate |
| **POF** | Plastic optical fibre |
| **PON** | Passive optical network |
| **PSD** | Power spectral density |
| **PSF** | Pulse shaping filters |
| **QAM** | Quadrature amplitude modulation |
| **QPSK** | Quadrature phase-shift keying |
| **RBF** | Radial-basis function |
| **RBP** | Resilient BP |
| **RC-LED** | Resonant cavity LED |
| **RF** | Radio frequency |
| **RLS** | Recursive least squares |
| **RMS** | Root mean square |
| **RNRM** | Required number of real-valued multiplications |
| **RRC** | Root raised cosine |

| | |
|---|---|
| **RS-FEC** | Reed-Solomon FEC |
| **S/P** | Serial-to-parallel |
| **SC-MLP/SC-MLPDFE** | Split-complex MLP/Split-complex MLPDFE |
| **SCM** | Single-carrier modulation |
| **SER** | Symbol-error-rate |
| **SI-POF** | Step index POF |
| **SM-GOF** | Single-mode GOF |
| **SOHO** | Small office/home office |
| **SONET** | Synchronous optical network(ing) |
| **SNR** | Signal-to-noise-ratio |
| **SNDR** | Signal-to-noise-plus-distortion-ratio |
| **TD** | Time-domain |
| **TD-MLPDFE** | Time-domain based MLPDFE |
| **TD-NLE** | Time-domain based NLE |
| **TD-VOLT2DFE** | Time-domain based VOLT2DFE |
| **TDM** | Time division multiplexing |
| **THP** | Tomlinson-Harashima precoding |
| **THD** | Total harmonic distortion |
| **TIA** | Trans-impedance amplifier |
| **TRDFE** | Transversal DFE |
| **TWDM** | Time and wavelength division multiplexing |
| **UTP** | Unshielded twisted pair |
| **VCSEL** | Vertical-cavity surface-emitting laser diode |
| **VDSL** | Very high DSL |
| **VLC** | Visible light communication |
| **VGA** | Variable gain amplifier |
| **VOLT2DFE** | $2^{nd}$ Order Volterra DFE |
| **VOLT3DFE** | $3^{rd}$ Order Volterra DFE |
| **WDM** | Wavelength division multiplexing |
| **Wi-Fi** | Wireless fidelity |
| **Wi-Max** | Worldwide interoperability for microwave access |
| **XG-PON** | X-Gigabit PON |

# Notations and symbols

| | |
|---|---|
| $\otimes$ | convolution operator |
| $\odot$ | Element-wise multiplication operator for vectors (or matrices) |
| $\lceil . \rceil$ | Ceil operator |
| $(.)^*$ | Conjugate operator of a complex number |
| $[.]^{\mathbf{T}}$ | Transpose operator of a vector/matrix |
| $[.]^{\mathbf{H}}$ | Hermitian operator of a vector/matrix |
| $\mathbf{0}^{\mathbf{m,n}}$ | A zeros-element vector/matrix with $m$ rows and $n$ columns |
| $\mathbf{1}^{\mathbf{m,n}}$ | A ones-element vector/matrix with $m$ rows and $n$ columns |
| $n_{co}$ | Refractive index of fibre core |
| $n_{cl}$ | Refractive index of fibre cladding |
| $c_{light}$ | Speed of light in vacuum |
| $M$ | Size of modulation format |
| $N_t$ | Total number of taps for an equaliser |
| $N_{ft}$ | Number of feedforward taps for an equaliser |
| $N_{bt}$ | Number of feedback taps for an equaliser |
| $N_{hn}$ | Number of hidden-layer neurons for an MLP equaliser |
| $I(t)$ | Bipolar input current signal |
| $\hat{I}(t)$ | Clipped $I(t)$ |
| $I_{rp}(t)$ | Bipolar output current of receiver |
| $I_{clip}$ | Clipping level for $I(t)$ |
| $I_{mod}$ | Maximum amplitude of input current signal |
| $\mathbb{E}[.]$ | Expectation function |
| $I_{rms}$ | RMS of current signal |
| $I_{bias}$ | input DC bias current signal |
| $I_{th}$ | Threshold current |
| $\rho_{papr}$ | PAPR of signal |
| $\rho_{clip}$ | Clipping ratio |
| $P_{omod}$ | Optical modulation amplitude |
| $P_{oavg}$ | Mean transmitted optical power |

| | |
|---|---|
| $P_{opt}(t)$ | optical signal at the transmitter |
| $\eta_{mod}$ | Modulation index |
| $\eta_{cp}$ | Coupling loss |
| $\eta_b$ | Link spectral efficiency |
| $\eta_{ld}$ | Optical source slope efficiency |
| $t$ | time variable |
| $f$ | frequency variable |
| $\theta$ | modal angular distribution variable |
| $\theta_0$ | mean of the angle distribution |
| $h_{ld}(t)$ [$H_{ld}(f)$] | Impulse [Frequency] response of optical source |
| $h_{ao}(t)$ [$H_{ao}(f)$] | Impulse [Frequency] response of background electronics |
| $h_{pof}(t)$ [$H_{pof}(f)$] | Impulse [Frequency] response of POF |
| $h_{pd}(t)$ [$H_{pd}(f)$] | Impulse [Frequency] response of receiver |
| $h_{ptot}(t)$ [$H_{ptot}(f)$] | Impulse [Frequency] response of overall POF system |
| $l_{pof}$ | POF length |
| $\alpha_{pof}$ | POF attenuation in dB |
| $\alpha_{pc}$ | POF attenuation coefficient in dB/m |
| $\mathcal{R}_{pd}$ | Responsivity of PD |
| $\mathcal{N}_{nep}$ | Noise equivalent power |
| $\mathcal{N}_{p,s}$ | Shot noise |
| $n_p(t)$ | AWGN from POF receiver |
| $q_e$ | Quantity of charge in an electron |
| $R_b$ | Bit rate |
| $F_s$ | Sampling rate |
| $R_{b,max}$ | Maximum capacity |
| $R_{b,max} \times l_{pof}$ | Maximum bit-rate length product |
| $\gamma_b$ | SNR per bit |
| $\gamma_{nm}$ | Signal-independent SNR |
| $\gamma_{snm}$ | Bandwidth-independent SNR |
| $f_{p3dB}$ | -3 dB electrical bandwidth of POF channel |
| $f_{p3dBl}$ | bandwidth-length product of POF channel |
| $f_{N0}$ | Equivalent noise bandwidth |
| $f_{nl}(I)$ | Non-linear estimate of P-I curve for an optical source |

| | |
|---|---|
| $f_{avn}(.)$ | Activation function for an MLP equaliser |
| $f_{sgm}(.)$ | Sigmoid activation function |
| $p(\theta, l_{pof}, t)$ | Continuous power distribution in the time domain |
| $P(\theta, l_{pof}, \omega)$ | Continuous power distribution in the frequency domain |
| $\alpha(\theta)$ | angle dependent attenuation of a mode |
| $D(\theta)$ | angle dependent diffusion parameter |
| $\tau_{del}(\theta)$ | relative mode delay |
| $G_r(f)$ | PSD of $I_{rp}(t)$ |
| $G_i(f)$ | PSD of $I(t)$ |
| $G_{noise}(f)$ | PSD of noise with POF linear distortions |
| $G_{sig}(f)$ | PSD of signal |
| $P_{sig}$ | Power of signal |
| $P_{noise}$ | Noise power or Noise variance |
| $P_{txelect}$ | mean transmitted electrical power |
| $\text{NA}_{ld}$ | Numerical aperture of optical source |
| $r_{pd}$ | Photodiode radius |
| $r_{pof}$ | POF radius |
| $\beta$ | RRC filter's roll-off factor |
| $G_s$ | RRC filter's symbol span |
| $N_{sps}$ | Oversampling factor |
| $\alpha_2$ | Truncation factor for the FD-NLE |
| $N_{FFT}$ | FFT/IFFT size |
| $N_{cp}$ | Cyclic prefix length |
| $N_{dsub}$ | Number of data-carrying sub-carriers in a DMT symbol |
| $N_{bdmt}$ | Number of bits in a DMT symbol |
| $N_{dbit}$ | Number of bits in a DMT frame |
| $N_{dsym}$ | Number of DMT data symbols in a frame |
| $N_{dest}$ | Number of DMT pilot symbols in a frame |
| $N_{spb}$ | Number of symbols per block for the FD-NLE |
| $\mathbf{y}(\mathbf{b_0})$ | Input column vector for the FD-NLE |
| $\mathbf{y}(\mathbf{b_c})$ | $c$ delayed version of $\mathbf{y}(\mathbf{b_0})$ |
| $\tilde{\mathbf{w}}_\mathbf{1}$ | Feedforward weight column vector for the FD-NLE |
| $\tilde{\mathbf{w}}_{\mathbf{2,c}}$ | 2[nd]-order Volterra weight column vector for the FD-NLE |

| | |
|---|---|
| $\mathbf{y_{cir}(b_c)}$ | Circulant matrix of $\mathbf{y(b_c)}$ |
| $\boldsymbol{\mathcal{F}^{-1}}$ | Inverse FFT/DFT matrix |
| $\boldsymbol{\mathcal{F}}$ | FFT/DFT matrix |
| $\boldsymbol{\mathcal{Y}(\mathbf{b})_{\mathcal{F}}}$ | Diagonal matrix from the FFT/DFT of $\mathbf{y(b_0)}$ |
| $\boldsymbol{\mathcal{W}_{\mathcal{F}}}$ | Column vector from the FFT/DFT of $\mathbf{\tilde{w}_1}$ |
| $\boldsymbol{\mathcal{W}_{\mathcal{F},2,c}}$ | Column vector from the FFT/DFT of $\mathbf{\tilde{w}_{2,c}}$ |
| $\boldsymbol{\mathcal{Y}(\mathbf{b})_{\mathcal{F},2,c}}$ | Diagonal matrix from the FFT/DFT of $\mathbf{y(b_c)^* \odot y(b_0)}$ |
| $\mathcal{R}_{\frac{fd}{td}}$ | Ratio of the RNRM of FD-NLE over that of TD-NLE |
| $\mathcal{R}_{\frac{fd}{td},0}$ | $\mathcal{R}_{\frac{fd}{td}}$ at $N_{bt} = 0$ |
| $\mathfrak{R}_{bit}$ | RNRM per bit |

# Chapter 1
# Introduction

With the growing penetration of smart devices, the emergence of "Internet of Things" (IoT), and the increasing usage of data-hungry applications (e.g. video streaming and cloud computing), the fixed/non-mobile internet traffic has been predicted to triple approximately within five years. Cisco has reported the global monthly fixed internet traffic to be 110.8 exabytes (EB) in 2017 and has foreseen this to exceed 318 EB in 2022 [1]. Analysis from the same report has shown that about 79% of global internet traffic will come from fixed networks in 2022. The non-mobile data traffic mostly originates from indoor communication networks like those within small office/home offices (SOHO), data centres, and factories. Presently, the dominant media available to the end-users for indoor transmission is either wired (e.g. copper, fibre) or wireless (e.g. wireless fidelity (Wi-Fi), worldwide interoperability for microwave access (Wi-Max)) [2–4]. Compared to communications with wireless media, the wired ones are more reliable and stable. They also offer higher communication speeds with better security. Although wireless communication systems are prefered for their mobility, they are usually backhauled with the wired media. These benefits of wired communication have increased fixed network traffic and have, therefore motivated research interest in improving wired access technologies.

For fixed broadband services to be provided to the end-users, there is an intense competition between various types of wired technologies used in the last mile of the network towards the users [5]. One of these access technologies is the digital subscriber line (DSL) that employs twisted-pair copper cables as its medium. The two commonly deployed DSL standards are the asymmetrical DSL (ADSL) and the very high DSL (VDSL). The earlier offers data rates of tens of megabits-per-seconds (Mbps) while the latter offers up to 100 Mbps per subscriber [6]. Another copper-based media is the coaxial cable, which is used for video transmission and offers a bit-rate of about 40 Mbps [7].

Wired communication technologies are commonly applied in SOHO networks as they are used to backhaul wireless media (e.g. Wi-Fi) and connect non-mobile data devices (e.g. PC, servers, printers). From now till the next decade, a typical SOHO network will host at least these following set of services [8–10]:

- **Smart-home**: They are mostly offered by IoT technologies, which are small, resource-constrained devices, like sensors, actuators and controllers. The devices participate in different automation and monitoring of home applications - like automated billing, smart lighting, smart energy consumption, surveillance, and healthcare.

- **Entertainment**: This covers video streaming, gaming and virtual reality (VR) applications. These services consume far more bandwidth than many other home network services. For instance, streaming a Netflix high-definition (HD) and an ultra-HD (4K) content requires roughly 5 Mbps and 25 Mbps, respectively [11]. In comparison, web browsing does not need more than about 0.05 Mbps.

- **Remote-working**: This includes multi-room digital video recording (DVR), video conferencing, virtual private networking (VPN) and "all-in-the-cloud." Demand for these services has progressed due to changing behaviours from the coronavirus pandemic [12].

These services have pushed the required home network speed beyond 100 Mbps. By the next decade, the user demand for data throughput will reach the gigabit-per-seconds (Gbps) range. Thus, the copper-based DSL solutions would have reached their limits for these services. This increasing demand has brought about the need for migration of long-haul optical fibre technologies into short-range fibre systems, giving place to the "fibre-to-the-x" (FTTx) solutions: where "x" could represent the home (FTTH), the building (FTTB), or the cabinet (FTTC).

The FTTx technologies are passive optical network (PON) standards that use single-mode glass optical fibre (SM-GOF) as their media for communication. They are usually deployed at 10 km to 50 km lengths from an optical line termination (OLT) point for the service provider to the optical network unit (ONU) for the subscribers [13, 14]. The first generation PON standards (like ethernet PON (E-PON) and Gigabit PON (G-PON)) were deployed at the start of the 21st century; they offer bit-rates from 1 Gbps to 2.5 Gbps to the ONUs [7,13,14]. With time-division multiplexing (TDM), these PON standards were migrated to the first next-generation PON (NG-PON1 like 10 Gigabit ethernet PON (10GE-PON) and X-Gigabit PON (XG-PON)) standards in 2009 [13–15]. The NG-PON1 standard is the most dominant PON standard around the world, and it presents a bit-rate of 10 Gbps for each subscriber. Wave-division multiplexing (WDM) was used jointly with TDM to improve the NG-PON1 standards to the second next-generation PON (NG-PON2) standard, which is also termed the time-and-wave division multiplexing PON (TWDM-PON) standard [14]. The three classes of PON standards are back-to-back compatible

with each other. Several experimental works on TWDM-PON have been demonstrated since 2012, presenting high bit-rates of 40 Gbps to 128 Gbps [16–29].

To meet the ever-increasing bandwidth demand, service providers will need to deploy FTTx access technologies. Consequently, it is expected that FTTH/Building (FTTH/B) will be the highest provider of fixed broadband technology by the year 2035 [14]. Statistics reported by the FTTH Council in 2017 indicated that approximately 456 million FTTH/B subscribers worldwide were already connected by optical fibre and this is projected to rise annually by 14% in 2022 [31]. The vast majority of the subscribers are from the Asia Pacific Region with 374.0 million, followed by Europe with 54.7 million, North America with 13.7 million users. Further analysis made by the same organisation, verified that the widespread deployment of high-speed connections to the doorstep of the end-user, together with the rising presence of interconnected devices supporting different types of data (e.g. HD video, mp3, etc.) had shifted the network bottleneck to the short-range networks inside the home.

Figure 1.1 shows the global ranking of countries with more than 1% penetration rate of FTTH and FTTB plus Local Access Networks (LANs) for the last quarter of 2018 [30]. The United Arab Emirates has the highest penetration rate of FTTH/B of 95.7% and the United Kingdom enters the global ranking for the first time, reaching a modest penetration rate of 1.3%. In a sense, Fig. 1.1 shows a prospective market for short-range optical fibre systems. According to the graph, subscribers categorised as FTTB+LAN have access to fibre connections through LANs using copper cables. Hence, the market opportunity here lies in applying optical fibre for these connections. LANs can strongly benefit from the fibre's overall performance, which is better than its copper-cable counterparts in delivering information at high bit rates. In particular, optical fibre provides symmetrical access and larger bandwidth. It does not require electricity to transmit information; therefore, it is immune to electromagnetic interference (EMI) so that it could be deployed through power supply ducts. On the other hand, it is precisely the intrinsic roughness of such in-building/in-home installation environments, which makes it challenging to use the standard and widely spread glass optical fibres (GOFs). Furthermore, deploying GOFs requires specialised equipment and trained personnel, which implies more expenses and therefore, a higher cost for Telecom Operators (Telcos).

SOHO networks use conventional media technologies such as Wi-Fi, power line communication (PLC), solutions with coaxial and unshielded twisted pair (UTP) CAT cables. Each of these technologies has both its advantages and limitations. Wi-Fi, for instance, is easy to in-

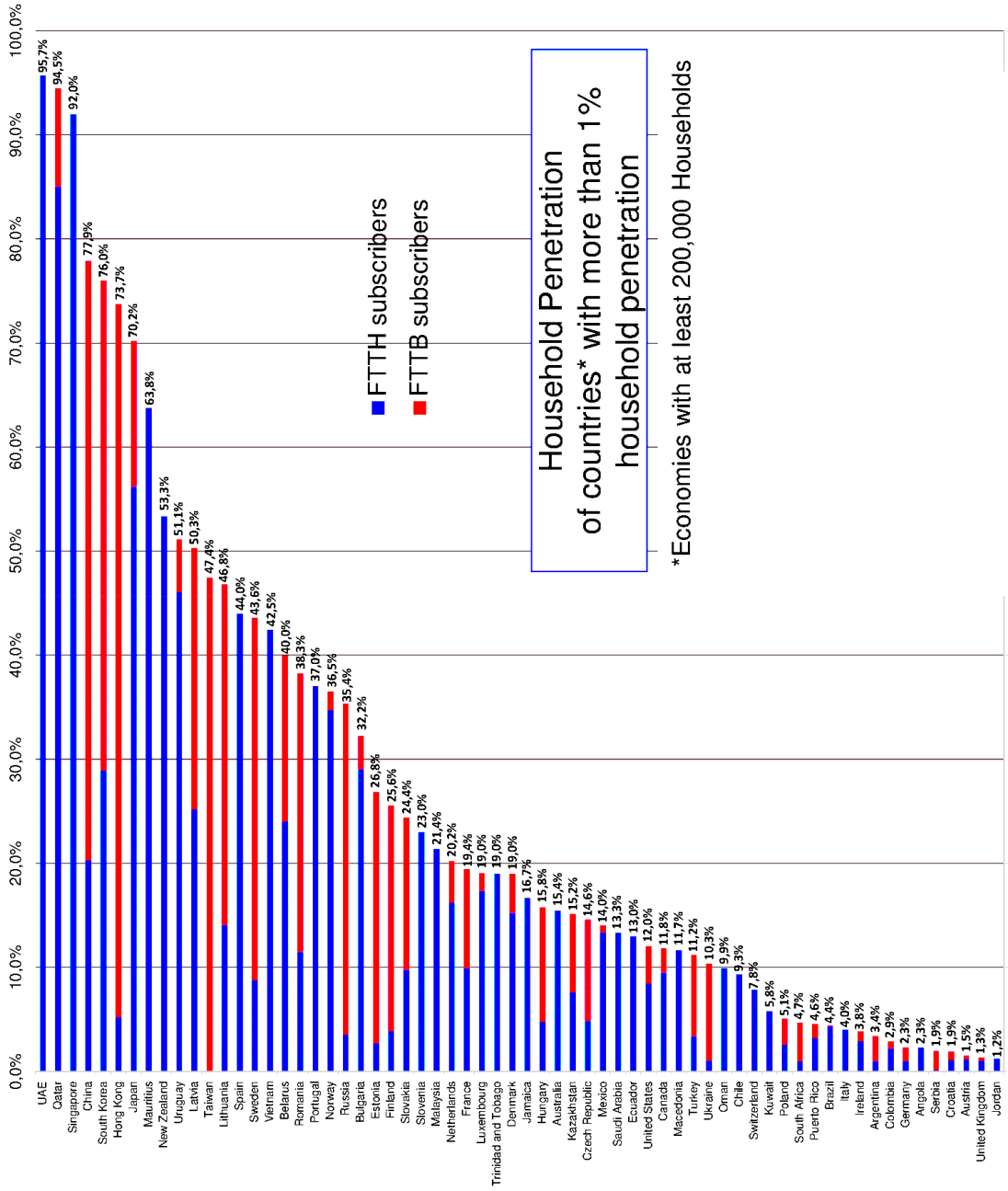


**Figure 1.1:** *Countries with the highest penetration of FTTH/B as at September 2018 [30]*

stall and configure. However, its future improvements are challenged by an already congested radio-frequency (RF) spectrum, which makes the allocation of new services difficult. It also has access issues related to its distribution within or outside a building – which could make Wi-Fi insecure. Hence, future broadband access networks have to deal with this reality and consider not only improving current technologies and creating new ones but also try to integrate them properly. In this sense and as an alternative to improve bandwidth limitations due to in-building cabling, novel systems based on both plastic optical fibre (POF) and multimode GOF (MM-GOF) have been studied and demonstrated [32]. Even if these fibre cabling solutions were proven feasible, they still need to be deployed by expert personnel, and therefore the challenge still lies in finding a solution that allows a safe and convenient "do-it-yourself" installation. Under these circumstances and for these requirements, solutions based on POF are better than those based on MM-GOF. The most popular and cheapest POF in the market is the polymethylacrylate step-index POF (PMMA SI-POF) that has its numerical aperture (NA) as 0.5 [33–35]. The SI-POF is also the easiest to handle among all the POFs as it has the largest diameter (0.98 mm), and it is the most resilient to bending due to its large NA [33, 34].

## 1.1 POF Applications and Market Availability

The market for POF has undergone constant growth, and many factors indicate that this will not only go on but may increase as well. This market growth is illustrated from a study from IGI consulting incorporated, which estimates a constant compound annual growth rate (CAGR) of $\sim$11% up to the year 2019 [36], as shown in Fig 1.2a. A cost comparison of optical fibres is shown in Table 1.1, and it illustrates that POF has the least cost compared to the other optical fibres. The low-cost of POF and its other advantages significantly contributes to its market growth.

| | **POF** | **SM-GOF** | **MM-GOF** |
|---|---|---|---|
| Core Diameter[1] [$\mu$m] | 240 - 2980 | 3.5 - 9.5 | 50 - 2000 |
| Minimum Bend Radius[1] [mm] | 9 - 20 | 5 - 25 | 7.5 - 400 |
| Cost Estimate[2] [£/m] | 0.48 - 2.01 | 3.94 - 19.40 | 1.05 - 5.69 |

[1] Values of core diameter and bend radius are obtained from amsTechnologies [37].
[2] The costs of the fibres are from Industrial fibre optics [38] and Newport [39].

**Table 1.1:** *Technical and cost comparisons of optical fibres*

Furthermore, POFs can be applied to a multitude of substantially different applications - for

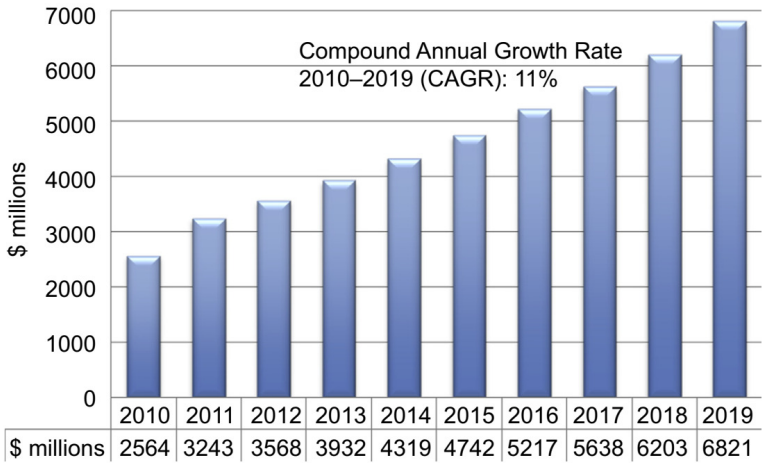


| | 2010 | 2011 | 2012 | 2013 | 2014 | 2015 | 2016 | 2017 | 2018 | 2019 |
|---|---|---|---|---|---|---|---|---|---|---|
| $ millions | 2564 | 3243 | 3568 | 3932 | 4319 | 4742 | 5217 | 5638 | 6203 | 6821 |

**(a)**

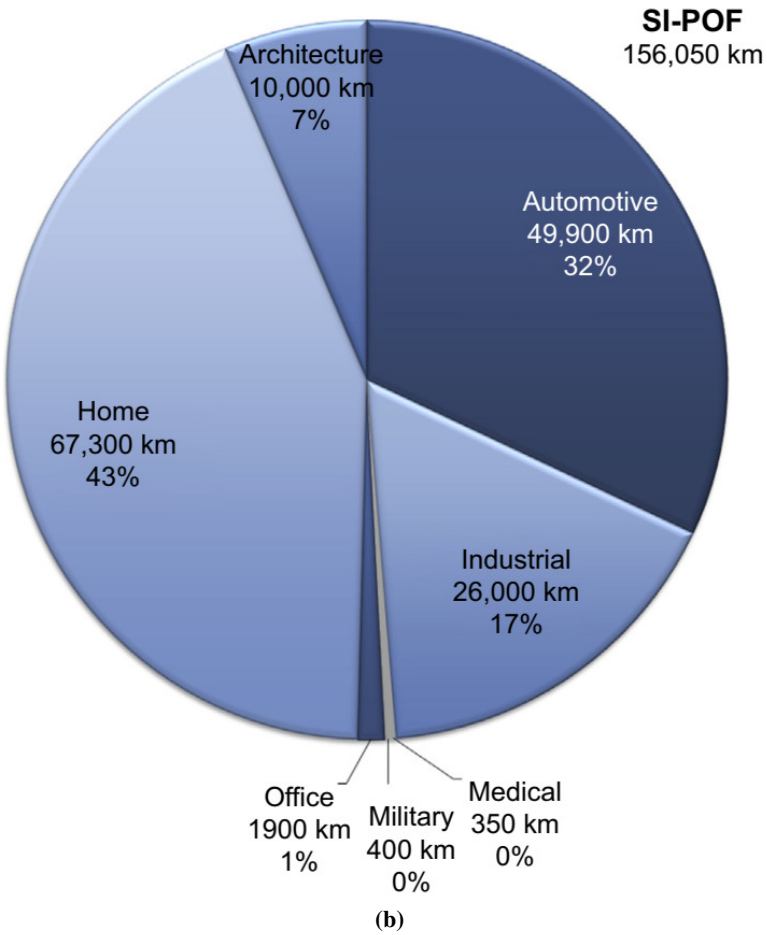


**(b)**

**Figure 1.2:** *(a) Worldwide POF Market (b) SI-POF demand for different applications (adopted from [36])*

example, SOHO, automotive/vehicular, industrial, medical, and military. Figure 1.2b illustrates the distribution of the SI-POF market for these applications as of 2015 [36]. The figure shows that the SI-POF market dominates SOHO, automotive and industrial markets. Digital signalling, especially in the fields of industrial controls and automotive applications, will be a future-proof market driver for POFs. But the main driver for POF in these applications is their use for short-range data links that resist EMI. Some common standards for major POF applications are summarised in Table 1.2 from works in [34, 40].

| **Application** | **Standard(s)** | **Bit-rate [Mbps]** | **fibre-length [m]** |
|---|---|---|---|
| SOHO | Ethernet | 100 - 10,000 | 50 - 200 |
| Automotive | Media oriented systems transport (MOST) | 25 - 150 | 5 - 70 |
| Industrial | Profibus, Sercos, InterBus | 2 - 1000 | 10 - 165 |

**Table 1.2:** *SI-POF applications and their common standards*

## 1.2 POF for fibre-in-the-home

POF systems have been implemented in SOHO networks as part of the fibre-in-the-home (FITH) concept by companies like Telefónica from Spain and Nitto from Japan [41, 42]. The first company had conducted POF installation in about 30 homes, while the latter one plans to carry 8K television signals in Japan for the Tokyo 2020 Olympics through a single POF cable without compressing the signal. FITH is the term given for the foreseen future broadband in-home/in-building networks. A network in which the service provider will ensure high bit-rate transmission service inside the user's house. Figure 1.3 illustrates the envisioned residential network with POF as the backhaul to various wired and wireless technologies. Explicitly, Fig 1.3 depicts light fidelity (Li-Fi) technology as an access point to the POF-based backbone, as it is a feasible and better option to Wi-Fi since it uses the optical spectrum that is less congested than its RF counterpart.

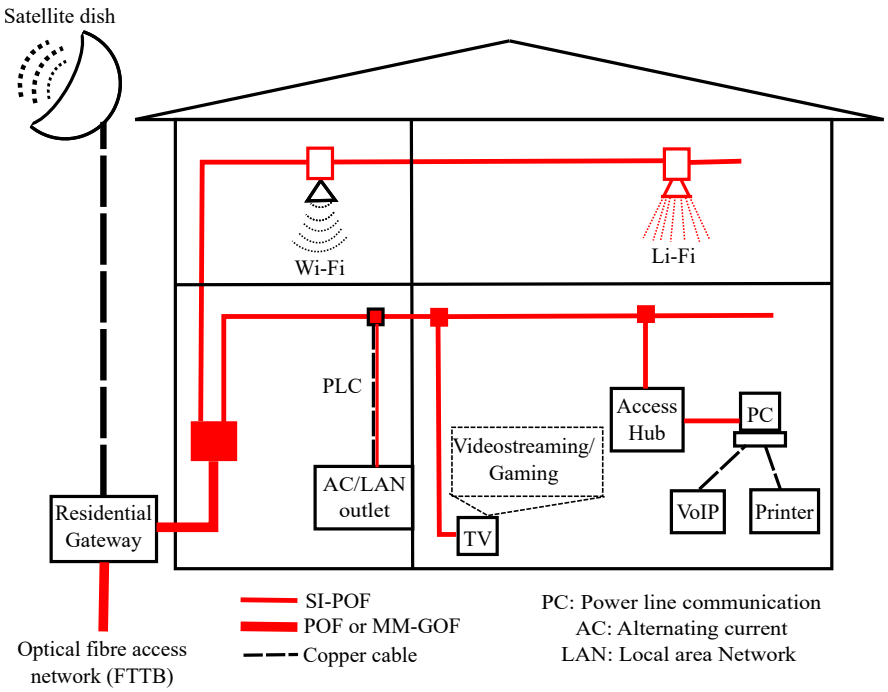


**Figure 1.3:** *FITH concept with POF as backhaul*

## 1.3 Motivation and Scope

The major disadvantage of SI-POF is that it has the lowest bandwidth among multimode fibres. For instance, the bandwidth of the PMMA SI-POF is ∼45 MHz at 100 m length [34]. However, it is 10 GHz for an MM-GOF with the same length. The small bandwidth of the SI-POF restricts the maximum data rate that it can transmit as transmission at higher rates results in inter-symbol interference (ISI) [34,43]. While ISI causes linear distortions, there are potential non-linearities inherent in the front-end devices that could further distort the POF system.

There are two methods to solve the SI-POF limited bandwidth problem. The first one is to use multilevel modulation schemes like $M$-ary pulse amplitude modulation (PAM-$M$) and $M$-ary quadrature amplitude modulation (QAM-$M$), and multi-carrier modulation techniques like orthogonal frequency division multiplexing (OFDM). The second method involves using equalisation techniques to mitigate the effect of ISI due to the SI-POF limited bandwidth. Equalisation requires accurate channel information that is fixed and is known apriori. Nevertheless, an SI-POF channel information depends on factors like bending, fibre-length, and temperature: hence, the need for adaptive equalisation.

Adaptive equalisation for SI-POF links is either done before transmission to the light source or

after reception from the optical receiver. A pre-equaliser does the former while a post-equaliser does the latter. Both methods are at the expense of the system power budget as the post-equaliser enhances the noise at the receiver while the pre-equaliser reduces the signal power before transmission. Post-equalisers has the edge over pre-equalisers as unlike the latter, they do not require back-to-back communication to obtain the channel information.

The channel distortion due to ISI is usually mitigated with the linear transversal (or FIR-filter based) equalisers. However, these equalisers are not optimum for a non-linear system. Hence, two notable solutions have been reported in previous studies to reduce the effect of the non-linear distortions. One is by applying non-linear pre-distortion techniques, the popular one being the inverse non-linear polynomial pre-distorter. This method requires knowledge about the estimated polynomial function that represents the non-linear response of the system. The inverse of this function is acquired and applied to the input signal before transmission. This way, the overall response of the system becomes more linear. The pre-distorter can be used in conjunction with the linear equaliser to mitigate both ISI and non-linearities in the system. The other solution is by applying non-linear post-equalisation schemes as they are capable of effectively decreasing the linear and non-linear distortions. A vital advantage of the non-linear equaliser (NLE) over the pre-distorter is that it can minimise both memory (or frequency-dependent) and memoryless non-linearities. But the inverse pre-distorter considers only the memoryless non-linear distortion.

Previous studies have adopted four kinds of NLEs for various communication channels. They are the decision feedback equaliser (DFE), the Volterra-based equaliser, the artificial neural network (ANN) based equaliser, and the maximum likelihood sequence estimator (MLSE). The DFE is similar to the linear transversal equaliser except that it has feedback from its output to its input. The Volterra equaliser is also identical to the transversal equaliser, but it involves computing the Volterra inputs before equalisation. These inputs come from the Volterra series, which is a memory-based Taylor polynomial series [44]. The Volterra equalisers can be used jointly with the DFE to achieve even better performance. The ANN-based equalisers adopt some underlying machine learning structures for mitigating ISI as well as the system non-linearities.

The MLSE offers the best symbol-error-rate (SER) performance of all the NLEs because unlike the other NLEs, the MLSE tests all possible symbol sequences and chooses the sequence with the maximum probability as the output. The MLSE does this with the Viterbi algorithm. How-

ever, it has the highest computational requirement when compared to the other NLEs. While the computational complexity of the other NLEs is either a linear or a polynomial function of their tap length, it varies exponentially with the tap length for the MLSE. The high computational complexity makes the MLSE impractical for most communication channels, mainly if a high-order modulation scheme is employed. Consequently, the MLSE will not be under consideration for this thesis.

For SI-POF systems, little has been done to investigate the Volterra and the ANN equaliser. Hence, the thesis focuses on the investigation and comparison of these NLEs for high-order modulation schemes in order to achieve high data rates for an SI-POF system. The NLEs under study are adaptive post-equalisers. Figure 1.4 illustrates the scope of the thesis and highlights the feasible NLEs with the SI-POF channel.

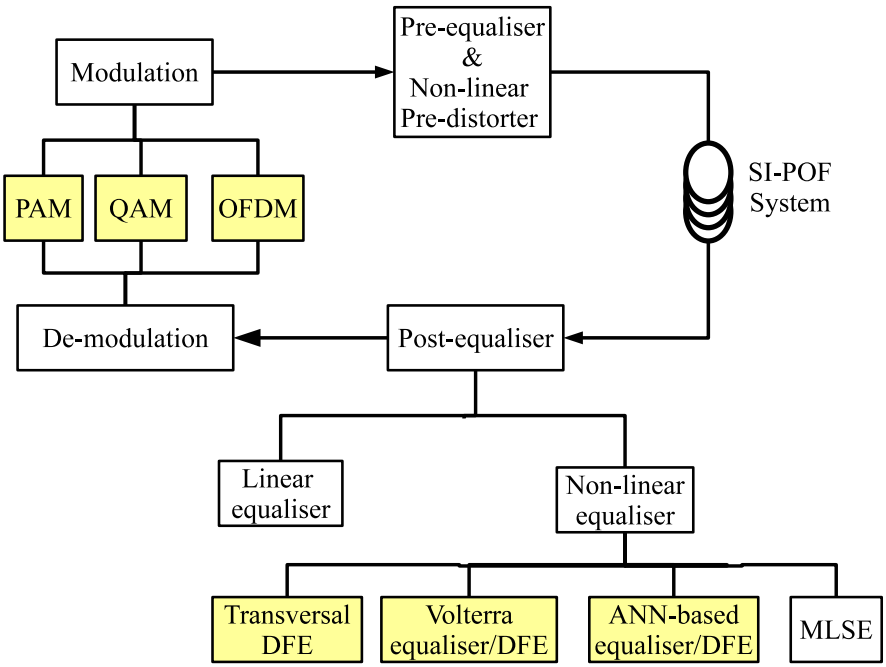


**Figure 1.4:** *Synopsis of thesis*

## 1.4 Objectives

This thesis aims explicitly to improve the bit-rate performance of SI-POF systems by implementing the NLE schemes discussed in the previous section. The performances of these NLEs are validated through extensive simulation studies and proof-of-concept experimental demonstrations.

Performance criteria such as bit-error-rate (BER), bit-rate ($R_b$), optical transmit power ($P_{oavg}$), and computational complexity are assessed widely for the NLEs. With valid state-of-the-art methods, the study examines the NLEs for a non-linear SI-POF system to quantify and compare these criteria; thus selecting the NLE suitable for the SI-POF system. At the end of this study, we should have an SI-POF link with a bit-rate of at least 500 Mbps using a minimum optical transmit power of 1 mW (which is the eye-safety/consumer-friendly power level [34]). The target BER of the link is below $3 \times 10^{-3}$, which is the standard forward error correction (FEC) limit with $\sim$7% overhead [43]. The length of the SI-POF link is between 10 m to 60 m. The target values for these criteria makes the SI-POF system to be applicable for SOHO, automotive and industrial applications (see Table 1.2).

It is also essential to minimise the power consumption from the optical transmitter, the optical receiver and the digital signal processor (which contain the modulator/demodulator and NLEs). For the NLEs, this is achieved by reducing its computational complexity without compromising the bit-rate and BER performance of the SI-POF link. The use of NLEs reduces the transmitted power of the SI-POF link, and this would be explored in later chapters.

In order to achieve the goals mentioned above, the specific thesis objectives are as follows:

- Identify and model the channel characteristics of an SI-POF system: This objective considers the standard fibre models used to obtain the frequency response of an SI-POF at different lengths. An experiment is used to validate the fibre models and explore the sources of non-linearities in the SI-POF system.

- Implement the NLEs in the time-domain (TD) for single-carrier modulation schemes: Equalisation is implemented in the TD using tapped delay line or transversal filters. They are used mostly for single-carrier modulation (SCM) schemes. The NLEs would, therefore, be investigated as TD equalisers for SCM schemes like PAM and QAM. Also, the BER performance and complexity of the NLEs is compared with one another to determine the optimum NLE for a non-linear SI-POF channel.

- Implement the NLEs in the FD: FD equalisers offers superior BER performance than TDE for highly dispersive channels [45]. Because it uses the fast Fourier transform (FFT) algorithm that is very efficient, FD equalisers are computationally less complex than TD equalisers. For this study therefore, the NLEs will be transformed from the TD to the FD and they are applied to SCM as well as multi-carrier modultion (MCM) schemes.

The complexity reduction from this transformation will be analysed extensively. And the BER performance of the NLEs in FD will be compared with one another.

- Compare the performance of PAM, QAM and OFDM when used with the NLEs: This comprises choosing the optimum modulation scheme and the optimum NLEs that offer the best bit-rate performance for a non-linear SI-POF system with minimal computational complexity and electrical power.

## 1.5 Contributions and Publications

In this thesis, the standard fibre model was used to estimate the frequency response of the SI-POF channel. The channel response is then used to evaluate the maximum capacity (or data rate) of the SI-POF channel for a given fibre length, transmitted optical power, receiver noise sensitivity, and coupling efficiency. The study also offers the optimum length for the SI-POF required to maximise the data-rate length product. The simulation results are experimentally validated. The non-linearities for the SI-POF system are measured at different fibre lengths with various setups of the modulation amplitudes and bias point of the optical source. Not only do the results show that the non-linearities increase with the modulation amplitudes, but also they show an optimal bias point that offers the minimum non-linearity.

An MLP architecture was implemented for the non-linear equalisation of PAM and QAM signals. An experimentally validated SI-POF model is used to compare the bit error rate (BER) performances of the MLP based equaliser with those of the transversal DFE and Volterra DFE. The three equalisers offer comparable BER performance at low-level modulation format when the non-linearity of the SI-POF system is negligible. However, for a high-level modulation format, the MLP equaliser presents the best BER performance. The simulation study has led to the publication of [46, 47]. Offline experiments are also used to compare the equaliser for an SI-POF channel that applied a high-level modulation scheme. The experimental work has led to the publication of [48]. Even though SI-POF system non-linearities increase with the modulation amplitude, it is shown in this study that the MLP equaliser significantly mitigate the effect of the non-linearities compared to the other equalisers.

The NLEs are converted from TD to FD not only for their reduced complexity but also for their usage with MCM schemes like OFDM. OFDM has a problem of high crest factor that can be solved simply by clipping, which induces more non-linear penalty to the system. The

experimental results obtained suggest that clipping the signal while using the FD based NLE improves the BER performance of the system compared to when the MCM scheme used the conventional equaliser. This result holds when the sub-carriers are mapped with low-level QAM format. The computational complexity for each NLE is analysed and compared with one another in TD as well as FD. And the results of the analysis give the condition for which the FD based NLE reduces the complexity of its TD counterpart.

For a highly non-linear SI-POF, the results from the comparison of the modulation formats used and their respective NLEs suggest that the MCM scheme is optimal for shorter SI-POF lengths while PAM is for longer SI-POF lengths.

These contributions have resulted in the following publications:

### 1.5.1 Journal articles

**I. N. Osahon**, S. Rajbhandari, and W. O. Popoola, "Performance comparison of equalisation techniques for SI-POF multi-gigabit communication with PAM-*M* and device non-linearities," *Journal of Lightwave Technology*, vol. 36, no. 11, pp. 2301–2308, 2018.

**I. N. Osahon**, M. Safari, and W. O. Popoola, "10-Gb/s Transmission Over 10-m SI-POF With $M$-PAM and Multilayer Perceptron Equaliser," *IEEE Photonics Technology Letters*, vol. 30, no. 10, pp. 911–914, 2018.

### 1.5.2 Conferences

**I. N. Osahon**, E. Pikasis, S. Rajbhandari, and W. O. Popoola, "SI-POF Transmission with CAP Modulation and Split-Complex MLP Equaliser," in *2018 IEEE International Conference on Communications (ICC)*. IEEE, 2018, pp. 1–6.

**I. N. Osahon**, C. Ziyan, T. Adiono, and W. O. Popoola, "SI-POF Transmission with OFDM and Sub-carrier Pairwise Coding," in *2018 IFIP/IEEE International Conference on Performance Evaluation and Modeling in Wired and Wireless Networks (PEMWN)*. IEEE, 2018, pp. 1–5.

**I. N. Osahon**, E. Pikasis, S. Rajbhandari, and W. O. Popoola, "Hybrid POF/VLC link with M-PAM and MLP equaliser," in *2017 IEEE International Conference on Communications (ICC)*. IEEE, 2017, pp. 1–6.

W. O. Popoola, E. Pikasis, and **I. Osahon**, "Hybrid polymer optical fibre and visible light communication link for in-home network," in *2017 26th Wireless and Optical Communication Conference (WOCC)*. IEEE, 2017, pp. 1–6.

**I. N. Osahon**, S. Rajbhandari, and W. O. Popoola, "Multi-layer perceptron as equalisers for multilevel pulse amplitude modulation scheme in SI-POF," in *International Conference for Students on Applied Engineering (ICSAE)*. IEEE, 2016, pp. 318–322.

### 1.5.3 Posters

**I. N. Osahon** and W. O. Popoola, "Equalisation Techniques for Plastic Optical Fibre Communication," in *School of Engineering Research Conference*. University of Edinburgh, 2017.

**I. N. Osahon**, S. Rajbhandari, and W. O. Popoola, "Multi-layer perceptron as equalisers for multilevel pulse amplitude modulation scheme in SI-POF," in *International Conference for Students on Applied Engineering (ICSAE)*. IEEE, 2016.

## 1.6 Thesis Outline

This chapter has provided the motivation and introduction for high-speed SI-POF communication with the aid of spectrally efficient modulation techniques and NLEs. The chapter also highlights the importance of the NLEs for SI-POF. The remainder of this thesis is structured as follows:

**Chapter 2** gives a background on POF communication and non-linear equalisation schemes. It begins with an overview of the history and the fundamentals of POF communication. It also looks into the sources of linear and non-linear distortions in a POF system. Additionally, the essential knowledge of the NLE schemes under this study is reviewed and discussed in more detail. The chapter then surveys the concept of frequency domain equalisation for single-carrier modulation schemes (like PAM and QAM). The final section of this chapter gives a review of the state-of-the-art for high-speed SI-POF transmission with the NLEs considered in the thesis.

**Chapter 3** extends chapter 2 by describing the SI-POF transmission via intensity-modulation and direct-detection (IM/DD). The modulation schemes suitable for IM/DD transmission are reviewed. In the second section of this chapter, a description of the IM/DD model for an SI-

POF channel is presented. From this section, the Butterworth model [49, 50] , the Gaussian estimation model [33, 51] and the time-dependent power flow equation [52–55] are used to evaluate the frequency response of the SI-POF channel. The capacities from these models are analysed and compared for varying SI-POF lengths. The third section describes two IM/DD experimental setups that would be used to demonstrate the performance of the NLEs throughout the thesis. The first one involves a red laser diode (LD) as the transmitter, while the second one includes a red resonant cavity light-emitting diode (RC-LED). The non-linearities of these setups are then measured and evaluated in the last section.

**Chapter 4** evaluates and compares the performance of the NLEs in the time-domain for PAM and CAP transmission over SI-POF. It starts this evaluation with the IM/DD model discussed in chapter 3, and the model considers the device non-linearities. The experimental setups addressed previously are also used to assess the performance of the NLEs. The NLEs are then compared based on their computational complexities to account for their power consumption and practical system implementations.

**Chapter 5** presents the implementation of a recently developed FD based NLE (FD-NLE) for DMT transmission over SI-POF. The FD-NLE is an FD representation of the Volterra equaliser [56]. The chapter also assesses and compares the performance of the FD-NLE to that of the conventional frequency-domain equaliser. The comparison is considered in a non-linear SI-POF system for DMT transmission both with and without clipping. In addition, the chapter demonstrates a conversion of the Volterra and the MLP equalisers from the TD to the FD for single-carrier (PAM and QAM) transmission over SI-POF. The computational complexity of the equalisers is evaluated and compared for both TD and FD.

**Chapter 6** presents an experimental investigation and comparison of the modulation formats (PAM, CAP and DMT) using the NLEs for high-speed SI-POF communication. The comparisons of the modulation schemes are based on their bit-rate performance, their computational complexities and the average electrical power of their transmitted signal.

**Chapter 7** highlights the main findings and limitations of the research work. Recommendations for further research are identified here.

## 1.7 Summary

The rapid growth in indoor data traffic requires the need for short-range optical fibre technologies. The SI-POF system is among these technologies and has been envisioned as the candidate media for FITH. A deep understanding of the underlying issues with SI-POF communication has been discussed. Despite the notable research efforts and commercial standards employed for SI-POF communications, the question of using NLE such as the Volterra and the ANN equaliser remains open. The current work provides a further understanding of these NLE techniques for high-speed transmission over the SI-POF. It also proposes their feasibility to improve the system implementation at the physical layer significantly.

# Chapter 2
# Background and Literature Review

This chapter covers the background concepts of the SI-POF system and the NLE schemes that are considered in this thesis. Regarding these concepts, a review of the state-of-the-art from recent literature is presented to lay a solid background for the techniques that are later developed in the thesis. The chapter also comments on the history of POF communication, working principles of the optical sources and receivers, the sources of distortion for a high-speed SI-POF system, and the notion behind FD based equalisation.

## 2.1 Historical development of POF communication

POFs were initially manufactured with polymethacrylate (PMMA) polymers in the early 1960s by Pilot Chemical of Boston [33,57]. They later underwent significant developments by DuPont in the late sixties. Due to the incomplete purification of the source materials used, the fibre attenuation was still about 1 dB/m before DuPont decided to handover the POF business to Mitsubishi Rayon. During the seventies, Mitsubishi Rayon was able to reduce the attenuation nearly to the theoretical limit of approximately 0.125 dB/m at a wavelength of 650 nm [33, 57]. The fibre was an SI-POF with a bandwidth of 50 MHz over 100 m. Then, glass fibres with losses significantly below 1 dB/km at 1,300 nm and 550 nm were already available in large volumes and at low prices. These fibres were exclusively used for long-range digital transmission systems that require high bit-rates. Copper cables were the dominant media in local computer networks because they were entirely adequate for the typical data rates of up to 10 Mbps usually accepted then. There was hardly any demand for an optical medium for short distances so that the development of POF was slowed down for many years. A pointer to this is the fact that at the beginning of the nineties the company Hochst stopped manufacturing plastic fibres altogether.

During the nineties, after data communication for long-haul transmission had become completely digitalized, the advancement of digital systems for individual users commenced on a

massive scale. This development increased the demand for short-range media that support higher transmission speeds of at least 100 Mbps. POFs were able to meet this requirement to an optimum degree and were thus becoming of increasing interest. Consequently, the first annual international conference for polymer fibres and applications took place in 1992. The conference presented the most significant scientific event in this specialized field, one of which was by Prof. Koike and his colleagues at Keio University. Their work involved the manufacture of a graded-index POFs (GI-POFs) using PMMA material. The POF has a bandwidth of 3 GHz.km with an attenuation of about 0.15 dB/m at 650 nm wavelength [58, 59]. The progress by Koike solved the bandwidth problem of the PMMA SI-POFs, but attenuation was still high. The next significant development was a perfluorinated GI-POF (PF-GI-POF), which was also developed by Prof. Koike and his partners at Keio University in 1995. This POF has an attenuation of less than 0.05 dB/m over a range of 650–1300 nm wavelength [60]. With the lesser attenuation and higher bandwidth of the PF-GI-POF, Bell Laboratories reported in the year 1999 that they had achieved 11 Gbps transmission over 100 m [61].

At the start of the 21st century, a research group from Australia led by Van Eijkelenborg reported the development of a microstructured POF (m-POF) [62]. This POF is similar to ”holey” or ”bandgap” glass fibres and gives higher bandwidths than GI-POF. However, the attenuation of the first m-POF was 30 dB/m as of 2001. Since then, there has been much interest in the fabrication processes that reduce their attenuation. The best m-POFs today have an attenuation of about 0.2 dB/m at a wavelength of 650 nm for fibre lengths below 20 m [63]. Thus, they have a competitive advantage over the other POFs in short-distance/ high-bandwidth applications.

Since 2002, Asahi Glass has been manufacturing PF-GI-POF to use them for in-building networks in Japan. The PF-GI-POF cable was not available until it was introduced commercially in 2005 by Chromis Optical Fibre. Chromis Optical Fibre, which was once a spin-off of Optical Fibre Solutions (OFS) and Bell Laboratories, licensed the manufacture of the GI-POF from Asahi. Chromis developed a continuous extrusion process for the manufacture of GI-POF compared to the batch process developed by Asahi. The Chromis fibre process produces higher-quality fibres at a lower cost. Fuji Photo Film announced the first commercially available data link using a GI-POF in 2005 [64]. The link was a 30 m digital-visual-interface (DVI) operating at 1 Gbps using a 780 nm laser diode (LD). The link used a PMMA GI-POF developed by Fuji Photo under license from Keio University. In early 2005 PMMA GI-POF became commercially available from the Optimedia Company of Korea.

From the year 2010 till date, two standardization bodies have been developing gigabit communication standards for SI-POF aimed towards home networking applications. The first is a gigabit Ethernet standard over POF (GEPOF) that was initiated by VDE (verband der elektrotechnik elektronik informationstechnik) [65, 66]. It was expected to be released at the beginning of 2012 but was withdrawn and handed over to an IEEE (institute of electrical and electronics engineers) task force. The task force has been meeting since then until the publication on 2017 of the IEEE802.3bv standard [67]. The IEEE 802.3bv (also termed 1000BASE-RH) defines an error-free (BER $< 10^{-12}$) 1 Gbps full-duplex transmission over a 50 m SI-POF using a red resonant cavity LED (RC-LED) [65–67].

## 2.2 Features of POF Communication

POF communication links, as optical systems, essentially consist of three components: transmitter, receiver and the optical fibre. The transmitter converts an electrical sequence of signals into an optical one and inputs it into the optical fibre. The optical signal in the fibre is then forwarded into the receiver. Here, the signal is converted back into an electric signal that is then available for further processing. The widely accepted optical fibre is a solid dielectric cylinder, known as the core of the fibre. The core is an optical waveguide that has a refractive index $n_{co}$. And it is surrounded by another solid dielectric called cladding, whose refractive index $n_{cl}$ is less than that of the core. The cladding reduces losses due to the optical signals that escape the core and it adds mechanical strength to the fibre [68].

### 2.2.1 Step-index and graded-index POF

POFs are multi-mode fibre optic cables as they have a large diameter core ($> 500$ $\mu$m), which allows the propagation of several modes (or "streams") of light [33, 34]. One class of these POFs has its core with a constant refractive index. From Fig. 2.1, the refractive index profile for these POFs looks like a pulse or step, and thus this kind of fibre is called the step-index POF (SI-POF). In the SI-POF, some light rays may travel a direct route, while the others zigzag as they bounce off the cladding. These alternate paths cause the different groups of light rays to arrive separately at the receiving point. The pulse that generates the light rays broadens as a result and loses its well-defined shape. This phenomenon causes dispersion in the SI-POF. Minimal dispersion is favourable for high-speed communication as the effect of dispersion

increases at higher data rates.

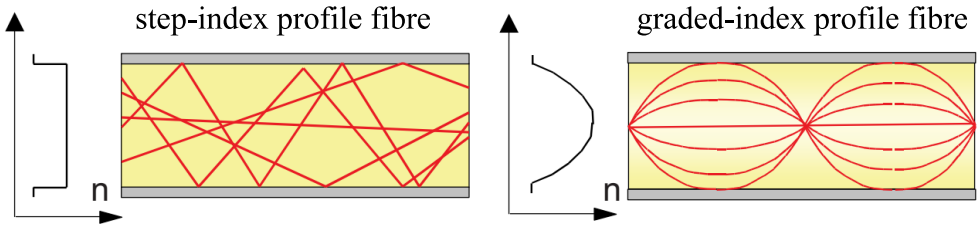


**Figure 2.1:** *Ray path and refractive index profile for SI-POF and GI-POF adopted from [57]*

The standard SI-POFs are manufactured with PMMA, whose attenuation profile is depicted in Fig. 2.2a. The PMMA material has several attenuation windows that enable it to be used with different visible light sources that go from the blue to red wavelength. The SI-POF has the lowest attenuation of ∼50 dB/km the fibre is at the 520 nm (green) wavelength, while its highest attenuation is ∼150 dB/km at the 650 nm (green) wavelength [57, 69]. This type of fibre is best suited for transmission over distances shorter than 100 m at data rates less than 100 Mbps.

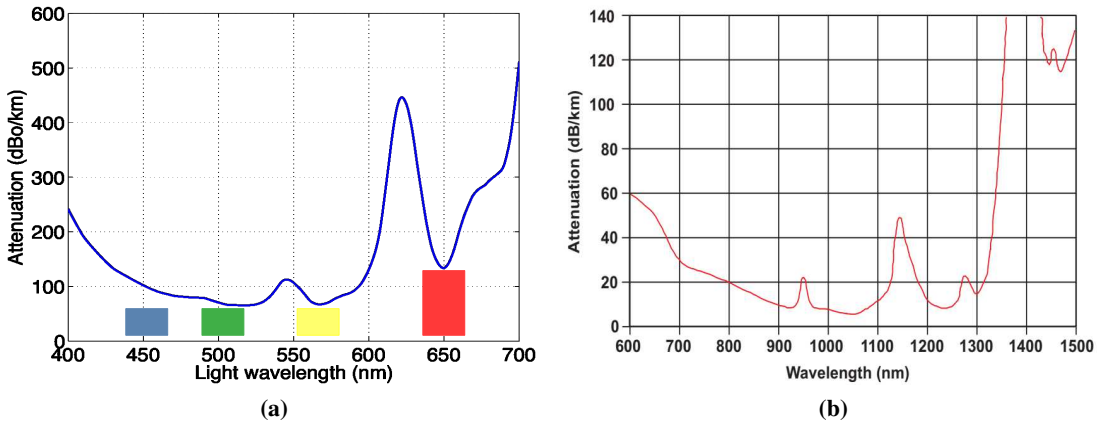


**Figure 2.2:** *Attenuation as a function of optical wavelength for: (a) PMMA SI-POF (b) PF-GI-POF (adopted from [57])*

Graded-index POF (GI-POF) contains a core, whose refractive index diminishes gradually from the centre axis out toward the cladding, as illustrated in Fig. 2.1. The light rays at the centre with higher refractive index advance at the fibre axis more slowly than those near the cladding. Due to this graded-index profile, light in the core curves helically rather than zigzag off the cladding, thus reducing its travel distance. The shortened path and the higher speed allow the rays at the edge to arrive at the receiver at about the same time as the slow but straight rays in the core axis. Consequently, the pulse that generates the light rays suffers from smaller dispersion

with GI-POF compared to that with SI-POF.

Some GI-POFs are made of PMMA, and they have a bandwidth of about 1 GHz at 100 m length. Another set of GI-POFs that are presently available in the market is based on amorphous fluoropolymers (like CYTOP): this POF is called PF-GI-POF [64]. The attenuation profile of the PF-GI-POF is presented in Fig. 2.2, and it shows that the POF operates at optical wavelengths from visible-red (650 nm) to infra-red (1300 nm) region. The minimal attenuation of the PF-GI-POF is $\sim$10 dB/km at an optical wavelength of 1100 nm. Hence, this type of fibre is best suited for gigabit communication at long-range ($> 100$ m) local-area networks [33].

### 2.2.2 Optical sources and receivers for POF transmission

The light sources that transmit data through optical fibres include the light-emitting diodes (LEDs), resonant cavity LEDs (RC-LEDs), laser diodes (LDs) and vertical-cavity surface-emitting laser diodes (VCSELs). The parameters of these sources are compared in Table 2.1 for an SI-POF system [33,69]. The simplest and oldest form of a light source for POF transmission systems is the LED. It emits incoherent light with a relatively broad spectral width ($\sim$30 nm). The bandwidth and the optical power of the LEDs are the least of all the optical sources used in SI-POF systems. However, the LEDs are very cheap, and they have the longest life-span of all the optical sources. Several studies have demonstrated that equalisation can significantly improve the performance of LED-based SI-POF systems [65, 66, 70–78]. The transversal DFE and Volterra DFE are the equalisers used with these systems.

In contrast, the LDs have the highest bandwidth and power of all the optical sources. They also emit coherent light with narrow spectral widths below 2 nm. The LDs have a common feature known as the threshold current ($I_{th}$). The LD emits coherent light with high power when the input current is above $I_{th}$. If the input current is less $I_{th}$, the LD radiates incoherent light at relatively low power. This radiation is termed "spontaneous emission", and it happens for an LED [68, 79]. LDs are the most expensive, and they have the shortest life-span of all the optical sources. The LEDs and LDs for SI-POF systems are manufactured with wavelengths that span across the visible light spectrum (400 nm - 700 nm) as shown in Table 2.1.

The LED has a very broad beam characteristic with an NA of 0.8, and this is disadvantageous in terms of coupling to the fibre, as the PMMA SI-POF only has an NA of 0.5. Thus, a direct coupling between LED and the fibre leads to a power loss due to the LED's large NA. Therefore,

| Parameters | LED | LD | VCSEL | RC-LED |
|---|---|---|---|---|
| Wavelength(s) [nm] | 470, 520, 570, 650 | 405, 442, 488, 520, 650 | 660 | 650 |
| Spectral width [nm] | 25-40 | 2 | 1 | 10 |
| Threshold current [mA] | - | $> 15$ | 2 | - |
| Average optical power [mW] | 0.2-1 | 2-20 | 1 | 0.2-1 |
| Electrical 3 dB bandwidth [MHz] | 10-50 | $> 1000$ | $> 1000$ | 70-100 |
| Cost | Very cheap | relatively cheap for 650 nm; LDs with other wavelengths are expensive | Less expensive than LDs | Cheap |
| Maximum operating temperature [°C] | 85 | 50 | 40 | 85 |
| Launch NA | 0.8 | 0.15 | 0.25 | 0.35 |

**Table 2.1:** *Comparison of light sources for POF systems [33, 69]*

studies have been executed for LEDs to form a narrower beam. A result of these studies was the resonant-cavity LED (RC-LED). The basic structure of the RC-LED is formed by a thin quantum well active region sandwiched by two mirrors that form a Fabry-Perot cavity [80]. This cavity effect produces a smaller launching beam, and the modulation bandwidth is additionally increased. RC-LEDs are manufactured at visible wavelengths across the red, blue and green window. But only the red one is commercially available for SI-POF systems because it offers the highest optical power (of $\sim$1 mW). The blue and green RC-LED offer optical powers below 0.2 mW, and this power constraint makes them impractical for longer ($>$ 30 m) SI-POF links [81, 82]. Hence they are rarely used in high-speed SI-POF systems.

An alternative to the LD is the VCSEL, as its vertical structure can be produced in a much cheaper process. Another advantage of the VCSEL is that it requires a smaller threshold current than that needed from the LD. Thus, the driving current is much smaller, as it can be seen in Table 2.1. The drawbacks of the VCSEL to the LD are that it has a larger NA, and its centre wavelength is 665 nm. The first drawback is still an advantage, as it is within the SI-POF coupling tolerance. But the latter is a significant disadvantage because the spectral attenuation at 665 nm is $\sim$225 dB/km, in comparison to 150 dB/km at the optimum wavelength of 650 nm in the red window (as illustrated in Fig. 2.2a). VCSEL in SI-POF systems is manufactured presently at visible wavelengths only across the red window.

The optical receiver converts an optical signal into its electrical form and recovers the data transmitted through a lightwave system. It comprises of two elements, which are the photodetector and the electronic amplifier circuitry. The first component converts the optical into an electrical signal through the photoelectric effect while the latter magnifies the electrical signal so that subsequent electronics can process the signal.

The requirements for a photodetector are fast response, low noise, low cost, and high reliability. The photodetectors are classified as photoconductors, phototransistors and photodiodes: these are made of semiconductor materials [68]. Among the photodetectors, the photodiode (PD) is used almost exclusively in fibre optic communication as its size is compatible with the fibre-core size. Three types of PDs are employed in SI-POF systems, and they are the pin PD (PIN-PD), the avalanche PD (APD) and the metal-semiconductor-metal PD (MSM-PD) [57].

| **Parameters** | **PIN-PD** | **APD** | **MSM-PD** |
|---|---|---|---|
| Electrical 3 dB bandwidth [GHz] | 0.3-7 | 0.17-3.5 | $> 20$ |
| Sensitivity | High | Very high | Very low |
| Reverse Voltage [V] | 5-10 | 20-400 | 0.5-1 |
| Responsivity [A/W] | 0.4-0.95 | Very high: varies with APD internal gain | 0.01-0.35 |
| Cost | Cheap | Expensive | Very Expensive |

**Table 2.2:** *Comparison of Photodiodes for POF systems [33, 83]*

The PIN-PD consists of an intrinsically doped interface layer between the p and n zones. The light absorption primarily takes place in this area. The APD has a highly doped layer in which the electrons produced are multiplied and accelerated by a strong local electric field. With the MSM-PD, there is no p-n junction. Finger-like electrodes are applied to an absorbing semiconductor surface. The bias voltage applied pulls off the ensuing charge carriers. The construction of most PIN-PD and APD is realised with silicon as well as with other semiconductor materials.

The internal gain of an APD can amount to 400. Since the gain is not the same for every generated electron, the APD produces additional noise. However, the noise of the amplifier section of the receiver generally exceeds that in the PD by far. Since the APD already generates high amplification before the first stage, the electronic noise thus plays a much smaller role. On average, APD receivers are about 10 dB more sensitive than pin-PD receivers [57]. MSM-PDs are the fastest PDs with bandwidths up to 30 GHz. However, due to their high cost, they

have been rarely used commercially for POF systems. A qualitative comparison of the most important characteristics of these three types of PDs can be found in Table 2.2. The PIN-PD represents a good compromise in all parameters and is furthermore moderately priced. Practically all commercial POF receivers are indeed based on the PIN-PD with the most reasonably priced semiconductor materials. All the receivers used in this study contain a Silicon PIN-PD (Si-PIN-PD). The responsivity of a Si-PIN-PD is presented as a function of optical wavelengths in Fig. 2.3 [57].

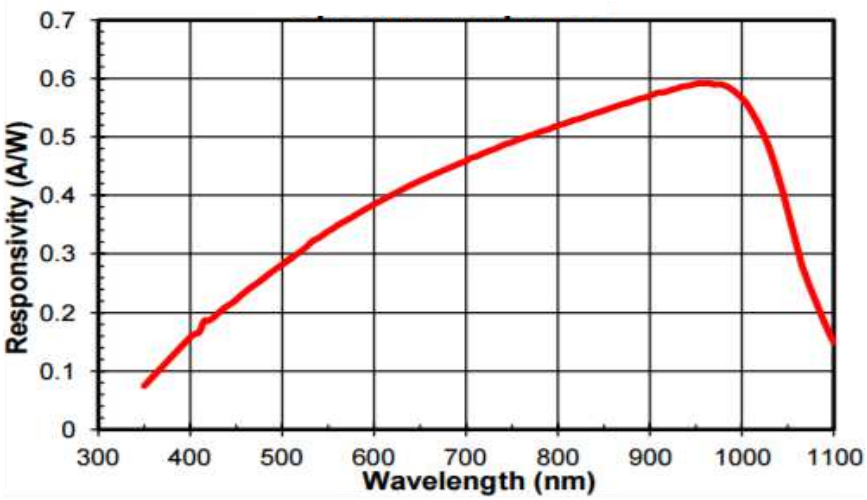


**Figure 2.3:** *Responsivity of a Silicon PIN-PD as a function of wavelength adopted from [57]*

The amplifier section of the optical receiver has a compromise between the gain, bandwidth and the noise sensitivity of the amplifier. The trans-impedance amplifier (TIA) is the most suitable amplifier configuration used in optoelectronic receivers. Its gain depends proportionally to the choice of its feedback resistance. Increasing the feedback resistance reduces the bandwidth as well as the noise of the optical receiver.

### 2.2.3 POF coupling and bending losses

Macro bends usually occur during the POF installation process. When the curvature is small, losses are practically negligible. As the bend radius decreases radiation losses increase, but the losses being higher for GOFs than for SI-POFs of the same diameter. For instance, the total radiation loss caused by a full turn in a typical PMMA SI-POF of 1 mm diameter and NA $= 0.5$ for bend radii of 5 mm and 15 mm is 2.1 dB and 0.5 dB, respectively [34,57]. The bending loss in optical power also exponentially depends on the light wavelength and NA.

The high NA (of 0.5) for 1 mm PMMA SI-POF makes the light launch into the fibre easier and allows simple coupling from the light source to the POF. The guaranteed output power from VCSEL and LD is much higher than that of RC-LED and worst for LED. To the SI-POF, the coupling loss is lesser from VCSEL and LD than that from the RC-LED. And it is even much higher for the LED. Coupling the SI-POF to a PD is not an easy task. The POF needs to be relatively close to a PD of $\sim$1 mm diameter to transmit all of its light. One main problem is that the large-area PD has a large capacitance, which limits the bandwidth of the optical receiver. The bandwidth can be increased by decreasing the TIA feedback resistance to obtain the required bandwidth. Using small-area PDs (of 300 $\mu$m to 500 $\mu$m diameter) will, therefore, improve the receiver bandwidth. But to minimise the coupling loss, the POF can be coupled to the PD via a lens or taper. Table 2.3 summarises a comparison between the coupling efficiencies for PDs of different diameters [33,34,57]. The coupling efficiency with the direct butt coupling is the worst of all the coupling methods, and it is observed to be approximately equal to the ratio of the PD area to the POF area. The taper has a better coupling efficiency than the lens, and it is favourable for coupling 1 mm POF to smaller diameter PDs.

| PD diameter [$\mu$m] | Butt coupling [%] | Lens [%] | Taper [%] |
|---|---|---|---|
| 300 | 8.3 | 31.6 | 50.5 |
| 400 | 16.4 | 46.6 | 75.5 |
| 500 | 23.4 | 60.6 | 83.2 |

**Table 2.3:** *Comparison of efficiencies for various methods of coupling the SI-POF to PDs of different diameters [34, 57]*

## 2.3 Distortions in SI-POF Communication Systems

Apart from noise from the receiver, there are elements of SI-POF systems that contribute to their linear distortions, which result in ISI during high-speed communication. SI-POF systems also consist of components that induce non-linearities, which distort the systems even further [56].

### 2.3.1 Linear distortions

One source of linear distortion in high-speed SI-POF systems is the optoelectronic devices that include the optical transmitters and receivers. And it mostly comes from the limited modulation

bandwidth that dictates how fast the electrical input signal can drive the optical output for the transmitters and how fast the optical signal is converted to the electrical output for the receivers. Besides, there are background electronics like amplifiers for these devices that further restricts the modulation bandwidth of the SI-POF.

The POFs used today are generally multi-mode fibres so that chromatic dispersion, waveguide dispersion and polarisation-mode dispersion can be neglected as their sources of linear distortions [53, 54, 84]. This leaves out mode dispersion as the relevant process to be considered since it dominates the other sources of dispersion in the fibre. There are three dominant multi-mode impairments of the SI-POFs that are considered in recent studies, and they are the mode-dependent attenuation, the modal dispersion, and the mode coupling [53, 54, 84]. Because the core size of the fibre is much larger than the wavelength of light (about 1 $\mu$m), the propagation mechanism of multi-mode fibres can be analysed with geometric (ray) optics representation.

The mode-dependent attenuation for SI-POF can be modelled with three attenuation sources. The first is due to the different path lengths of different modes. The second is due to reflections at the core-cladding interface. And the third is from the Goos-Haenchen effect, which suggests that the total reflection occurs mostly in the cladding and not in the core-cladding interface [50]. Modal dispersion is a distortion effect in multi-mode fibres, in which the signal is spread in time because of separate transit times of different modes. This effect is similar to the multi-path propagation problem in wireless environments. In the step-index fibre, the different transit times are due to the different path lengths of different modes. Modes with a larger angle, also have a longer path, which leads to a longer transit time. Mode coupling refers to the process of transferring power between modes. The power transfer can happen at scattering centres inside the fibre, which are mainly caused by density variations of the core material and Rayleigh scattering. Since light-scattering in an SI-POF generates the biggest contribution to the attenuation, this process is always present.

### 2.3.2 Non-linear distortions

SI-POF systems may contain many non-linear components including driving circuits, digital-to-analogue converters (DACs), analogue-to-digital converters (ADCs), optical sources (LEDs or LDs) and optical receivers. Among all these non-linear components, the optical source is the primary cause of non-linearities in the POF channel [85]. The POF non-linearity is insignificant compared to those of the optical sources [86].

For an electric signal to drive the optical source, the input signal must be higher than the turn-on value and less than the maximum permissible value or the saturation point of the source. When the signal is beyond the required dynamic-range, clipping on both sides occurs. Clipping results in distortions and degrades the POF performance. Even when the signal is within the dynamic range, the input-output relationship may not be linear due to the non-linear transfer function of the electrical and the optoelectronic front-ends.

## 2.4 Non-linear Equalisers

Equalisers are the common methods used to solve the ISI caused by modal dispersion in the POF channel. They are broadly classified as linear equalisers and NLEs. The output of a linear equaliser is a linear combination of scaled and delayed versions of the input of the equaliser. The drawback of a linear equaliser is that it cannot distinguish between the signal and the noise [34, 43]. As such, it amplifies the noise at high frequencies while mitigating ISI. This noise enhancement causes transmission at high data rates for a band-limited channel to be severely limited by SNR. The NLE schemes are therefore commonly used in applications where the channel ISI distortion is too severe. There are four groups of adaptive NLE methods employed in digital communication systems:

- Transversal (or conventional) decision feedback equalisation (DFE).
- Volterra-based equalisation (including Volterra DFE)
- Machine learning (or ANN) based equalisation
- Maximum likelihood sequence estimator (MLSE).

The MLSE is the optimum equalisation scheme among all the NLEs in the sense that it minimises the BER of a channel with ISI [43]. It has a computational complexity that grows exponentially with the length of the channel time dispersion. If the size of the symbol alphabet is $M$ and the number of interfering symbols contributing to ISI is $N_t$, the Viterbi algorithm computes $M^{N_t+1}$ metrics for each new received symbol [34, 43]. For communication methods that apply a modulation scheme with high values of $M$ over channels with considerable ISI, the resulting computational complexity is prohibitively expensive to implement. Furthermore, the other NLEs give a similar BER performance like that from the MLSE. Consequently, this thesis will not focus on MLSE, as previously discussed in section 1.3.

### 2.4.1 Transversal Decision feedback equalisers (TRDFE)

The conventional DFE consists of two filters, a feedforward filter and a feedback filter arranged as shown in Fig. 2.4. The input to the feedforward filter is the received signal sequence, while that of the feedback filter is the sequence of decisions on previously detected symbols. All the inputs and outputs to the DFE can be real-valued or complex-valued. Functionally, the feedback filter is used to remove that part of the ISI caused by previously detected symbols. Since the detector feeds hard decisions to the feedback filter, the DFE is nonlinear. The conventional DFE can also be called transversal DFE (TRDFE) because its output is a direct function of tap-delay (or transversal) versions of both feedforward and feedback inputs as Fig. 2.4 shows. The equalised output for TRDFE is expressed as [43]:

$$\tilde{z}_n = \sum_{a=0}^{N_{ft}-1} w_a^* y_{n-a} + \sum_{b=1}^{N_{bt}} w_b^* \hat{z}_{n-b}, \tag{2.1}$$

where $\{y_n, ..., y_{n+1-N_{ft}}\}$ is the unequalised input sequence, $\{\tilde{z}_{n-1}, ..., \tilde{z}_{n-N_{bt}}\}$ is the set of previously detected symbols; $w_a$ and $w_b$ are the co-efficient of the feedforward and feedback tap weights respectively; $N_{ft}$ and $N_{bt}$ denotes the number of feedforward and feedback taps for the DFE respectively, while $^*$ represents the complex conjugate operation (if the inputs of the TRDFE are complex-valued).

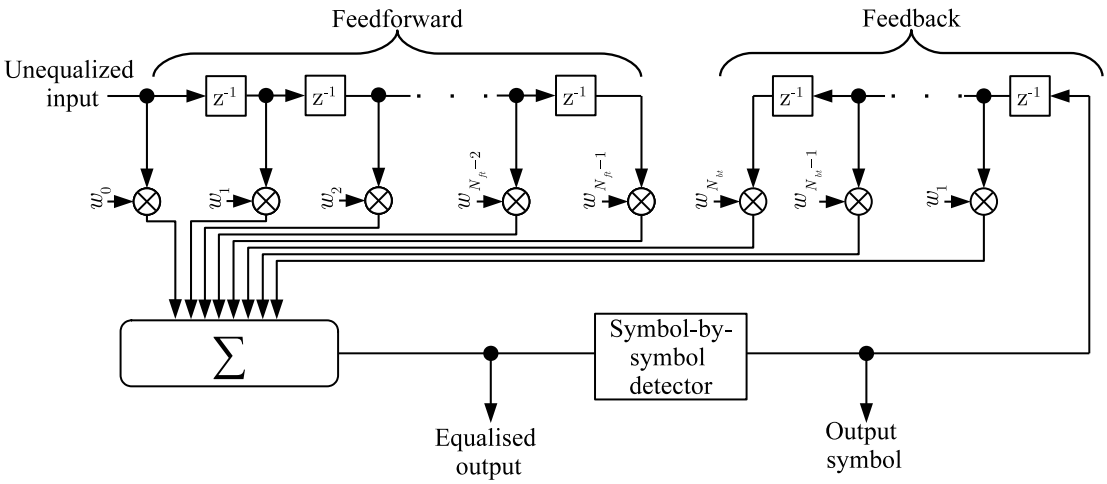


**Figure 2.4:** *Block diagram illustrating the structure of a transversal DFE (TRDFE)*

The tap weights of the TRDFEs are estimated with either zero-forcing algorithms or the minimum mean square error (MMSE) adaptation algorithms. Zero-forcing is simpler than the MMSE algorithm but results in more noise enhancement. The common MMSE algorithms are

the least mean squares (LMS) and recursive least squares (RLS) [34, 43]. LMS is simpler (and executes faster) than RLS, but RLS has better convergence than LMS in the sense that it requires less training symbols [34, 44]. Therefore, the RLS algorithm would be used for conventional DFE unless otherwise stated in this study.

The algorithms for the TRDFE have two modes of operation: training mode and decision-directed mode [34,43]. In training mode, the transmitter generates data symbol sequence known to the receiver; and the sequence is used to train the equaliser. In decision-directed mode, the equaliser is trained with its detected output.

### 2.4.2 Volterra equalisers

As discussed in Section 1.3, the inputs to the Volterra equaliser is based on the Volterra series. Nonetheless, the equaliser is similar to the transversal equaliser because its output also depends linearly on the input coefficients of the equaliser. Hence, the theory of the Volterra equaliser is an extension of that of the transversal equaliser. In other words, the Volterra equaliser can be adapted with the MMSE algorithms (LMS and RLS) just like the transversal equaliser; and the inputs and outputs to the Volterra equaliser can be real-valued or complex-valued. Adding a feedback filter to the Volterra equaliser produces a Volterra DFE as Fig. 2.5 shows.

A drawback of the Volterra equaliser is the computational complexity if the full polynomial series of its input is employed. By truncating the Volterra inputs of the equaliser, one can reduce the computational complexity at the cost of lower BER performance. Even with reduced order, the Volterra equaliser is quite computationally complex even when the orders of the series and the filter are moderate. In practical systems, the Volterra equaliser can be either the second order, third order or the combination of both orders of its inputs [77, 78, 87–89].

In this study, therefore, either second-order Volterra DFE (VOLT2DFE) or the third-order Volterra DFE (VOLT3DFE) will be considered. The optimal choice of which order depends on the non-linear properties of the POF channel (this will be examined later in chapter 3). The expression of the equalised output for the complete VOLT2DFE is [87]:

$$\tilde{z}_n = \sum_{a=0}^{N_{ft}-1} w_a^* y_{n-a} + \sum_{b=1}^{N_{bt}} w_b^* \hat{z}_{n-b} + w_{dc}^* + \sum_{a=0}^{N_{ft}-1} \sum_{c=a}^{N_{ft}-1} w_{a,c}^* y_{n-a} y_{n-c}^*, \tag{2.2}$$

where $w_{a,c}$ denotes the second-order Volterra kernels, and $w_{dc}$ is a constant. Similarly, the

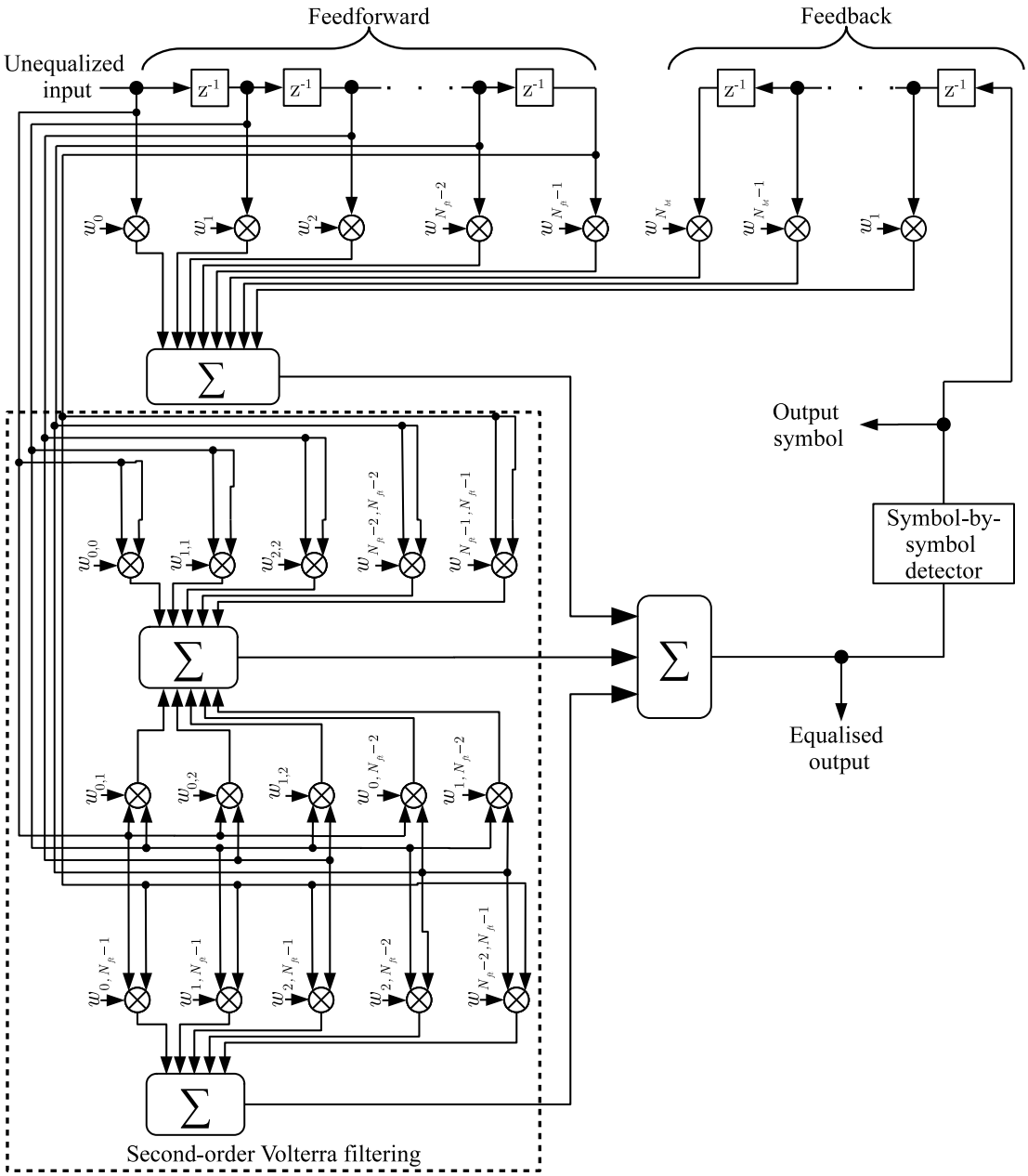


**Figure 2.5:** *Block diagram illustrating the structure of a 2nd-order Volterra DFE (VOLT2DFE)*

expression of the equalised output for the complete VOLT3DFE is [87]:

$$\tilde{z}_n = \sum_{a=0}^{N_{ft}-1} w_a^* y_{n-a} + \sum_{b=1}^{N_{bt}} w_b^* \hat{z}_{n-b} + w_{dc}^* + \sum_{a=0}^{N_{ft}-1} \sum_{c=a}^{N_{ft}-1} \sum_{d=c}^{N_{ft}-1} w_{a,c,d}^* y_{n-a} y_{n-c}^* y_{n-d}^*, \quad (2.3)$$

where $w_{a,c,d}$ represents the third-order Volterra kernels. The RLS algorithm is also considered in this study to train the Volterra DFE.

### 2.4.3 Machine learning based equalisers

The machine learning (or ANN) based equalisers are another set of adaptive non-linear equalisers used in digital communication [90]. They have been shown to perform better than conventional equalisers (like the linear equaliser and TRDFE) in terms of minimising the BER though at the cost of high computational complexity [90]. Furthermore, previous works in optical communications, especially in visible light communication (VLC), have demonstrated the superiority of ANN equalisers over the conventional equalisers in terms of BER performance [91–94]. A key advantage of ANN over the conventional equalisers is that they not only compensate for ISI but also non-linearities in the channel. Moreover, while the conventional equalisers use the principle of calculating the ISI contribution from previous symbols, ANN equalisers classify or estimate the received samples from the system with the aid of non-linear functions [90, 95].

The study from [90] explores the ANN architectures used for channel equalisation. They were broadly classified into the feedforward neural networks (NN) (e.g. multi-layer perceptron (MLP), functional link NN (FLNN), radial basis function(RBF)) and feedback NN (e.g. recurrent Hopfield NN (RHNN)). The feedback NN is computationally more complex than the feedforward NN and thus requires more training time. This study will focus entirely on the MLP for channel equalisation as it is most fundamental of all the feedforward NN.

#### 2.4.3.1 Multi-layer perceptron (MLP) based equaliser

The MLP is a collection of neurons (or perceptrons) that are organised into layers, as illustrated in Fig. 2.6. Each neuron computes a linear combination of its inputs, as well as incorporates an externally applied bias. The result of this combination is applied to an activation function. The

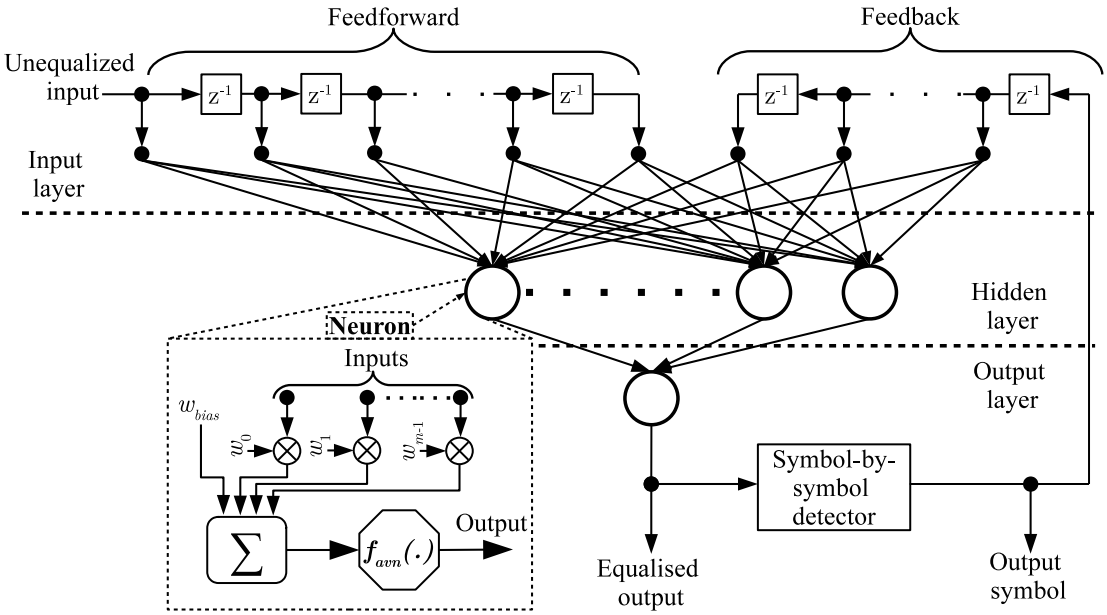


**Figure 2.6:** *Block diagram illustrating the structure of a multilayer perceptron based DFE (MLPDFE)*

expression for the output of a perceptron is [95]:

$$y = f_{avn}\left(w_{bias} + \sum_{i=0}^{m-1} w_i x_i\right), \tag{2.4}$$

where $m$ denotes the number of inputs to the neuron and $f_{avn}(.)$ is the activation function of the neuron; $x_i$ denotes the neuron inputs, $w_i$ denotes the weight for each input $x_i$; $w_{bias}$ denotes the neuron bias.

For the purpose of equalisation, three layers (one input layer, one hidden layer and one output layer) are sufficient for the MLP because of the universal approximation theorem [95]. The theorem acknowledges that for a non-linear input-output mapping; if the activation function of the neurons in the hidden layer is monotonously continuous, bounded and non-constant, a finite number of neurons in the layer is sufficient to obtain an approximate realisation of the mapping. The sigmoid function satisfies this condition and is, thus, the most widely used activation function of the neurons in the hidden layer [95]. It is defined in (2.5) as:

$$f_{sgm}(x) = \frac{2a_1}{1 + \mathrm{e}^{-a_2 x}} - a_1 = a_1 \tanh(a_2 x), \tag{2.5}$$

where $a_1$ and $a_2$ are suitably chosen constants. In line with [91] and [96], tan-sigmoid ($a_1 =$

$a_2 = 1$) is employed in this study as the activation function. The activation function for the neuron in the output layer is the linear function ($f_{lin}(x) = x$). The feedback inputs can be sent to the the MLP equaliser just like with the TRDFE and VOLT2DFE as illustrated in Fig. 2.6. This MLP equaliser is known as the MLP based DFE (MLPDFE) and can be expressed as:

$$\tilde{z}_n = \sum_{c=1}^{N_{hn}} \left[ w_c \tanh \left( w_{c,bias} + \sum_{a=0}^{N_{ft}-1} w_{c,a} y_{n-a} + \sum_{b=1}^{N_{bt}} w_{c,b} \hat{z}_{n-b} \right) \right] + w_{bias}, \tag{2.6}$$

where $N_{hn}$ is the number of hidden layer neurons; $w_{c,a}$ and $w_{c,b}$ are the synaptic weights for processing the feedforward and feedback inputs, respectively for a hidden layer neuron (with index $c$); $w_c$ denotes the weight used to process the neuron at the output layer; $w_{c,-1}$ and $w_{-1}$ denotes the bias of a hidden layer neuron and the output layer neuron, respectively.

The performance of MLP is greatly influenced by the number of neurons in the hidden layer. Too few hidden neurons mean less computational complexity but may cause poor error performance. Too many neurons, on the other hand, may cause irregular error performance due to poor fitting [95]. The algorithm for training the MLP equaliser is the back-propagation (BP) algorithm. There are multiple variants of this algorithm, including the resilient BP (RBP), the conjugate gradient BP (CGBP) and the Levenberg-Marquardt BP (LMBP). The LMBP algorithm is considered in this study as it has the best convergence and mean-square-error (MSE) performance [95]. However, it uses batch training which requires more computing memory than the other BP algorithms (and notably the RLS algorithm).

#### 2.4.3.2 Split-complex MLP equaliser

For the equalisation of complex-valued signal, ANN with complex-valued activation function can be considered [97]. However, there is a conflicting issue between the boundedness and differentiability of a non-linear complex-valued function. Another approach is to "split" two real-valued activation functions in order to process the in-phase and quadrature-phase components separately, as illustrated in Fig. 2.7. The MLP equaliser with this approach is termed "split-complex" MLP (SC-MLP) [98].

While the real-valued MLP equaliser uses the LMBP algorithm for training in this study, the SC-MLP equaliser will employ the RBP algorithm as this is what has been used in previous studies [99–101]. The RBP has good convergence and requires less computational load than

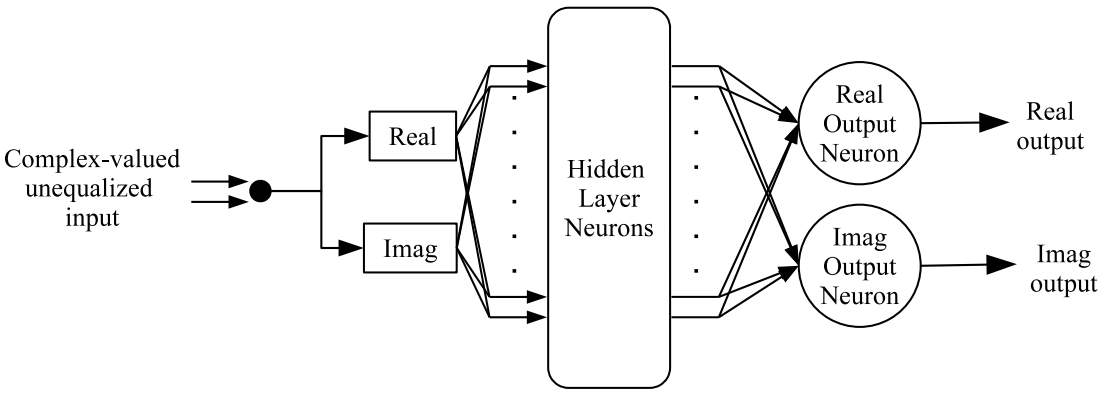


**Figure 2.7:** *An illustration on the structure of the split-complex multilayer perceptron based DFE (SC-MLPDFE)*

the LMBP algorithm. This advantage is useful since the parameters for the SC-MLP equaliser is twice as much as those of the real-valued MLP equaliser [90]. Like the other NLEs, the DFE can be adapted to the SC-MLP equaliser to form the SC-MLP based DFE (SC-MLPDFE). If the tan-sigmoid is used as the activation function for the hidden layer neurons, and the linear function is for the output layer neurons, then the equalised output for the SC-MLPDFE can be derived from [97] as:

$$\begin{aligned}\tilde{z}_n = \sum_{c=1}^{N_{hn}} \Bigg[ (w_c + jx_c) \tanh \Bigg( w_{c,bias} + \sum_{a=0}^{N_{ft}-1} \left( w_{c,a} y_{n-a}^{\mathbb{R}} + x_{c,a} y_{n-a}^{\mathbb{I}} \right) \\ + \sum_{b=1}^{N_{bt}} \left( w_{c,b} \hat{z}_{n-b}^{\mathbb{R}} + x_{c,b} \hat{z}_{n-b}^{\mathbb{I}} \right) \Bigg) \Bigg] + (w_{bias} + jx_{bias}),\end{aligned} \tag{2.7}$$

where $w_c$, $w_{c,b}$ and $w_{c,a}$ are the synaptic weights for processing the real component while $x_c$, $x_{c,b}$ and $x_{c,a}$ are for the imaginary component. The notations $(.)^{\mathbb{R}}$ and $(.)^{\mathbb{I}}$ represent the real and imaginary components for the equaliser inputs. Unlike in (2.1) and (2.2), all variables in (2.7) are real-valued.

It should be noted in this study that all inputs for the NLEs are symbol-spaced unless stated otherwise.

## 2.5 Frequency Domain Equalisation

For channels with severe ISI, the frequency domain (FD) equaliser is computationally simpler to execute than the time domain (TD) equaliser [45]. Because while the latter computes a single data symbol, the prior equaliser processes a block of data symbols at a time. The block processing involves a serial-to-parallel (S/P) conversion of the input data, parallel processing of the collected data, and then parallel-to-serial conversion of the generated output data. Another advantage of the FD equaliser over the TD equaliser is that it requires the use of the fast Fourier transforms (FFT) operation, which is the most efficient algorithm of the discrete Fourier transforms (DFT).

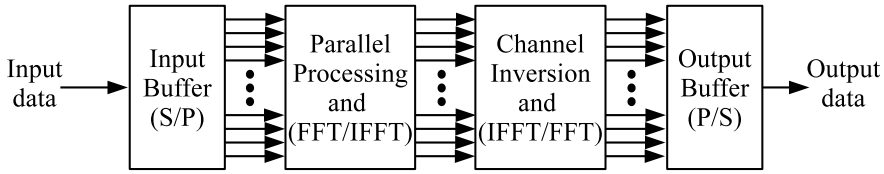


**Figure 2.8:** *A schematic of a frequency domain equaliser*

The essential operation underlying an FD equaliser is illustrated in Fig. 2.8. It involves the transformation of a block of input data from the TD to the FD with the FFT algorithm. The equalisation is then executed by channel inversion with a single-tap multiplication of each FD output. However, this procedure yields a circular convolution, which is unacceptable as the desired result of an equaliser is a linear convolution. Hence, by developing the block of input data, three methods have been used to allow linear convolution with the FD equaliser [45, 102].

The first and most common method is to append a cyclic prefix to the input data block sequence, as illustrated in Fig. 2.9 [43,45,103]. The cyclic prefix method can be applied in both SCM and MCM schemes for FD equalisation. However, it requires an extra overhead which reduces the bit-rate of the system. The other two techniques for performing a linear convolution with the FD equaliser are the overlap-save and the overlap-add sectioning methods [45, 103]. They can only be used in SCM schemes, and they avoid the extra overhead of the cyclic prefix. Nevertheless, these sectioning methods are computationally more complex than the cyclic prefix, and the overlap-add method is more intricate than the overlap-save method. Thus, in this study, the SCM schemes will use the overlap-save method while the MCM schemes will employ the cyclic prefix method for FD equalisation.

For SCM schemes, the FD equaliser can offer better performance in severe ISI channels by adding a decision feedback filter (DFF) [102]. However, the FD equaliser operates with the

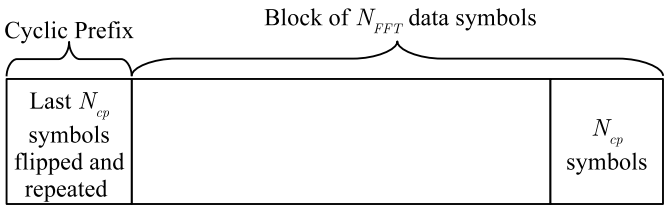


**Figure 2.9:** *Block processing for frequency domain equalisation with cyclic prefix*

block FFT signal processing while the DFF requires an immediate filtered decision to be fed back on a symbol-by-symbol basis. Thus, the DFF cannot be done in the FD. A hybrid time-frequency domain DFE approach avoids the abovementioned feedback delay problem. The method involves the use of FD filtering only for the feedforward filter part of the equaliser, while the feedback part implements TD filtering. The feedback filter is relatively simple in TD since it performs multiplications only on data symbols, and usually requires fewer taps than the feedforward filter for adequate performance.

## 2.6 State-of-the-Art for High-speed SI-POF Communication

The IEEE 802.3bv GEPOF standard (earlier discussed in section 2.1) uses a frame structure with PAM-16 modulation, Tomlinson-Harashima precoding (THP) scheme for pre-equalisation, TRDFE for post-equalisation and multilevel coset coding [65, 66]. The combination of all these digital techniques was proven to be an efficient way of approaching the transmission theoretical maximum capacity of the POF. The fibre-coupled optical power is -3 dBm, as it falls within the linear region of the RC-LED. The receiver consists of a silicon PIN-PD (Si-PIN-PD, Hamamatsu S5971), a TIA (based on the high-speed op-amp LMH6624), a variable gain amplifier (VGA, VCA824), and a fifth-order Butterworth anti-aliasing filter.

The investigative effort by the VDE group for GEPOF encouraged a high research interest in real-time communications over SI-POF at around the year 2010. The first collection of real-time setups for gigabit communication over SI-POF involves the use of a field-programmable gate array (FPGA) [70–72, 104]. The FPGA handles the digital signal processes that include modulation, synchronisation, and equalisation. With the FPGA, a binary non-return-to-zero (NRZ) signal at a bit rate of 1 Gbps was transmitted over a 25 m SI-POF [70]. A Firecomms RC-LED with an optical output power of -1.5 dBm was used to realise this; and the receiver comprises a Si-PIN-PD (0.54 mm diameter) with an integrated TIA and a fifth-order active Bessel filter. A BER of about $7 \times 10^{-4}$ was achieved with this setup. The transmitter setup

used in [70] is similar to that in [71] and [72]. However, while the receiver in [71] consists of a Si-PIN-PD, a TIA (Maxim 3266) and a tunable high-pass filter coupled with a TRDFE; the receiver in [72] is the model SPD-2 manufactured from Graviton linked to a TRDFE. While the earlier receiver is off-the-shelf with a bandwidth of less than 500 MHz, the latter has a bandwidth of 1.2 GHz. Correspondingly, 1.25 Gbps was realised over a 50 m SI-POF at a BER of about $10^{-6}$ in the earlier setup. While in the latter, 1 Gbps was achieved over a 75 m SI-POF at a BER of about $10^{-8}$. The received optical power for the setup in [72] was -13 dBm. All the FPGA setups were for a unidirectional SI-POF link except for the study done in [104]. This work presented a 1 Gbps bidirectional transmission over a single SI-POF of 75 m. This transmission is viable with the use of passive optical splitters, and it encourages full-duplex transmission over the SI-POF link. However, the splitters incur an optical loss of about 6 dB; thus, the transmission is only possible with an LD (of 7 dBm optical power). A BER of about $10^{-7}$ was achieved for this link with a received optical power of -15.2 dBm. An alternative to applying the FPGA setup for real-time transmission is to use an arbitrary waveform generator with a real-time oscilloscope. The study done in [105] applies this option and was able to achieve a bit-rate of 10.7 Gbps over 10 m SI-POF at a BER of about $3 \times 10^{-4}$. The transmitter used in this study was a VCSEL with an optical power of 0 dBm, and the receiver was a gallium arsenic MSM-PD (GaAs-MSM-PD) coupled with a TIA with a -3 dB of 8 GHz. The MLSE was used to obtain this high-speed real-time transmission.

The second collection of real-time setups for gigabit communication over SI-POF is more recent than the first. The setups involve the integration of an analogue equaliser to the optical receiver into a single chip [73, 106, 107]. In [73], the analogue equaliser is designed to support a bit-rate of 1.25 Gbps over a 50 m SI-POF. The transmitter was a Firecomms RC-LED, and the modulation scheme is binary NRZ or PAM-2. The receiver was a Si-PIN-PD (Hamamatsu, 0.8 mm diameter, 0.44 A/W responsivity at 660 nm wavelength) that is connected to a TIA. The analogue equaliser for this setup offered a BER of about $10^{-12}$ at a received optical power of -15 dBm. However, the equaliser only works at a fixed bit-rate over a constant SI-POF length. Thus, a multi-rate adaptive analogue equaliser was implemented first in [106, 107] for transmission up to 50 m SI-POF. The equaliser is suitable for high-speeds ranging from 400 Mbps to 2.5 Gbps. The transmitter used in this setup was a 650 nm aluminium gallium indium phosphide (AlGaInP) LD (from Sanyo DL-3147-021) that generated an optical power of +7 dBm, and the modulation scheme is also binary. The receiver is similar to the one used in [73] except that its equaliser is adaptive. A BER of about $10^{-8}$ was achieved for a bit-rate of 2.5 Gbps over

50 m SI-POF. This BER is with a received optical power of -15 dBm.

| **Ref.** | **Transmitter (Wavelength/ Optical Power) + Receiver** | **Modulation + Equaliser** | **Bit rate [Gbps] (BER)** | **length [m]** | **Bit-rate length product [Gbps.m]** |
|---|---|---|---|---|---|
| [70] | Firecomms RC-LED (650 nm/ -1.4 dBm) + Si-PIN-PD & TIA | PAM-4 +TRDFE | 1 ($\approx 7 \times 10^{-4}$) | 25 | 25 |
| [71] | Firecomms RC-LED (650 nm/ -1.5 dBm) + Si-PIN-PD & TIA | PAM-2 +TRDFE | 1.25 ($< 10^{-6}$) | 50 | 62.5 |
| [72] | Firecomms RC-LED (650 nm/ -1.5 dBm) + Graviton SPD-2 | PAM-2 +TRDFE | 1 ($\approx 10^{-8}$) | 75 | 75 |
| [65, 66] | Firecomms RC-LED (650 nm/ -3 dBm) + Si-PIN-PD & TIA | PAM-16 +THP & TRDFE | 1 ($\lesssim 10^{-12}$) | 50 | 50 |
| [104] | Union Optronics LD (655 nm/ +7 dBm) + Graviton SPD-2 | PAM-2 +TRDFE | 1 ($\approx 10^{-7}$) | 75 | 75 |
| [105] | VCSEL (680 nm/ 0 dBm) + GaAs-MSM PD & TIA | PAM-2 + MLSE | 10.7 ($\approx 3 \times 10^{-4}$) | 10 | 107 |
| [73] | Firecomms RC-LED (650 nm/ +0.5 dBm) + Si-PIN-PD & TIA | PAM-2 + Analog equaliser | 1.25 ($\approx 10^{-12}$) | 50 | 62.5 |
| [106, 107] | AlGaInP LD (650 nm/ +7 dBm) + Si-PIN-PD & TIA | PAM-2 + Analog equaliser | 2.5 ($\lesssim 10^{-8}$) | 50 | 125 |

**Table 2.4:** *Real-time high-speed transmission over SI-POF with equalisation*

A comparison between different real-time systems for high-speed transmission over SI-POF with equalisation is introduced in Table 2.4. The bit-rate length product can give a comparison between different systems using different lengths and data rates (see Table 2.4). However, the system components, power consumption, cost and BER must be taken into account for a detailed comparison. The measurements introduced in [106] and [107] represent the maximum bit-rate length product in a real-time transmission (125 Gbps·m). Nevertheless, both systems need a high laser optical power (+7 dBm) to achieve this result, which violates the human eye safety level of 0 dBm. The system implemented in [105] follow this with a bit-rate length

product of 100 Gbps·m, using an LD of 0 dBm optical power. The next higher bit-rate length product is 75 Gbps·m that was deployed by systems in [72] and [104]. The system in [104] is more expensive and consumes more power than that in [72] as the earlier uses a laser diode while the latter applies an RC-LED. The results in [71] and [107] show a bit-rate length product of 62.5 Gbps·m using binary modulation with a low power RC-LED. The work in [70] offers a 25 Gbps·m bit-rate length product using the RC-LED but with PAM-4 modulation.

The results from Table 2.4 suggest that for real-time transmission over SI-POF, the systems with binary modulation offer the best performance, provided that the receiver is embedded to an analogue equaliser and the transmitter has considerable optical power. The next best systems adopt digital equalisation techniques with optical power below the eye-safe level. The system in the IEEE 802.3bv standard uses both pre-equaliser and post-equaliser and thus provides enough margin for PAM-16 modulation scheme.

Compared to the real-time experiments, there were offline experimental studies that demonstrated higher rates over the SI-POF link. Two of these studies are from [74, 76], and they considered a comparison of PAM-2, PAM-4, and duo-binary modulation formats: the duo-binary format is a PAM-2 format that uses a pre-encoder. The transmission part is the RC-LED setup that was executed in [71]; the receiver is a model SPD-2 manufactured from Graviton, and it is coupled with the TRDFE. The duo-binary format offered the highest data rate of 1 Gbps over a 50 m SI-POF at a BER of $\sim 10^{-10}$ in this study. Using the same optical transmitter and receiver in [74, 76], a data rate of 1.1 Gbps was achieved in [75] for a 50 m SI-POF with PAM-2 and the MLSE. The RC-LED is also used as the transmitter with a fibre-coupled power of -1.5 dBm, -0.8 dBm and -0.8 dBm in [108], [88], and [89], respectively. The receiver in [108] is an APD model (AD800-11) coupled with a low-noise amplifier (LNA) and a TRDFE. The receiver in both [88] and [89] is the model SPA-2 manufactured from Graviton linked to a VOLT2DFE, and both studies employed PAM-8 modulation format for transmission. The study with the APD-based receiver used PAM-32 modulation format to obtain an error-free 5 Gbps transmission over a 25 m SI-POF. At a BER of $\sim 10^{-3}$, [88] offers 2.7 Gbps over a 30 m SI-POF while [89] offers a data rate of 2.25 Gbps over a 50 m SI-POF. Another set of LED used for offline SI-POF systems is the GaN LED, which was used for the study in [77, 78]. The GaN LED is shown in [77, 78] to be more useful than the RC-LED in a high-temperature environment. The receiver employed in [77, 78] is a Si-PIN-PD connected to a TIA with a 3 dB bandwidth of $\sim$700 MHz. The studies presented a bit-rate of 3 Gbps over a 20 m SI-POF at a BER of $10^{-3}$ using PAM-4

with the VOLT3DFE. The work in [109] employs a gallium nitride (GaN) $\mu$LED for a bidirectional 5 Gbps transmission over a 10 m SI-POF at a BER of $10^{-6}$. The receiver used in this study is an APD coupled with a TIA.

Another collection of offline setups for high-speed communication over SI-POF is with the LD transmitter. The study in [110] uses an indium GaN (InGaN) LD transmitter with the fibre-coupled optical power of 0 dBm, which is the eye safety level. The receiver in the study is similar to that used in [77]. A BER of about $\sim 10^{-5}$ was achieved for a bit-rate of 1.25 Gbps over 100 m SI-POF. This BER is with a received optical power of -14 dBm using PAM-2 and the TRDFE. A different setup with a red (655 nm) LD transmitter was implemented in [111] using CAP-64 modulation format and the TRDFE. The LD transmitter was coupled with the SI-POF at a high optical power of $\sim$11 dBm. The receiver was a PD integrated to a TIA with a bandwidth of 1 GHz. The study in [111] reported a bit-rate of 2.1 Gbps over a 100 m SI-POF at a BER of $10^{-3}$. Another study that implemented a red (650 nm) LD obtained a bit-rate of 2.81 Gbps over a 100 m SI-POF at a BER of $10^{-3}$. The bit-rate was achieved using DMT modulation with bit-loading, clipping, and the conventional single-tap FD equaliser [112]. The fibre-coupled power of the LD in [112] was $\sim$7 dBm. With the same red LD, a bit-rate of 5 Gbps over a 100 m SI-POF was achieved at a BER of $10^{-3}$ [113]. The bit-rate was obtained with a fibre-coupled power of $\sim$6 dBm using the CAP-16 modulation format and the TRDFE [113]. The study in [114] also used a red (650 nm) LD transmitter to obtain a bit-rate of 10.7 Gbps over a 25 m SI-POF at a BER of $10^{-3}$. The fibre-coupled power of the LD in this study was $\sim$10 dBm.

Based on the bit-rate length product, a comparison of the different offline systems for high-speed transmission over SI-POF with equalisation is summarised in Table 2.5. The bit-rate length product of most of the offline systems is much higher than that of the real-time systems. The result obtained from [113], which uses a high LD optical power (+6 dBm), represents the maximum bit-rate length product in an offline transmission (500 Gbps·m). The next higher bit-rate length product is 267.5 Gbps·m that was deployed by [114] using an LD. The works executed in both [111] and [112] offer subsequent higher bit-rate length product of 210 Gbps·m and 140 Gbps·m, and they both deployed LDs with optical power higher than +6 dBm. The system implemented in [110] follow this with a bit-rate length product of 125 Gbps·m, using an LD of 0 dBm optical power. The next system is from [108] that adopts an RC-LED (with an optical power of -1.5 dBm) and offers a bit-rate length product of 125 Gbps·m. The systems

deployed in [88] and [89] use the same LED but with a higher optical power of -0.8 dBm. With the use of Volterra DFE at the receiver, the setups in [88] and [89] offer the next best bit-rate length product of 81 Gbps·m and 112.5 Gbps·m, respectively. The next best work is from [77, 78], and it offers a bit-rate length product of 60 Gbps·m using a GaN LED (with an optical power of -1.8 dBm). Other systems that use the RC-LED with an optical power of -1.5 dBm were deployed in [75] and [74, 76]; they offer a bit-rate length product of 55 Gbps·m and 50 Gbps.m, respectively· The work from [109] offers a bit-rate length product of 50 Gbps·m using a 0 dBm $\mu$LED.

The results from Table 2.5 infer that for offline transmission over SI-POF, the systems with multilevel PAM, multilevel CAP and DMT modulation offer the best performance when the receiver is coupled with the transversal DFE, and the transmitter has considerable optical power (of more than +6 dBm). The next best systems adopt LDs with optical power at the eye-safety level. These LD setups are followed by LED systems that use both TRDFE and Volterra DFE at the receiver and transmit at an optical power less than or equal to the eye-safety level. It is noteworthy to mention that little to no SI-POF transmission has been done with an ANN-based equaliser for both the offline and the real-time systems.

Currently, the SI-POF systems reported with the highest capacity are realised with WDM and an advanced modulation format like multilevel PAM or DMT. Though, it is costly to implement as it requires multiplexers/demultiplexers and multiple optical sources with their receivers that operate at different wavelengths. Moreover, further losses occur with the WDM systems compared to the single wavelength SI-POF systems due to crosstalk, insertion and multiplexing [83, 122]. Therefore, there have been neither any commercial applications nor standards for SI-POF systems with WDM. These SI-POF systems have been presented with offline-processing in the literature. Nevertheless, SI-POF systems with WDM have potential applications in high-capacity in-home networks that require minimal cabling [34, 122].

The first gigabit-communication over SI-POF WDM was reported in [115, 116] using three LDs, each at a visible light wavelength of 405 nm (violet), 515 nm (green) and 650 nm (red). With this setup, an aggregate bit-rate of 10.7 Gbps was achieved over a 50 m SI-POF at a BER of $10^{-3}$. The setup used DMT modulation with bit-loading for each wavelength. The WDM setup in [117] is similar to that in [115, 116] with the three LDs, except that it used more optical power and that a fourth LD at the 450 nm (blue) wavelength was added. As expected, an improved aggregate bit-rate of 14.7 Gbps was achieved over the 50 m SI-POF at a BER of

| Ref. | Transmitter (Wavelength/ Optical Power) + Receiver | Modulation + Equaliser | Bit rate [Gbps] (BER) | length [m] | Data-rate length product [Gbps.m] |
|---|---|---|---|---|---|
| [74, 76] | Firecomms RC-LED (650 nm/ -1.5 dBm) + Graviton SPD-2 | Duo-binary +TRDFE | 1 ($\approx 10^{-10}$) | 50 | 50 |
| [75] | | PAM-2 + MLSE | 1.1 ($\approx 10^{-5}$) | 50 | 55 |
| [110] | InGaN LD (515 nm/ 0 dBm) + Si-PIN-PD & TIA | PAM-2 +TRDFE | 1.25 ($\approx 10^{-5}$) | 100 | 125 |
| [111] | LD (655 nm/ +11 dBm) + Integrated PD & TIA | CAP-64 + TRDFE | 2.1 ($\approx 10^{-3}$) | 100 | 210 |
| [112] | LD (650 nm/ +7 dBm) + Si-PIN-PD & TIA | DFT-Spread DMT with Bit-loading and Clipping + FD Equaliser | 2.81 ($\approx 10^{-3}$) | 50 | 140.5 |
| [113] | LD (650 nm/ +6 dBm) + Si-PIN-PD & TIA | CAP-16 + TRDFE | 5 ($\approx 10^{-3}$) | 100 | 500 |
| [77, 78] | GaN LED (475 nm/ -1.8 dBm) + Si-PIN-PD & TIA | PAM-4 + VOLT3DFE | 3 ($\approx 10^{-3}$) | 20 | 60 |
| [108] | Firecomms RC-LED (650 nm/ -1.5 dBm) + AD800-11 & LNA | PAM-32 + TRDFE | 5 ($< 10^{-12}$) | 25 | 125 |
| [89] | Firecomms RC-LED (650 nm/ -0.8 dBm) + Graviton SPA-2 | PAM-8 + VOLT2DFE | 2.25 ($\approx 10^{-3}$) | 50 | 112.5 |
| [88] | | | 2.7 ($\approx 10^{-3}$) | 30 | 81 |
| [114] | Fabry-Perot LD (650 nm/ +10 dBm) + Si-PIN-PD & TIA | PAM-4 + TRDFE | 10.7 ($\lesssim 10^{-3}$) | 25 | 267.5 |
| [109] | GaN $\mu$LED (450 nm/ 0 dBm) + APD & TIA | PAM-32 + TRDFE | 5 ($\lesssim 10^{-6}$) | 10 | 50 |

**Table 2.5:** *Offline High-speed transmission over SI-POF with equalisation*

| Ref. | Transmitter (Wavelength/ Optical Power) + Receiver | Modulation + Equaliser | Bit rate [Gbps] (BER) | length [m] | Bit-rate length product [Gbps.m] | Real time |
|---|---|---|---|---|---|---|
| [115, 116] | 3 LDs (405 nm/+7.1 dBm), (515 nm/ +5.4 dBm) & (650 nm/ +4 dBm) + Si-PIN-PD & TIA | WDM and DMT with bit-loading | 10.7 ($\approx 10^{-3}$) | 50 | 535 | No |
| [117] | 4 LDs (405 nm/+11.79 dBm), (450 nm/+9.12 dBm), (515 nm/ +5.01 dBm) & (639 nm/ +7.96 dBm) + Graviton SPD-2 | WDM and DMT with bit-loading | 14.77 ($\approx 10^{-3}$) | 50 | 738.5 | No |
| [118] | 6 LDs (405 nm/+8 dBm), (442 nm/+12 dBm), (459 nm/+10 dBm), (490 nm/+10.2 dBm), (515 nm/ +9 dBm) & (655 nm/ +6 dBm) + Graviton SPD-2 | WDM and DMT with bit-loading | 21.42 ($\approx 10^{-3}$) | 50 | 1071 | No |
| [119] | 6 LDs (405 nm/+13 dBm), (442 nm/+13 dBm), (459 nm/+11 dBm), (490 nm/+11.5 dBm), (515 nm/ +9.8 dBm) & (660 nm/ +11 dBm) + Graviton SPD-2 | WDM and DMT with both bit and power loading | 10.89 ($\approx 10^{-3}$) | 100 | 1089 | No |
| [120] | 5 LDs/LEDs (405 nm/+4.37 dBm), (470 nm/-3.5 dBm), (530 nm/-4.4 dBm), (588 nm/ -3.5 dBm) & (650 nm/ -3.15 dBm) + Integrated PD & TIA | WDM and PAM-16 | 5 ($< 10^{-10}$) | 50 | 250 | Yes |
| [121] | 3 $\mu$LEDs 410 nm/-9.3 dBm), (450 nm/ -10.2 dBm) & (520 nm/ -11.8 dBm) + AD800-11 & LNA | WDM and PAM-$M$ + TRDFE | 11 ($< 10^{-3}$) | 10 | 110 | No |

**Table 2.6:** *High-speed transmission over SI-POF with WDM*

$10^{-3}$ with this setup using DMT modulation and bit-loading for each wavelength. The highest number of LDs reported for the WDM transmission over an SI-POF is six [118, 119]: all the LDs are in the visible light spectrum at wavelengths of 405 nm (violet), 442 nm (bluish-violet), 459 nm (blue), 490 nm (cyan), 515 nm (green) and 655/660 nm (red). With this WDM setup, an aggregate bit-rate of 21.42 Gbps over a 50 m SI-POF was reported in [118] with DMT and bit-loading. An aggregate bit-rate of 10.89 Gbps over a 100 m SI-POF was also reported in [119] with a similar WDM setup from [118].

WDM technology has also been implemented with LEDs and PAM modulation. A real-time experiment with WDM was demonstrated in [120] with five optical sources: a combination of LDs and LEDs of visible wavelengths ranging from 405 nm to 650 nm. An aggregate bit-rate of 5 Gbps was achieved over the 50 m SI-POF at a BER of $10^{-10}$ with this setup using PAM-16 modulation and no equalisation for each wavelength. An offline WDM experiment was also demonstrated with three $\mu$LEDs in [121], each with a wavelength of 410 nm, 450 nm and 520 nm. A total bit-rate of 11 Gbps was achieved over the 10 m SI-POF at a BER of $10^{-3}$ with this setup using PAM-$M$ modulation and the TRDFE for each wavelength. The number of PAM levels ($M$) was optimally selected for each wavelength.

In terms of the bit-rate length product, a comparison of the different WDM systems for high-speed transmission over SI-POF is highlighted in Table 2.6. It is observed that the bit-rate length product of the WDM systems that uses a higher number of LDs (with more optical power) offer the highest bit-rate length product. In contrast, the WDM systems with low-power LEDs give the lowest bit-rate length product.

## 2.7 Summary

POF communication has been realised for the past six decades with the use of fluorinated polymers and polymethylacrylate. This chapter comments on some features and background knowledge required for SI-POF systems. It explicitly remarks on the optical sources and receivers for SI-POF systems and the sources of distortion for a high-speed SI-POF system. The chapter then discusses the structure of the NLEs that include the TRDFE, the Volterra-based equaliser and the ANN-based equaliser.

A thorough review of the state-of-the-art for high-speed communication over an SI-POF has been shown in this chapter. An analysis of the literature indicates the use of the advanced modulation formats (like PAM, CAP and DMT) with equalisation schemes for high-speed SI-POF communication. The common NLEs for SI-POF systems is the TRDFE for PAM and CAP schemes and the conventional single-tap FD equaliser for DMT. However, there has been little to no work on the other NLEs for SI-POF systems. The review reports a maximum bit-rate length product of 125 Gbps.m for real-time systems with PAM-2 and an analogue equaliser, 500 Gbps.m for offline systems with CAP-16 and the TRDFE, and 1089 Gbps.m for WDM systems with DMT and bit-loading.

The rest of the thesis will discuss the use of the NLEs for the advanced modulation formats employed for high-speed SI-POF communication. The discussion includes some theoretical analysis, simulation results and experimental demonstrations.

# Chapter 3
# Evaluation of the Channel Capacity and Non-linearity for IM/DD SI-POF systems

The two methods for lightwave transmission are intensity-modulation/direct-detection (IM/DD) scheme and the coherent detection scheme. The first scheme communicates with only the intensity (or power) but ignores both the frequency and phase of the optical carrier. For the latter system, all features of the optical carrier are used for communication. Due to costs reasons, the IM/DD scheme is commonly used for short-range optical communication systems (like SI-POF). However, such a cost advantage also comes at the expense of lower performance than that of coherent optical systems. It is therefore of interest to be able to characterise a short-range optical communication system using several key parameters and estimate the maximum achievable transmission rates using these parameters.

In this chapter, the features of the IM/DD scheme in SI-POF systems are fully explored. First, the bandwidth-efficient modulation schemes implemented with IM/DD for high-speed SI-POF systems are discussed. Then, theoretical investigations of the SNR and the Shannon capacity of an IM/DD SI-POF channel are performed based on its optical power, receiver sensitivity and fibre length. The capacity calculations are based on recent frequency response models that have been defined in the literature. What follows is a description of the setup for the experiments that will be used throughout this thesis. The non-linearities of these setups are then measured and analysed.

## 3.1 Bandwidth-Efficient Modulation Schemes

As previously discussed in Section 2.6, the most commonly used modulation methods in high-speed SI-POF systems today are pulse amplitude modulation (PAM), carrier-less amplitude and phase modulation (CAP), and discrete multi-tone (DMT). The methods are bandwidth-efficient

as they require one symbol to carry multiple information bits. The first two methods are single-carrier modulation (SCM) schemes as they transmit a data stream with one high-frequency carrier. The third method is a multi-carrier modulation (MCM) scheme, as the transmitted data stream is divided among a large number of sub-carriers so that the system as a whole operates at a low symbol rate. All these methods modulate the amplitude to the form that drives the intensity of an optical source.

### 3.1.1 Pulse amplitude modulation (PAM)

PAM transmits symbols as pulses in a signal waveform, and their amplitudes distinguish the different symbols. A PAM transmission with $M$ different amplitudes (or "levels") represent $\log_2 M$ bits in each level. Among the other bandwidth-efficient modulation schemes, PAM is the simplest as it only deals with real-valued symbols. PAM is thus a one-dimensional signalling scheme.

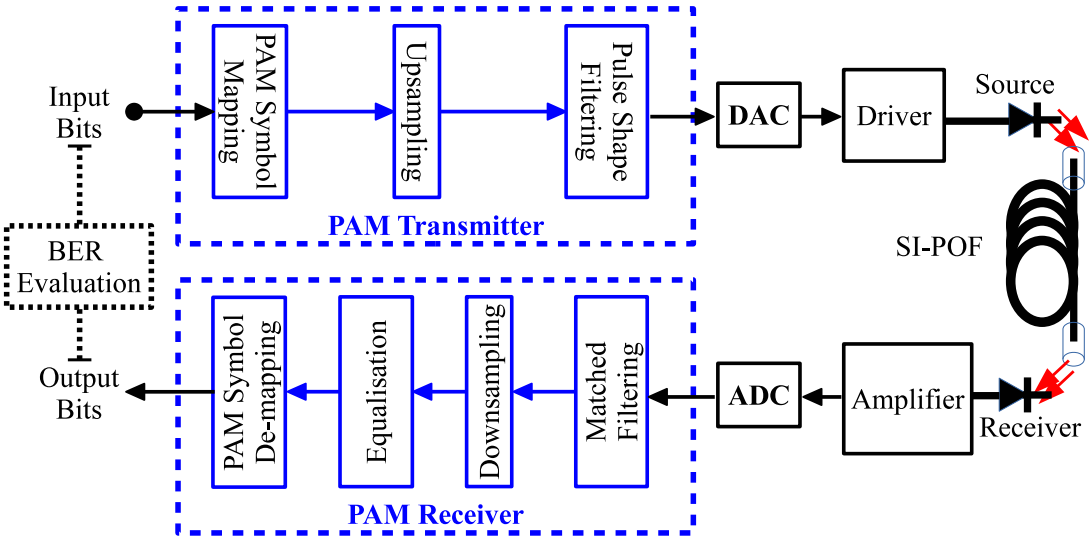


**Figure 3.1:** *DSP flow chart at transmitter and receiver for PAM*

The digital signal processes (DSP) of the PAM transceiver used throughout this study is shown in Fig. 3.1. The binary data is PAM-$M$ modulated by mapping $\log_2 M$ bits to one of $M$ amplitude levels with gray coding. The data symbols are preceded with a preamble of symbols. And these are used for synchronisation at the receiver and for training the equaliser. The resulting symbol sequence is upsampled and fed through a root raised cosine (RRC) filter for pulse shaping. The pulse-shaped symbols are then sent out to a DAC for transmission into the IM/DD

SI-POF system. After this transmission, the signal is taken from an ADC. The resulting signal then goes through matched filtering, down-sampling and equalisation. Finally, the equalised signal is demodulated, thus offering the received binary data.

### 3.1.2 Carrier-less amplitude and phase modulation (CAP)

CAP is a two-dimensional signalling scheme that was proposed as an alternative to QAM, as it creates a passband transmit signal with characteristics very similar to the latter [123]. But, it uses digital filtering instead of multiplication by the carrier frequency. This use of filtering makes CAP implementation simpler than QAM and avoids carrier recovery in the receiver. A drawback with CAP, however, is its relatively high sampling rate compared to PAM. Furthermore, the spectral efficiency of the CAP technique is half that of PAM, which implies that CAP with $M^2$ constellation points (CAP-$M^2$) offers the same spectral efficiency as PAM with $M$ points (PAM-$M$) [124]. This drawback makes CAP inconvenient for applications when the ratio of its sampling frequency to the symbol rate is small (below three): PAM is feasible at a ratio of two.

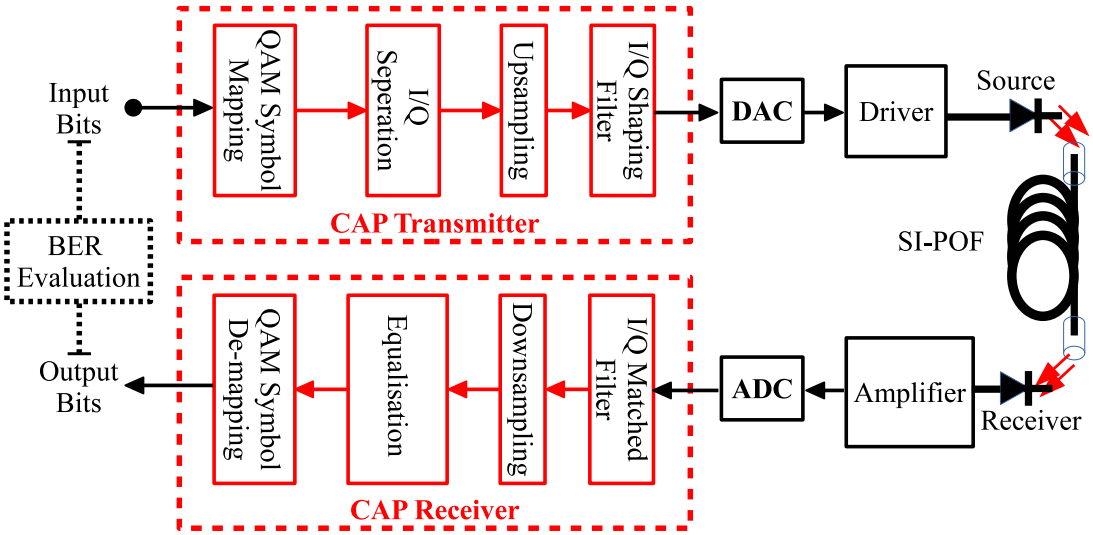


**Figure 3.2:** *DSP flow chart at transmitter and receiver for CAP*

The block diagram of a CAP transceiver before the DAC and ADC is illustrated in Fig. 3.2. The transmitted bits are mapped to the corresponding complex quadrature amplitude modulated (QAM) symbols, with their in-phase and quadrature-phase (I/Q) components being separated from each other. The resulting symbols are upsampled and passed through I/Q RRC pulse

shaping filters (PSF), whose impulse responses form a Hilbert pair. The pulse-shaped symbols are then passed on to the DAC for analogue transmission into the SI-POF channel. The output signal digitally obtained from the ADC is passed through the I/Q matched filters. This filtered output is then downsampled, equalised and demodulated to get the resulting binary data.

### 3.1.3 OFDM and discrete multi-tone (DMT)

Discrete multi-tone modulation (DMT) is the baseband version of OFDM. OFDM is known for its mass-application in radio networks like Wi-Fi, Wi-Max and terrestrial digital video broadcasting (DVB-T). Similarly, DMT is widely used in DSL for providing high-speed Internet access via ADSL and very VDSL.

Like OFDM, DMT is an MCM technique where a high-speed serial data stream is segmented into multiple parallel lower-speed streams and modulated onto multiple sub-carriers for simultaneous transmission. Both multi-carrier modulation schemes use the fast Fourier transform (FFT) algorithm for their efficient modulation and demodulation process. Unlike OFDM, however, the DMT modulator output signal after the inverse FFT (IFFT) is real-valued and no I/Q modulation onto a radio frequency (RF) carrier is required. Therefore, the necessary RF-components for I/Q modulation are omitted from DMT transceivers; thus reducing system costs and complexity.

As an MCM scheme, DMT has high spectral efficiency, offers flexibility in the sense of sub-carrier resource allocation, and is more tolerant of ISI than the SCM schemes discussed previously [125]. However, a significant limitation of DMT is its high peak-to-average-power-ratio (PAPR). This constraint is because the DMT signal is a sum of a large number of independently modulated sub-carriers. These sub-carriers may incidentally add up constructively, leading to high peak amplitude values in the transmitted time signal. When $N$ sub-carriers add up in phase, they may produce instantaneous peak amplitude values that are $N$ times the average. The high PAPR from DMT results in a significant penalty of more than 10 dB for a dynamical range limited SI-POF system [126].

The block diagram of a DMT transceiver is shown in Fig. 3.3. First, the transmitted bit-stream passed on to a serial-to-parallel (S/P) converter so that the resulting parallel bit-stream is mapped onto a QAM symbol per sub-carrier. This process is then followed by framing that includes imposing the Hermitian symmetry and oversampling: both of which are fully presented

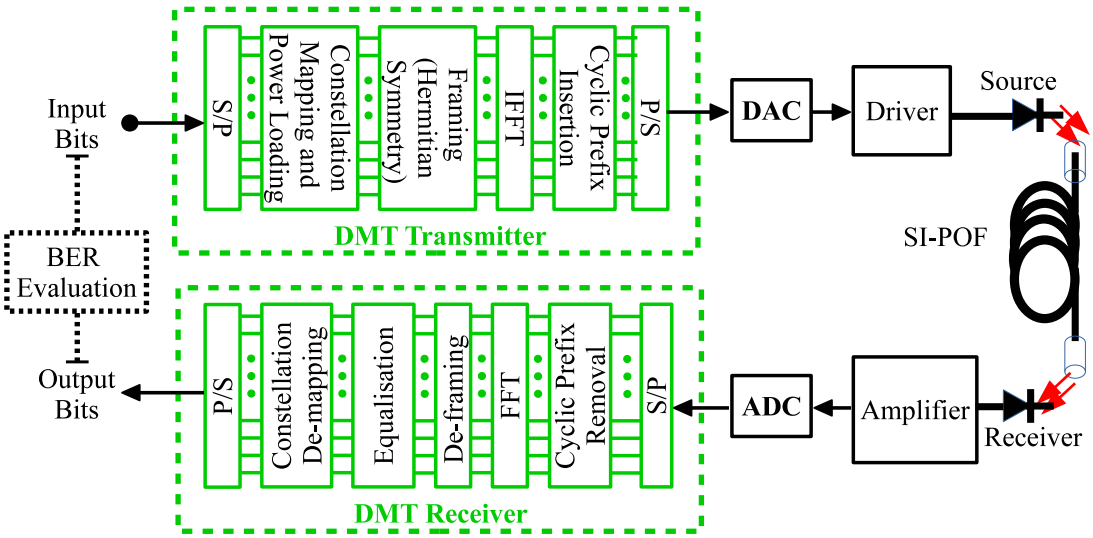


**Figure 3.3:** *DSP flow chart at transmitter and receiver for DMT*

in [127]. The framed symbols are then assigned to the orthogonal sub-carrier frequencies with IFFT to obtain the real-valued time-domain DMT signal. The cyclic prefix is then inserted to each DMT block. Every DMT data-stream is preceded with a set of DMT blocks for training the post-equaliser and for synchronisation. The DMT signal is then serialised with a parallel-to-serial (P/S) converter for onward transmission through the channel. The signal recovery process follows the inverse of the DMT signal generation. First, S/P conversion and de-framing are implemented on the received signal from the oscilloscope. Then, FFT is applied to the resulting signal to generate the received QAM symbols. The symbols are then equalised and demodulated to get the received binary data.

#### 3.1.3.1 Bit and power loading technique for DMT

An essential feature of DMT is the possibility to allocate the energy and the number of bits per sub-carrier according to its corresponding signal-to-noise ratio (SNR). This feature is typically known as bit-and-energy-loading. The bit-loading method is accomplished by selecting the corresponding QAM constellation size of each sub-carrier according to the number of bits that are allocated to it. The power loading involves normalising the QAM constellation to the energy allocated to each sub-carrier.

Bit-and-energy-loading can be divided into two categories: rate-adaptive and margin-adaptive algorithms. Rate-adaptive algorithms maximise the bit rate for a fixed BER and given power

constraint, while margin-adaptive algorithms minimise the BER for a particular bit rate. Rate-adaptive loading algorithm has found widespread use in commercial systems. The reason is that no matter how bad the channel is, the loading algorithm ensures that data transmission (even at very low bit-rates) is always possible. On the contrary, the margin-adaptive algorithm is useful only if a constant bit-rate is required for the channel. Several loading algorithms have been proposed in the literature, with some demanding more computational complexity than the others. Among these algorithms, the ones offered by Campello [128, 129] and Chow [130] have been widely used in practical OFDM systems. The bit-and-energy-loading that is adopted in this thesis is based on Campello's algorithm.

In practice, bit-and-energy-loading is often used in wireline communications such as DSL, because wireline transmission channels do not vary significantly with time, resulting in a substantial performance gain at relatively low complexity. Hence, the loading algorithms only have to be computed during the setup of a transmission link and do not need to be processed continuously. Consequently, various high-speed SI-POF transmission has been implemented with both DMT and bit-and-energy-loading algorithm [112, 118, 119].

## 3.2 IM/DD Model for SI-POF

In SI-POF systems, IM/DD involves modulating only the intensity of light. The application of conventional modulation formats to an IM/DD optical channel is different from standard electrical systems, where a bipolar baseband signal is used. However, the intensity of the optical source can only have positive values. In IM/DD systems, this problem is commonly solved by adding a DC-bias to the bipolar DMT signal to make it unipolar. The DC-bias is added to the electrical (AC-coupled) waveform before driving the LD or LED of the SI-POF system. At the receiver, a simple (low-cost) PD is used to detect the intensity of the received light.

### 3.2.1 Estimate of the SNR

The block diagram, which is shown in Fig. 3.4, represents the channel model for a typical SI-POF system that employs IM/DD [84, 108, 109]. The SI-POF links - used for in-home, automotive and industrial-control networks - have been accurately estimated with this model [40, 84]. The model requires the different values of the gain and frequency response for each compo-

nent of the SI-POF system. Separate component studies have been carried out to determine the characteristics of the optical source, POF and detectors. At the same time, the value of the remaining parameters required is based on their datasheets. Hence, this model is the basis for all theoretical investigations throughout this chapter, including the SNR estimation. Each block is taken step by step in order to derive the POF channel model. The optical sources and detectors are assumed to operate in their linear regions.

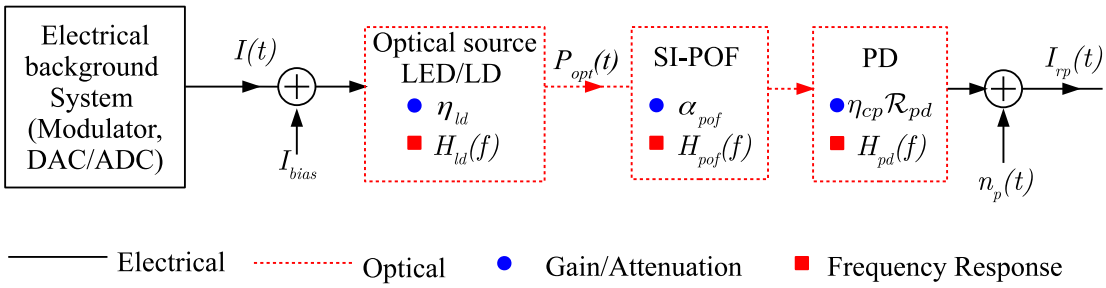


**Figure 3.4:** *A block illustration of a linear IM/DD SI-POF system*

First, the incoming binary data is modulated either as a PAM, CAP or an OFDM signal: the modulation schemes have been discussed in Section 3.1. The modulated signal is a bipolar electrical current $I(t)$ used to intensity modulate an optical source such as an LED or an LD. The real-valued current signal $I(t)$ is peak limited with a maximum value of:

$$I_{mod} = \max(|I(t)|) \tag{3.1}$$

Furthermore, the mean value of the bipolar signal is $\mathbb{E}[I(t)] = 0$ and the mean power of the signal (normalised on 1 Ω) is $\mathbb{E}[I^2(t)] = I_{rms}^2$. Hence, the peak-to-average-power ratio (PAPR) of the resulting signal $\rho_{papr}$ is defined as

$$\rho_{papr} = \left(\frac{I_{mod}}{I_{rms}}\right)^2. \tag{3.2}$$

Figure 3.5 depicts the an optical intensity modulator (or source) that is ideally linear. The DC-bias current $I_{bias}$ is added to the bipolar signal to drive the optical source. Subsequently, the ratio of the signal peak to the $I_{bias}$ is defined as the optical modulation index $\eta_{mod}$. That is:

$$\eta_{mod} = \frac{P_{omod}}{P_{oavg}} = \frac{I_{mod}}{I_{bias} - I_{th}} = \frac{I_{mod}}{I'_{bias}} \qquad 0 < \eta_{mod} \leq 1, \tag{3.3}$$

where $I_{th}$ is the threshold current of the source below which no optical power is emitted. So if $\eta_{ld}$ and $h_{ld}(t)$ represent the electrical-to-optical conversion ratio (in W/A) and impulse response

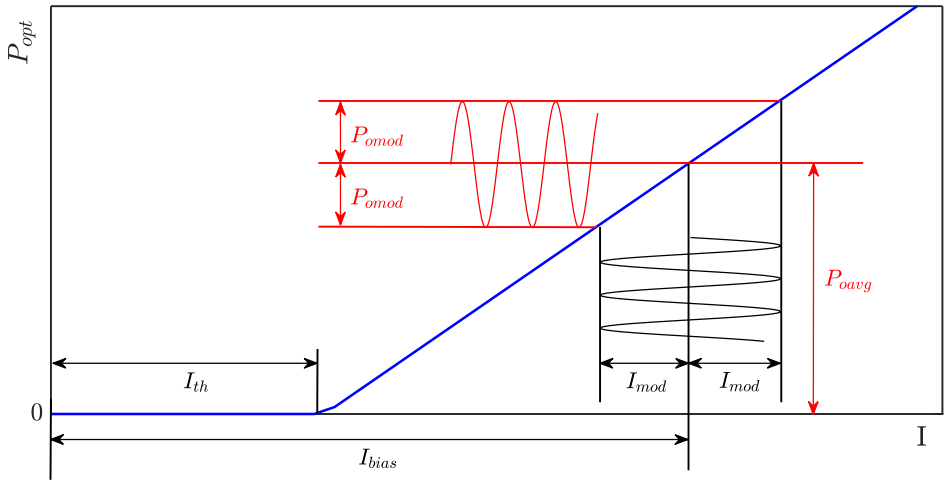


**Figure 3.5:** *P-I curve of a linear IM/DD optical source*

of the optical source respectively, then the optical signal output of the source is:

$$P_{ld}(t) = \eta_{ld}(I'_{bias} + I(t)) \otimes h_{ld}(t). \tag{3.4}$$

It is also assumed that $h_{pof}(t)$ and $\alpha_{_{pof}}$ represents the impulse response and attenuation of the POF channel respectively. Other losses in the POF, including those from bending, splicing and coupling, are denoted as $\eta_{cp}$. Therefore, the optical signal from the POF channel is:

$$P_{pof}(t) = \alpha_{_{pof}} \eta_{cp}(P_{ld}(t) \otimes h_{pof}(t)). \tag{3.5}$$

It should be noted that $\alpha_{_{pof}} = 10^{-0.1 \times \alpha_{pc} \times l_{pof}}$ where $l_{pof}$ is the POF length in metres and $\alpha_{_{pc}}$ is the POF attenuation coefficient in dB/m. The optical signal from the POF channel is converted to an electrical current $I_{rp}(t)$ given by:

$$I_{rp}(t) = \mathcal{R}_{pd}(P_{pof}(t) \otimes h_{pd}(t)) + n_p(t), \tag{3.6}$$

where $\mathcal{R}_{pd}$ denotes the receiver's responsivity (in A/W), $h_{pd}(t)$ is the receiver's impulse response and $n_p(t)$ is the additive white Gaussian noise. By combining (3.4), (3.5) and (3.6), $I_{rp}(t)$ can be rewritten as

$$I_{rp}(t) = \mathcal{R}_{pd}\alpha_{_{pof}} \eta_{cp}\eta_{ld}(I(t) \otimes h_{ptot}(t)) + n_p(t) \tag{3.7}$$

where,

$$\begin{aligned} h_{ptot}(t) &= h_{ld}(t) \otimes h_{pof}(t) \otimes h_{pd}(t)) \text{ in TD,} \\ H_{ptot}(f) &= H_{ld}(f) H_{pof}(f) H_{pd}(f) \text{ in FD.} \end{aligned} \tag{3.8}$$

In addition, $I'_{bias}$ is ignored in (3.7), since there is no information content in the signal's DC component.

The noise for the POF link comes from the POF receiver. The considered noise power spectral density (PSD) for the POF receiver can be calculated as

$$\mathcal{N}_p = \mathcal{N}_{p,s} + (\mathcal{R}_{pd}\mathcal{N}_{nep})^2, \tag{3.9}$$

where $\mathcal{N}_{nep}$ is the noise equivalent power (NEP) in W/Hz$^{\frac{1}{2}}$, which is a common metric used to characterize the noise performance of photo-receivers [68]; $\mathcal{N}_{p,s}$ is the shot noise caused by the received optical signal from the POF channel and is defined in this context as

$$\mathcal{N}_{p,s} = 2q_e\mathcal{R}_{pd}\alpha_{_{pof}}\eta_{cp}P_{oavg}, \tag{3.10}$$

where $q_e = 1.6 \times 10^{-19}$ C is the quantity of charge in an electron. The maximum estimate of the SNR (for PAM-$M$, CAP-$M^2$ and DMT_QAM-$M^2$) can be written as [49, 84]:

$$\begin{aligned} \gamma_{sig} &= \frac{P_{sig}}{P_{noise}} = \frac{P_{sig}}{f_{_{N0}}\mathcal{N}_p} = \frac{(\alpha_{_{pof}}\eta_{cp}\mathcal{R}_{pd}\eta_{mod}P_{oavg})^2}{f_{_{N0}}\rho_{_{papr}}\left((\mathcal{R}_{pd}\mathcal{N}_{nep})^2 + 2q_e\mathcal{R}_{pd}\alpha_{_{pof}}\eta_{cp}P_{oavg}\right)} \\ &= \frac{(\alpha_{_{pof}}\eta_{cp}\eta_{mod}P_{oavg})^2}{f_{_{N0}}\rho_{_{papr}}\left(\mathcal{N}_{nep}^2 + \frac{2q_e\alpha_{_{pof}}\eta_{cp}P_{oavg}}{\mathcal{R}_{pd}}\right)}, \end{aligned} \tag{3.11}$$

where $P_{sig}$ and $P_{noise}$ denotes the electrical power of the signal and noise, respectively, at the receiver. And $f_{_{N0}}$ denotes the equivalent noise bandwidth.

Assuming the ISI and the non-linear penalties are ignored, the signal-to-noise ratio (SNR) per bit ($\gamma_b$ in dB) can be computed as a function of the signal's bit rate ($R_b$ in Gbps) and PAPR

($\rho_{papr}$) from Eq. (3.11) as [84]:

$$\begin{aligned} \gamma_b &= \gamma_{nm} - 10\log_{10}\left(\frac{R_b\rho_{papr}}{2}\right), \\ \text{and } \gamma_{nm} &= 10\log_{10}\left(\frac{(\alpha_{pof}\eta_{cp}\eta_{mod}P_{oavg})^2}{\left(\mathcal{N}_{nep}^2 + \frac{2q_e\alpha_{pof}\eta_{cp}P_{oavg}}{\mathcal{R}_{pd}}\right)}\right) - 90, \end{aligned} \tag{3.12}$$

where $\gamma_{nm}$ denotes the normalised SNR per bit that is independent of the signal parameters like $R_b$ and $\rho_{papr}$. The PAPR ($\rho_{papr}$) is dependent on the PSF used in the case of PAM and CAP modulation schemes. Moreover, it increases with the modulation size $M$. For instance, $\rho_{papr} = \frac{3\rho_{papr,2}(M-1)}{M+1}$ for PAM-$M$, where $\rho_{papr,2}$ is the PAPR of the signal for $M = 2$ with the same PSF [84, 131]. The value of $\rho_{papr,2}$ with the non-return-to-zero (NRZ) rectangular pulse is 1. For an RRC PSF, $\rho_{papr,2}$ is between two and seven, depending on the PSF's roll-off factor [131].

### 3.2.2 Frequency response Model

Three models are used to estimate the frequency response of an IM/DD SI-POF channel, and they are the:

- first-order low-pass or Butterworth model [49, 50]
- Gaussian model [51, 109] and
- time-dependent power flow model [52–55, 132, 133]

The frequency response of the SI-POF channel based on the first-order Butterworth filter is expressed as [49]:

$$H_{pof}(f) = \left(1 + j\frac{f}{f_{p3dB}}\right)^{-1}, \tag{3.13}$$

while, the frequency response of the SI-POF channel based on the Gaussian filter is expressed as [50, 134]:

$$H_{pof}(f) = \mathrm{e}^{-\frac{1}{2}\left(\frac{f}{f_0}\right)^2}, \text{with } f_0 = \frac{f_{p3dB}}{\sqrt{\ln 2}}, \tag{3.14}$$

where $f_{p3dB}$ denotes the -3 dB electrical bandwidth in MHz, and it is expressed as a function of

the bandwidth-length product $f_{p3dBl}$ in MHz.m as

$$f_{p3dB} = \frac{f_{p3dBl}}{l_{pof}}, \tag{3.15}$$

where $l_{pof}$ is the SI-POF length in metres.

Compared to the two previous models, the time-dependent power flow equation is the best model for estimating the SI-POF frequency response. This is because it describes how the modes of light in the travels within the core of the SI-POF. The power flow equation is expressed as [52–55, 132, 133]:

$$\frac{\partial p(\theta, l_{pof}, t)}{\partial l_{pof}} = -\underbrace{\alpha(\theta)p(\theta, l_{pof}, t)}_{\substack{\text{mode-dependent} \\ \text{attenuation}}} - \underbrace{\tau_{del}(\theta)\frac{\partial p(\theta, l_{pof}, t)}{\partial t}}_{\text{modal dispersion}} + \underbrace{\frac{1}{\theta}\frac{\partial}{\partial \theta}\left[\theta D(\theta)\frac{\partial p(\theta, l_{pof}, t)}{\partial \theta}\right]}_{\text{mode coupling}}. \tag{3.16}$$

The equation describes the sources of impairments in the SI-POF with three functions, each of which represent the mode-dependent attenuation, modal dispersion and mode coupling. The direction of an incident ray (or mode) to the SI-POF is denoted by the angle $\theta$, where $0 \leq \theta \leq \theta_c$ for the ray to be fully reflected in the fibre. $\theta_c$ is the complement of the critical angle inside the SI-POF, defined as [50]:

$$\theta_c = \arcsin\left(\frac{\text{NA}}{n_{co}}\right), \tag{3.17}$$

The amount of optical power in one mode that is identified as $\theta$ relative to the fibre axis is defined as $p(\theta, l_{pof}, t)$, and this is a function of the SI-POF length $l_{pof}$ and time $t$. The mode-dependent attenuation for an SI-POF is denoted as $\alpha(\theta)$, which is a function of the angle $\theta$. The mode coupling is defined by a diffusion function $D(\theta)$, which describes how the optical power is transferred from one mode to the neighbouring ones. The attenuation functions and diffusion functions of three PMMA SI-POFs from different manufacturers are presented in Fig. 3.6a and Fig. 3.6b, respectively [53]. The PMMA SI-POFs are ESKA-PREMIER GH4001 (GH) from Mitsubishi, HFBR-RUS100 (HFB) from Agilent (HFB), and PGU-FB1000 from Toray (PGU).

The function of $\theta$ that relates to the modal dispersion is defined as $\tau_{del}(\theta)$. It is expressed in [50] as

$$\tau_{del}(\theta) = \frac{n_{co}}{c_{light}}\left(\frac{1}{\cos(\theta)} - 1\right), \tag{3.18}$$

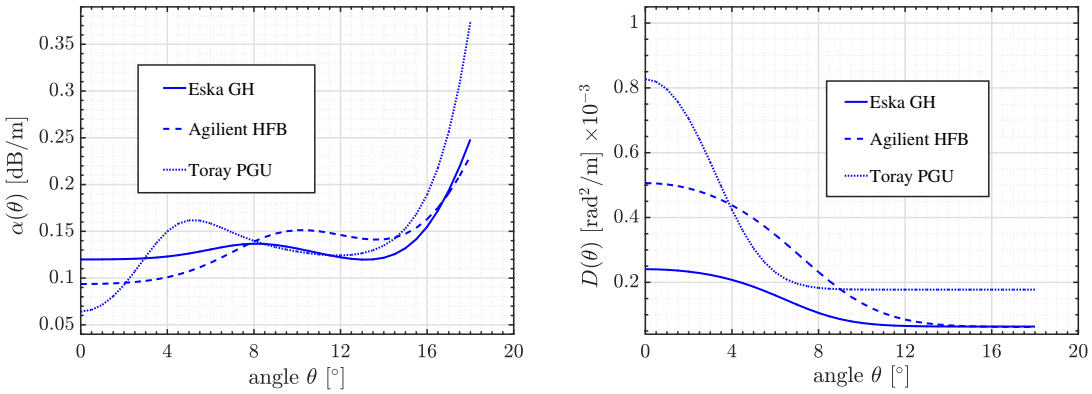


**(a)** **(b)**

**Figure 3.6:** *Modal characterisation of PMMA SI-POFs from different manufacturers with the : (a) attenuation function (b) diffusion function [53]*

where $c_{light}$ denotes the velocity of light in vacuum, which is $\sim 2.998 \times 10^8$ m/s.

To obtain the frequency response with the power flow equation, Eq. (3.16) can be converted from the time-domain to the frequency-domain with the help of the Fourier transforms. Thus, we obtain:

$$\frac{\partial P(\theta, l_{pof}, \omega)}{\partial l_{pof}} = -\left[\alpha(\theta) + j\omega\tau_{del}(\theta)\right] P(\theta, l_{pof}, \omega) + \frac{1}{\theta}\frac{\partial}{\partial \theta}\left[\theta D(\theta)\frac{\partial P(\theta, l_{pof}, \omega)}{\partial \theta}\right], \quad (3.19)$$

where $P(\theta, l_{pof}, \omega)$ is the Fourier transforms of $p(\theta, l_{pof}, t)$ and $\omega$ is the angular frequency in rad/s. The initial condition for Eq.( 3.19) is the angular power distribution of the optical source for the SI-POF. In [84], the light sources are assumed to have a Gaussian launching beam distribution that is defined as

$$P(\theta, l_{pof} = 0, \omega) = \mathrm{e}^{-\frac{1}{2}\left(\frac{\theta-\theta_0}{\sigma_{bm}}\right)^2}, \text{with } \sigma_{bm} \approx \frac{\arcsin(\mathrm{NA}_{ld})}{\sqrt{2\ln 2}}, \quad (3.20)$$

where $\mathrm{NA}_{ld}$ denotes the numerical aperture of the optical source, and $\theta_0$ denotes the mean value of the angle distribution for the optical source. $\theta_0$ is optimal at $0°$ [84].

The value of $P(\theta, l_{pof}, \omega)$ has been solved multiple times in literature with different numerical methods [52–55, 84, 132, 133]. Various assumptions with their approximations have been employed in these studies either for simplicity in solving for $P(\theta, l_{pof}, \omega)$ or to explore the effects of the fibre impairments. In this study, the finite difference scheme is applied as the numerical method used to solve for $P(\theta, l_{pof}, \omega)$ in Eq. (3.19). Details of this numerical method can be

explored in [84]. The normalised frequency response of the SI-POF of $l_{pof}$ metres in length can be obtained from $P(\theta, l_{pof}, \omega)$ as follows:

$$H_{pof}(\omega) = \frac{\int_0^{\theta_c} P(\theta, l_{pof}, \omega)\, \partial\theta}{\int_0^{\theta_c} P(\theta, l_{pof}, 0)\, \partial\theta}$$
$$\text{similarly, } H_{pof}(f) = \frac{\int_0^{\theta_c} P(\theta, l_{pof}, f)\, \partial\theta}{\int_0^{\theta_c} P(\theta, l_{pof}, 0)\, \partial\theta} \tag{3.21}$$

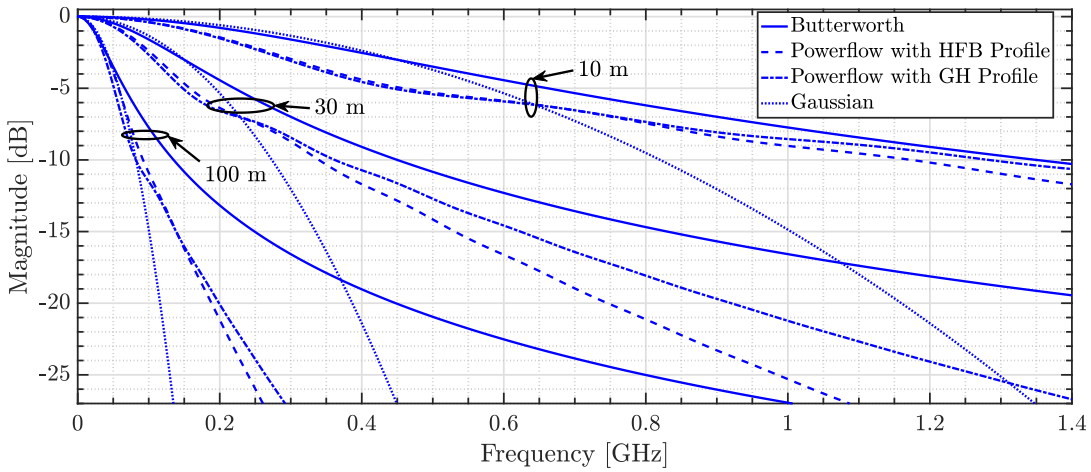


**Figure 3.7:** *Simulated results of the frequency response using the Butterworth model from Eq. (3.13), the Gaussian model from Eq. (3.14) and the the power flow model from Eq. (3.21). The results are taken at fibre lengths of 10 m, 30 m and 100 m.*

The magnitude response (i.e. $20\log_{10}|H_{pof}(f)|$) of the SI-POF for lengths of 10 m, 30 m and 100 m is depicted in Fig. 3.7 using the three models discussed earlier. The bandwidth-length product selected for the Butterworth and Gaussian model is 4500 MHz.m, according to that of the standard PMMA SI-POF. The power flow model is implemented with parameters from both the HFB profile and the GH profile. The value of $\text{NA}_{ld}$ is 0.17 because it is assumed that the LD is the input source to the SI-POF.

The results in Fig. 3.7 suggest that the Butterworth filter is the most optimistic estimation for the frequency response of the SI-POF channel. In contrast, the Gaussian filter is the worst-case estimation for the SI-POF channel. Furthermore, SI-POF at shorter lengths (10 m) the shape of the frequency response tends toward the Butterworth filter while at longer lengths (100 m), the POF response tends towards the Gaussian filter. This result is because the mode-dependent attenuation predominantly influences the frequency response for the short-length SI-POF. In contrast, with increasing fibre length, the mode-coupling process interacts more

and more with the mode-dependent attenuation, which leads to a more Gaussian-like shape. Another observation from Fig. 3.7 is that the frequency response from the GH profile surpasses that from the HFB profile at all SI-POF lengths. This pattern is because the first profile requires less diffusion than the latter profile as Fig. 3.6b illustrates.

### 3.2.3 Channel capacity analysis

The bandwidth is one of the constraints that restrict transmission at higher data rates in an optical IM/DD SI-POF channel. The bandwidth limitations can either originate from the transmitter, channel, receiver, or combinations of all mentioned. With some knowledge of the frequency response of the channel and SNR, the Shannon capacity of an SI-POF channel was calculated with the well-known water-filling method in the literature [43, 50, 84, 135, 136]. However, these studies only considered the capacity of the SI-POF channel at varying lengths while using the same SNR values for each length. The study in [135] by Gaudino et al. has first presented the idea for the SI-POF channel analysis, and this forms the basis of the first part presented in this section.

The rest of the analysis is based on the results shown in [50, 84], and they are further extended in this thesis by considering the capacity at different SI-POF lengths. The main findings are achieved by reviewing the theory for the evaluation of the channel capacity for the general case of a receiver characterised by its noise PSD $G_{noise}(f)$, and a received signal with PSD $G_{sig}(f)$. The latter PSD is influenced by the bandwidth-limiting response of the entire transmission system (transmitter, receiver, and channel). For convenience in the rest of this chapter, $G_{sig}(f)$ will be related as $H_{ptot}(f)$, which is the overall frequency response of the channel. The Shannon capacity will be analysed for an SI-POF channel that is modelled with the Gaussian low-pass filter, the first-order Butterworth low-pass filter and the power flow equation.

#### 3.2.3.1 Review on the derivation of the capacity for IM/DD SI-POF

The maximum capacity $R_{b,max}$ in bps is obtained from an SI-POF system by treating this channel as a sum of infinitesimal subchannels and applying the advanced but well-known results from information theory [43]. Thus,

$$R_{b,max} \leq \int_{-\infty}^{+\infty} \frac{1}{2} \log_2 \left( 1 + \frac{G_{sig}(f)}{G_{noise}(f)} \right) \, df, \tag{3.22}$$

under the average received power constraint

$$P_{sig} = \int_{-\infty}^{+\infty} G_{sig}(f)\, df. \tag{3.23}$$

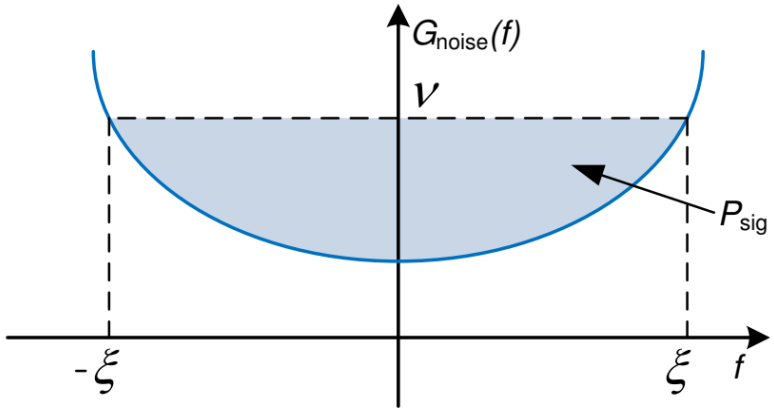


**Figure 3.8:** *An illustration of the water-filling method adopted from [84]*

The problem to solve is to find the PSD $G_{sig}(f)$ that maximises $R_{b,max}$ in Eq. (3.22). A Lagrange multiplier can be used to find the solution to the optimisation problem [43, 136]. It can be expressed as

$$G_{sig}(f) = (\nu - G_{noise}(f))^{+}, \tag{3.24}$$

where $\nu$ is a constant value that satisfies $\int_{-\infty}^{+\infty} (\nu - G_{noise}(f))^{+}\ df = P_{sig}$. The operation $(.)^{+}$ is defined as

$$(x)^{+} = \begin{cases} x & \text{if } x \geq 0 \\ 0 & \text{if } x < 0 \end{cases}. \tag{3.25}$$

This procedure is termed in the literature as "water-filling" [136], and it is illustrated in Fig. 3.8. Finding $\nu$ in Eq. (3.24) means finding the water level $\nu$ so that the coloured area, which is enclosed by $\nu$ and $G_{noise}(f)$ in Fig. 3.8, is equal to $P_{sig}$. Particularly, no energy is allocated outside the frequency $\xi$, which satisfies the equation $G_{noise}(\xi) = \nu$. The parameter $\xi$ is called "critical frequency", and it will play a key role in the following calculations regarding the Shannon capacity.

The PSD of the (AC-coupled) received signal can be derived from Eq. (3.7) as

$$G_r(f) = (\alpha_{pof}\eta_{ld}\eta_{cp}\mathcal{R}_{pd}|H_{ptot}(f)|)^2 G_i(f), \tag{3.26}$$

where $G_i(f)$ is the PSD of the DC-free transmitted signal $I(t)$. The noise at the receiver is an

additive white Gaussian noise (AWGN) with a PSD of

$$\frac{\mathcal{N}_p}{2} = \frac{(\mathcal{R}_{pd}\mathcal{N}_{nep})^2 + 2q_e\mathcal{R}_{pd}\alpha_{_{pof}}\eta_{cp}P_{oavg}}{2}. \tag{3.27}$$

The capacity of the SI-POF channel from Eq. (3.22) becomes

$$R_{b,max} \leq \int_{-\infty}^{+\infty} \frac{1}{2}\log_2\left(1 + \frac{2G_i(f)\left(\alpha_{_{pof}}\eta_{ld}\eta_{cp}\mathcal{R}_{pd}|H_{ptot}(f)|\right)^2}{(\mathcal{R}_{pd}\mathcal{N}_{nep})^2 + 2q_e\mathcal{R}_{pd}\alpha_{_{pof}}\eta_{cp}P_{oavg}}\right)\, df. \tag{3.28}$$

With the aid of Eq. (3.28), the two PSDs $G_{sig}(f)$ and $G_{noise}(f)$ from the general optimisation problems in Eq. (3.22) and Eq. (3.23) can be re-formulated so that all the distortions and losses are assigned to $G_{noise}(f)$ while the average transmitted optical power can be assigned to $G_{sig}(f)$. Applying this re-formulation results in

$$G_{noise}(f) = \frac{(\mathcal{R}_{pd}\mathcal{N}_{nep})^2 + 2q_e\mathcal{R}_{pd}\alpha_{_{pof}}\eta_{cp}P_{oavg}}{2\left(\alpha_{_{pof}}\eta_{cp}\mathcal{R}_{pd}|H_{ptot}(f)|\right)^2} = \frac{\mathcal{N}_{nep}^2 + \frac{2q_e\alpha_{_{pof}}\eta_{cp}P_{oavg}}{\mathcal{R}_{pd}}}{2\left(\alpha_{_{pof}}\eta_{cp}|H_{ptot}(f)|\right)^2} \tag{3.29}$$

and

$$G_{sig}(f) = \eta_{ld}^2 G_i(f). \tag{3.30}$$

From Eq. (3.30), the power constraint in Eq. (3.23) can now be derived from the mean optical transmit power ($P_{oavg}$), the modulation index ($\eta_{mod}$) and the PAPR ($\rho_{_{papr}}$) as follows:

$$\begin{aligned} P_{sig} &= \int_{-\infty}^{+\infty} G_{sig}(f)\, df = \eta_{ld}^2\mathbb{E}[I^2(t)] = \eta_{ld}^2 I_{rms}^2 \\ &= \frac{(\eta_{ld}I_{mod})^2}{\rho_{papr}} = \frac{P_{omod}^2}{\rho_{papr}} = \frac{(\eta_{mod}P_{oavg})^2}{\rho_{papr}}. \end{aligned} \tag{3.31}$$

Using the water-filling solution given by Eq. (3.24) and Eq. (3.25), and by explicitly inserting the parameter $\xi$, the power constraint equation is re-written as

$$\int_{-\xi}^{+\xi} \left(G_{noise}(\xi) - G_{noise}(f)\right)\, df = P_{sig} \tag{3.32}$$

By inserting Eq. (3.29) and Eq. (3.31) in Eq. (3.32), the power constraint can be written as

follows:

$$\begin{aligned}\int_{-\xi}^{+\xi} \frac{\mathcal{N}_{nep}^2 + \frac{2q_e\alpha_{_{pof}}\eta_{cp}P_{oavg}}{\mathcal{R}_{pd}}}{2\left(\alpha_{_{pof}}\eta_{cp}\right)^2}\left(\frac{1}{|H_{ptot}(\xi)|^2} - \frac{1}{|H_{ptot}(f)|^2}\right)\,df &= \frac{(\eta_{mod}P_{oavg})^2}{\rho_{papr}} \\ \int_{-\xi}^{+\xi}\left(\frac{1}{|H_{ptot}(\xi)|^2} - \frac{1}{|H_{ptot}(f)|^2}\right)\,df &= \frac{2\left(\alpha_{_{pof}}\eta_{cp}\eta_{mod}P_{oavg}\right)^2}{\rho_{papr}\left(\mathcal{N}_{nep}^2 + \frac{2q_e\alpha_{_{pof}}\eta_{cp}P_{oavg}}{\mathcal{R}_{pd}}\right)}\end{aligned} \tag{3.33}$$

By inserting the SNR $\gamma_{_{sig}}$ from Eq. (3.11) into the above equation, the power constraint problem simplifies to

$$\int_{-\xi}^{+\xi}\left(\frac{1}{|H_{ptot}(\xi)|^2} - \frac{1}{|H_{ptot}(f)|^2}\right)\,df = \gamma_{_{sig}} f_{N0} = \gamma_{snm} \tag{3.34}$$

Equation (3.34) is a non-linear problem of the unknown parameter $\xi$, which can be solved numerically. After the optimum $\xi$ has been found, the capacity of the SI-POF channel can be calculated as

$$R_{b,max} \leq \int_{-\xi}^{+\xi} \frac{1}{2}\log_2\left(1 + \frac{G_{noise}(\xi) - G_{noise}(f)}{G_{noise}(f)}\right)\,df, \tag{3.35}$$

which can be rewritten as

$$R_{b,max} \leq \int_{-\xi}^{+\xi} \frac{1}{2}\log_2\left(\frac{G_{noise}(\xi)}{G_{noise}(f)}\right)\,df. \tag{3.36}$$

Inserting Eq. (3.29) in Eq. (3.36) results in

$$R_{b,max} \leq \int_{-\xi}^{+\xi} \frac{1}{2}\log_2\left(\frac{|H_{ptot}(f)|^2}{|H_{ptot}(\xi)|^2}\right)\,df. \tag{3.37}$$

The above equation shows the dependence of the maximum capacity on the frequency response of the SI-POF system. A closed-form expression of the capacity was derived for the SI-POF system if its frequency response is represented with the Gaussian model and the first-order Butterworth model [50]. For the Gaussian model, the capacity is defined in terms of the -3 dB bandwidth $f_{_{p3dB}}$ and the bandwidth-independent SNR ($\gamma_{_{snm}}$) as

$$R_{b,max} = \frac{2f_{_{p3dB}}\varrho^3}{3\ln 2\sqrt{\ln 2}}, \text{where } \varrho = \Psi\left(\frac{\gamma_{_{snm}}\sqrt{\ln 2}}{f_{_{p3dB}}}\right) \tag{3.38}$$

The function $y = \Psi(x)$ is not a closed-form expression but it can be solved numerically. The

relation between $y$ and $x$ with the function $\Psi(.)$ is expressed as

$$y\mathrm{e}^{y^2} - \frac{1}{2}\int_{-y}^{+y} \mathrm{e}^{b^2}\, db = x. \tag{3.39}$$

For the Butterworth model, the closed-form expression for the capacity is defined as

$$R_{b,max} = \frac{2f_{_{p3dB}}}{\ln 2}\left[\left(\frac{3\gamma_{_{snm}}}{2f_{_{p3dB}}}\right)^{\frac{1}{3}} - \arctan\left(\frac{3\gamma_{_{snm}}}{2f_{_{p3dB}}}\right)^{\frac{1}{3}}\right]. \tag{3.40}$$

#### 3.2.3.2 Numerical results for the channel capacity

Previous studies have estimated the capacity of the SI-POF channel for varying lengths by using the SNR as the main parameter [50, 70, 84]. However, the main parameter is the mean optical power of the transmitter and the NEP at the receiver. This setting implies that the SNR will reduce with increasing SI-POF lengths, which is contrary to what was done in previous studies. This assessment of the capacity is more feasible than that in [50, 70], as it emphasises on not only the SI-POF channel but also the optical transmitter and receiver. It is noted in this section that the capacity of the SI-POF is evaluated at lengths from 10 m to 100 m. These SI-POF lengths are selected as they are used for short-range applications that include networks in SOHO, vehicles and the industry. The channel capacity of the SI-POF channel will be measured with the bit rate $R_{b,max}$ in Gbps and the bit-rate length product in $R_{b,max} \times l_{pof}$ in Gbps.m.

| Parameters | Symbol | Values |
|---|---|---|
| POF attenuation coefficient | $\alpha_{_{pc}}$ | 0.18 [dB/m] |
| PD responsivity | $\mathcal{R}_{pd}$ | 0.4 [A/W] |
| Overall coupling efficiency | $\eta_{cp}$ | 0.7 |
| Receiver NEP | $\mathcal{N}_{nep}$ | 35 [pW/Hz$^{\frac{1}{2}}$] |
| PAPR of signal | $\rho_{_{papr}}$ | 6 [dB] |
| Mean transmitted optical power | $P_{oavg}$ | 1 [mW] |
| Optical modulation index | $\eta_{mod}$ | 1 |

**Table 3.1:** *Parameters used to obtain the results in Fig. 3.9 and Fig. 3.10*

The channel capacity of the SI-POF is first considered without any band-limitation from the transmitter or receiver devices. Therefore, the frequency responses $H_{ld}(f)$ and $H_{pd}(f)$ have

both of their magnitudes as equal to one at all frequencies. This setting is used to investigate the capacities of the SI-POF channel alone. The results are depicted in Fig. 3.9, and they compare the capacity curves for the Gaussian, Butterworth and power-flow approximations of the SI-POF channel. The -3 dB bandwidth of the first two approximations is obtained from Eqs. (3.14) and (3.13) using a bandwidth-length product of 4500 MHz.m. The frequency response with the power-flow is for the HFB and the GH profiles, and it is implemented with an optical source NA of 0.17.

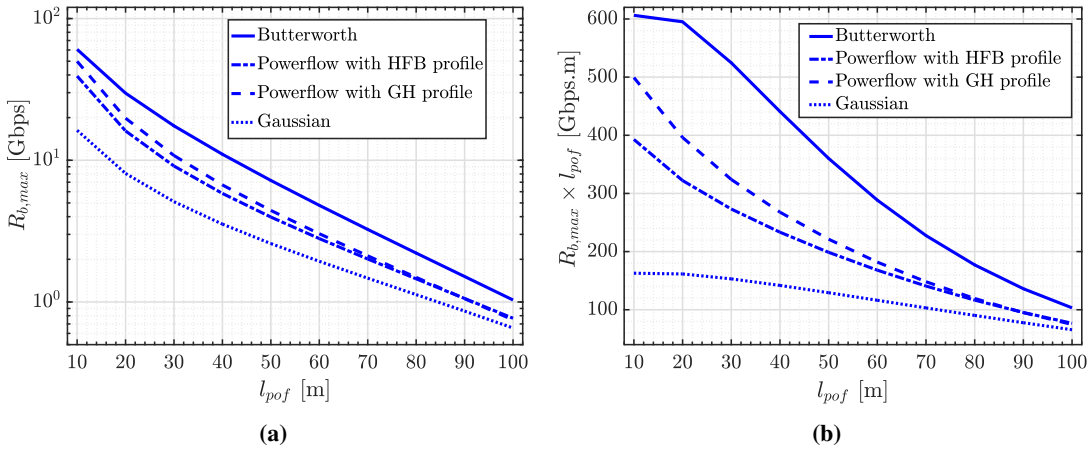


**Figure 3.9:** *Measure of channel capacity of SI-POF at varying lengths with the: (a) bit rate $R_{b,max}$ (b) bit-rate length product $R_{b,max} \times l_{pof}$ . There is no bandwidth limitation from the optical source and receiver so that $H_{ld}(f) = H_{pd}(f) = 1$ and $H_{ptot}(f) = H_{pof}(f)$; the Gaussian and Butterworth low-pass channel capacities are included for comparison purpose.*

For short SI-POF lengths, the capacity from the power-flow model tends towards the first-order Butterworth approximation. With increasing fibre length, the capacity from the power-flow model moves down to that from the Gaussian model, and the latter model is the lower-bound. The capacity from the power-flow model with the GH profile marginally outperforms that with the HFB profile. From Fig. 3.9a for instance, the capacities of the SI-POF at 10 m length are ∼60 Gbps, ∼50 Gbps, ∼40 Gbps and ∼16 Gbps from the Butterworth model, the power-flow model with the GH profile, the power-flow model with the HFB profile and the Gaussian model, respectively. But at 60 m length, their capacities are ∼5 Gbps, ∼3 Gbps, ∼2.8 Gbps and ∼2 Gbps, correspondingly. This behaviour agrees very well with the conclusions mentioned in [50], where the Butterworth model is used for SI-POF lengths up to 30 m, and the Gaussian model is used for fibre lengths of 30 m up to 200 m. Figure 3.9b shows the capacities of the SI-POF channel by using the bit-rate length product. The channel setting is similar to that used

in Fig. 3.9a, where there is no band-limitation from the transmitter and receiver. It is observed that the maximum bit-rate length product is obtained at an SI-POF length of 10 m regardless of the model used for the SI-POF channel. The bit-rate length product reduces significantly as the SI-POF lengths increases.

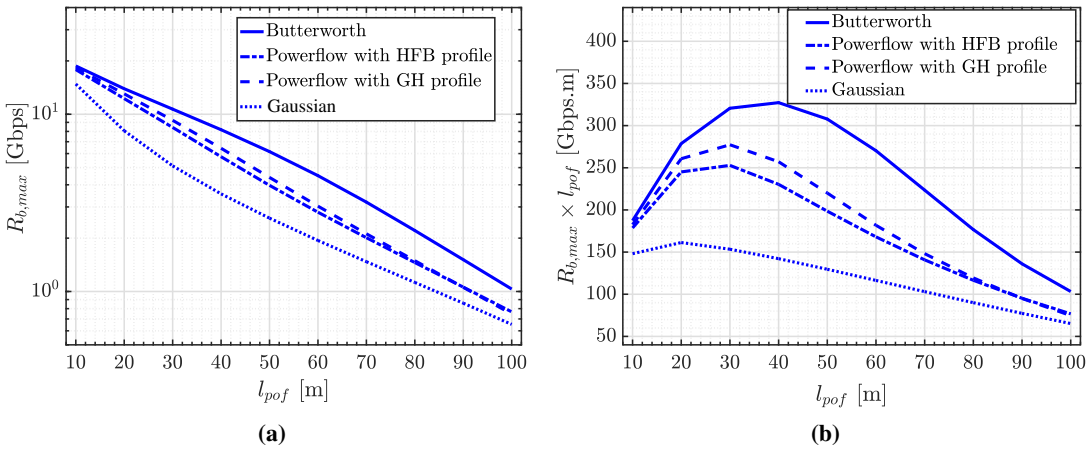


**Figure 3.10:** *Measure of channel capacity of SI-POF at varying lengths with the: (a) bit rate $R_{b,max}$ (b) bit-rate length product $R_{b,max} \times l_{pof}$ . A fourth-order Butterworth low-pass filter is used to model the bandwidth constraint from the optical source and receiver; the Gaussian and Butterworth low-pass channel capacities are included for comparison purpose.*

It is more practical to consider the channel capacity of the SI-POF, whose bandwidth is limited from the transmitter and receiver. The capacities of the SI-POF channel with the band-limitation are presented in Fig. 3.10. A fourth-order Butterworth low-pass filter – with a -3 dB bandwidth of 1 GHz – is used to model the bandwidth constraint from the optical source and receiver. Compared to the results from Fig. 3.9a, the capacities from Fig. 3.10a at 10 m length are reduced to ∼18 Gbps, ∼17 Gbps, ∼17 Gbps and ∼15 Gbps with the Butterworth model, the power-flow model with the GH profile, the power-flow model with the HFB profile and the Gaussian model, respectively. But at 60 m length, their capacities are ∼4.7 Gbps, ∼3 Gbps, ∼2.8 Gbps and ∼2 Gbps, correspondingly. The band-limitation of the optical front-end devices significantly reduces the capacity of the SI-POF system at shorter lengths, but does so slightly or even trivially for the system at longer lengths. Unlike in Fig. 3.9b, a convex relationship between the bit-rate length product and fibre length is observed for the SI-POF channel in Fig. 3.10b. Thus, there is an optimum fibre length that offers the maximum bit-rate length product of the SI-POF channel that is band-limited from the optical front-end devices. This length {maximum bit-rate length product} is 40 m {∼330 Gbps.m}, 30 m {∼275 Gbps.m}, 30 m {∼250 Gbps.m} and

20 m {∼160 Gbps.m} from the Butterworth model, the power-flow model with the GH profile, the power-flow model with the HFB profile and the Gaussian model, respectively.

## 3.3 Experiment Setup

The SI-POF based system for the thesis is experimentally investigated with the setup illustrated in Fig. 3.11. The block diagram and the photo of the setup are shown in Fig. 3.11a and Fig. 3.11b, respectively. The signal modulation and demodulation process are done in a computer, and the DSP for these processes are discussed in Section 3.1. The modulated signal from the computer is loaded to an arbitrary waveform generator (AWG, Keysight 81180A, 12 bits digital-to-analogue converter (DAC) resolution, 1 GHz bandwidth, 4.2 Gsa/s sampling rate).

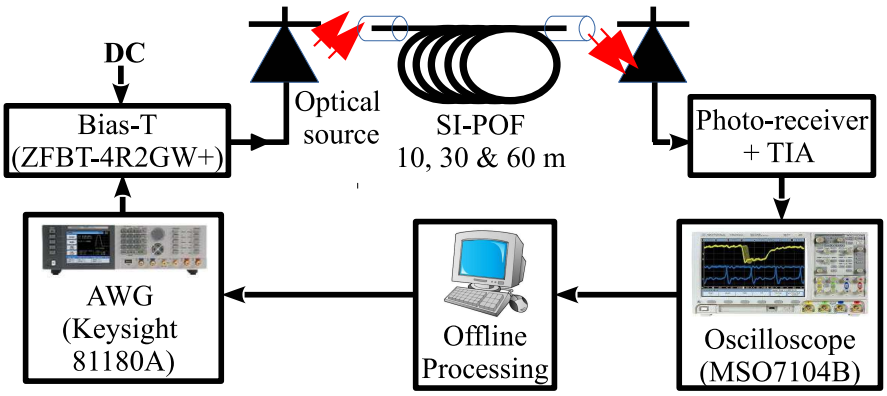


**(a)** Block diagram illustrating experiment setup

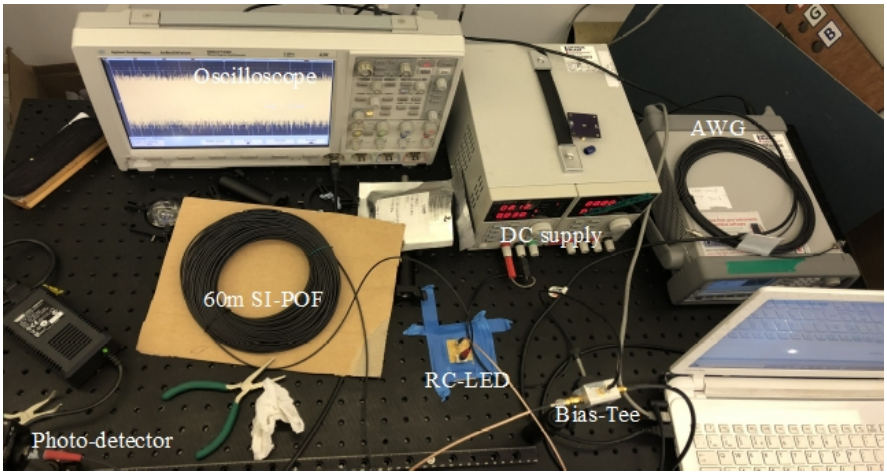


**(b)** Photo of the setup in the laboratory

**Figure 3.11:** *Description of experiment setup*

The AWG's output voltage signal is converted to a unipolar current signal with the addition of direct current (DC) via a bias-T (ZFBT-4R2GW+). This addition is implemented to drive the optical source. The output of the optical source is transmitted through an SI-POF (HFBR-RUD500Z) with a measured attenuation of ∼0.18 dB/m at 650 nm wavelength. Three SI-POFs, each of 10 m, 30 m and 60 m lengths, are used experimentally throughout this thesis. The optical signal from the SI-POF is then sent to a photo-receiver, whose output electrical signal is captured with an oscilloscope (MSO7104B, 1 GHz bandwidth, 4 Gsa/s, 8 bits ADC vertical resolution). The captured signal is then imported into the computer for further signal processing and demodulation. It takes about 45 seconds to run one experimental session to obtain the received bits from the setup.

Two experiment setups are explored throughout this thesis, with each using a different transmitter and receiver. The first (LD) setup uses an LD transmitter and a high-speed (1 GHz) photo-receiver while the other (RC-LED) setup uses an RC-LED transmitter and a lower-speed (150 MHz) photo-receiver. The lower-speed photo-receiver is selected for the latter setup as it has a higher amplifier gain than the first setup. Also, the RC-LED has a lower bandwidth than that of the receiver. The receiver from both setups uses the Si-PIN-PD as their PD.

The measured electrical-to-optical (E/O) conversion of the optical sources is defined by its optical power-to-electrical current (P-I) curve, and it is shown in Fig. 3.12a for the LD and in Fig. 3.12b for the RC-LED. Based on the LD's P-I curve, the DC bias current can be selected from ∼27 mA to ∼30 mA, which translates accordingly to an average optical fibre-coupled power ranging from ∼5.5 mW of ∼8 mW. From the RC-LED's P-I curve, the DC bias current can be selected from ∼20 mA to ∼30 mA, which translates accordingly to an average optical fibre-coupled power ranging from ∼1 mW of ∼1.3 mW. More details of the transmitter and the receiver for these setups are presented in Table 3.2.

The capacity of the LD and the RC-LED setups can be obtained by using the parameters from Table 3.2 and by applying them to the equations in Section 3.2.3.1. The PAPR is assumed to be 6 dB, but it could be above this value depending on the type of modulation. The frequency response of the overall SI-POF system $H_{ptot}(f)$ is needed to calculate the capacity, and it comprises the response from the optical source ($H_{ld}(f)$), the response from the SI-POF ($H_{pof}(f)$) and the response from the receiver ($H_{pd}(f)$). For the LD setup, the bandwidth of the LD can be assumed to be flat within the overall system bandwidth so that $H_{ld}(f) = 1$. The POF frequency response ($H_{pof}(f)$) is obtained from the power-flow model with the HFB profile using

| **Parameters** | **Symbol** | **LD setup** | **RC-LED setup** |
|---|---|---|---|
| ***Optical Transmitter*** | | ***Thorlabs L650P007 (650 nm)*** | ***Hamamatsu L10762 (650 nm)*** |
| Mean transmitted optical power | $P_{oavg}$ | 5 mW | 1 mW |
| Numerical aperture | $\text{NA}_{ld}$ | 0.17 | 0.35 |
| Modulation index | $\eta_{mod}$ | 1 | |
| -3 dB electrical bandwidth | | >1 GHz | 70 MHz |
| ***Optical Receiver*** | | ***New Focus 1601*** | ***Thorlabs PDA10A*** |
| PD radius | $r_{pd}$ | 0.2 mm | 0.5 mm |
| PD coupling efficiency | $\eta_{cp}$ | 0.16 | 1 |
| PD responsivity at 650 nm | $\mathcal{R}_{pd}$ | 0.45 A/W | |
| NEP at 650 nm | $\mathcal{N}_{nep}$ | 35 pW/Hz$^{\frac{1}{2}}$ | |
| -3 dB electrical bandwidth | | 1 GHz | 150 MHz |
| TIA gain | | 700 V/A | 5000 V/A |

**Table 3.2:** *Parameters of the optical transmitter and receiver for the SI-POF links with the LD setup and the RC-LED setup. The values are adopted from the datasheet of each optical source and receiver in [137–140].*

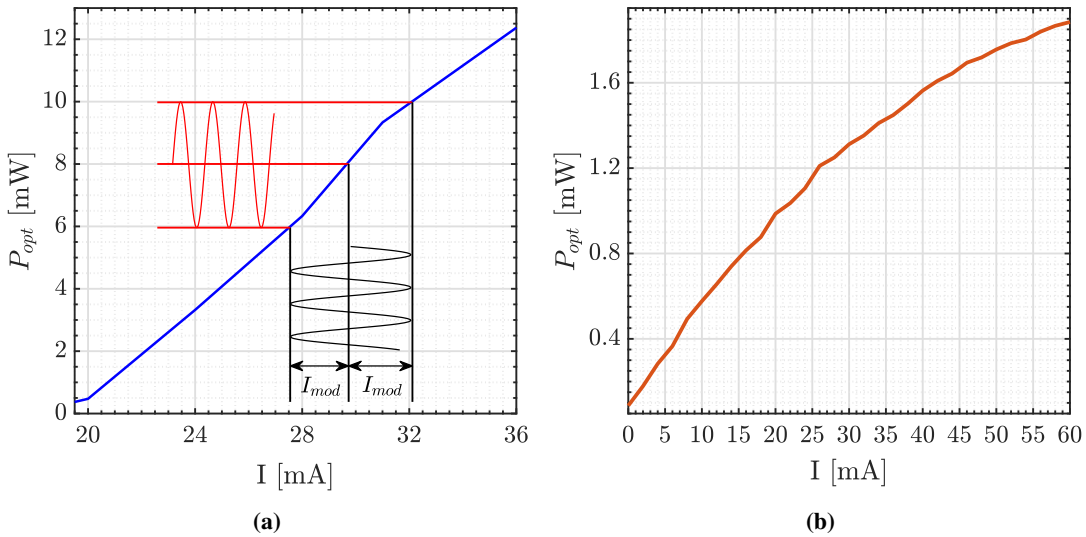


**Figure 3.12:** *Measured P-I curve of the: (a) LD L650P007 (b) RC-LED L10762*

an NA of 0.17; $H_{pd}(f)$ is modelled as a fourth-order Butterworth low-pass filter with a -3 dB bandwidth of 1 GHz. For the RC-LED setup, $H_{ld}(f)$ is modelled as a first-order Butterworth low-pass filter with a -3 dB bandwidth of 70 MHz; $H_{pof}(f)$ is obtained from the power-flow model with the HFB profile using an NA of 0.35; $H_{pd}(f)$ is modelled as a fourth-order Butterworth low-pass filter with a -3 dB bandwidth of 150 MHz.

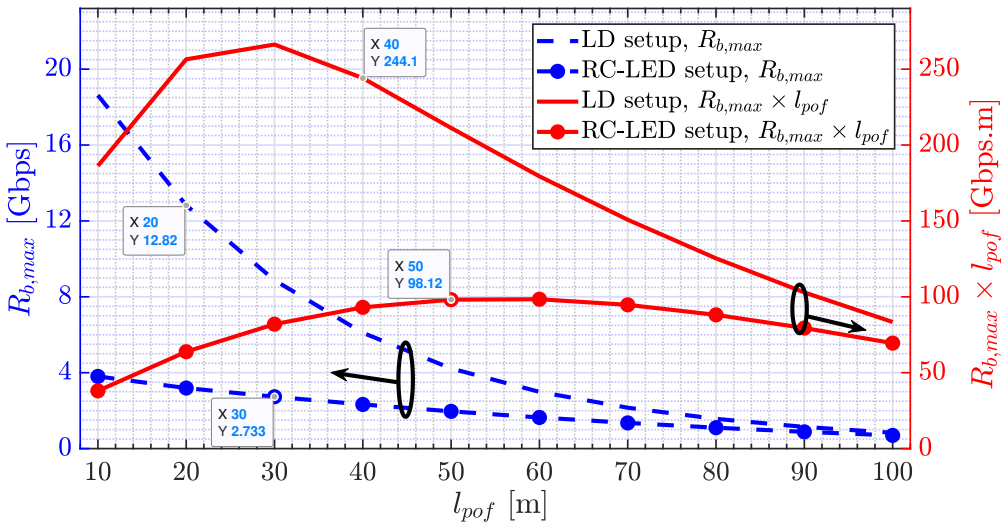


**Figure 3.13:** *Measure of channel capacity of SI-POF at varying lengths with the bit rate ($R_{b,max}$) and the bit-rate length product ($R_{b,max} \times l_{pof}$) using the parameters from Table 3.2.*

The theoretical capacities of the SI-POF system with the LD and RC-LED setups are presented

in Fig. 3.13 at varying fibre lengths. The capacities presented for each setup are the bit-rate and the bit-rate length product. The bit-rates of the SI-POF at 10 m length are ∼18.5 Gbps and ∼3.7 Gbps from the LD setup and the RC-LED setup, respectively. At 30 m length, the bit-rates are ∼9 Gbps and ∼2.7 Gbps, respectively. At 60 m length, they are ∼3 Gbps and ∼1.6 Gbps, respectively. A convex relationship is also observed between the bit-rate length product and fibre length. The convex curve for the LD setup is steeper than that for the RC-LED setup. The gentle curve from the RC-LED setup is due to the band-limitation of its transmitter. The optimum fibre length {and maximum bit-rate length product} of the SI-POF channel is 30 m {∼270 Gbps.m} and 60 m {∼96 Gbps.m} from the the LD setup and the RC-LED setup, respectively.

## 3.4 Non-linearity measurements with Total Harmonic Distortion

The total harmonic distortion (THD) is a well-known measure of non-linearity, which requires the use of a sinusoidal input to measure the amplitude (or power) of the generated harmonics. Figure 3.14 illustrates the use of an oscilloscope to measure the THD with the first five harmonics. The THD in dBc is defined as [141]:

$$\text{THD} = 10\log_{10}\left(\frac{1}{P_1}\sum_{n=2}^{\infty} P_n\right), \tag{3.41}$$

where $P_n$ is the power (in Watts) for the $n^{\text{th}}$ harmonic with $n = 1$ being the fundamental frequency. The THD is obtained by measuring the power of the first five harmonics using a fundamental frequency of 5 MHz as shown in Fig. 3.14.

In Fig. 3.15, the THD is computed for $I_{mod}$ and $I_{bias}$ using both the LD and the RC-LED setup. To maximise the SNR of an SI-POF link, a high value of $I_{mod}$ (or $\eta_{mod}$) is desirable as shown in Eqs. (3.12) and (3.11). However, it is seen in Fig. 3.15 that the non-linear distortion increases with $\eta_{mod}$ for both the LD and RC-LED setups. Furthermore, the THD is significantly higher for the LED than that for the LD. From Fig. 3.15a for instance, the THD from the LD setup is ∼-36 dBc and ∼-31 dBc at $\eta_{mod}$ values of 0.4 and 0.8, respectively. But from the RC-LED setup, the THD is increased to ∼-28 dBc and ∼-22.5 dBc, respectively. Hence using the RC-LED setup brings about a non-linear penalty of ∼8 dB and ∼8.5 dBc at $\eta_{mod} = 0.4$ and $\eta_{mod} = 0.8$, respectively. And this penalty remains constant at about 8 dB irrespective of the value of the modulation index. Figure 3.15a particularly shows that for the LD setup, the

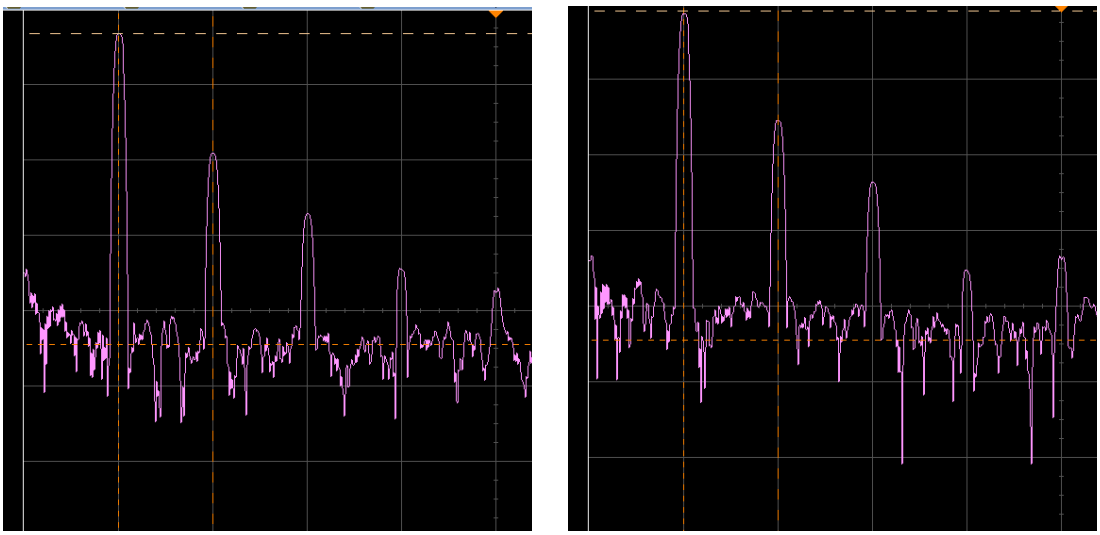

(a) (b)

**Figure 3.14:** *A capture of the first five harmonics from the oscilloscope at a fundamental frequency of 5 MHz for $I_{bias} = 28\ mA$ and: (a) $I_{mod} = 5$ mA (b) $I_{mod} = 7$ mA. The X-scale and Y-scale for the oscilloscope are 5 MHz/div and 25 dB/div, respectively.*

non-linearity diminishes slightly with the increasing length of the SI-POF. This observation is expected as an increase in the SI-POF length reduces the signal swing (peak-to-peak value) at the receiver, thus reducing the non-linearity contribution from the receiver.

In Fig. 3.15b, the THD is computed for the LD setup at different values of $I_{bias}$ with $I_{mod}$ of 5 mA and 7 mA. This measurement is implemented with a 10 m SI-POF. Fig. 3.15b shows a convex relationship between THD and $I_{bias}$ irrespective of the value of $I_{mod}$. Thus, there is an optimum value of $I_{bias}$ that offers the minimum THD of the LD. $I_{bias}$ must not exceed this value as it would increase not only the THD of the LD but also reduce the lifetime of (or even damage) the LD. The minimum THD for $I_{mod} = 5\ mA$ and $I_{mod} = 7\ mA$ is about -39 dBc and -34 dBc, respectively with $I_{bias} = 30\ mA$. For the RC-LED setup, the THD is computed with $I_{mod}$ of 15 mA and 20 mA. It is observed that for both values of $I_{mod}$ the non-linear distortion is either constant or it slightly varies with respect to the bias current. This pattern is due to the effect of non-linearity contributed from low-level clipping at lower values of $I_{bias}$ and the effect of from the highly non-linear P-I curve for moderate to higher values of $I_{bias}$ (see Fig. 3.12b). The THD for $I_{mod} = 15\ mA$ and $I_{mod} = 20\ mA$ is about -26 dBc and -24 dBc, respectively with $I_{bias} = 30\ mA$.

The THD is just the average sum of the power of the harmonics, and it does not show whether

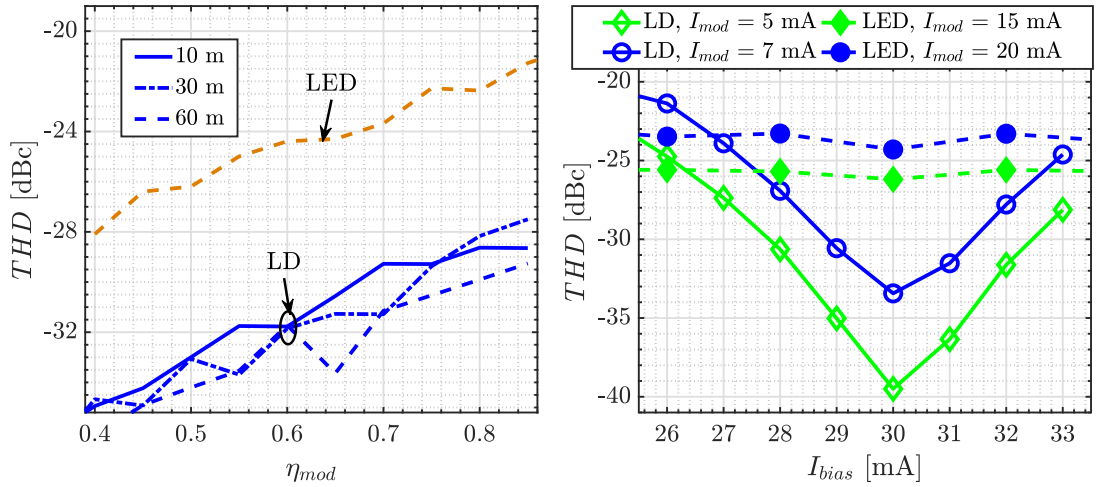


**Figure 3.15:** *Measured total harmonic distortion (THD) for values of the: (a) modulation index ($\eta_{mod}$) at a bias current of 28 mA and 30 mA for the LD and the RC-LED setup, respectively (b) bias current ($I_{bias}$).*

one harmonic dominate another or if the harmonics are comparable to each other. Therefore, the magnitude of distortion from two constituent harmonics are presented in Fig. 3.16. The distortions under consideration are the second-order harmonic distortion (HD2) and the third-order harmonic distortion (HD3). In Fig. 3.16a, the values of HD2 and HD3 are presented for the LD setup with the same settings used in Fig. 3.15b. For the LD setup, the HD2 has a convex relationship with $I_{bias}$ irrespective of the value of $I_{mod}$. But HD3 does not follow this pattern. Instead, it stays constant at ∼-40 dBc and ∼-33 dBc for $I_{mod} = 5\ mA$ and $I_{mod} = 7\ mA$, respectively. For the values of the bias current that ranges between 29 mA and 31 mA, HD3 dominates over HD2 and vice versa. This observation suggests that even though the non-linear distortion is minimal for the bias current within these values, it is greatly dominated by third-order non-linearity. Hence, the VOLT3DFE would offer superior BER performance than the VOLT2DFE at this range of values for the bias current. Otherwise, the VOLT2DFE would offer a superior BER performance than VOLT3DFE.

In Fig. 3.16a, the values of HD2 and HD3 are presented for the RC-LED setup with the same settings used in Fig. 3.15b. HD2 and HD3 are shown to be slightly constant to the bias current, and it is also observed that HD2 is significantly greater than HD3. For instance, the values of HD2 and HD3 for $I_{mod} = 15\ mA$ are about -26 dBc and -51 dBc, respectively. Thus, HD2 dominates over HD3 by a gain of 25 dB. For $I_{mod} = 20\ mA$, the values HD2 and HD3 are

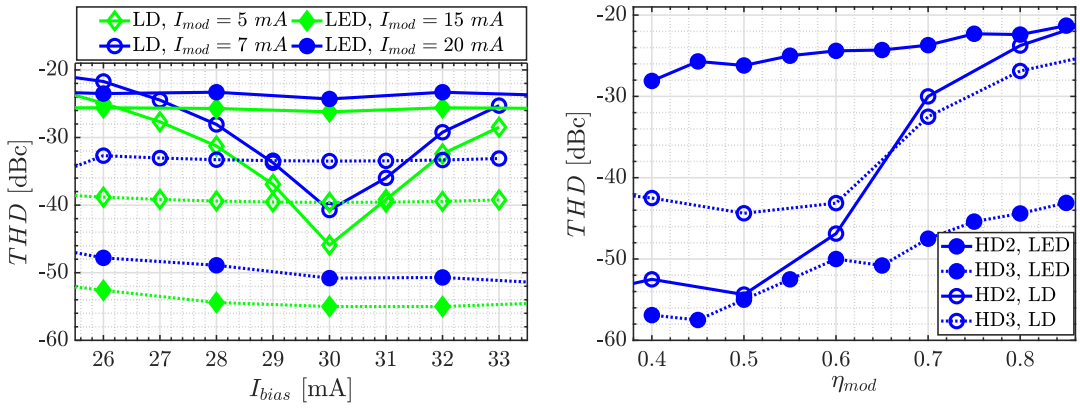


**(a)** **(b)**

**Figure 3.16:** *Measured second-order and third-order harmonic distortion (HD2 and HD3) for values of the: (a) bias current ($I_{bias}$) (b) modulation index ($\eta_{mod}$) at a bias current ($I_{bias}$ =) of 28 mA and 30 mA for the LD and the RC-LED setup, respectively. The straight and dotted lines denote the values of HD2 and HD3, respectively.*

27 dBc and -55 dBc, respectively. So, HD2 dominates over HD3 by a gain of 28 dB. Therefore, the second-order non-linearity is the most significant component of the system non-linearities in an RC-LED setup, irrespective of the value of the bias current. This result suggests that the VOLT2DFE is better than the VOLT3DFE for the RC-LED setup at all bias current points for the RC-LED.

Figure 3.16b depicts the values of HD2 and HD3 for values of $\eta_{mod}$ with both the LD and the RC-LED setups. The same setting used in Fig. 3.15a is used to obtain the results in Fig. 3.16b. Like previous results from Fig. 3.16a, the second-order harmonic distortion still fully dominates the system non-linearities for the RC-LED setup. The values of HD2 and HD3 with this setup are $\sim$-28 dBc and $\sim$-57 dBc, respectively at $\eta_{mod} = 0.4$: HD2 stands out above HD3 by a gain of 29 dB. At $\eta_{mod} = 0.8$, the values of of HD2 and HD3 for the RC-LED setup are $\sim$-22 dBc and $\sim$-44 dBc, respectively. These values imply that HD2 overshadows HD3 by a gain of 22 dB in terms of non-linearity. It can be inferred from these results that as $\eta_{mod}$ increases, the rate at which the third-order distortion increases is more than that for the second-order distortion for the RC-LED setup. With the LD setup, the third-order harmonic distortion still fully dominates the system non-linearities for values of $\eta_{mod}$ less than 0.65. Otherwise, the second-order harmonic distortion dominates the system non-linearities.

## 3.5 Summary

In this chapter, the IM/DD channel for the SI-POF has been fully explored in detail. A description of the modulation formats for this channel was first discussed. The channel capacity was calculated for the commonly used approximations, the Gaussian, the Butterworth, and the power-flow model. Unlike the studies done in [50, 84], the capacity is assessed here in terms of the maximum achievable bit-rates and bit-rate length products by using a constant mean optical transmitted power and the receiver's noise sensitivity. The results first confirm the observations from recently published work [50, 84], that for short fibre length ($<$ 30 m) the Butterworth model is the best approximation while for longer fibre length ($>$ 100 m) the Gaussian model can be used. The capacity results also add some knowledge to these published work. They prove that the bit-rate length product of the SI-POF channel can be maximised by selecting an optimum length, provided there is a band-limitation from the optical source and receiver. With no bandwidth constraint from the front-end devices, the bit-rate length product of the IM/DD SI-POF channel reduces with the SI-POF length.

The two experiment setups considered for this thesis are described in this chapter. The first uses the LD transmitter with a high-speed receiver, while the other uses an RC-LED as the transmitter and a relatively low-speed receiver. The total harmonic distortion (THD) is used to measure the non-linearities of these setups based on their DC bias current and their modulation index. For the LD setup, there is an optimal bias current that minimises the non-linearity of the SI-POF system. For the RC-LED setup, the non-linearity is slightly constant irrespective of the bias current. With both the LD and RC-LED setups, the system non-linearities increase as the modulation index increases. Also, the THD from the RC-LED setup is $\sim$8 dB higher than that from the LD setup at a fundamental frequency of 5 MHz. The contribution of the second-order harmonics and third-order harmonics were considered for both setups as well. For the RC-LED setup, the second-order harmonic distortion significantly dominates the system non-linearities compared to the third-order harmonic distortion by at least a gain of $\sim$20 dB. For the LD setup, the distortion from two harmonics each has a fair chance at dominating the system non-linearities. They depend on the value of the bias current and the modulation index of the SI-POF system from the LD setup.

# Chapter 4
# Time Domain Non-linear Equalisers for Single-carrier Modulation Schemes over SI-POF

The previous chapter presented the linear IM/DD model of an SI-POF channel and assessed its capacity. It also presented an evaluation of the non-linearities for the experiment setups that will be used in this thesis. In this chapter, the performance of the SI-POF system is estimated with a non-linear model. For this purpose, a set of extensive simulations is used to evaluate the performance of the non-linear equalisers (NLEs) with this model. The NLEs are implemented in the time-domain (TD), and they are compared with the use of single-carrier modulation (SCM) schemes like PAM and CAP. The experiment setups are also used to evaluate the performance of the SCM schemes in combination with the NLEs.

The first section of this chapter presents a non-linear model of the SI-POF and highlights the parameters required for the simulation of this model. The second and the third section presents the results of the NLEs from the simulation for PAM and CAP schemes, respectively. The fourth section shows the complexity requirements for each NLE. With the SCM schemes and NLEs, the results from the experiment setups discussed in the previous chapter are displayed in the fifth section.

## 4.1 System Model and Parameters

The simulation model in this thesis is based on the LD experiment setup, which was described in Section 3.3. The model of an IM/DD SI-POF system was expressed previously in Eq. (3.7) as:

$$I_{rp}(t) = \mathcal{R}_{pd}\eta_{cp}\alpha_{pof}(P_{opt}(t) \otimes h_{ptot}(t)) + n_p(t), \tag{4.1}$$

where $\mathcal{R}_{pd}$ denotes the photodiode (PD) responsivity in A/W. $\eta_{cp}$ denotes the maximum coupling efficiency and this is significant when the radius of the POF cable $(r_{pof})$ is above the

radius of the PD ($r_{pd}$), so $\eta_{cp} = \left(\frac{r_{pd}}{r_{pof}}\right)^2$ with butt coupling; $\alpha_{pof}$ is the attenuation of the POF channel and $\alpha_{pof} = 10^{-0.1\times\alpha_{pc}\times l_{pof}}$ where $l_{pof}$ is the POF length in metres and $\alpha_{pc}$ is the POF attenuation coefficient in dB/m. To include the effect of the system non-linearities to the model, the optical signal intensity of the LD ($P_{opt}(t)$) is expressed as a non-linear estimate of the LD's measured P-I curve that is shown earlier in Fig. 3.12a. The estimate is a polynomial function $f_{nl}(I)$, which is

$$P_{opt}(t) = f_{nl}(I) = \begin{cases} -0.001414I^3 + 0.1278I^2 - 2.98I + 20.62 & I > 18.9 \\ 0 & \text{otherwise,} \end{cases} \tag{4.2}$$

where $I = I_{bias} + I(t)$.

The non-linear estimate of the P-I curve is depicted in Fig. 4.1, and the equivalent block diagram for this model is shown in Fig. 4.2. To assess the impact of the LD non-linearities, we consider two different setups for the input current signal to the LD. These are denoted as LDS1 and LDS2 in the rest of the paper. For LDS1, the input current signal is such that $I_{bias} = 30$ mA and $I_{mod} = 7$ mA, while for LDS2, $I_{bias} = 26$ mA and $I_{mod} = 7$ mA. The LDS2 setup has a higher non-linear distortion than the LDS1 setup as depicted in Fig. 3.15b. The non-linearity from the LDS2 setup is from low-level clipping due to its lower value of $I_{bias}$.

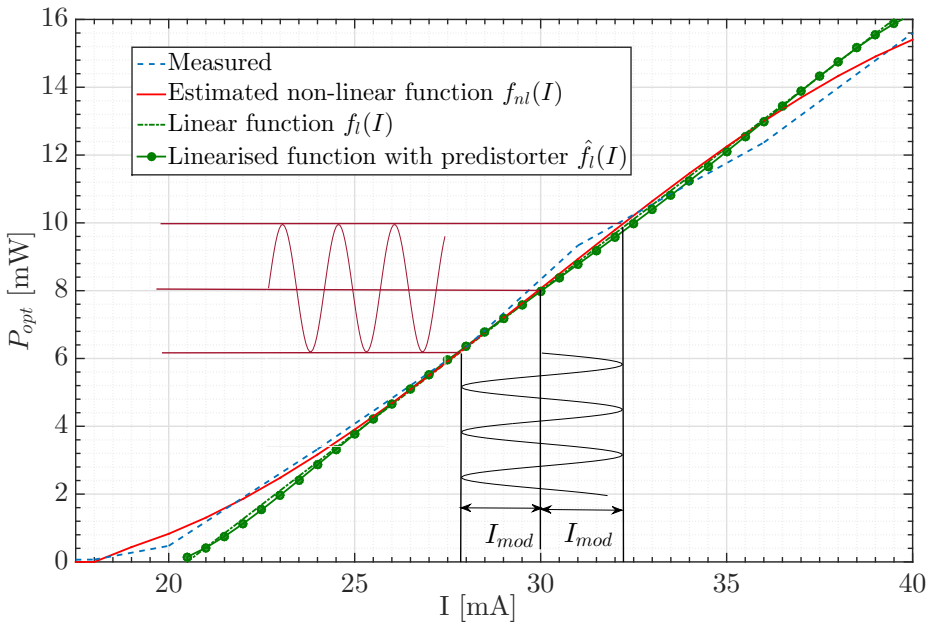


**Figure 4.1:** *Estimate of the LD's P-I curve*

In (4.1), $h_{ptot}(t)$ denotes the impulse response of the overall channel, which consists of the background system (AWG and oscilloscope) and the POF system (LD, POF and receiver). The

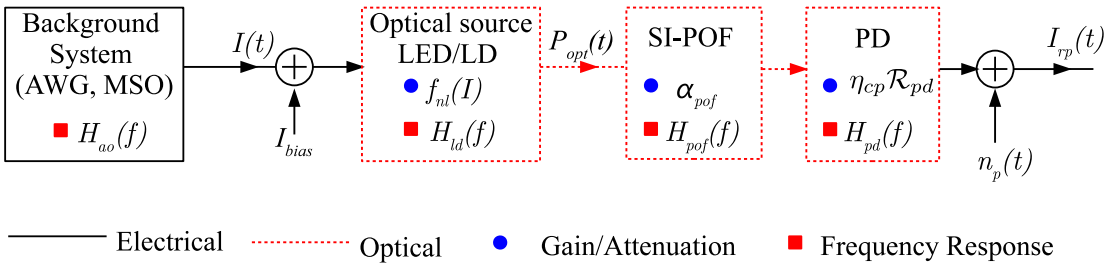


**Figure 4.2:** *Model illustration of the POF system*

combined response of the AWG and oscilloscope was measured and can be represented as a $1^{st}$ order Butterworth low-pass filter with a -3 dB bandwidth of 800 MHz. LDs generally have bandwidth ranging from few GHz to tens of GHz [68, 79, 84], so the response of the LD can be assumed to be flat within the overall system bandwidth. The POF channel response is estimated with the power-flow model, and the PD's response is estimated as a $1^{st}$ order Butterworth low-pass filter with a -3 dB bandwidth of 1 GHz. Hence,

$$\begin{aligned} h_{ptot}(t) &= h_{ao}(t) \otimes h_{pof}(t) \otimes h_{pd}(t)) \text{ in TD,} \\ H_{ptot}(f) &= H_{ao}(f) H_{pof}(f) H_{pd}(f) \text{ in FD.} \end{aligned} \tag{4.3}$$

where $h_{ao}(t)$ is the combined impulse response for the AWG and oscilloscope; $h_{pof}(t)$ is the impulse response for the SI-POF channel; and $h_{pd}(t)$ is the impulse response for the receiver. The plots of the magnitude response for $H_{ptot}(f)$ are presented in Fig. 4.3 for SI-POFs of length 10 m, 30 m and 60 m.

The noise, denoted by $n_p(t)$, is the additive white Gaussian noise (AWGN) at the receiver. It is assumed here that the dominant noise source is derived from the receiver's sensitivity and the shot noise. Thus, the noise variance is obtained from Eq. (3.11), and it can be written as:

$$P_{noise} = f_{N0} \left( (\mathcal{R}_{pd} \mathcal{N}_{nep})^2 + 2 q_e \mathcal{R}_{pd} \alpha_p \eta_{cp} P_{oavg} \right), \tag{4.4}$$

where $f_{N0}$ is the effective noise bandwidth of the channel, which is defined as the bandwidth of a brick-wall filter that has the same power (or energy) as the channel [142]. This can be obtained as:

$$f_{N0} = \int_0^\infty |H_{psf}(f) H_{ptot}(f)|^2 \, df, \tag{4.5}$$

where $H_{psf}(f)$ denotes the frequency response of the PSF for the SCM schemes.

In a band-limited channel like that of the SI-POF, the optimum PSF for both PAM and CAP

schemes is the Nyquist RRC filter [43]. The three vital parameters for this filter are its roll-off factor, its span and its oversampling factor. The RRC roll-off factor ($\beta$) varies from 0 to 1, and it determines the SCM signal's PAPR as well as its excess bandwidth. A low value of $\beta$ results in less bandwidth usage but leads to high PAPR [131]. A roll-off factor of 0.4 is therefore selected for both PAM and CAP throughout this thesis. An ideal PSF requires an infinite symbol span ($G_s$) to give zero ISI at the sampling instant when combined with the matched filter at the receiver [43]. However, for viable systems, the span is finite; hence the filter is truncated. Therefore, the value of $G_s$ for the RRC filter is chosen based on the compromise between computational complexity and BER performance. A span of ten is shown to be sufficient in [143], but there are eight spans for the RRC filter throughout this thesis. The optimum value for $\beta$ varies between 0.4 and 0.55 depending on the SCM scheme and the equaliser that is used [131]. The oversampling factor ($N_{sps}$) is an important parameter to consider for PAM scheme with $M$ symbols (PAM-$M$) and for CAP scheme with $M^2$ symbols (CAP-$M^2$). For the first scheme, it is defined with the sampling rate $F_s$ and the bit-rate $R_b$ as:

$$N_{sps} = \frac{F_s \log_2 M}{R_b}, \tag{4.6}$$

For similar values of $F_s$ and $R_b$, CAP-$M^2$ requires twice the oversampling factor as that of PAM-$M$. The value of $N_{sps}$ can be kept constant so that $F_s$ increases proportionally with $R_b$. Otherwise, $F_s$ can be kept constant so that $N_{sps}$ varies inversely with $R_b$.

### 4.1.1 Inverse polynomial pre-distorter model

The relation between the input current and the optical power for the LD is modelled as the 3$^{\text{rd}}$ degree polynomial function $f_{nl}(I)$ expressed in Eq. (4.2). The function shows that the current range for the LD is within the range of ∼19 mA up to ∼40 mA. The pre-distorter linearises $f_{nl}(I)$ by using the inverse polynomial function $f_{nl}^{-1}(I)$ and a linear function $f_l(I)$. The polynomial function for the pre-distorter can, therefore, be obtained as [85]:

$$\begin{aligned} f_{pred}(I) &= f_{nl}^{-1}(f_l(I)), \\ \text{where } f_l(I) &= 0.8421I - 17.26, \\ \text{and } f_{nl}^{-1}(I) &= 0.005623I^3 - 0.14I^2 + 2.247I + 18.07. \end{aligned} \tag{4.7}$$

The output of the pre-distorter is then passed through the LD to obtain the linearised response ($\hat{f}_l(I)$). It is shown in Fig. 4.1 that the linearised function from the pre-distorter $\hat{f}_l(I)$ matches the linear function $f_l(I)$. However, the current range that can be modulated linearly is from $\sim$ 20.5 mA to $\sim$37 mA.

### 4.1.2 Experimental validation of simulation Model

To validate this simulation model, Fig. 4.3 shows and compares the frequency response of $h_{ptot}(t)$ from simulation and experiment for three different SI-POF lengths of 10 m, 30 m and 60 m. It is observed that the frequency response from the model matches that measured from the experiment at frequencies below 900 MHz.

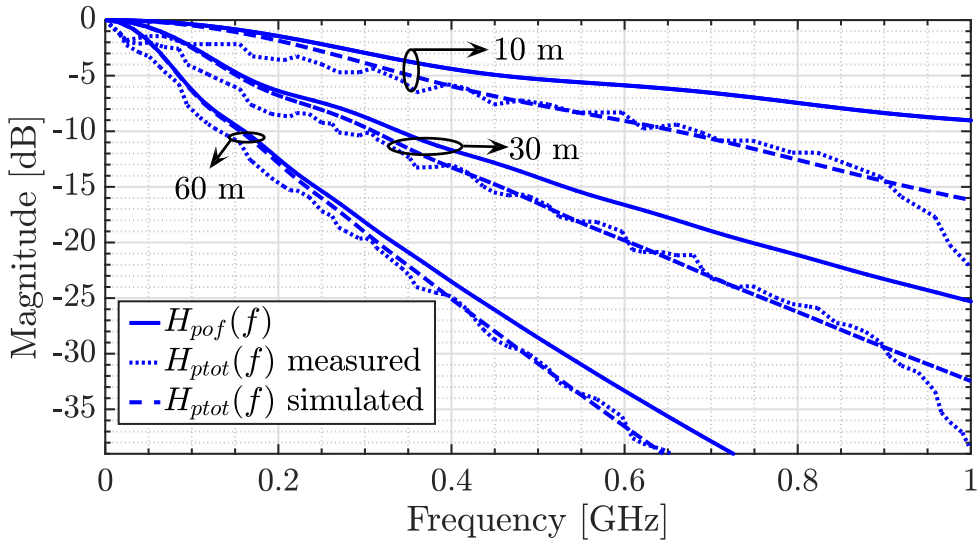


**Figure 4.3:** *The magnitude response of the system under various SI-POF length. $H_{pof}(f)$ is generated with the power-flow model using the HFB profile*

In Fig. 4.3, the BER result from the simulation model is compared with that from the experiment setup for $M \in \{4, 8, 16\}$ using the LDS1 setup ($I_{bias} = 30$ mA, $I_{mod} = 7$ mA). The POF length is 60 m, and the transversal DFE is used to obtain this BER result. It is observed that the simulation model provides a good estimate of the experiment for PAM-4 and PAM-8. At a BER of $10^{-3}$ for PAM-16, the bit rate from the experiment is 0.2 Gbps higher than that from the simulation. The difference in results for PAM-16 suggests that the simulation model is slightly more non-linear than the experiment setup. Therefore, the simulation model is useful for assessing and evaluating the performance of the NLEs for the SI-POF channel under LD non-linearities. The common parameters for the simulation model and the NLEs are provided

in Table 4.1.

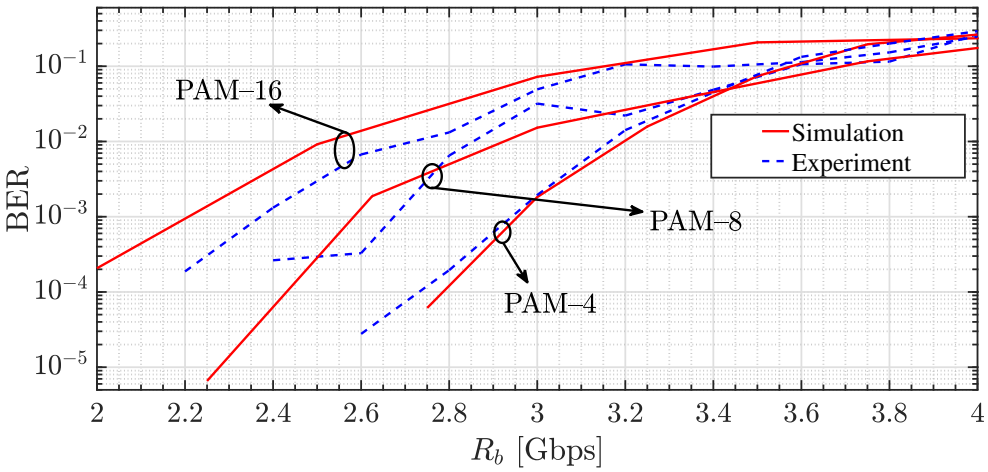


**Figure 4.4:** *BER plot for $M \in \{4, 8, 16\}$ comparing the results from simulation with those of experiment using the transversal DFE. $l_{pof} = 60$ m, $I_{bias} = 30$ mA, $I_{mod} = 7$ mA*

| Parameters | Symbol | Values |
|---|---|---|
| POF attenuation coefficient | $\alpha_{pc}$ | 0.18 [dB/m] |
| POF PD responsivity @ 650 nm | $\mathcal{R}_p$ | 0.45 [A/W] |
| Overall coupling efficiency | $\eta_{cp}$ | 0.16 |
| Receiver NEP @ 650 nm | $\mathcal{N}_{nep}$ | 35 [pW/Hz$^{\frac{1}{2}}$] |
| Number of bits for BER testing | $N_{bit}$ | $10^6$ |
| Equaliser's number of feedforward taps | $N_{ft}$ | 22 |
| Equaliser's number of feedback taps | $N_{bt}$ | 18 |
| Equaliser's number of training examples | $N_{tr}$ | 4000 |
| Number of hidden-layer neurons for the MLP equalisers | $N_{hn}$ | 6 |

**Table 4.1:** *Simulation setup parameters*

## 4.2 Comparison of Real-valued TD-NLE for PAM-*M*

The PAM modulation and de-modulation process are highlighted in Fig. 3.1. A constant over-sampling factor ($N_{sps}$) of four is used for the simulation model irrespective of the signal's bit rate. Each simulation result displayed is the average of ten independent realisations. The tap (or synaptic) weights of the TD based NLEs (TD-NLEs) are real-valued as the voltage levels that correspond to the PAM symbols are real-valued. To evaluate and compare the performance

of the NLEs in the presence of ISI and non-linearity, we present the BER results at various bit rates for 60 m, 30 m and 10 m POF lengths. It should be noted that the three lengths are selected as they can be applied to automotive and industrial applications (see Table 1.2). However, the SOHO network can only work with the 60 m SI-POF link.

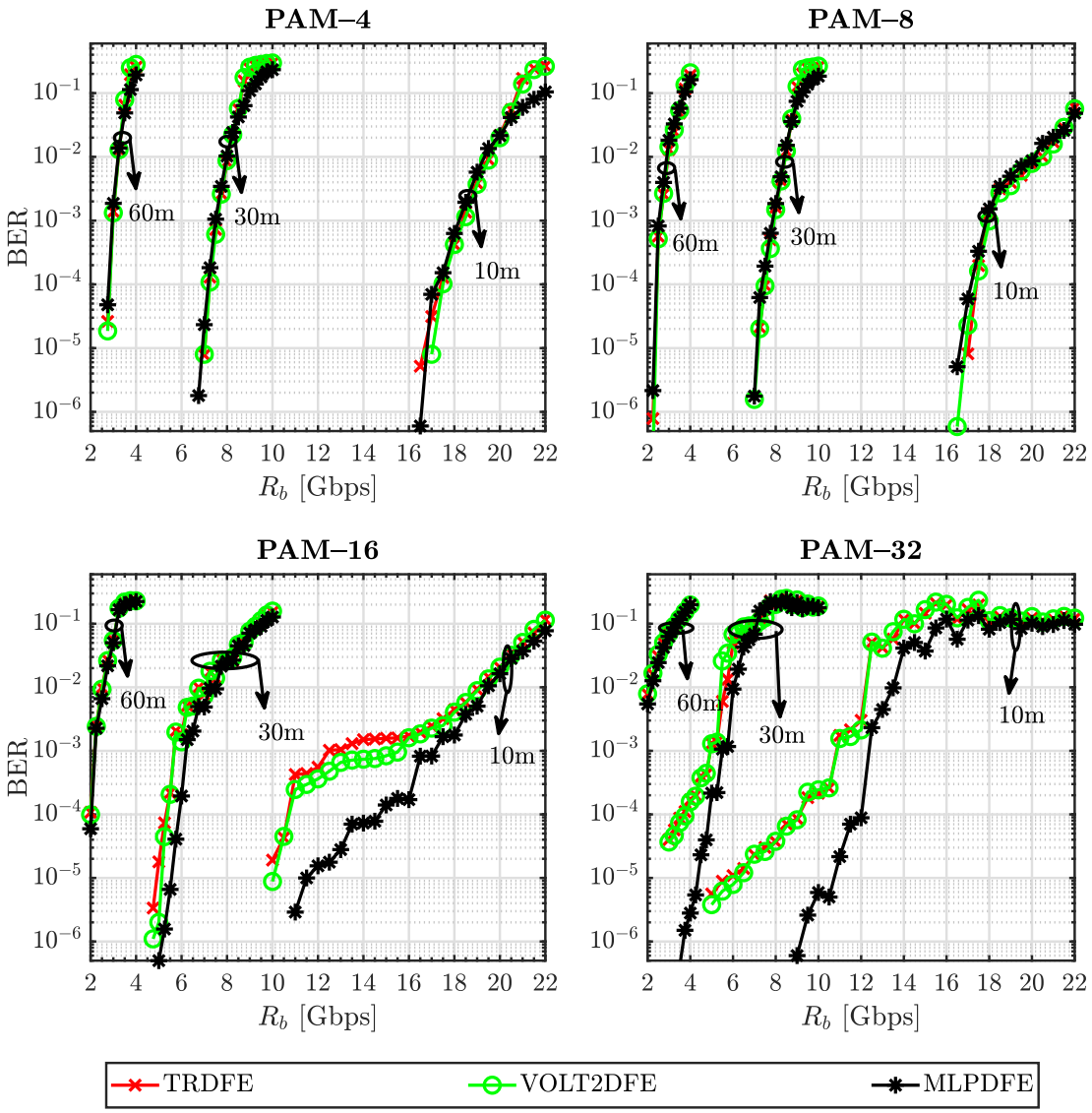


**Figure 4.5:** *BER result comparing the equalisers performance over SI-POF with LDS1 setup ($I_{bias}$ = 30 mA, $I_{mod}$ = 7 mA). $\gamma_{nm}$ is ∼37 dB, ∼47 dB and ∼53 dB for SI-POF lengths of 60 m, 30 m and 10 m respectively.*

In Fig. 4.5, the BER result for the equalisers with the LDS1 setup ($I_{bias}$ = 30 mA, $I_{mod}$ = 7 mA) is depicted for POF lengths of 10 m, 30 m and 60 m. It should be noted here that for the LDS1 setup, there are six hidden neurons ($N_{hn}$ = 6) for the MLPDFE for it to achieve the

best performance while not compromising computational complexity. The plots in Fig. 4.5 are waterfall curves that express the BER response, which rises to the increasing signal bit rate. This curve pattern is because the signal bandwidth increases at higher bit-rates and this leads to a noise increase (or an SNR reduction). As the SI-POF length increases, the BER curves are at lower bit-rate regions, and they become slightly steeper. This steepness is appropriate as the SNR at the receiver reduces for longer SI-POF links for the same optical source and receiver.

Another observation with the BER curve is that its slope is smaller with a high-order PAM scheme, but is relatively higher with a low-order PAM scheme. For the 10 m SI-POF link for instance, if bit-rate increases by 12.5% (from 16 Gbps to 18 Gbps), the BER increases by a factor of 6300 from $\sim 10^{-7}$ to $\sim 6.3 \times 10^{-4}$. This result is achieved with PAM-4 modulation and the MLPDFE. But with PAM-16 and the same NLE, the BER rises by a factor of 10.60 ($\sim 1.7 \times 10^{-4}$ to $\sim 1.8 \times 10^{-3}$). This pattern happens because, at a constant bit rate, the signal bandwidth for a higher-order PAM scheme is smaller compared to that with a low-order PAM scheme. Nevertheless, the low-order PAM scheme offers superior BER performance than that from higher-order PAM schemes due to SNR constraint of the latter.

It is seen for the LDS1 that the highest bit rate obtained at a BER of $10^{-3}$ with the three DFEs is ∼3 Gbps for 60 m POF with PAM-4, ∼7.8 Gbps for 30 m POF with PAM-8, and ∼18 Gbps for 10 m POF with PAM-8. Also, the three DFEs offer similar BER for $M \leq 8$. This is because the non-linear distortion is minimal for the LDS1 setup with negligible effect at lower modulation order. The optimum PAM scheme with the LDS1 setup is PAM-4 for 60 m POF and PAM-8 for both 30 m and 10 m POF. With $M > 8$ however, the MLPDFE BER performance is superior to both VOLT2DFE and TRDFE for 10 m and 30 m POF lengths. For example, with PAM-16 ∼6.2 Gbps bit-rate is achieved with MLPDFE at a BER of $10^{-3}$, while the other DFEs offer ∼5.7 Gbps for a 30 m POF. Similarly for a 10 m POF with PAM-16, ∼17 Gbps bit-rate is obtained with MLPDFE, while this is ∼16 Gbps with the other DFEs. For PAM-32, the achievable bit-rate at 30 m is ∼5.7 Gbps with MLPDFE while it is ∼5.2 Gbps with both VOLT2DFE and TRDFE. For 10 m POF with PAM-32, this is ∼12.3 Gbps with MLPDFE while it is ∼10.8 Gbps with the other DFEs.

With higher amount of non-linear distortion represented as LDS2 setup ($I_{bias} = 26$ mA, $I_{mod} = 7$ mA), the BER against bit-rate results are presented in Fig. 4.6. Unlike with the LDS1 setup, 24 hidden neurons ($N_{hn} = 24$) is used for the MLP's optimal performance with the LDS2 setup since it has more non-linear distortion than the LDS1 setup. It is observed in Fig. 4.6 that the

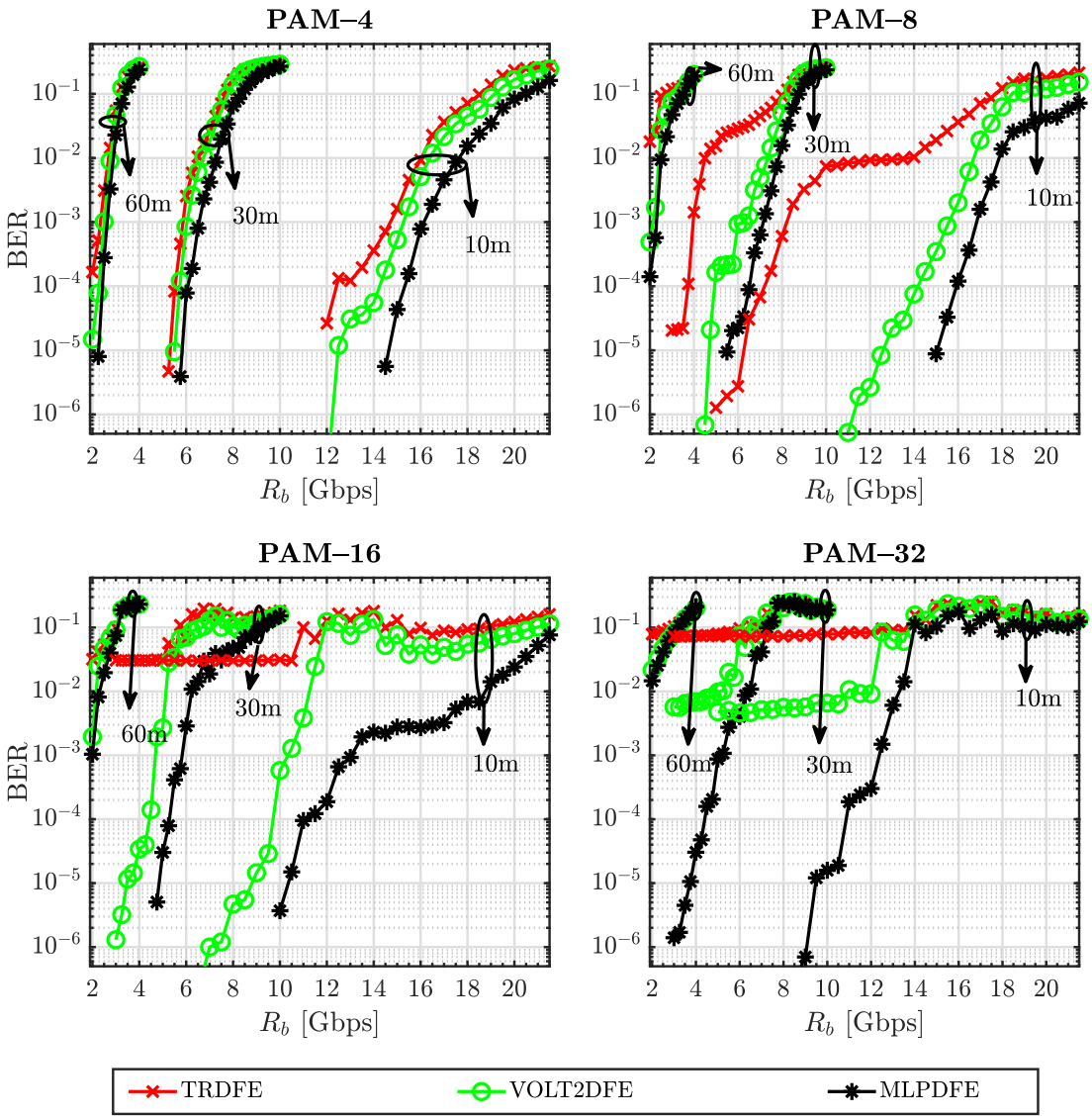


**Figure 4.6:** *BER result comparing the equalisers performance over the SI-POF with the LDS2 setup ($I_{bias} = 26$ mA, $I_{mod} = 7$ mA). $\gamma_{nm}$ values are similar to those in Fig. 4.5*

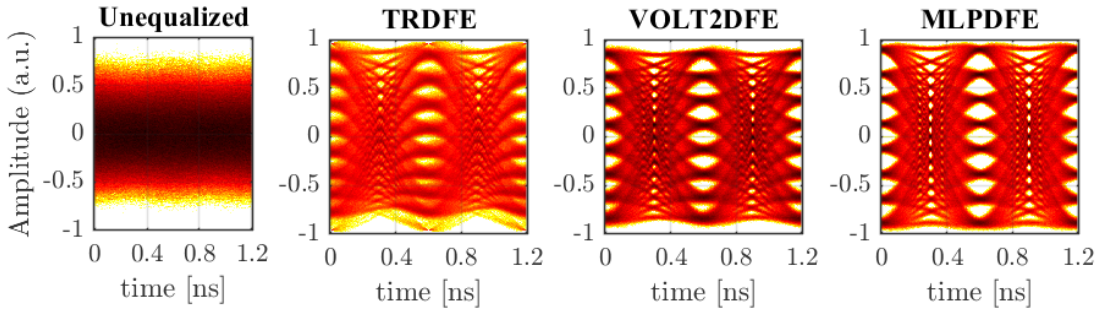


**Figure 4.7:** *Computed eye diagram for PAM-8 at 5 Gbps over 30 m SI-POF using the setup in Fig. 4.6*

highest bit rate achieved at a BER of $10^{-3}$ with the TRDFE is ∼2.3 Gbps for 60 m, ∼5.8 Gbps for 30 m, and ∼14.3 Gbps for 10 m POF with PAM-4 scheme used for all the POF lengths. For VOLT2DFE, the values are 2.5 Gbps for 60 m with PAM-4, 6.25 Gbps for 30 m with PAM-8, and ∼15.6 Gbps for 10 m with PAM-8. For MLPDFE, this is ∼2.8 Gbps for 60 m with PAM-4, ∼7.2 Gbps for 30 m with PAM-8, and ∼16.8 Gbps for 10 m with PAM-8. Furthermore, there is no reliable transmission when the TRDFE is used with $M \in \{16, 32\}$ as the BER is greater than 0.02. This is higher than the forward error correction (FEC) limit of $3.8 \times 10^{-3}$. Also, for VOLT2DFE, the BER is always higher than FEC limit with PAM-32. This is however not the case with MLPDFE for all bit rates considered with the exception of PAM-32 at 60 m POF length. Here, it can be inferred that in the presence of non-linear distortion, the MLPDFE is the most appropriate of the three equalisers. As an example, the eye diagrams for the output of each equaliser with PAM-8 scheme is shown in Fig. 4.7. The diagrams are computed for 30 m SI-POF at a bit rate of 5 Gbps. Without equalisation, the PAM-8 waveform is severely distorted due to ISI and the corresponding eye diagram is completely closed. With TRDFE, the eye diagram is opened but the levels are unequally spaced and this is because the equaliser does not mitigate the system non-linearity. More uniform spacing between levels is observed for the eye diagram with VOLT2DFE and MLPDFE as they compensate for the non-linearity inherent in the system. Moreover, the eye spacing with MLPDFE ($\gtrapprox 0.155$ a.u.) is greater than that of VOLT2DFE ($\gtrapprox 0.070$ a.u.) and this is evident in the BER plot in Fig. 4.6.

In Fig. 4.8, the BER result is used to compare the performance of the TRDFE that uses the inverse polynomial pre-distorter with that of the MLPDFE. $I_{bias}$ is setup as 26 mA as this is the point on the LD with high non-linearity. Due to the limited current range of the pre-distorter as previously discussed in Section 4.1.1, $I_{mod} = 5$ mA is used here. Similarly, 24 hidden layer neurons are used in the MLPDFE for it to achieve its best BER performance. Using the pre-distorter significantly improves the link performance especially at higher PAM levels. For $M \leq 8$, it is shown in Fig. 4.8 that when the TRDFE is used with the pre-distorter, it offers marginally better BER performance than the MLPDFE. For instance, the bit rate at a BER of $10^{-3}$ offered by the MLPDFE is 15.5 Gbps for 10 m POF using PAM-4 scheme, but this is ∼16.2 Gbps with TRDFE using the pre-distorter. For $M > 8$ however, the MLPDFE outperforms the TRDFE even with the non-linear pre-distortion. There is still some non-linearity in the system with the pre-distorter. This is because the polynomial equation, from which the pre-distorter is obtained, is an approximation of the LD transfer function but not an exact expression.

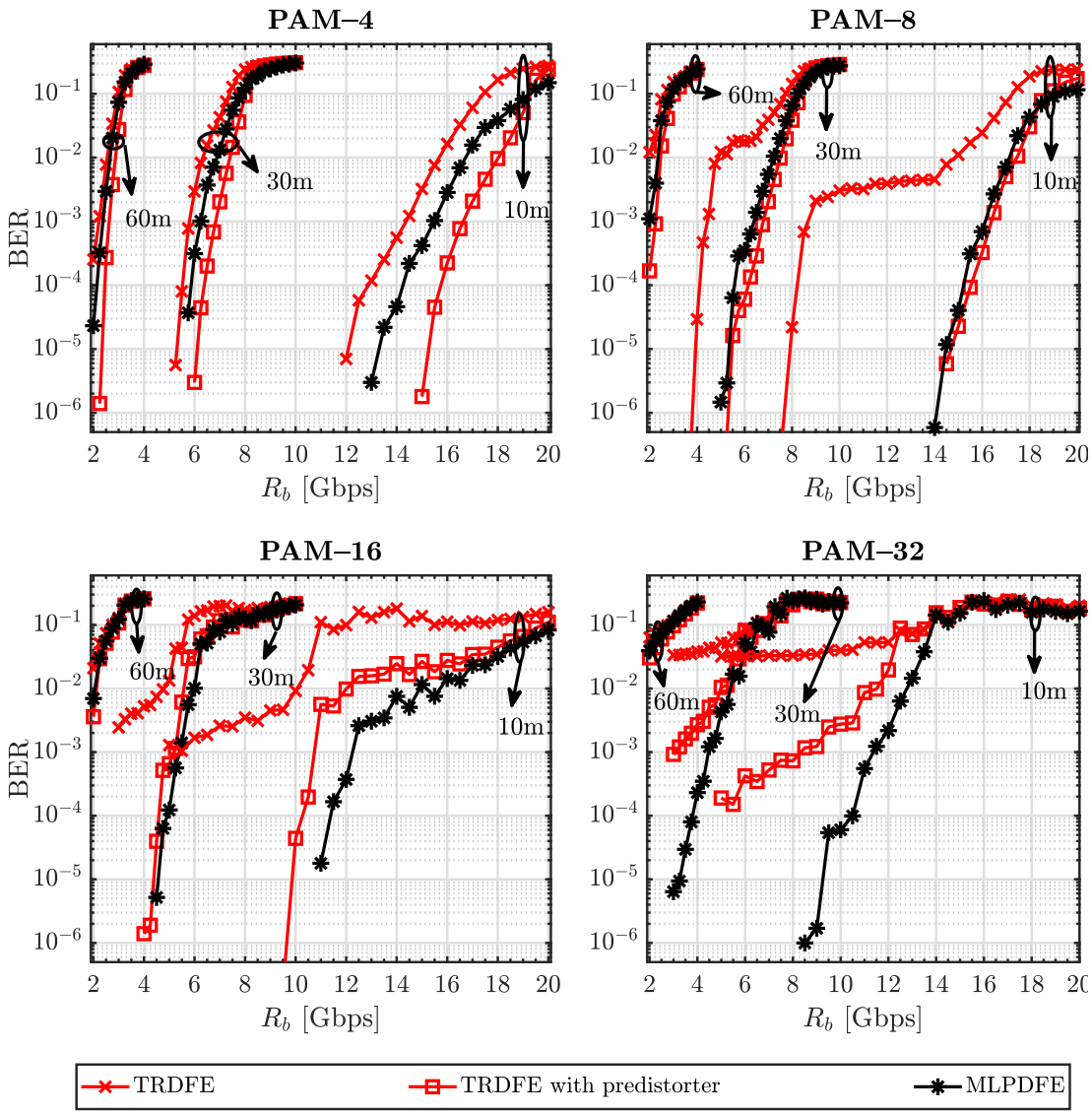


**Figure 4.8:** *BER result comparing the performance of MLPDFE with that of TRDFE with non-linear pre-distortion ($I_{bias}$ = 26 mA, $I_{mod}$ = 5 mA). $\gamma_{nm}$ is ∼34 dB, ∼44 dB and ∼49 dB for SI-POF lengths of 60 m, 30 m and 10 m respectively.*

From these results, it can be concluded that the MLP based equaliser offers the best mitigation against POF channel distortion and non-linearity. The Volterra equaliser only mitigates $2^{nd}$ order non-linearities so its BER performance is not as good as that of the MLP equaliser. The transversal equaliser on the other hand only mitigates the ISI and does not consider the non-linear distortion inherent in the system. Hence, it offers the least BER result. However, at lower PAM levels of $M = 4$ and 8, the non-linear pre-distortion techniques with TRDFE is the best approach. For this study, the maximum bit rates recorded are 18 Gbps for 10 m POF, 7.8 Gbps for 30 m POF and 3 Gbps for 60 m POF at a BER of $10^{-3}$.

## 4.3 Comparison of Complex-valued TD-NLE for CAP-$M^2$

The CAP modulation and de-modulation process for the QAM symbols are highlighted in Fig. 3.2. A constant upsampling factor of eight is used for the simulation model irrespective of the signal's bit rate. As the QAM symbols are complex-valued, The tap weights of the TD-NLEs for are complex-valued as the voltage levels that correspond to the .

To illustrate the effect of non-linear distortion, CAP-64 signal is transmitted through a 10 m SI-POF at a baud rate of 250 MHz (equal to a bit rate of 1.5 Gbps) for LDS1 and LDS2 setup. The resulting (unequalised) QAM constellation is shown in Fig. 4.9 and it shows more uniform symbol spacing with the LDS1 setup compared to the LDS2 setup.

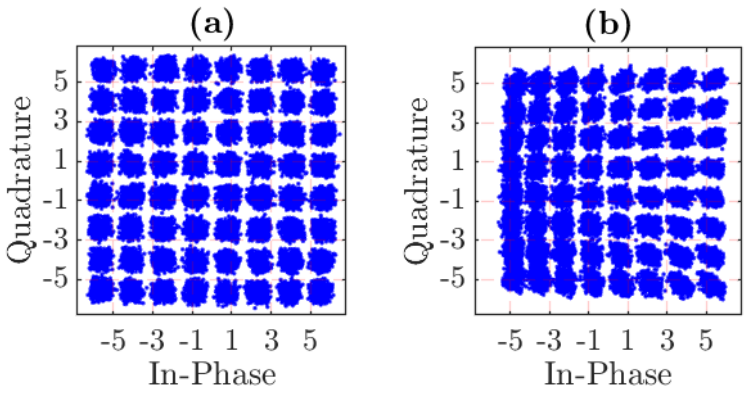


**Figure 4.9:** *CAP-64 constellation for 250 MHz baud rate via 10 m SI-POF with no equalisation using the: (a) LDS1 setup (b) LDS2 setup*

The same parameters for PAM in Section 4.2 are used to obtain subsequent results in this section, and they are shown in Table 4.1. Using these parameters and ignoring the ISI and non-

linearity penalty of the system, the average SNR per bit ($\gamma_b$) at a bit-rate of 4 Gbps is estimated as 20 dB for 60 m, 30 dB for 30 m and 37 dB for 10 m SI-POF.

Figure 4.10 shows the BER result for the equalisers with the LDS1 setup at POF lengths of 10 m, 30 m and 60 m. With the BER plot from Fig. 4.10, the maximum bit rate achieved at a BER $\approx 10^{-3}$ is presented in Table 4.2 for each POF lengths using the equalisers. Apparently, the optimum CAP modulation format with the LDS1 setup for SI-POF of lengths 60 m, 30 m and 10 m is CAP-4, CAP-16 and CAP-64 respectively. With the optimum CAP modulation format, the SC-MLPDFE offers marginally better BER performance compared to both the complex VOLT2DFE and the complex TRDFE for all POF lengths. This is as a result of the low non-linearity from the LDS1 setup.

| $l_{pof}$ [m] | TRDFE | | VOLT2DFE | | SC-MLPDFE | |
|---|---|---|---|---|---|---|
| | $R_b$ | $M^2$ | $R_b$ | $M^2$ | $R_b$ | $M^2$ |
| 10 | 16 | 64 | 17 | 64 | 17.5 | 64 |
| 30 | 7.5 | 16 | 8.5 | 16 | 8.7 | 16 |
| 60 | 3.5 | 4 | 3.5 | 4 | 4 | 4 |

$R_b$ = Bit rate in Gbps; $M^2$ = CAP/QAM constellation size

**Table 4.2:** *Maximum bit rate with the equalisers at a BER $\approx 10^{-3}$ for LDS1 setup*

The BER results for the equalisers with the LDS2 setup at POF lengths of 10 m, 30 m and 60 m are depicted in Fig. 4.11. The BER plots with CAP-4 scheme for the LDS1 setup and the LDS2 setup shows a bit rate difference of less than 250 Mbps indicating that there is the minimal effect of non-linearity for CAP-4 scheme. With higher modulation order however, non-linearity significantly diminishes the link performance. An instance of this is shown with CAP-16, where for 60 m SI-POF and the LDS2 setup, the bit rate at a BER of $10^{-3}$ is 2.7 Gbps with the complex TRDFE. But this is 3.2 Gbps for the LDS1 setup, which translates to a difference of 500 Mbps.

The highest bit rate achieved at BER $\approx 10^{-3}$ with the LDS2 setup is highlighted in Table 4.3 for different POF lengths. The optimum CAP modulation format for 10 m SI-POF with both TRDFE and VOLT2DFE is CAP-16 (but is CAP-64 with the LDS1 setup). This is due to the increasing non-linearity of the LDS2 setup. However, the optimum CAP modulation format with SC-MLPDFE is CAP-64 for a POF length of 10 m just like with the LDS1 setup. For CAP-256, the the BER is not below $3 \times 10^{-3}$ and $0.01$ with VOLT2DFE and TRDFE respectively. However with SC-MLPDFE, the bit rate achieved at a BER of $10^{-3}$ is 12 Gbps and

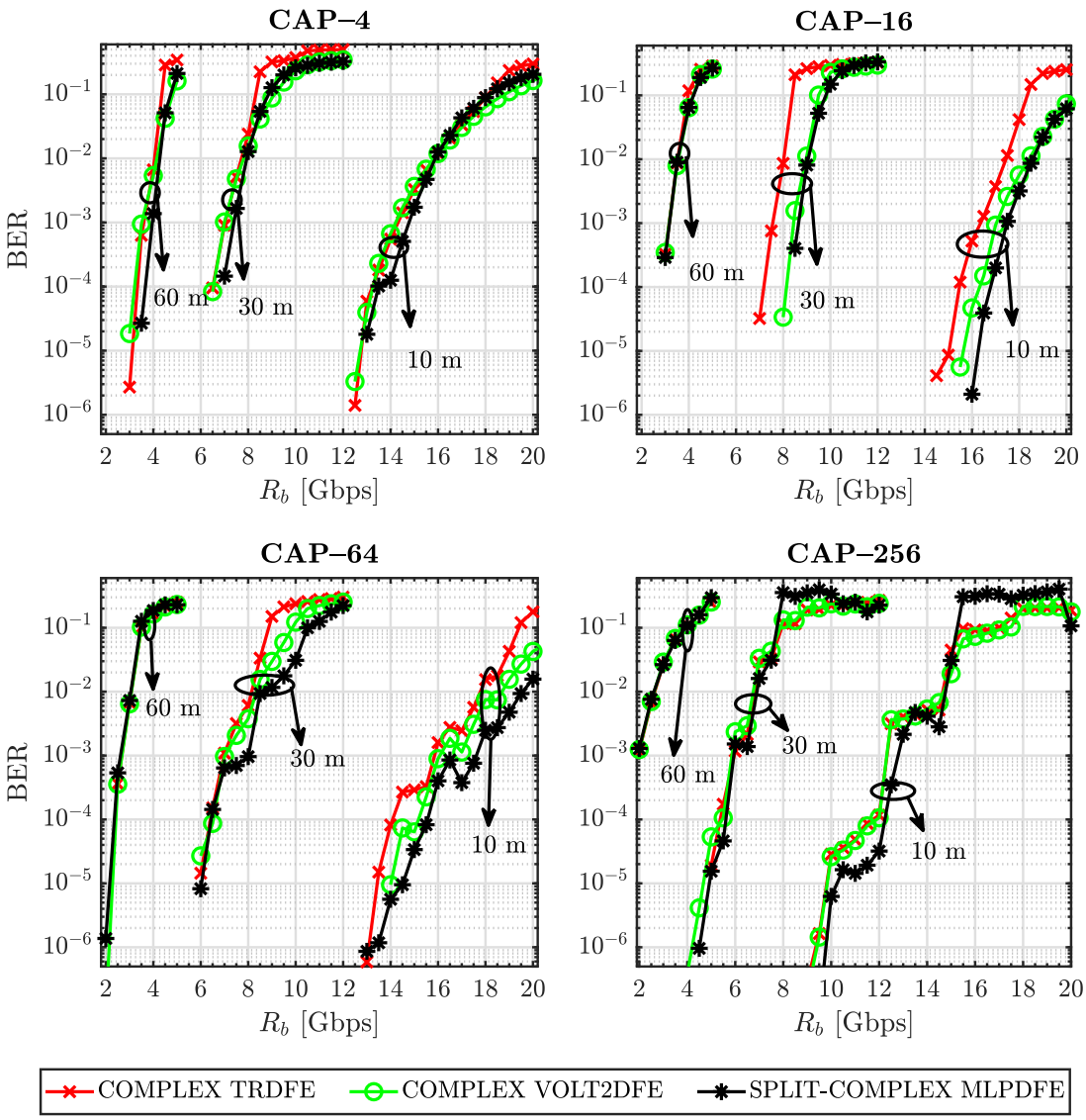


**Figure 4.10:** *BER plot comparing the equalisers performance over the SI-POF with the LDS1 setup ($I_{bias} = 30$ mA, $I_{mod} = 7$ mA).*

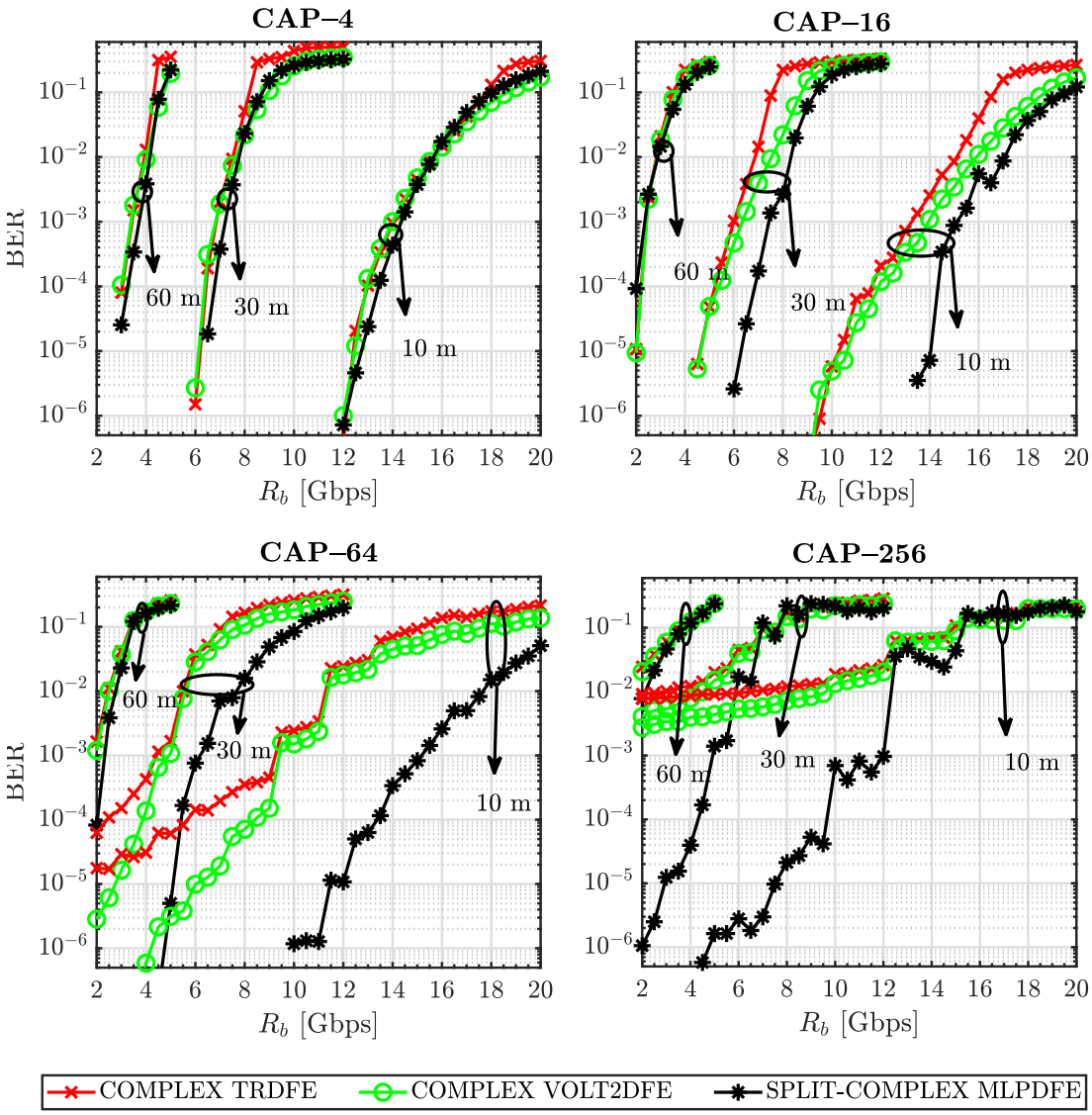


**Figure 4.11:** *BER plot comparing the equalisers performance over the SI-POF with the LDS2 setup ($I_{bias} = 26$ mA, $I_{mod} = 7$ mA).*

5.5 Gbps for POF lengths of 30 m and 10 m respectively. Consequently, the SC-MLPDFE outperforms both the complex VOLT2DFE and the complex TRDFE for higher CAP modulation formats if the LDS2 setup (with high non-linearity) is used.

| $l_{pof}$ [m] | TRDFE | | VOLT2DFE | | SC-MLPDFE | |
|---|---|---|---|---|---|---|
| | $R_b$ | $M^2$ | $R_b$ | $M^2$ | $R_b$ | $M^2$ |
| 10 | 13.5 | 16 | 14 | 16 | 15 | 64 |
| 30 | 6 | 16 | 6.5 | 16 | 7.5 | 16 |
| 60 | 3.5 | 4 | 3.5 | 4 | 3.75 | 4 |

$R_b$ = Bit rate in Gbps; $M^2$ = CAP/QAM constellation size

**Table 4.3:** *Maximum bit rate with the equalisers at a BER* $\approx 10^{-3}$ *for LDS2 setup*

From these results, it is confirmed that non-linearity can significantly deteriorate the overall performance of the POF system. With this deterioration however, significant bit rate is obtainable with the SC-MLP equaliser. The complex transversal equaliser only mitigates the ISI and hence offers the least BER performance. The complex Volterra equaliser only mitigates $2^{\text{nd}}$ order non-linearities so its BER performance is better than that of the transversal equaliser. However, the best performance is obtained using the SC-MLP equaliser. The non-linearity severely affects the performance at higher CAP modulation level and hence the ANN offers higher performance gain for higher CAP level.

## 4.4 Equaliser Computational Complexity Analysis

The computational complexity of the equalisers (with and without the algorithm) is compared and presented in Table 4.4. The average training time is computed for 4000 training symbols ($N_{tr} = 4000$) with MATLAB using a computer with Intel®Xeon®Processor E5-1660 v3 @ 3.00 GHz $\times 16$. The average training time represents the number of seconds required for the equaliser to reach convergence at $N_{tr} = 4000$. The values from Table 4.4 suggests that if the number of hidden-layer neurons is significantly less than the number of the equaliser's feed-forward taps (i.e if $N_{hn} \ll N_{ft}$), then VOLT2DFE has higher computational order than the MLPDFE. Also, the TRDFE is the least complex of the three equalisers considered.

The number of input taps and training examples are important parameters required for the NLEs. The optimum number of taps for an NLE depends on the channel delay spread, the bit rate $R_b$ and the size of the modulation format ($M$). But for fair comparison under similar

| Equaliser | Training algorithm | Number of input taps (or synaptic weights) | Complexity of Equaliser: | | Average training time (seconds) |
|---|---|---|---|---|---|
| | | | with training algorithm | without training algorithm | |
| TRDFE | RLS | $N_t = N_{ft} + N_{bt}$ | $O(N_t^2)$ | $O(N_t)$ | 0.111 |
| VOLT2DFE | RLS | $N_{2t} = \frac{N_{ft}^2+3N_{ft}}{2} + N_{bt}$ | $O(N_{2t}^2)$ | $O(N_{2t})$ | 1.259 |
| MLPDFE | LMBP | $W = N_{hn}(N_{ft} + N_{bt} + 2)$ | $O(W^2 + WN_{tr})$ | $O(W)$ | 0.615 |

– The computational complexity for TRDFE, VOLT2DFE and MLPDFE is derived from [43], [144] and [95] respectively.
– The number of hidden neurons for MLPDFE, denoted as $N_{hn}$, is six in order to compute the average training time.
– Unlike TRDFE and VOLT2DFE, MLPDFE has $N_{hn}$ non-linear functions.

**Table 4.4:** *Comparison of the Computational Complexities for each the TD-NLE*

conditions, all three NLEs have 22 forward taps and 18 feedback taps. At various number of training examples $N_{tr}$ for each NLE, the BER plots is presented for PAM and CAP schemes in Fig. 4.12a and Fig. 4.12b, respectively. For the first scheme, the plots are obtained at a bit-rate of 18 Gbps over a 10 m SI-POF. For the latter scheme, they are obtained at a bit-rate of 3 Gbps over a 60 m SI-POF.

It is observed from Fig. 4.12a that a similar BER performance is achieved when more than 2000 training examples are used for both TRDFE and VOLT2DFE. However, with MLPDFE the performance improves with increasing training examples. The plots in Fig. 4.12b shows that while 2000 symbols are enough for the transversal DFE, the MLPDFE requires at least 3000. Thus, 4000 training symbols are selected for all the NLEs in this study, as shown in Table 4.1. Both Fig. 4.12a and Fig. 4.12b suggest that the RLS algorithm used for TRDFE and VOLT2DFE requires less training symbols than the LMBP algorithm for the MLPDFE. Hence, both TRDFE and VOLT2DFE are more useful than the MLPDFE for mobile channels as the first two NLEs require less training overhead than the third NLE. Because most SI-POF channels are stationary, the effect of more training overhead becomes negligible so that the MLPDFE is more applicable to them.

The RLS algorithm (for both TRDFE and VOLT2DFE) adapts the equalisers' tap weights on a symbol-by-symbol basis. This process is called on-line or sequential training. Hence, the convergence for the RLS algorithm is measured with only the number of training symbols. On the other hand, most algorithms for the MLPDFE (and ANN systems) use the batch training method. In this training method, the equaliser's synaptic weights are adapted when all the training symbols are processed in the equaliser. Thus, the convergence of the MLPDFE is

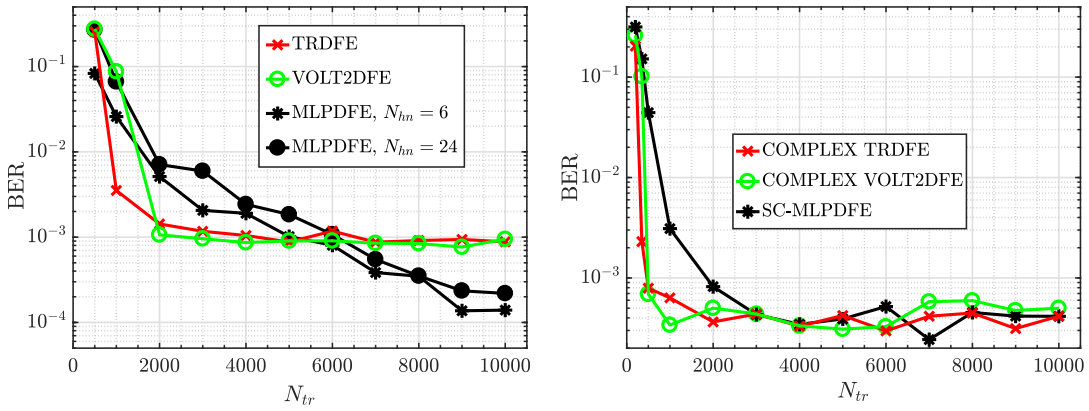


**(a)** **(b)**

**Figure 4.12:** *BER plots comparing the NLEs' performance for different number of training symbols ($N_{tr}$) at a bit-rate of: (a) 18 Gbps over a 10 m SI-POF with PAM-8 (b) 3 Gbps over a 60 m SI-POF with CAP-16*

defined not only with the number of training symbols but also with the number of epochs ($N_{ep}$).

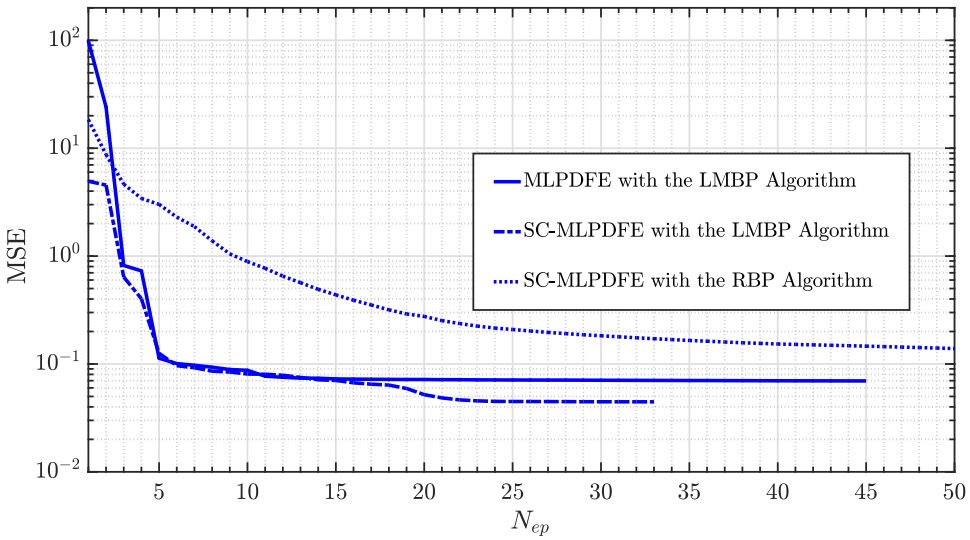


**Figure 4.13:** *Convergence of the LMBP algorithm and the RBP algorithm with the number of epochs ($N_{ep}$)*

Plots of the mean square error (MSE) against the number of epochs are presented in Fig. 4.13 to determine the convergence of both the LMBP algorithm and the RBP algorithm for the MLP equalisers. The number of training symbols per epoch is 4000. The LMBP algorithm converges after ∼10 epochs of training symbols while the RBP algorithm converges after ∼35 epochs. Increasing the epochs of training further does not have a significant impact on the

error minimisation of both algorithms for the MLP equalisers. For instance, the MSE remains constant at $\sim 0.080$ after ten epochs of training the LMBP algorithm.

## 4.5 Experiment Results

This section gives a survey of the performance of the receiver NLE with the SCM schemes in terms of results from the offline experiment setups discussed in Section 3.3. The LD setup is implemented at SI-POFs of lengths 10 m, 30 m and 60 m while the RC-LED configuration is applied only for a 60 m SI-POF. The LD is driven with a DC bias current of 28 mA combined with the signal at a modulation index of 0.85.

### 4.5.1 Laser diode

The LD experiment setup is described in Section 3.3, where it uses a 1 GHz photo-receiver. For both PAM-$M$ and CAP-$M^2$, the performance of the TD-NLEs will be compared with the experiment setup for SI-POFs of length 10 m with $M = 16$, 30 m with $M = 8$ and 60 m with $M = 4$. The sampling rate for this experiment is kept constant at 4 Gsa/s so that the oversampling factor reduces at higher bit rates.

It is necessary to determine the optimum number of taps for the equalisers to get the best error performance without compromising computational complexity. This number was done by varying $N_{ft}$ from 8 to 26 and $N_{bt}$ from 0 to 18. An example of this is illustrated in Fig. 4.14, which shows a BER contour plot for a 60 m SI-POF at a bit-rate of 3 Gbps (in Fig. 4.14a) and another contour plot for a 30 m SI-POF at a bit-rate of 7 Gbps (in Fig. 4.14b). To select the optimum $N_{ft}$ and $N_{bt}$, the bit rates used at each SI-POF length are those that offer a BER of $10^{-3}$, as this is closer to the forward error correction (FEC) limit. The results of this selection are highlighted in Table. 4.5, and they are used for the NLEs in the LD experiment setup. The number of training symbols for all the equalisers is 4000, and six hidden-layer neurons are used for the MLP equalisers.

At various bit-rates, the BER results with PAM transmission are presented for the NLEs in Fig. 4.15. In Fig. 4.15a, the BER plots are depicted for PAM-4 transmission over a 60 m SI-POF. The MLPDFE offers a superior BER result than that from both TRDFE and VOLT2DFE. The bit rate achieved at a BER of $10^{-3}$ is $\sim$2.8 Gbps with both TRDFE and the VOLT2DFE.

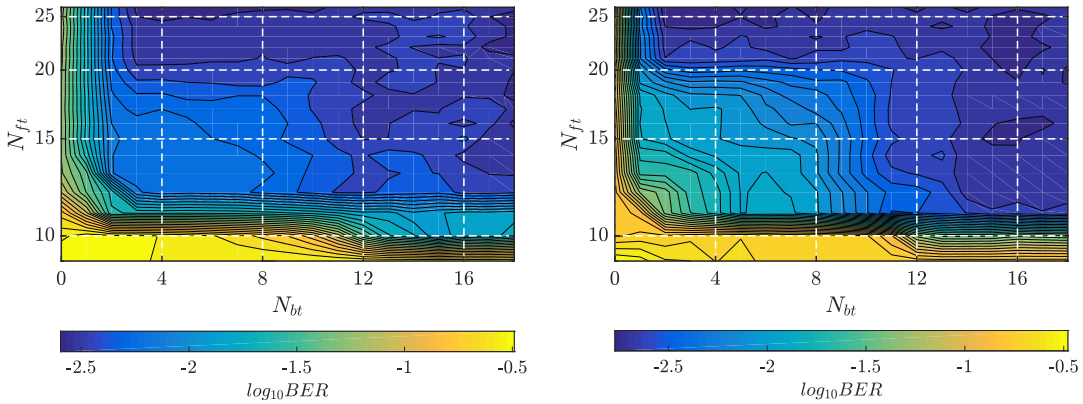


**Figure 4.14:** *BER contour plots used to derive the optimal $N_{ft}$ and $N_{bt}$ for: (a) 60 m SI-POF at 3 Gbps bit-rate (b) 30 m SI-POF at 7 Gbps bit-rate*

| **Parameters** | **Values at SI-POF length of:** | | |
|---|---|---|---|
| | **60 m** | **30 m** | **10 m** |
| $M$ | 4 | 8 | 16 |
| $N_{ft}$ | 22 | 24 | 22 |
| $N_{bt}$ | 18 | 3 | 8 |

**Table 4.5:** *Optimal number of taps for different SI-POF lengths with the LD setup*

But this is ∼2.92 Gbps with the MLPDFE. In Fig. 4.15b, the BER plots are depicted for PAM-8 transmission over a 30 m SI-POF. If the TRDFE is applied to the POF link, the bit rate at a BER of $10^{-3}$ is ∼4.8 Gbps. The VOLT2DFE further increases this bit rate to ∼5.9 Gbps. With the MLPDFE, the bit rate goes up to ∼6.8 Gbps. The BER plots are presented in Fig. 4.15c for PAM-16 transmission over a 10 m SI-POF. The bit rate achieved at a BER of $10^{-3}$ is ∼8 Gbps, ∼9.3 Gbps and ∼10 Gbps with the TRDFE, VOLT2DFE and the MLPDFE, respectively. Furthermore, the BER does not go below an error floor of $6 \times 10^{-5}$ with the TRDFE at bit rates above 1 Gbps.

A drawback of the DFE configuration is their susceptibility to error-propagation due to occasional decision error of their input feedback symbols. The BER result is computed for the three NLEs using the transmitted symbols as feedback data to assess this error-propagation effect. This way, the feedback signal is always error-free, and therefore no error propagation occurs; the BER results are shown in dashed lines in Fig. 4.15. As expected, the effect of decision error on both DFEs becomes more significant with increasing bit rate due to increasing ISI. The emphasis is, therefore, on the highest bit rate to explore the effect of decision error on the

DFEs. For 10 Gbps with PAM-16 (over a 10 m SI-POF), the BER achieved if the transmitted symbols (i.e. no error propagation) are fed back to the TRDFE is 0.03. But this is $\sim 3.5 \times 10^{-3}$ when the detected symbols are fed back to the DFE. If the transmitted symbols are fed back to the VOLT2DFE, the BER is $\sim 7 \times 10^{-3}$, while the BER is $\sim 4.5 \times 10^{-4}$ with the detected symbols. For MLPDFE, the BER is $\sim 10^{-3}$ with the transmitted symbols, but it is $\sim 5 \times 10^{-5}$ when the correct symbols are fed back.

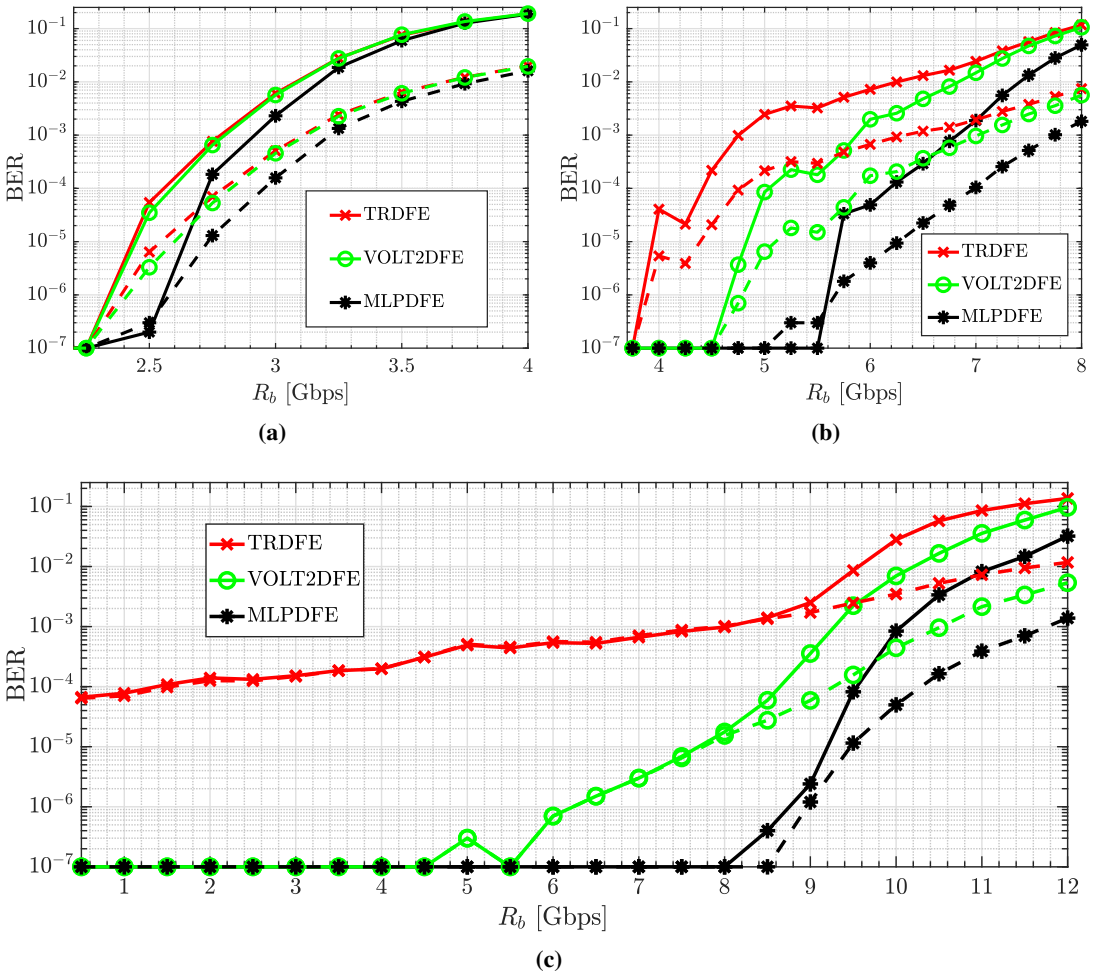


**Figure 4.15:** *The measured BER versus bit rate with $\eta_{mod} = 0.85$ for comparing the performance of the NLEs for: (a) PAM-4 via a 60 m SI-POF (b) PAM-8 via a 30 m SI-POF (c) PAM-16 via a 10 m SI-POF. The solid and dashed lines represents the BER if the feedback inputs for the DFEs are the detected and transmitted symbols, respectively*

Another method used to gauge and compare the effect of error-propagation for each DFE is by getting the bit rates achieved at a BER of $10^{-3}$ when the transmitted symbols are used as feedback (i.e. no error-propagation). The bit rates with error-propagation are less than those

without error-propagation as expected. So the bit-rate reduction due to error-propagation from the DFEs is used to assess the performance of the NLEs. For PAM-4 transmission over a 60 m SI-POF, the bit rate without error-propagation is ∼3.1 Gbps with both the TRDFE and the VOLT2DFE. Hence, the bit-rate reduction from error-propagation is 0.3 Gbps for the two NLEs. With the MLPDFE, the bit rate without error-propagation is ∼3.22 Gbps, so that the bit-rate reduction is also 0.3 Gbps. The DFE's error-propagation similarly affects the three NLEs for PAM-4 transmission over a 60 m SI-POF.

For PAM-8 transmission over a 30 m SI-POF, the bit rate without the error-propagation is ∼6.4 Gbps with the TRDFE, and the corresponding bit-rate reduction is 1.6 Gbps. With the VOLT2DFE, it is ∼7 Gbps so that the bit-rate reduction becomes 1.1 Gbps. With the MLPDFE, the bit rate without error-propagation is ∼7.8 Gbps, so that the bit-rate reduction is 1 Gbps. For PAM-8 transmission over a 30 m SI-POF, the DFE's error-propagation affects the TRDFE more than the VOLT2DFE and the MLPDFE. For PAM-16 transmission over a 10 m SI-POF, the bit rate without the error-propagation is ∼8 Gbps with the TRDFE, which implies there is no bit-rate reduction. With the VOLT2DFE, it is ∼10.5 Gbps so that the bit-rate reduction becomes 1.2 Gbps. With the MLPDFE, the bit rate without error-propagation is ∼11.8 Gbps, so that the bit-rate reduction is 1.8 Gbps. For PAM-16 transmission over a 10 m SI-POF, the MLPDFE is mostly affected by the DFE's error-propagation. The VOLT2DFE and the TRDFE follow this, consecutively. Consequently, the MLPDFE is more prone to error-propagation than the other NLEs for high-level PAM format ($M > 16$). This result further confirms the findings from [48], where the PAM-32 modulation scheme is used for transmission over a 10 m SI-POF.

The three NLEs are prone to error propagation from the wrong detected symbols that are fed back. With the error propagation effect, however, FEC codes can still be used to improve the BER performance for both DFEs as Table 4.6 and Table 4.7 shows with the Reed-Solomon FEC (RS-FEC) code for the 10 m and 30 m SI-POF, respectively. The RS-FEC code is chosen because it is the most efficient in terms of the ratio of the number of errors corrected to the code algorithm complexity [43, 145]. It is also commonly used in optical fibre standards like the synchronous optical networking (SONET) [68, 79]. Furthermore, it is readily available and accessible in hardware like the field-programmable gate array (FPGA) and the application-specific integrated circuit (ASIC).

From the 10 m SI-POF, the RS-FEC code achieves an error-free bit rate of 8.31 Gbps, 8.66 Gbps and 9.38 Gbps with TRDFE, VOLT2DFE and MLPDFE, respectively. From the 30 m SI-POF,

it is 5.01 Gbps, 5.89 Gbps and 6.21 Gbps, respectively. With interleaving and more robust FEC schemes (e.g. turbo code and low-density parity-check code), the BER performance can be further improved with less overhead.

| **Parameters** | **TRDFE** | **VOLT2DFE** | **MLPDFE** | |
|---|---|---|---|---|
| Input BER | $2.5 \times 10^{-3}$ | $2.2 \times 10^{-3}$ | $3.4 \times 10^{-3}$ | $8 \times 10^{-4}$ |
| Gross bit rate [Gbps] | 9.0 | 9.5 | 10.5 | 10.0 |
| RS-FEC {n,k} | {2047, 1889} | {2047, 1865} | {2047, 1683} | {2047, 1921} |
| Overhead [%] | 7.72 | 8.89 | 17.78 | 6.16 |
| Net bit rate [Gbps] | 8.31 | 8.66 | 8.63 | 9.38 |
| Output BER | $\approxeq 7.25 \times 10^{-8}$ | $\approxeq 7.31 \times 10^{-8}$ | $\approxeq 8.13 \times 10^{-8}$ | $\approxeq 7.11 \times 10^{-8}$ |

**Table 4.6:** *Performance of Reed-Solomon FEC code (RS-FEC) for PAM-16 transmission over 10 m SI-POF*

| **Parameters** | **TRDFE** | **VOLT2DFE** | **MLPDFE** | |
|---|---|---|---|---|
| Input BER | $3.2 \times 10^{-3}$ | $2.6 \times 10^{-3}$ | $5.6 \times 10^{-3}$ | $2.0 \times 10^{-3}$ |
| Gross bit rate [Gbps] | 5.50 | 6.25 | 7.25 | 7.00 |
| RS-FEC {n,k} | {2047, 1863} | {2047, 1929} | {2047, 1709} | {2047, 1817} |
| Overhead [%] | 8.99 | 5.76 | 16.51 | 11.24 |
| Net bit rate [Gbps] | 5.01 | 5.89 | 6.05 | 6.21 |
| Output BER | $\approxeq 7.39 \times 10^{-8}$ | $\approxeq 7.00 \times 10^{-8}$ | $\approxeq 8.11 \times 10^{-8}$ | $\approxeq 7.56 \times 10^{-8}$ |

**Table 4.7:** *Performance of RS-FEC code for PAM-8 transmission over 30 m SI-POF*

With the NLEs, the BER results are also presented for CAP transmission in Fig. 4.16. For CAP-16 transmission over a 60 m SI-POF, the three NLEs offer a marginal BER performance and shows a bit rate of ∼1.9 Gbps at a BER of $10^{-3}$. For CAP-64 transmission over a 30 m SI-POF, the MLPDFE slightly outperforms the other two NLEs. Both TRDFE and VOLT2DFE offer a bit-rate of ∼5.2 Gbps at a BER of $10^{-3}$, and this is slightly increased to ∼5.3 Gbps with the SC-MLPDFE. For CAP-256 transmission over a 10 m SI-POF, the MLPDFE significantly outperforms the other two NLEs. Both TRDFE and VOLT2DFE offer a bit-rate of ∼9 Gbps at a BER of $10^{-3}$, and this is increased to ∼9.8 Gbps with the SC-MLPDFE. Furthermore, the BER does not go below an error floor of $10^{-4}$ and $3 \times 10^{-4}$ for the TRDFE and the VOLT2DFE.

The results from the LD validate those from the simulation model in the sense that at high-level modulation formats, the non-linearities can significantly worsen the overall performance of the POF system. With this deterioration, however, significant bit rates are obtainable with the MLP equalisers, when compared to the other two NLEs. Using the LD experiment setup,

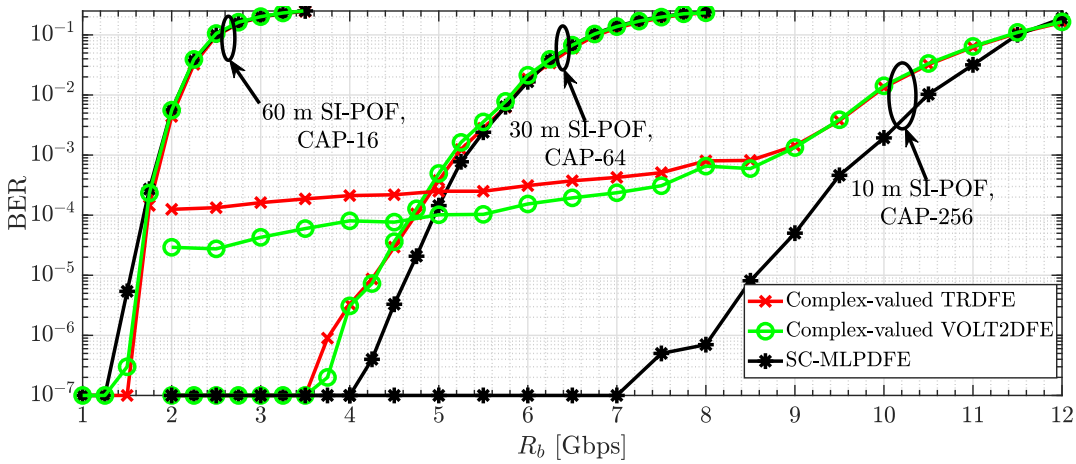


**Figure 4.16:** *The measured BER versus bit rate with $\eta_{mod} = 0.85$ for comparing the performance of the NLEs for CAP transmission over the SI-POF system of 10 m, 30 m and 60 m lengths*

the highest bit-rate achieved at a BER of $10^{-3}$ with the MLPDFE is about 2.92 Gbps, 6.8 Gbps and 10 Gbps for SI-POF at lengths of 60 m, 30 m and 10 m, respectively.

### 4.5.2 RC-LED

Like the LD experiment, the setup with the RC-LED is also described in Section 3.3, where it uses a 150 MHz photo-receiver. In this section, the performance of the TD-NLEs will be compared with the RC-LED experiment setup for a 60 m SI-POF. This fibre length is selected as it offers the highest bit-rate length product with the RC-LED setup as Fig. 3.13 shows. The measured frequency response of the 60 m SI-POF link is depicted in Fig. 4.17, indicating a 3-dB bandwidth of ∼40 MHz. The difference between the theoretical Gaussian approximation and the measured response can be attributed to the background system (AWG, RC-LED, and photo-receiver). The sampling rate for this experiment is kept constant at 1 Gsa/s for this experiment.

The performance of the TD-NLEs is assessed based on the bit-rates that are obtained at a BER of $\sim 10^{-3}$. The bit-rates are for values of the modulation index $\eta_{mod}$ with a bias-current of 30 mA. This measure is used to evaluate the impact of the system non-linearities on the bit-rate performance of the SI-POF link. Because the non-linearities increase for higher values of $\eta_{mod}$ as depicted in Fig. 3.15a. The non-linearity analysis in Section 3.4 also suggests that the second-order harmonic distortion fully dominates the system non-linearities in the SI-POF system. Therefore, it would be interesting to observe and compare the bit-rate performance of

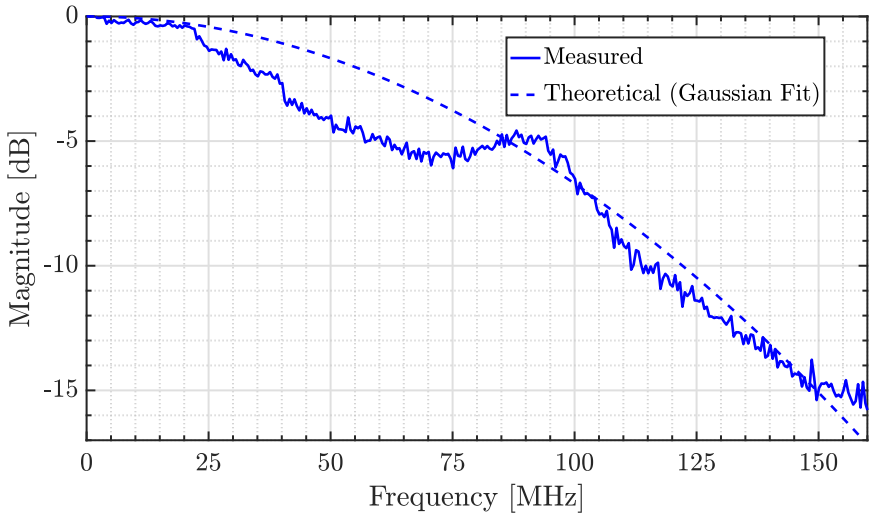


**Figure 4.17:** *Measured frequency response of a 60 m SI-POF link with the RC-LED setup at* $\eta_{mod} = 0.5$ *and* $I_{bias} = 30$ *mA*

the VOLT2DFE with that of the MLPDFE. With the same method illustrated in Fig 4.14, the number of feedforward and feedback taps selected for this comparison is 16 and 8, respectively through this section. And six hidden-layer neurons are used for the MLP equalisers. The number of training symbols for all the equalisers is 4000. The comparisons for this section are implemented for the SCM schemes (PAM and CAP) as well.

Using the RC-LED setup, the bit-rate plots from each NLE are depicted in Fig. 4.18a for different values of $\eta_{mod}$ with PAM-2 or on-off keying (OOK) scheme. Without any equalisation, the bit-rate remains slightly constant at ∼230 Mbps for values of $\eta_{mod}$ ranging from 0.35 to 1. This bit-rate significantly increases to ∼530 Mbps at $\eta_{mod} = 0.35$ when the TRDFE is applied to the SI-POF system. With the same NLE, the bit-rate rises to ∼610 Mbps as $\eta_{mod}$ increases from 0.35 to 0.85, then it remains constant at this bit-rate as $\eta_{mod}$ further rises to 1. With the VOLT2DFE, the bit-rate gently increases from ∼540 Mbps to ∼720 Mbps at values of $\eta_{mod}$ from 0.35 to 1. With the MLPDFE, the bit-rate rises from ∼560 Mbps to ∼780 Mbps at values of $\eta_{mod}$ from 0.35 to 0.95, and it remains constant at ∼780 Mbps for $\eta_{mod} = 1$. For PAM-2 transmission via the RC-LED setup, the MLPDFE offers the best bit-rate performance of the NLEs. The VOLT2DFE and the TRDFE follows this.

The eye diagrams for the output of each NLE with PAM-2 scheme is shown in Fig. 4.18b. The diagrams are computed for the SI-POF system at a bit rate of 700 Mbps at $\eta_{mod}$ values of 0.45 and 0.9. The eye diagram is slightly opened at these values of $\eta_{mod}$ with the TRDFE and

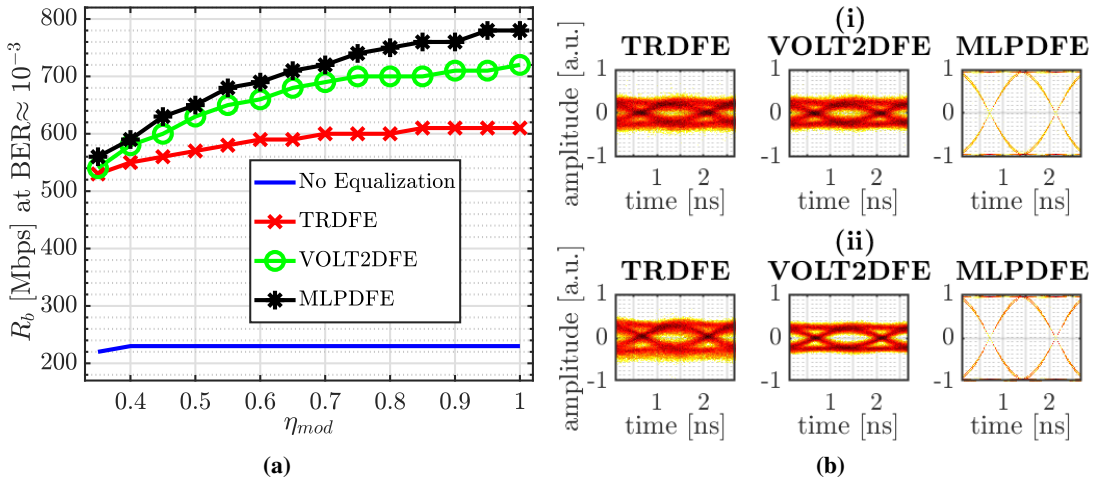


**Figure 4.18:** *(a) Performance comparison of the NLEs using the achievable bit-rate (at a BER≈ $10^{-3}$) versus the modulation index $\eta_{mod}$ with PAM-2 modulation scheme. (b) Computed PAM-2 eye diagram for 700 Mbps bit-rate with: (i) $\eta_{mod} = 0.45$ and (ii) $\eta_{mod} = 0.9$. Transmission is with the RC-LED over a 60 m SI-POF.*

more so with the VOLT2DFE. But for the MLPDFE, the diagram is fully opened and typically, this should translate to an error-free BER. But the BER is above $10^{-3}$ for $\eta_{mod} = 0.45$ and above $10^{-4}$ at $\eta_{mod} = 0.9$. The inconsistency from the eye-diagrams and the BER results from the MLPDFE is because the equaliser acts as a classifier for PAM transmission of two levels [92]. This conflict is also due to the nature of the sigmoid activation function used for the MLPDFE. In other words, the outputs of this equaliser are values either close to the symbol "1" or "-1". Hence, the errors from the MLPDFE come from a false classification, which is not so uncommon in ANN classifiers. The eye-diagram is thus not to a viable tool used to assess the performance of the MLP equaliser when it processes PAM-2 signals.

The bit-rate plots from each NLE are depicted in Fig. 4.19a for different values of $\eta_{mod}$ with PAM-4 scheme. Without any equalisation, the bit-rate is constant at ∼200 Mbps for values of $\eta_{mod}$ ranging from 0.35 to 0.8. The bit-rate drops slightly to ∼190 Mbps for $\eta_{mod}$ more than or equal to 0.85. With the TRDFE, the bit-rate rises from ∼460 Mbps to ∼510 Mbps at values of $\eta_{mod}$ from 0.35 to 0.7. The bit-rate then decreases when $\eta_{mod}$ increases further until it reaches ∼460 Mbps at $\eta_{mod} = 1$. Both VOLT2DFE and MLPDFE offer about the same bit-rates that increase from ∼480 Mbps to ∼640 Mbps at values of $\eta_{mod}$ from 0.35 to 0.65. With the VOLT2DFE, the bit-rate rises further until it becomes ∼660 Mbps at $\eta_{mod} = 0.8$. Then it drops down slightly to ∼640 Mbps at $\eta_{mod} = 1$. With the MLPDFE, the bit-rate rises further until it becomes ∼710 Mbps at $\eta_{mod} = 0.95$, and it remains constant at this value for

$\eta_{mod} = 1$. For PAM-4 transmission via the RC-LED setup, the MLPDFE also offers the best bit-rate performance of the NLEs.

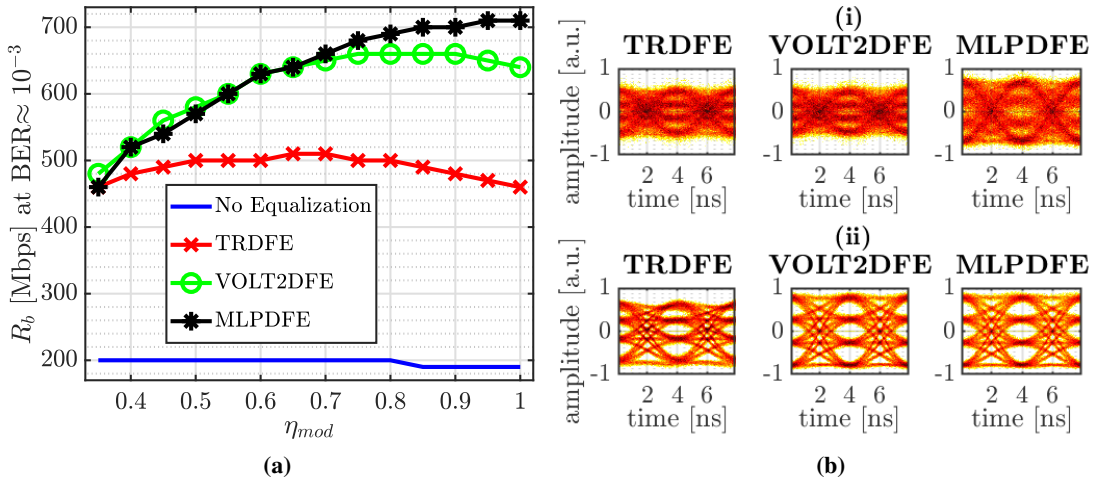


**Figure 4.19:** *(a) Performance comparison of the NLEs using the achievable bit-rate (at a BER$\approx 10^{-3}$) versus the modulation index $\eta_{mod}$ with PAM-4 modulation scheme. (b) Computed PAM-4 eye diagram for 500 Mbps bit-rate with: (i) $\eta_{mod} = 0.45$ and (ii) $\eta_{mod} = 0.9$. Transmission is with the RC-LED over a 60 m SI-POF.*

The eye diagrams for the output of each NLE with PAM-4 scheme is shown in Fig. 4.19b. The diagrams are computed for the SI-POF system at a bit rate of 500 Mbps at $\eta_{mod}$ values of 0.45 and 0.9. The eye diagram is slightly opened for the three NLEs at $\eta_{mod} = 0.45$, though the MLPDFE shows a wider opening than the other NLEs for the same value of $\eta_{mod}$. In contrast, the eye diagram is fully opened for the three NLEs at $\eta_{mod} = 0.9$. But the levels are unequally spaced with the TRDFE while they are uniformly spaced with both VOLT2DFE and MLPDFE. For PAM transmission more than two levels, the MLPDFE acts as an estimator rather than a classifier. Thus, the outputs of the equaliser can be distant from the values of the symbols from the PAM constellation. Furthermore, the eye diagram agrees with the BER result for the MLPDFE.

Figure 4.20a presents the bit-rate plots from each NLE for different values of $\eta_{mod}$ with PAM-8 scheme. For values of $\eta_{mod}$ ranging from 0.35 to 1, bit-rates below 20 Mbps are transmitted with PAM-8 scheme if no equaliser is used with the receiver. With the TRDFE, the bit-rate rises from $\sim$ 80 Mbps to $\sim$120 Mbps at values of $\eta_{mod}$ from 0.35 to 0.4. The bit-rate then decreases when $\eta_{mod}$ increases further until it reaches $\eta_{mod} = 0.5$, where the bit rates are below $\sim$20 Mbps for $\eta_{mod}$ above this value. The TRDFE is, therefore, not a viable option for PAM-8 transmission over the SI-POF with the RC-LED setup. With the VOLT2DFE, the

bit-rate increases from ∼310 Mbps to ∼580 Mbps at values of $\eta_{mod}$ from 0.35 to 0.8. Then it reduces from ∼580 Mbps to ∼530 Mbps when $\eta_{mod}$ is further increased to 1. With the MLPDFE, the bit-rate rises continuously from ∼290 Mbps to ∼650 Mbps as $\eta_{mod}$ increases from 0.35 to 1. The MLPDFE outperforms the VOLT2DFE for values of $\eta_{mod}$ above 0.7, where the system non-linearities is much higher.

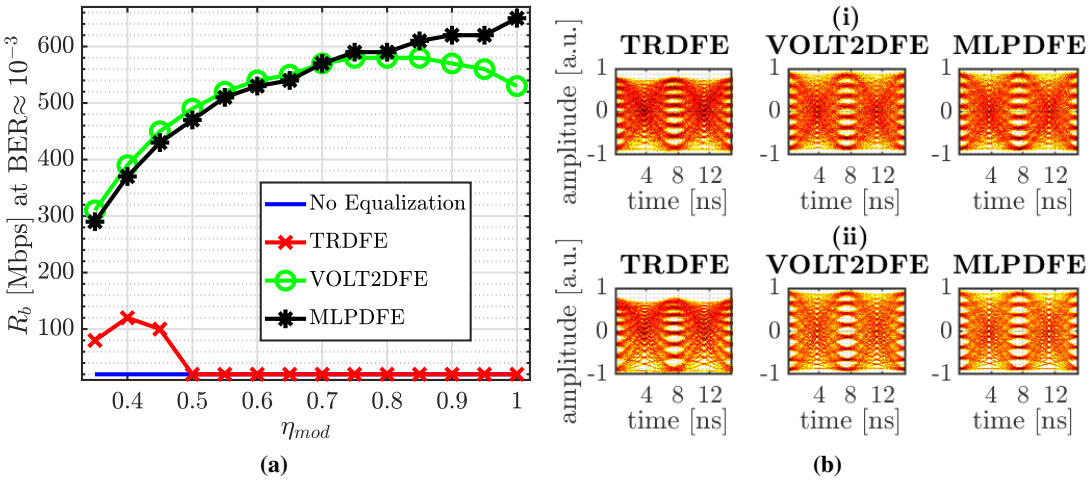


**Figure 4.20:** *(a) Performance comparison of the NLEs using the achievable bit-rate (at a BER≈ $10^{-3}$) versus the modulation index $\eta_{mod}$ with PAM-8 modulation scheme. (b) Computed PAM-8 eye diagram for 400 Mbps bit-rate with: (i) $\eta_{mod} = 0.45$ and (ii) $\eta_{mod} = 0.9$. Transmission is with the RC-LED over a 60 m SI-POF.*

The eye diagrams for the output of each NLE with PAM-8 scheme is shown in Fig. 4.20b. The diagrams are computed for the SI-POF system at a bit rate of 400 Mbps at $\eta_{mod}$ values of 0.45 and 0.9. The eye-diagram is opened for the three NLEs at both values of $\eta_{mod}$, and the opening is slightly wider with $\eta_{mod} = 0.9$ than that with $\eta_{mod} = 0.45$. The levels are unequally spaced with the TRDFE while they are uniformly spaced with both VOLT2DFE and MLPDFE.

Figure 4.21 presents the bit-rate plots for the RC-LED setup with CAP at modulation sizes of 4, 8, 16 and 32. In Fig. 4.21a, the bit-rate plots from each NLE are depicted for different values of $\eta_{mod}$ with CAP-4 scheme. Without any equalisation, the bit-rate is constant at ∼190 Mbps for values of $\eta_{mod}$ ranging from 0.4 to 1. Both VOLT2DFE and TRDFE offer about the same bit-rates that increase from ∼300 Mbps to ∼480 Mbps at values of $\eta_{mod}$ from 0.35 to 1. The MLPDFE in comparison offers a slightly worse performance than the two NLEs, since it presents a bit-rate of ∼280 Mbps and ∼450 Mbps for values of $\eta_{mod}$ at 0.35 to 1. The effect of non-linearities is minimal for the RC-LED with CAP-4 scheme, so that the TRDFE is the most viable NLE.

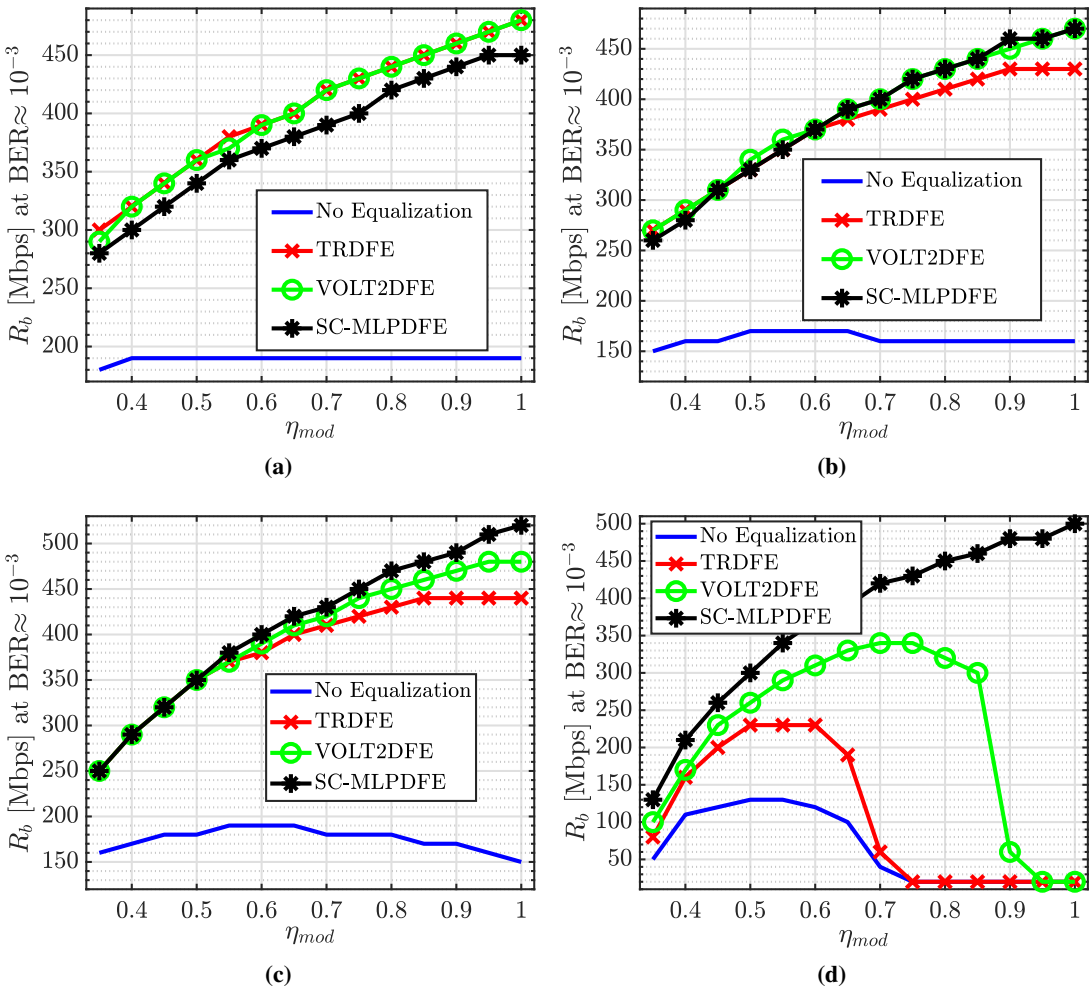


**Figure 4.21:** *Performance comparison of the NLEs using achievable bit-rate (at a BER≈ $10^{-3}$) versus the modulation index $\eta_{mod}$ with: (a) CAP-4 (b) CAP-8 (c) CAP-16 and (d) CAP-32 modulation schemes. Transmission is with the RC-LED over a 60 m SI-POF.*

The bit-rates obtained with CAP-8 scheme are depicted in Fig. 4.21b for different values of $\eta_{mod}$. Without any equalisation, the bit-rate rises slightly from ∼150 Mbps to ∼170 Mbps for values of $\eta_{mod}$ ranging from 0.35 to 0.65. It then drops to ∼160 Mbps at $\eta_{mod} = 0.7$ and remains constant at this bit-rate as $\eta_{mod}$ rises to 1. The three NLEs offer a marginal bit-rate performance that rises from ∼270 Mbps to ∼370 Mbps as $\eta_{mod}$ increases from 0.35 to 0.6. However, both VOLT2DFE and MLPDFE offer a superior bit-rate performance than that from the TRDFE for $\eta_{mod} \geq 0.65$. The first two NLEs present the same bit-rates that rise from ∼390 Mbps to ∼480 Mbps as $\eta_{mod}$ increases from 0.65 to 1. The TRDFE however, offers lower bit-rates of ∼390 Mbps to ∼430 Mbps at the same range of values for $\eta_{mod}$.

Figure 4.21c shows the achievable bit-rates with CAP-16 for different values of $\eta_{mod}$. Without any equalisation, the bit-rate rises slightly from ∼160 Mbps to ∼190 Mbps for values of $\eta_{mod}$ ranging from 0.35 to 0.65. It then drops from ∼190 Mbps to ∼150 Mbps as $\eta_{mod}$ rises from 0.65 to 1. The three NLEs offer a marginal bit-rate performance that rises from ∼250 Mbps to ∼350 Mbps as $\eta_{mod}$ increases from 0.35 to 0.55. For $\eta_{mod} \geq 0.6$, the MLPDFE offer a superior bit-rate performance than that from the VOLT2DFE followed by the TRDFE. For instance, with the TRDFE, the bit-rate rises from ∼350 Mbps to ∼440 Mbps as $\eta_{mod}$ increases from 0.6 to 1. With the same range of values for $\eta_{mod}$, the bit-rate increases from ∼370 Mbps to ∼480 Mbps with the VOLT2DFE. It also increases from ∼380 Mbps to ∼520 Mbps with the MLPDFE with the same range of values for $\eta_{mod}$.

Figure 4.21d presents the bit-rate plots from each NLE for different values of $\eta_{mod}$ with CAP-32 scheme. Without equalisation, the bit-rate rises from ∼ 50 Mbps to ∼130 Mbps at values of $\eta_{mod}$ from 0.35 to 0.55. The bit-rate then decreases when $\eta_{mod}$ increases further until it reaches $\eta_{mod} = 0.75$, where the bit rates are below ∼20 Mbps for $\eta_{mod}$ above this value. Using no equaliser causes transmission over the SI-POF system with CAP-32 scheme to be possible at $\eta_{mod}$ from 0.35 to 0.7. With the TRDFE, the bit-rate rises from ∼ 80 Mbps to ∼230 Mbps at values of $\eta_{mod}$ from 0.35 to 0.6. The bit-rate then decreases when $\eta_{mod}$ increases further until it reaches $\eta_{mod} = 0.75$, where the bit rates are below ∼20 Mbps for $\eta_{mod}$ above this value. Thus, the TRDFE supports transmission over the SI-POF system with CAP-32 scheme also for values of $\eta_{mod}$ from 0.35 to 0.7. With the VOLT2DFE, the bit-rate increases from ∼ 100 Mbps to ∼340 Mbps at values of $\eta_{mod}$ from 0.35 to 0.75. The bit-rate then reduces as $\eta_{mod}$ increases further until it reaches $\eta_{mod} = 0.95$, where the bit rates are below ∼20 Mbps for $\eta_{mod}$ above this value. Hence, the VOLT2DFE supports transmission over the SI-POF system with CAP-32

scheme for values of $\eta_{mod}$ from 0.35 to 0.9. This range of $\eta_{mod}$ from the VOLT2DFE is an improvement from the TRDFE. Unlike the other NLEs, the MLPDFE supports transmission over the SI-POF system with CAP-32 scheme for $\eta_{mod}$ up to 1. With the MLPDFE, the bit-rate rises from $\sim$ 130 Mbps to $\sim$500 Mbps at values of $\eta_{mod}$ from 0.35 to 1. The MLPDFE outperforms the VOLT2DFE, which in turn offers better bit-rate performance than the TRDFE.

The received signal constellations from the RC-LED experiment are rescaled and plotted in Fig. 4.22a and Fig. 4.22b for CAP-16 and CAP-32 schemes, respectively. The constellations are taken from both schemes for the three NLEs, with each at modulation index of 0.45 and 0.9. The bit-rate selected to compute the constellation for both schemes is 300 Mbps. There is uniform symbol spacing with the three NLEs for the constellation at $\eta_{mod} = 0.45$ than that at $\eta_{mod} = 0.9$. The uniformity illustrates that the non-linearity is minimal at this modulation index with all three NLEs. However, at $\eta_{mod} = 0.9$, the MLPDFE presents more symbol spacing than the VOLT2DFE, which in turn shows more than the TRDFE. This observation further supports the results presented much earlier in this section for the two CAP schemes.

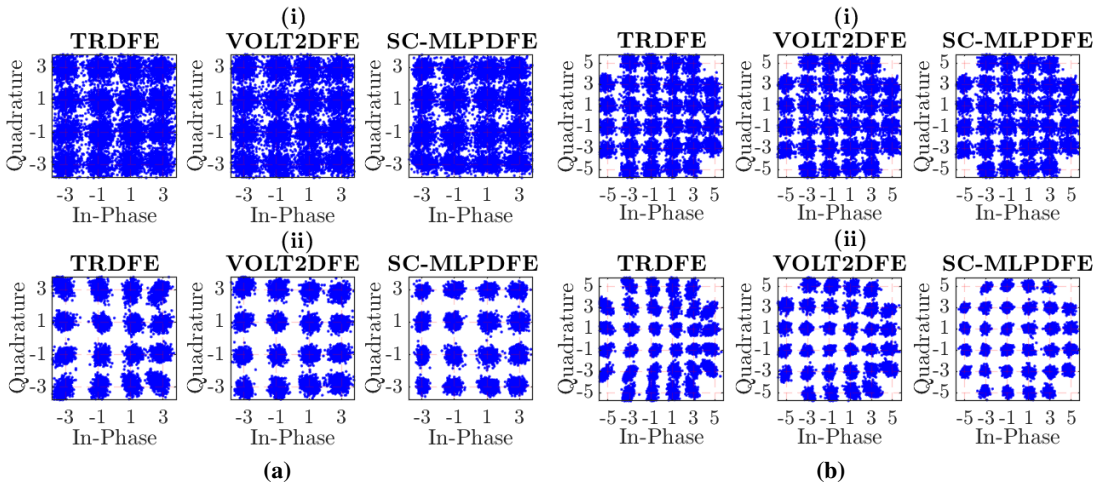


**Figure 4.22:** *Constellation diagrams from Fig. 4.21 at a bit-rate of 300 Mbps using: (a) CAP-16 at $\eta_{mod}$ values of (i) 0.45 and (i) 0.9 (b) CAP-32 at $\eta_{mod}$ values of (i) 0.45 and (i) 0.9.*

The results from the NLEs are assessed in this section by using varying modulation indices with the RC-LED setup. This assessment is with the knowledge that a higher modulation index increases the SNR and the non-linearities of the SI-POF system. For high-level modulation formats, there is always an optimum modulation index for each NLE, where the non-linearities that cancel out the SNR cannot be sufficiently mitigated with the equaliser. The index ranges

from 0.4 to 0.7 for the TRDFE and from 0.6 to 0.9 for the VOLT2DFE. However, the maximum modulation index of 1 is optimum with the MLP equalisers, signifying that they lessen all forms of the non-linearities significantly. The highest bit-rate at a BER of $10^{-3}$ is about 780 Mbps with the 60 m SI-POF. The bit-rate is obtained with PAM-2 and the MLPDFE.

## 4.6 Summary

The transmission of SCM signals through the SI-POF systems have been explored in this chapter. The SCM schemes are used in combination with the NLEs in the time-domain. The LD experiment setup is estimated with a non-linear model, which is used to compare the three NLEs in mitigating both ISI and non-linearities in the system. This model is then validated and shown to match the experiment results. With the model, the BER performances of the NLEs were considered in the presence of weak and extreme non-linear distortions. From all investigated scenarios, the MLP equalisers offer the best performance, especially for systems with high non-linear distortion and with high-level modulation formats. The Volterra equaliser and the transversal equaliser follows this.

A complexity study of each NLE is presented in this chapter. This study considers the computational complexity both with and without the training algorithm. The transversal DFEs has the least complexity of the NLEs. The MLP equalisers have a lower computational order than the Volterra equalisers if the number of hidden-layer neurons from the first one is less than its number of taps. The LMBP algorithm from the MLP equaliser demands more training symbols than the RLS algorithm for both transversal and Volterra DFE.

Both the LD and RC-LED setups have been experimentally demonstrated with PAM and CAP transmission schemes that are combined with the NLEs. With the LD setup, bit rates achieved at a BER of $10^{-3}$ are 10 Gbps, 6.8 Gbps and 2.92 Gbps for SI-POFs of 10 m, 30 m and 60 m length, respectively. Thus, the maximum bit-rate length product with the LD setup is 204 Gbps.m. This bit-rate length product is next to the ones presented in [113], [114] and [111]. The MLP equaliser is used to achieve these bit-rates for the LD setup. With the RC-LED setup, this equaliser is used to obtain a bit rate of 780 Mbps over a 60 m SI-POF – applying a 150 MHz band-limited receiver. The MLP equaliser is therefore shown to be the most viable of the NLEs considered in this chapter.

# Chapter 5

# Frequency Domain Non-linear Equalisation for SI-POF Transmission

The previous chapter explored the BER performance of the NLEs in the time domain (TD) and their required computational complexity. It emphasises that the NLEs complexity increases proportionally to the number of taps, which comes from increasing ISI from the high-speed transmission over the SI-POF system. Hence, communication at higher speeds would demand more computing resources for the NLEs to the point that they may become impractical to use.

In this chapter, we discuss an efficient way to implement the NLEs (i.e. Volterra and MLP equaliser) to reduce their computational complexities. The implementation involves the translation of the NLEs from the TD to the frequency domain (FD), with the advantage of the efficient Fourier transform algorithms. An adaptive equaliser in FD instead of the TD offers computational saving in a highly dispersive system. Despite this, FD equalisers are only used commercially with MCM schemes (like OFDM). The main reason is that these equalisers cannot function as well as their TD counterparts in fast-varying and mobile channels. Another reason is that OFDM requires the use of Fourier transforms while the SCM schemes do not. Fortunately, SI-POF links (especially those in SOHO networks) do not fall under this channel category. This makes FD equalisation applicable to an SI-POF system. There have been many studies that use the FD representation of conventional equaliser and DFE [45, 87, 102, 146]. But very little to no work has been done with FD implementation of the Volterra equaliser and the MLP equaliser, and this is what this chapter will explore.

The chapter is organised as follows: first, the translation the NLEs from the TD to the FD is described for MCM schemes (with cyclic prefix) and SCM schemes (with overlap-save). Then, the BER performance of the NLEs is addressed for DMT modulation, especially with non-linearities induced from clipping. Subsequently, the NLEs are compared when executed in the TD and the FD with the SCM schemes. The comparisons are in terms of their BER performances and their computational complexity.

## 5.1 Structure and description of the frequency domain non-linear equaliser (FD-NLE)

As mentioned earlier in Section 2.5, the MCM schemes will employ the cyclic prefix method while the SCM schemes will use the overlap-save method for FD equalisation. Furthermore, the TD based DFF is added to the FD-NLE only for the SCM scheme. With this in mind, we start this section with the implementation of the second-order Volterra equaliser in the FD for an MCM scheme (e.g. DMT). From Eq. (2.2), the TD expression of the second-order Volterra equaliser (with real-valued inputs and no decision feedback) can be rewritten as

$$\tilde{z}_n = w_{dc} + w_n \otimes y_n + \sum_{a=0}^{N_{ft}-1} \sum_{c=a}^{N_{ft}-1} w_{a,c} y_{n-a} y_{n-c}, \tag{5.1}$$

where $\otimes$ denotes the convolution operator. By rearranging the second-order Volterra terms in Eq. (5.1), we have:

$$\begin{aligned}
\tilde{z}_n &= w_{dc} + w_n \otimes y_n + \sum_{a=0}^{N_{ft}-1} w_{a,0} y_{n-a}^2 + \sum_{a=0}^{N_{ft}-2} w_{a,1} y_{n-a} y_{n-a-1} \\
&\quad + \sum_{a=0}^{N_{ft}-3} w_{a,2} y_{n-a} y_{n-a-2} + \cdots + \sum_{a=0}^{0} w_{a,N_{ft}-1} y_{n-a} y_{n-a-N_{ft}+1} \\
&= w_{dc} + w_n \otimes y_n + w_{n,0} \otimes (y_n^2) + w_{n,1} \otimes (y_n \cdot y_{n-1}) \\
&\quad + w_{n,2} \otimes (y_n \cdot y_{n-2}) + \cdots + w_{n,N_{ft}-1} \otimes (y_n \cdot y_{n-N_{ft}+1}) \\
\Rightarrow \tilde{z}_n &= w_{dc} + w_n \otimes y_n + \sum_{c=0}^{N_{ft}-1} w_{n,c} \otimes (y_n \cdot y_{n-c}).
\end{aligned} \tag{5.2}$$

Equation (5.2) shows that the second-order terms of the Volterra equaliser can be obtained via the sum of multiple linear convolutions. The Volterra terms of Eq. (5.2) can be truncated by including only the first $\alpha_2$ convolution terms to balance the complexity and performance so that Eq. (5.2) becomes

$$\tilde{z}_n = w_{dc} + w_n \otimes y_n + \sum_{c=0}^{\alpha_2-1} w_{n,c} \otimes (y_n \cdot y_{n-c}). \tag{5.3}$$

It is assumed that the cyclic prefix is appended to the DMT frames before transmission into the SI-POF channel as illustrated in Fig. 2.9. If the cyclic prefix length is more than the channel

delay spread and the equaliser truncation factor ($\alpha_2$), then the linear convolutions in Eq. (5.2) can be converted into an FD based NLE (FD-NLE) with FFT. Notably, the FD-NLE is realised with parallel multi-tap equalisers as

$$\tilde{Z}_{\mathcal{K}} = W_{dc} + W_{\mathcal{K}} Y_{\mathcal{K}} + \sum_{c=0}^{\alpha_2 - 1} W_{\mathcal{K},c} Y_{\mathcal{K},\mathcal{K}-c}, \tag{5.4}$$

where $\tilde{Z}_{\mathcal{K}}$, $W_{dc}$, $W_{\mathcal{K}}$, $W_{\mathcal{K},c}$ and $Y_{\mathcal{K},\mathcal{K}-c}$ are the FFT of $\tilde{z}_n$, $w_{dc}$, $w_n$, $w_{n,c}$ and $(y_n \cdot y_{n-c})$, respectively. The DC kernel $W_{dc}$ can be omitted because a DC blocker removes it at the receiver and no data is sent to the DC sub-carrier for the DMT signal. The values of the weights/kernels ($W_{\mathcal{K}}$ and $W_{\mathcal{K},c}$) for the sub-carrier index ($\mathcal{K}$) can be estimated with an MMSE algorithm (e.g. RLS).

### 5.1.1 Overlap-save method for the transversal equaliser

In Section 2.5, it was mentioned that only the feedforward section of the TRDFE is implemented in the FD. The same condition applies for the Volterra and the MLP equaliser. Hence, to separate the feedforward taps from the feedback taps in Eq. (2.1), we obtain the linear convolution of the feedforward input sequence $y_n$ with the tap weights $w_n$ as

$$u_n = \sum_{a=0}^{N_{ft}-1} w_a^* y_{n-a}, \text{ so that } \tilde{z}_n = u_n + \sum_{b=1}^{N_{bt}} w_b^* \hat{z}_{n-b}. \tag{5.5}$$

For the purpose of block processing, let us define the column vector $\mathbf{y}(\mathbf{b_0})$ of length $N_{FFT} = N_{spb} + N_{ft} - 1$ as

$$\mathbf{y}(\mathbf{b_0}) = [y_{bN_{spb}-N_{ft}+1}, y_{bN_{spb}-N_{ft}+2}, \cdots, y_{(b+1)N_{spb}-1}]^{\mathbf{T}}, \tag{5.6}$$

and column vector $\tilde{\mathbf{w}}_\mathbf{1}$ of length $N_{FFT}$ as

$$\tilde{\mathbf{w}}_\mathbf{1} = \left[w_0^*, w_1^*, \cdots, w_{N_{ft}-1}^*, \mathbf{0}^{\mathbf{1,N_{spb}-1}}\right]^{\mathbf{T}}, \tag{5.7}$$

where $N_{spb}$ denotes the number of symbols processed for a block index $b$, $\mathbf{0}^{\mathbf{1,N_{spb}-1}}$ refers to a row vector consisting of $N_{spb} - 1$ zeros, and $[.]^{\mathbf{T}}$ denotes the transpose operation of a vector or matrix. In order to maintain uniformity for derivations in subsequent sections, the block index $b$ has been added to the unequalised input sequence and not the tap weights. This

notation indicates that the input sequence and not the tap weights vary from block to block, as it happens for block processing without any adaptation algorithm.

From the properties of the DFT, it is known that the circular convolution of $\mathbf{y}(\mathbf{b_0})$ and $\tilde{\mathbf{w}}_\mathbf{1}$ can be obtained by transforming both vectors to their respective FD equivalents (using the DFT). The FD outputs go through an element-wise multiplication on the transformed samples and transforming the result back to the time domain (using the inverse DFT (IDFT)). This process can be efficiently implemented using the FFT and IFFT algorithms. The circular convolution of $\mathbf{y}(\mathbf{b_0})$ and $\tilde{\mathbf{w}}_\mathbf{1}$ is shown in Eq. (5.8), and it reveals that only the last $N_{spb}$ elements of the result coincide with the corresponding elements of the linear convolution [146]. The rest of the elements of the circular convolution do not provide any useful result as the elements of $\mathbf{y}(\mathbf{b_0})$ are wrapped around and are not in the right order, as required by the linear convolution. The computation of the circular convolution of $\mathbf{y}(\mathbf{b_0})$ and $\tilde{\mathbf{w}}_\mathbf{1}$ with the wraparound phenomenon is summarised as

$$\underbrace{\begin{bmatrix} \circ \\ \circ \\ \vdots \\ \circ \\ u_{bN_{spb}} \\ u_{bN_{spb}+1} \\ \vdots \\ u_{(b+1)N_{spb}-1} \end{bmatrix}}_{\tilde{\mathbf{u}}(\mathbf{b})} = \underbrace{\begin{bmatrix} y_{bN_{spb}-N_{ft}+1} & y_{(b+1)N_{spb}-1} & y_{(b+1)N_{spb}-2} & \cdots & y_{bN_{spb}-N_{ft}+2} \\ y_{bN_{spb}-N_{ft}+2} & y_{bN_{spb}-N_{ft}+1} & y_{(b+1)N_{spb}-1} & \cdots & y_{bN_{spb}-N_{ft}+3} \\ \vdots & \vdots & \vdots & \ddots & \vdots \\ y_{bN_{spb}-1} & y_{bN_{spb}-2} & y_{bN_{spb}-3} & \cdots & y_{bN_{spb}} \\ y_{bN_{spb}} & y_{bN_{spb}-1} & y_{bN_{spb}-2} & \cdots & y_{bN_{spb}+1} \\ y_{bN_{spb}+1} & y_{bN_{spb}} & y_{bN_{spb}-1} & \cdots & y_{bN_{spb}+2} \\ \vdots & \vdots & \vdots & \ddots & \vdots \\ y_{(b+1)N_{spb}-1} & y_{(b+1)N_{spb}-2} & y_{(b+1)N_{spb}-3} & \cdots & y_{bN_{spb}-N_{ft}+1} \end{bmatrix}}_{\mathbf{y_{cir}}(\mathbf{b_0})} \underbrace{\begin{bmatrix} w_0^* \\ w_1^* \\ \vdots \\ w_{N_{ft}-2}^* \\ w_{N_{ft}-1}^* \\ 0 \\ \vdots \\ 0 \end{bmatrix}}_{\tilde{\mathbf{w}}_\mathbf{1}}, \tag{5.8}$$

where $\mathbf{y_{cir}}(\mathbf{b_0})$ is the circulant $N_{FFT} \times N_{FFT}$ matrix for the column vector $\mathbf{y}(\mathbf{b_0})$, and $\tilde{\mathbf{u}}(\mathbf{b})$ denotes the output column vector of the circular convolution: and $\mathbf{u}(\mathbf{b})$ is the column vector of its last $N_{spb}$ elements. The FD implementation of Eq. (5.8) can now be obtained by simply noting by rewriting Eq. (5.8) as

$$\tilde{\mathbf{u}}(\mathbf{b}) = \boldsymbol{\mathcal{F}}^{-1}\boldsymbol{\mathcal{F}}\mathbf{y_{cir}}(\mathbf{b_0})\boldsymbol{\mathcal{F}}^{-1}\boldsymbol{\mathcal{F}}\tilde{\mathbf{w}}_\mathbf{1} \tag{5.9}$$

where $\boldsymbol{\mathcal{F}}/\boldsymbol{\mathcal{F}}^{-1}$ denotes the $N_{FFT} \times N_{FFT}$ DFT/inverse DFT (IDFT) matrix that is defined as

$$\boldsymbol{\mathcal{F}} = \begin{bmatrix} 1 & 1 & 1 & \cdots & 1 \\ 1 & \mathrm{e}^{-j\frac{2\pi}{N_{FFT}}} & \mathrm{e}^{-j\frac{4\pi}{N_{FFT}}} & \cdots & \mathrm{e}^{-j\frac{2\pi\left(N_{FFT}-1\right)}{N_{FFT}}} \\ 1 & \mathrm{e}^{-j\frac{4\pi}{N_{FFT}}} & \mathrm{e}^{-j\frac{8\pi}{N_{FFT}}} & \cdots & \mathrm{e}^{-j\frac{4\pi\left(N_{FFT}-1\right)}{N_{FFT}}} \\ \vdots & \vdots & \vdots & \ddots & \vdots \\ 1 & \mathrm{e}^{-j\frac{2\pi\left(N_{FFT}-1\right)}{N_{FFT}}} & \mathrm{e}^{-j\frac{4\pi\left(N_{FFT}-1\right)}{N_{FFT}}} & \cdots & \mathrm{e}^{-j\frac{2\pi\left(N_{FFT}-1\right)^2}{N_{FFT}}} \end{bmatrix}, \tag{5.10}$$

and $\boldsymbol{\mathcal{F}}^{-1} = \dfrac{1}{N_{FFT}}\boldsymbol{\mathcal{F}}^{*}$

Using the DFT matrix, the circulant matrix $\mathbf{y_{cir}}(\mathbf{b_0})$ has a special property that relates it to the column vector $\mathbf{y}(\mathbf{b_0})$. The property is defined as [146]:

$$\mathrm{diag}[\boldsymbol{\mathcal{F}}\mathbf{y}(\mathbf{b_0})] = \boldsymbol{\mathcal{F}}\mathbf{y_{cir}}(\mathbf{b_0})\boldsymbol{\mathcal{F}}^{-1}. \tag{5.11}$$

If we define $\boldsymbol{\mathcal{Y}}(\mathbf{b})_{\mathcal{F}} = \boldsymbol{\mathcal{F}}\mathbf{y_{cir}}(\mathbf{b_0})\boldsymbol{\mathcal{F}}^{-1}$ and $\boldsymbol{\mathcal{W}}_{\mathcal{F}} = \boldsymbol{\mathcal{F}}\tilde{\mathbf{w}}_1$, then Eq. (5.9) becomes:

$$\tilde{\mathbf{u}}(\mathbf{b}) = \boldsymbol{\mathcal{F}}^{-1}\boldsymbol{\mathcal{Y}}(\mathbf{b})_{\mathcal{F}}\boldsymbol{\mathcal{W}}_{\mathcal{F}}. \tag{5.12}$$

It is observed from Eq. (5.11) that $\boldsymbol{\mathcal{Y}}(\mathbf{b})_{\mathcal{F}}$ is the diagonal matrix consisting of the elements of the DFT of $\mathbf{y}(\mathbf{b_0})$. Therefore, Eq. (5.11) implies that $\boldsymbol{\mathcal{Y}}(\mathbf{b})_{\mathcal{F}}\boldsymbol{\mathcal{W}}_{\mathcal{F}}$ is the element-wise multiplication of the equaliser feedforward input and its tap weights in the FD, as this product is from a diagonal matrix and a column vector. The result is the output of the equaliser in the FD. Premultiplication of this result by the IDFT matrix converts the FD samples of the output to the TD. Furthermore, only the last $N_{spb}$ elements are required from the TD output, as they coincide with the required linear convolution samples. The background developed in this section will help with the derivation of the other equalisers with the overlap-save method.

### 5.1.2 Overlap-save method for the Volterra equaliser

From Eq. (2.2) and Eq. (5.2), we obtain the linear convolutions of the feedforward input sequence and the Volterra inputs from the TD-based VOLT2DFE (TD-VOLT2DFE) as

$$\begin{aligned} u_n = w_{dc}^* + \sum_{a=0}^{N_{ft}-1} w_a^* y_{n-a} + \sum_{a=0}^{N_{ft}-1} w_{a,0}^* y_{n-a}^2 + \sum_{a=0}^{N_{ft}-2} w_{a,1}^* y_{n-a} y_{n-a-1}^* \\ + \sum_{a=0}^{N_{ft}-3} w_{a,2}^* y_{n-a} y_{n-a-2}^* + \cdots + \sum_{a=0}^{0} w_{a,N_{ft}-1}^* y_{n-a} y_{n-a-N_{ft}+1}^*. \end{aligned} \tag{5.13}$$

The block implementation of the TD transversal equaliser (that is described in Eqs. (5.6), (5.7) and (5.8)) implies that Eq. (5.13) can be translated to:

$$\begin{aligned} \tilde{\mathbf{u}}(\mathbf{b}) &= w_{dc}^* \cdot \mathbf{1}^{\mathbf{N_{FFT},1}} + \mathbf{y_{cir}}(\mathbf{b_0})\tilde{\mathbf{w}}_{\mathbf{1}} + \mathbf{y}_{\mathbf{cir}}^{\mathbf{H}}(\mathbf{b_0})\mathbf{y_{cir}}(\mathbf{b_0})\tilde{\mathbf{w}}_{\mathbf{2},0} + \mathbf{y}_{\mathbf{cir}}^{\mathbf{H}}(\mathbf{b_1})\mathbf{y_{cir}}(\mathbf{b_0})\tilde{\mathbf{w}}_{\mathbf{2},1} \\ &\quad + \mathbf{y}_{\mathbf{cir}}^{\mathbf{H}}(\mathbf{b_2})\mathbf{y_{cir}}(\mathbf{b_0})\tilde{\mathbf{w}}_{\mathbf{2},2} + \cdots + \mathbf{y}_{\mathbf{cir}}^{\mathbf{H}}(\mathbf{b}_{\mathbf{N_{ft}-1}})\mathbf{y_{cir}}(\mathbf{b_0})\tilde{\mathbf{w}}_{\mathbf{2},N_{ft}-1} \\ &= w_{dc} \cdot \mathbf{1}^{\mathbf{N_{FFT},1}} + \mathbf{y_{cir}}(\mathbf{b_0})\tilde{\mathbf{w}}_{\mathbf{1}} + \sum_{c=0}^{N_{ft}-1} \mathbf{y}_{\mathbf{cir}}^{\mathbf{H}}(\mathbf{b_c})\mathbf{y_{cir}}(\mathbf{b_0})\tilde{\mathbf{w}}_{\mathbf{2},c}, \end{aligned} \tag{5.14}$$

where $\mathbf{y_{cir}}(\mathbf{b_c})$ is the circulant $N_{FFT} \times N_{FFT}$ matrix for the column vector $\mathbf{y}(\mathbf{b_c})$, which is the delayed version of $\mathbf{y}(\mathbf{b_0})$ and is derived from Eq. (5.6) as

$$\mathbf{y}(\mathbf{b_c}) = [y_{bN_{spb}-N_{ft}-c+1}, y_{bN_{spb}-N_{ft}-c+2}, \cdots, y_{(b+1)N_{spb}-c-1}]^{\mathbf{T}}, \tag{5.15}$$

and $\tilde{\mathbf{w}}_{\mathbf{2,c}}$ denotes the block of tap weights for the Volterra inputs, and it is a column vector of length $N_{FFT}$ defined as

$$\tilde{\mathbf{w}}_{\mathbf{2,c}} = \left[w_{a,0}^*, w_{a,1}^*, \cdots, w_{a,N_{ft}-1-c}^*, \mathbf{0}^{\mathbf{1,N_{spb}-1+c}}\right]^{\mathbf{T}}. \tag{5.16}$$

The notation $\mathbf{1}^{\mathbf{N_{FFT},1}}$ refers to a column vector consisting of $N_{FFT}$ ones as its element, and $[.]^{\mathbf{H}}$ denotes the Hermitian transpose of a vector or matrix.

The FD representation of the Volterra equaliser can now be obtained by adding the DFT/IDFT

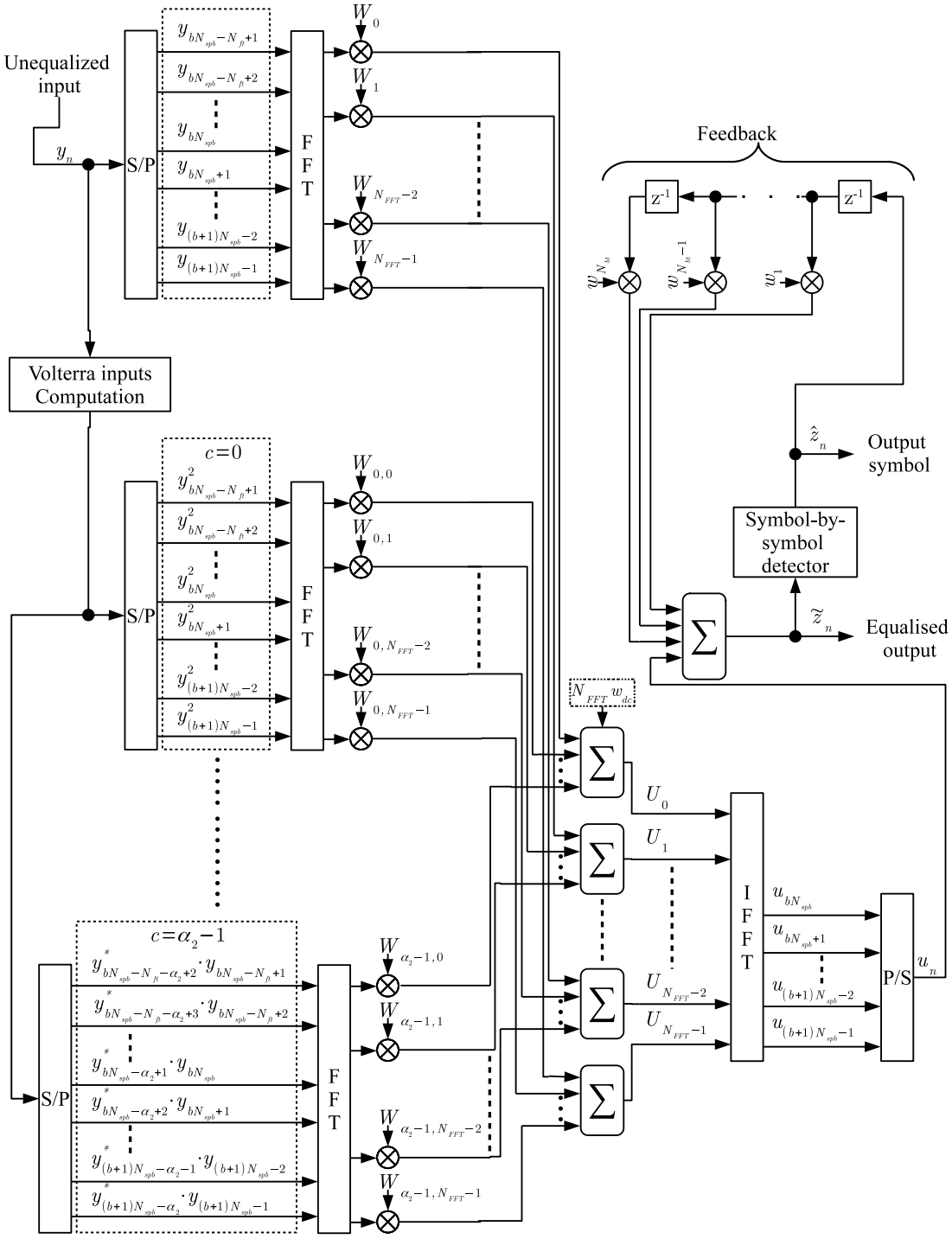


**Figure 5.1:** *Implementation of a second-order Volterra DFE (VOLT2DFE) in the frequency domain with the overlap-save method*

matrix to Eq. (5.14) just like with Eq. (5.9), Eq. (5.11) and Eq. (5.12). Hence we get:

$$\begin{aligned}\tilde{\mathbf{u}}(\mathbf{b}) &= w_{dc}^{*}\boldsymbol{\mathcal{F}}^{-1}\boldsymbol{\mathcal{F}}\left(\mathbf{1}^{\mathbf{N_{FFT},1}}\right) + \boldsymbol{\mathcal{F}}^{-1}\boldsymbol{\mathcal{F}}\mathbf{y_{cir}}(\mathbf{b_0})\boldsymbol{\mathcal{F}}^{-1}\boldsymbol{\mathcal{F}}\tilde{\mathbf{w}}_{\mathbf{1}} \\ &\quad + \sum_{c=0}^{N_{ft}-1}\boldsymbol{\mathcal{F}}^{-1}\boldsymbol{\mathcal{F}}\mathbf{y}_{\mathbf{cir}}^{\mathbf{H}}(\mathbf{b_c})\mathbf{y_{cir}}(\mathbf{b_0})\boldsymbol{\mathcal{F}}^{-1}\boldsymbol{\mathcal{F}}\tilde{\mathbf{w}}_{\mathbf{2,c}} \\ \Rightarrow \tilde{\mathbf{u}}(\mathbf{b}) &= \boldsymbol{\mathcal{F}}^{-1}\left\{\boldsymbol{\mathcal{W}}_{dc} + \boldsymbol{\mathcal{Y}}(\mathbf{b})_{\mathcal{F}}\boldsymbol{\mathcal{W}}_{\mathcal{F}} + \sum_{c=0}^{N_{ft}-1}\boldsymbol{\mathcal{Y}}(\mathbf{b})_{\mathcal{F},2,c}\boldsymbol{\mathcal{W}}_{\mathcal{F},2,c}\right\}, \qquad (5.17)\end{aligned}$$

$$\text{where } \boldsymbol{\mathcal{Y}}(\mathbf{b})_{\mathcal{F},2,c} = \boldsymbol{\mathcal{F}}\mathbf{y}_{\mathbf{cir}}^{\mathbf{H}}(\mathbf{b_c})\mathbf{y_{cir}}(\mathbf{b_0})\boldsymbol{\mathcal{F}}^{-1} = \operatorname{diag}\left[\boldsymbol{\mathcal{F}}\left(\mathbf{y}(\mathbf{b_c})^{*}\odot\mathbf{y}(\mathbf{b_0})\right)\right],$$

$$\boldsymbol{\mathcal{W}}_{dc} = w_{dc}\left[N_{FFT}, \mathbf{0}^{\mathbf{1,N_{FFT}-1}}\right]^{\mathbf{T}} \text{ and } \boldsymbol{\mathcal{W}}_{\mathcal{F},2,c} = \boldsymbol{\mathcal{F}}\tilde{\mathbf{w}}_{\mathbf{2,c}}.$$

The notation $\odot$ denotes the element-wise multiplication of two vectors (or matrices) of the same size.

Equation (5.17) shows that the FD output of the Volterra equaliser with the overlap-save method is a sum of the DC weight column vector $\boldsymbol{\mathcal{W}}_{dc}$, the feedforward output column vector $\boldsymbol{\mathcal{Y}}(\mathbf{b})_{\mathcal{F}}\boldsymbol{\mathcal{W}}_{\mathcal{F}}$ and the Volterra output column vectors $\boldsymbol{\mathcal{Y}}(\mathbf{b})_{\mathcal{F},2,c}\boldsymbol{\mathcal{W}}_{\mathcal{F},2,c}$. The equation of the FD Volterra equaliser with the overlap-save method is similar to that with the cyclic prefix method (see Eq. 5.4). Therefore, the Volterra terms of Eq. (5.17) can also be truncated by including only the first $\alpha_2$ terms to balance the complexity and performance so that Eq. (5.17) becomes:

$$\tilde{\mathbf{u}}(\mathbf{b}) = \boldsymbol{\mathcal{F}}^{-1}\left\{\boldsymbol{\mathcal{W}}_{dc} + \boldsymbol{\mathcal{Y}}(\mathbf{b})_{\mathcal{F}}\boldsymbol{\mathcal{W}}_{\mathcal{F}} + \sum_{c=0}^{\alpha_2-1}\boldsymbol{\mathcal{Y}}(\mathbf{b})_{\mathcal{F},2,c}\boldsymbol{\mathcal{W}}_{\mathcal{F},2,c}\right\}. \qquad (5.18)$$

If $\alpha_2 = 0$, the FD Volterra equaliser becomes the FD transversal equaliser or the FD linear equaliser (FD-LE).

Figure 5.1 depicts the block diagram of the FD-based VOLT2DFE (FD-VOLT2DFE), which is expressed earlier in Eq. (5.18). The diagram illustrates the steps applied for equalisation in FD. First, the input samples are collected in an input buffer (or S/P converter) whose output is the vector $\mathbf{y}(\mathbf{b_0})$, consisting of $N_{spb}$ new samples and $N_{ft}-1$ samples from the previous block. The same process is applied to the Volterra input samples to obtain the vector $(\mathbf{y}(\mathbf{b_c})^{*}\odot\mathbf{y}(\mathbf{b_0}))$. Then, the vectors are converted to the FD (with the FFTs) and are multiplied by their associated tap-weight vectors $\left(\boldsymbol{\mathcal{W}}_{\mathcal{F}} = \left[W_0, W_1, \cdots, W_{N_{FFT}-1}\right]^{\mathbf{T}}\right.$ and $\left.\boldsymbol{\mathcal{W}}_{\mathcal{F},2,c} = \left[W_{c,0}, W_{c,1}, \cdots, W_{c,N_{FFT}-1}\right]^{\mathbf{T}}\right)$, on an element-wise basis. The resulting FD vector outputs are then summed up, and the DC weight (i.e. $N_{FFT}w_{dc}$ from $\boldsymbol{\mathcal{W}}_{dc}$) is added to the

first element of the FD outputs. This gives the samples of the filter output in the FD, which are subsequently converted to the TD using an IFFT. The last $N_{spb}$ elements of the TD outputs are passed through a P/S converter a processed together with the DFF to obtain the final equalised output.

It is noteworthy to mention that the FD Volterra equaliser can be used with either real-valued inputs and tap weights (for PAM modulation) or with complex-valued inputs and tap weights (for CAP/QAM modulation). With real-valued inputs, about half of the FD samples are sufficient for processing the FD Volterra equaliser because of the complex-conjugate symmetry property of DFT: which shows that half of the DFT outputs is the complex conjugate of the other half [146, 147]. However, the FD equaliser with complex-valued inputs and weights requires the use of all FD samples.

### 5.1.3 Overlap-save method for the MLP equaliser

To separate the feedforward filtering section from the TD-based MLPDFE (TD-MLPDFE), Eq. (2.6) becomes:

$$\begin{aligned} \tilde{z}_n &= \sum_{c=1}^{N_{hn}} \left[ w_c \tanh\left( u_{c,n} + \sum_{b=1}^{N_{bt}} w_{c,b} \hat{z}_{n-b} \right) \right] + w_{bias}, \\ &\text{where } u_{c,n} = w_{c,bias} + \sum_{a=0}^{N_{ft}-1} w_{c,a} y_{n-a}. \end{aligned} \tag{5.19}$$

The expression in Eq. (5.19) shows that the TD-MLPDFE consists of multiple linear convolutions of the feedforward input sequence $y_n$, and the output of each convolution is for a hidden layer neuron (denoted with the index $c$). If we consider the FD conversion of the transversal equaliser described in Section 5.1.1 (with equations from Eq. (5.6) to Eq. (5.12)), then Eq. (5.19) can be translated to the FD as

$$\tilde{\mathbf{u}}(\mathbf{b})_{c} = \boldsymbol{\mathcal{F}}^{-\mathbf{1}} \left\{ \boldsymbol{\mathcal{W}}_{c,bias} + \boldsymbol{\mathcal{Y}}(\mathbf{b})_{\mathcal{F}} \boldsymbol{\mathcal{W}}_{\mathcal{F},c} \right\}, \tag{5.20}$$

where $\tilde{\mathbf{u}}(\mathbf{b})_{c}$ denotes the output column vector whose last $N_{spb}$ elements correspond to $u_{c,n}$; $\boldsymbol{\mathcal{W}}_{c,bias}$ denotes the bias column vector, which is equal to $w_{c,bias} \left[ N_{FFT}, \mathbf{0}^{\mathbf{1,N_{FFT}-1}} \right]^{\mathbf{T}}$; and $\boldsymbol{\mathcal{W}}_{\mathcal{F},c}$ denotes the FD tap-weight column vector assigned for each hidden layer neuron $c$.

The block diagram of the FD-based MLPDFE (FD-MLPDFE) is depicted Fig. 5.2, and it fur-

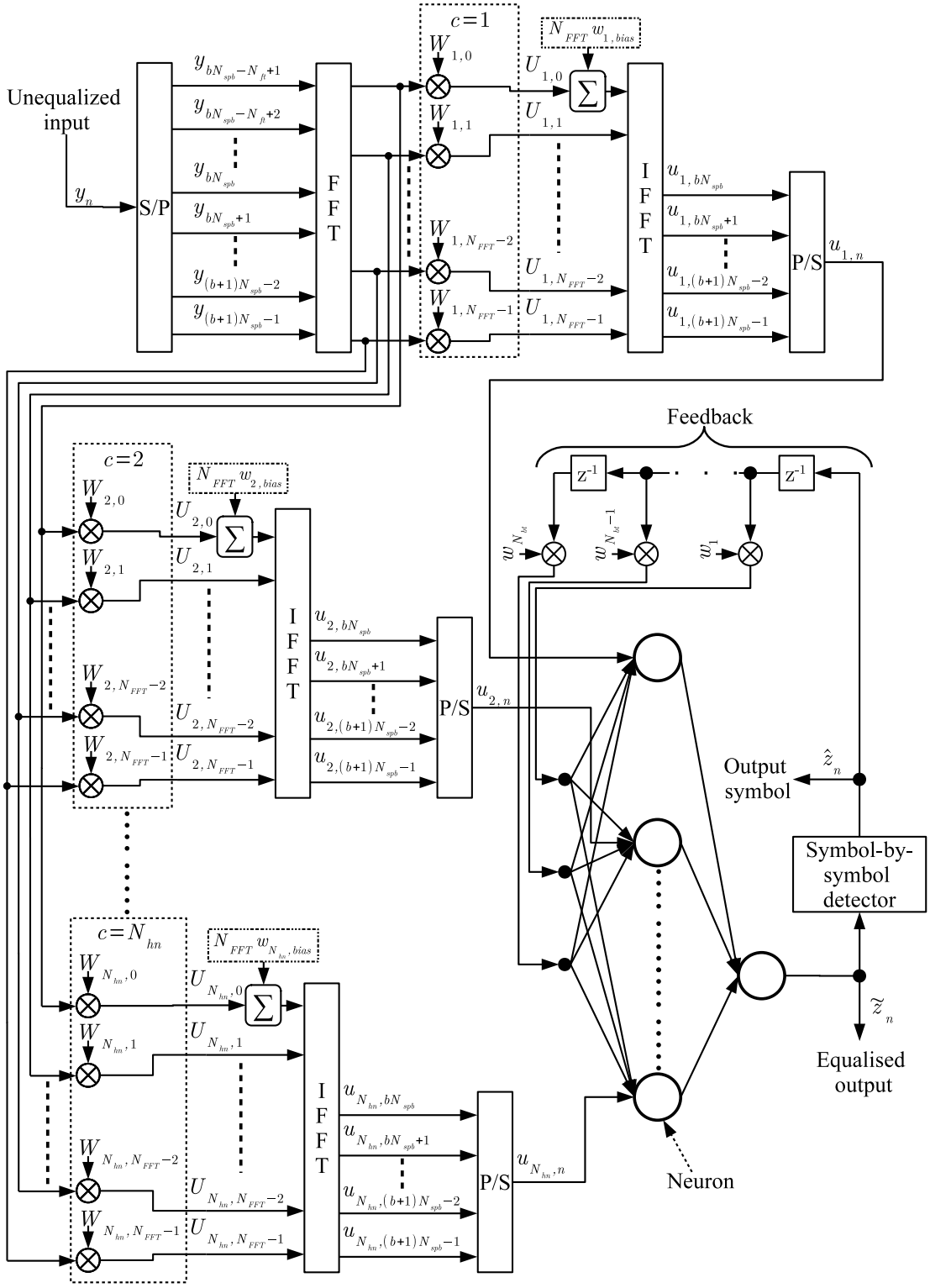


**Figure 5.2:** *Implementation of a multi-layer perceptron based DFE (MLPDFE) in the frequency domain with the overlap-save method*

ther describes the use of Eq. 5.20 for the MLPDFE in FD. The input samples are collected in an S/P converter whose output is the vector $\mathbf{y}(\mathbf{b_0})$, consisting of $N_{spb}$ new samples and $N_{ft}-1$ samples from the previous block. The vector is converted to the FD with an FFT to give $\boldsymbol{\mathcal{Y}}(\mathbf{b})_{\mathcal{F}}$. This FD vector is multiplied on an element-wise basis by several tap-weight vectors $\left(\boldsymbol{\mathcal{W}}_{\mathcal{F},c} = \left[W_{c,0}, W_{c,1}, \cdots, W_{c,N_{FFT}-1}\right]^{\mathbf{T}}\right)$. The first element of the resulting FD vector output for each hidden layer neuron is added to its associated bias (i.e. $N_{FFT}w_{c,bias}$ from $\boldsymbol{\mathcal{W}}_{c,bias}$). The following FD vector output from each hidden layer neuron is then converted to the TD with an IFFT, and the last $N_{spb}$ elements of the TD vector output are passed through a P/S converter. The result is processed together with the DFF for each hidden layer neuron. The outputs of the hidden layer neurons are then computed via the output layer neuron in order to obtain the final equalised output.

If the input sequence is complex-valued, then the SC-MLPDFE is used in place of the MLPDFE that deals with real-valued inputs. To distinguish the feedforward filtering section of the SC-MLPDFE, Eq. (2.7) becomes:

$$\begin{aligned}\tilde{z}_n = \sum_{c=1}^{N_{hn}} \left[ (w_c + jx_c) \tanh\left( u_{c,n} + \sum_{b=1}^{N_{bt}} \left( w_{c,b}\hat{z}_{n-b}^{\mathbb{R}} + x_{c,b}\hat{z}_{n-b}^{\mathbb{I}} \right) \right) \right] + (w_{bias} + jx_{bias}), \\ \text{where } u_{c,n} = w_{c,bias} + \sum_{a=0}^{N_{ft}-1} \left( w_{c,a}y_{n-a}^{\mathbb{R}} + x_{c,a}y_{n-a}^{\mathbb{I}} \right),\end{aligned} \tag{5.21}$$

which can be converted into the FD as

$$\tilde{\mathbf{u}}(\mathbf{b})_c = \boldsymbol{\mathcal{F}}^{-\mathbf{1}} \left\{ \boldsymbol{\mathcal{W}}_{c,bias} + \boldsymbol{\mathcal{Y}}(\mathbf{b})_{\mathcal{F},R} \boldsymbol{\mathcal{W}}_{\mathcal{F},c} + \boldsymbol{\mathcal{Y}}(\mathbf{b})_{\mathcal{F},I} \boldsymbol{\mathcal{X}}_{\mathcal{F},c} \right\}, \tag{5.22}$$

where $\boldsymbol{\mathcal{Y}}(\mathbf{b})_{\mathcal{F},R}$ and $\boldsymbol{\mathcal{Y}}(\mathbf{b})_{\mathcal{F},I}$ denote the FD equivalent for the real and imaginary component of the complex-valued inputs, respectively; and $\boldsymbol{\mathcal{W}}_{\mathcal{F},c}$ and $\boldsymbol{\mathcal{X}}_{\mathcal{F},c}$ denote column vector of the tap-weights in FD for $\boldsymbol{\mathcal{Y}}(\mathbf{b})_{\mathcal{F},R}$ and $\boldsymbol{\mathcal{Y}}(\mathbf{b})_{\mathcal{F},I}$, respectively.

In this section, the Volterra equaliser has been translated to the FD for MCM schemes using the cyclic prefix method. The equaliser has also been represented into the FD for SCM schemes with the overlap-save method. Like the TD-based Volterra equalisers, the FD-based equalisers can be trained with the MMSE algorithms. On the other hand, the MLP equaliser has been represented into the FD for SCM schemes but not for MCM schemes. Moreover, there is no

algorithm to train the FD-based MLP equaliser, and so it has to be trained in TD. These issues with the FD-based MLP equaliser can be resolved in later studies. The next section examines the performance of the FD-based Volterra equaliser for DMT.

## 5.2 FD-NLE for DMT

As discussed earlier in Section 3.1.3, DMT is an MCM scheme with high spectral efficiency and its flexibility with subcarrier allocation. But, it is limited by its high PAPR which can heavily contribute to the non-linearity of the SI-POF system [148]. Thus, the FD-NLE is required to further improve the performance of a DMT-modulated SI-POF system. The following section describe the experiment setup used to assess the performance of the equaliser.

### 5.2.1 Experimental setup for SI-POF with DMT modulation

It is assumed for DMT that prior information of the channel SNR per sub-carrier is known to ensure the bit-and-energy allocation. The channel estimation is performed with a pilot sequence that consists of random quadrature phase-shift keying (QPSK) symbols with constant energy. The relative channel gain and the absolute SNR values are obtained by estimating the error vector magnitude (EVM) of the QPSK constellations for the different sub-carriers as depicted in Fig. 5.3. The SNR profile of the SI-POF channel using the LD shows a similar pattern with the frequency response of the same channel depicted in Fig. 4.3. For instance, the 3 dB attenuation point of the 60 m SI-POF occurs at around 80 MHz for the SNR profile, while this is about 50 MHz with the frequency response. For the 30 m SI-POF, it is $\sim$150 MHz and $\sim$100 MHz with the SNR profile and the frequency response, respectively.

Two cases are therefore considered with the available channel SNR information. The first case (DMT_QAM-$M^2$) considers DMT with only power loading and all its data sub-carriers mapped with the QAM-$M^2$ format. The second case (bit-loaded DMT) allocates both the number of bits and the energy per sub-carrier with the Levin-Campello margin maximisation algorithm as illustrated in Fig. 5.4.

The DMT modulation parameters for this study are summarised in Table 5.1 for both the LD and the RC-LED setups that were discussed previously in Section 3.3. The value of these parameters is optimally selected with an exhaustive search to find those that achieve the best

| **Parameters** | **Symbol** | **Value with the:** | |
|---|---|---|---|
| | | **LD setup** | **RC-LED setup** |
| Number of bits for BER evaluation | $N_{bit}$ | $10^6$ | |
| Sampling rate | $F_s$ | 4 [GSa/s] | 1 [GSa/s] |
| FFT size (with Hermitian symmetry) | $N_{FFT}$ | 8192 | 2048 |
| Sub-carrier spacing | $\Delta f_s = \frac{F_s}{N_{FFT}}$ | 488.28 [kHz] | |
| Number of DMT blocks for training the FD equalisers | $N_{dtr}$ | 40 | |
| Cyclic prefix length | $N_{cp}$ | 64 | |

**Table 5.1:** *DMT modulation parameters*

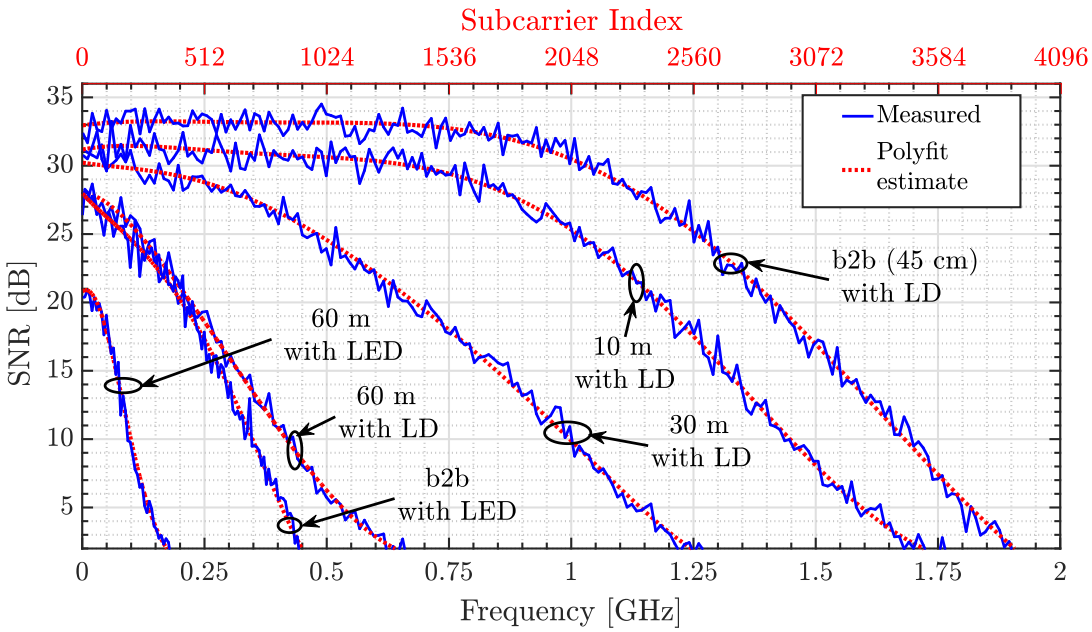


**Figure 5.3:** *SNR estimation of the SI-POF channel at 10 m, 30 m and 60 m lengths using the LD and the RC-LED setups. ($\eta_{mod}$ = 0.85)*

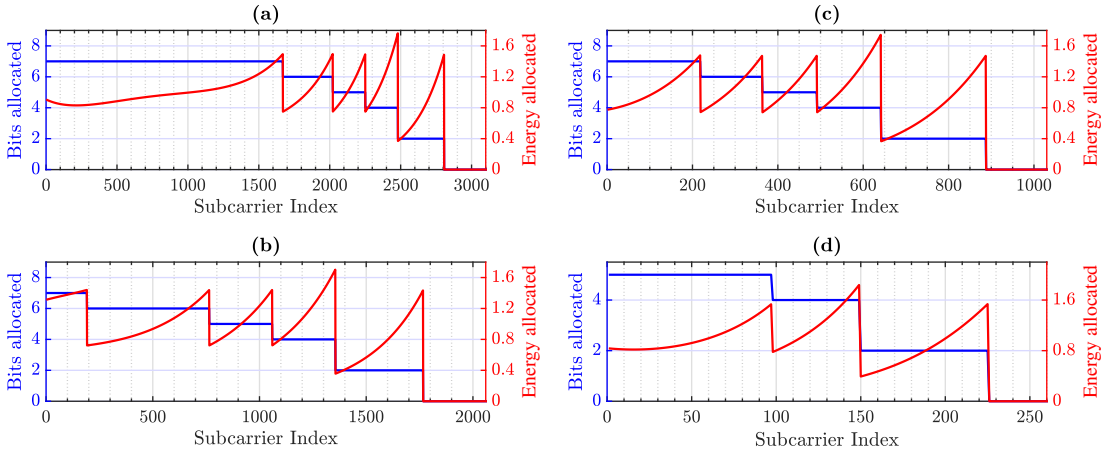


**Figure 5.4:** *Bit/power allocated per sub-carrier with the Levin-Campello margin maximisation algorithm for: (a) 8 Gbps bit-rate over 10 m SI-POF with LD (b) 4 Gbps bit-rate over 30 m SI-POF with LD (c) 2 Gbps bit-rate over 60 m SI-POF with LD (d) 0.4 Gbps bit-rate over 60 m SI-POF with RC-LED*

BER performance. For the LD setup, a modulation size $M$ of 4, 8 and 16 are used for SI-POF of lengths 60 m, 30 m and 10 m, respectively. And, $M = 4$ for the 60 m SI-POF using the RC-LED setup. The DMT signals are transmitted with a modulation index of 0.85 unless otherwise stated. These modulation sizes are selected from the identical experimental setups executed in Section 4.5.

The oversampling factor for DMT is expressed as

$$N_{sps} \approx \frac{N_{FFT}}{2N_{dsub}}, \tag{5.23}$$

where $N_{dsub}$ represents the number of data carrying sub-carriers. A parameter that is related to $N_{dsub}$ is the number of bits per DMT block $N_{bdmt}$ and for DMT_QAM-$M^2$ format, it is defined as $N_{bdmt} = 2N_{dsub} \log_2 M$. With respect to the sampling rate ($F_s$) and the bit rate ($R_b$), $N_{bdmt}$ is calculated as

$$N_{bdmt} = \left\lceil \frac{R_b(N_{FFT} + N_{cp})}{F_s} \right\rceil, \tag{5.24}$$

where $\lceil . \rceil$ represents the ceil operator. It is conventional to keep $N_{sps}$ constant so that $F_s$ increases proportionally with $R_b$: implying that $N_{FFT}$ should vary proportionately with $N_{dsub}$ as Eq. (5.23) shows. But for this study, both $F_s$ and $N_{FFT}$ are kept constant so that $N_{sps}$ varies inversely with $R_b$.

### 5.2.2 FD-NLE performance with Clipping

As discussed previously in Section 3.1.3, the main drawback of DMT is its large PAPR. For an SI-POF channel where the optical intensity is modulated, signals with higher PAPR suffer more from the impact of the receiver noise, resulting in lower SNR values as shown in Eq. (3.12). Clipping is the most direct and straightforward way to reduce the PAPR of DMT signals because, among the other PAPR reduction methods, it requires neither any additional overhead nor any computational requirement [148]. Furthermore, it takes place at the DMT transmitter in the TD before the DAC stage (see Fig. 3.3). And, it is used to accommodate the modulated signal within the dynamic range of the DAC, the amplifier, and the LED/LD. However, it introduces noise and non-linear distortions to the signal, and as a result, can lead to a degradation in performance.

In other studies, the DMT signal is usually clipped at lower and/or upper levels [127, 148, 149]. Furthermore, the study from [148] suggests that clipping both upper and lower levels of a DMT signal at similar values offers the maximum signal-to-noise-plus-distortion-ratio (SNDR) when compared to clipping either the upper or lower level. Hence, the thesis will use the clipping method suggested by [148] that converts the basic DMT signal $I(t)$ to the clipped DMT signal $\hat{I}(t)$ as

$$\hat{I}(t) = \begin{cases} I(t) & |I(t)| < I_{clip} \\ I_{clip} & I(t) \geq I_{clip} \\ -I_{clip} & I(t) \leq -I_{clip} \end{cases}, \tag{5.25}$$

where $I_{clip}$ denotes both the upper and lower clipping level as illustrated in Fig. 5.5(a). Consequently, clipping the signal reduces the maximum amplitude of the signal from $I_{mod}$ to $I_{clip}$. Using the clipping ratio $\rho_{_{clip}}$ in dB, the clipping level $I_{clip}$ can be expressed in terms of the signal variance $I_{rms}^2$ as

$$\rho_{_{clip}} = 20 \log_{10} \left( \frac{I_{clip}}{I_{rms}} \right). \tag{5.26}$$

Figure 5.5(a) also suggests that the higher the values of $\rho_{_{clip}}$, the smaller the amount of clipping and vice versa. Furthermore, the impact of both mild clipping ($\rho_{_{clip}} = 13$ dB) and extreme clipping ($\rho_{_{clip}} = 10$ dB) on the DMT signal is depicted with a QAM-64 data constellation in Fig. 5.5(b) and Fig. 5.5(c), respectively. The constellations are obtained for a 30 m SI-POF at a bit-rate of 250 Mbps using the LD setup. Comparing Fig. 5.5(b) and Fig. 5.5(c) shows that the signal distortion greatly increases with smaller values of the clipping ratio.

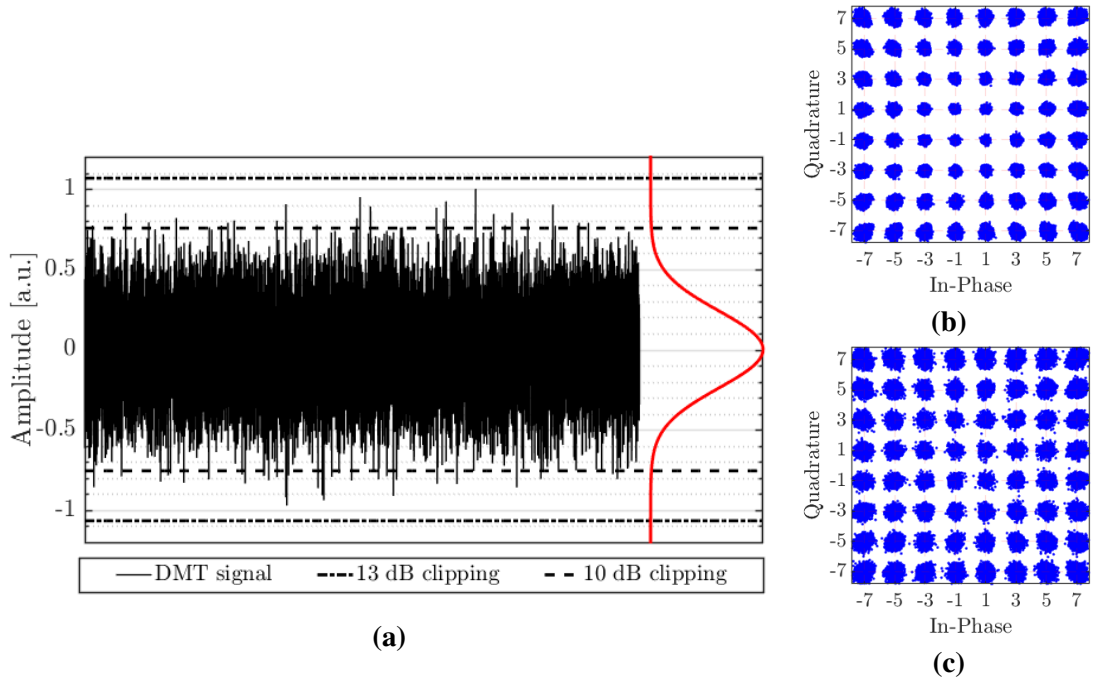


**Figure 5.5:** *(a) An illustration of the clipping levels for a DMT signal and the resulting QAM-64 constellation for 0.25 Gbps over 30 m SI-POF at (b) $\rho_{clip}$ =13 dB (c) $\rho_{clip}$ =10 dB.*

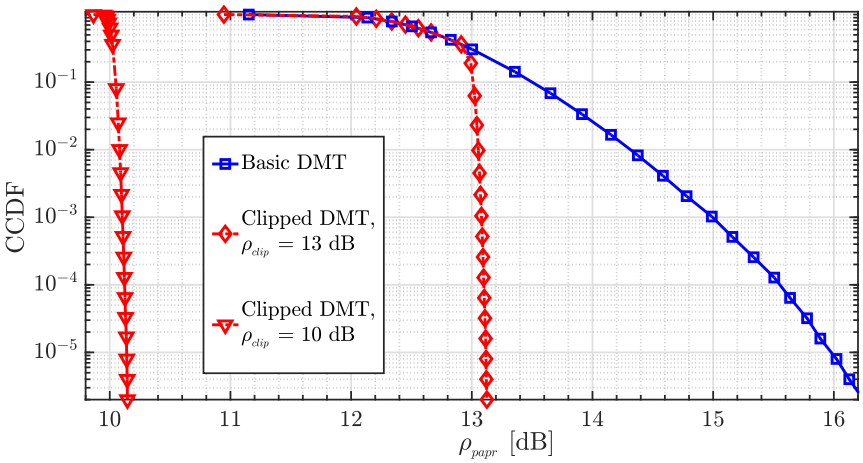


**Figure 5.6:** *The PAPR CCDF plots of the PAPR for basic and clipped DMT using QAM-64 ($N_{FFT}$ = 8192, $N_{dsub}$ = 1024)*

To illustrate the PAPR reduction capability of clipping, we show in Fig. 5.6 the complementary (CCDF) of the PAPR ($\rho_{papr}$) in dB. The figure shows that for basic DMT without clipping, the PAPR increases significantly with the number of DMT symbols/frames. For instance, one out of $10^3$ frames has its PAPR greater than 15 dB for the basic DMT. And out of $10^5$ frames, one has its PAPR greater than 16 dB. But, clipping both sides of the DMT signal results in a significant reduction in the PAPR. At a CCDF of $10^{-3}$, clipping a DMT signal for $\rho_{clip} = 13$ dB and $\rho_{clip} = 10$ dB reduces the PAPR of the DMT signal from 15 dB to 13.1 dB and 10.1 dB, respectively. The clipping for $\rho_{clip} = 13$ dB and $\rho_{clip} = 10$ dB results in a PAPR reduction of $\sim$2 dB and $\sim$5 dB, respectively, at the same CCDF of $10^{-3}$.

Clipping reduces the peak of the DMT signal by a factor of $\mu_{clip} = \frac{I_{mod}}{I_{clip}}$. Therefore, two options can be considered for transmitting the clipped DMT signal while keeping its modulation index $\eta_{mod}$ equal to that of the basic DMT signal without clipping. The first option is to reduce the dc-bias of the signal by the factor of $\mu_{clip}$ while keeping the clipped signal constant. The DMT signal that is sent prior to the DAC with this option becomes:

$$I_{DMT}(t) = \frac{I'_{bias}}{\mu_{clip}} + \hat{I}(t). \tag{5.27}$$

The advantage of this option is that it reduces the electrical power of the signal by a factor of $\mu^2_{clip}$. The other option is to increase the clipped signal by the factor of $\mu_{clip}$ while keeping the bias of the signal constant. The resulting DMT signal with this option is:

$$I_{DMT}(t) = I'_{bias} + \mu_{clip}\hat{I}(t). \tag{5.28}$$

Though this option does not reduce the electrical power of the signal, it can maximise the achievable bit-rate because of the increased amplitude of the clipped signal. The option described in Eq. (5.28) will, therefore, be considered in this study as it coincides with the thesis objective to maximise the bit-rate of the SI-POF channel.

A key design objective with signal clipping is to ensure high achievable SNDR at the receiver while keeping the non-linear distortion in an acceptable range. Acceptable values of the clipping ratio vary from $\sim$8 dB to $\sim$14 dB depending on the employed QAM constellation size [150]. The non-linearities of the system, including those from clipping, can be mitigated with the FD-NLE described in Eq. (5.4). Subsequently, we present plots of the BER against data rates to assess the performance of the FD-NLE in the presence of mild clipping ($\rho_{clip}$ =

13 dB) and extreme clipping ($\rho_{clip}$ = 10 dB).

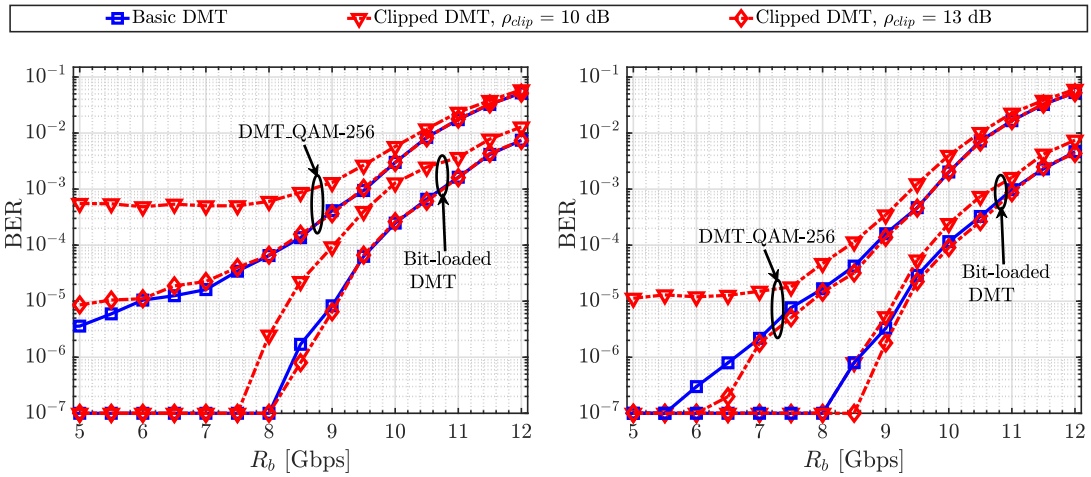


**Figure 5.7:** *The measured BER versus bit rate for DMT with and without clipping using: (a) FD-LE ($\alpha_2 = 0$) (b) FD-NLE ($\alpha_2 = 2$). Transmission is with the LD over a 10 m SI-POF at $\eta_{mod} = 0.85$.*

The BER results for a 10 m SI-POF with the LD setup are depicted in Fig. 5.7a in order to evaluate the performance of the conventional FD-LE. Using the DMT_QAM-256 format and the FD-LE, the BER increases from $\sim 3 \times 10^{-6}$ to $\sim 3 \times 10^{-3}$ as the bit rate increases from 5 Gbps to 10 Gbps. If the DMT signal is mildly clipped ($\rho_{clip}$ = 13 dB) before transmission, the BER performance of the SI-POF link is marginally worse than that of the DMT signal without clipping. If the DMT signal is severely clipped ($\rho_{clip}$ = 10 dB), the BER performance becomes significantly worse than that of the DMT signal without clipping. Moreover, the BER does not go below an error floor of $\sim 5 \times 10^{-4}$ with this clipping. For DMT transmission with bit loading, a bit rate of ∼8.7 Gbps is achieved at a BER of $3 \times 10^{-6}$: the bit rate is ∼5 Gbps at the same BER with DMT_QAM-256 format. Hence, the BER performance with bit loading is superior to that with no bit loading. Unlike with the DMT_QAM-256 format, the BER performance of the SI-POF link for the bit-loaded DMT with mild clipping is marginally better than that without clipping. This improvement is because the PAPR of the DMT signal with bit loading is less than that of the DMT signal without bit loading as the latter requires more low-level QAM formats while the former uses high-level QAM formats for each sub-carriers (see Fig. 5.4). With extreme clipping, the BER performance is significantly worse than that of the DMT signal without clipping. For instance, a bit rate of ∼10.7 Gbps is achieved at a BER of $10^{-3}$ without clipping. But with $\rho_{clip}$ = 10 dB, the bit rate reduces to ∼10 Gbps at the same BER.

The BER results are shown in Fig. 5.7b to assess the performance of the FD-NLE using the same setup for Fig. 5.7a. With the DMT_QAM-256 format and the FD-NLE, the BER increases from $\sim 3 \times 10^{-6}$ to $\sim 3 \times 10^{-3}$ as the bit rate increases from 7 Gbps to 11.5 Gbps. If the FD-NLE is used in place of the FD-LE, the result translates to a bit-rate increase of 2 Gbps to 1.5 Gbps at the BER of $\sim 3 \times 10^{-6}$ to $\sim 3 \times 10^{-3}$, respectively. With mild clipping, the BER performance of the SI-POF link is marginally better than that of the DMT signal without clipping. But with the extreme clipping of $\rho_{clip}$ = 10 dB, the BER performance becomes significantly worse than that of the DMT signal without clipping. Furthermore, the BER does not go below an error floor of $10^{-5}$ with this clipping. For DMT transmission with bit loading, a bit rate of ∼9 Gbps is achieved at a BER of $3 \times 10^{-6}$ with the FD-NLE, while the bit rate is ∼8.7 Gbps at the same BER with the FD-LE. Hence, the BER performance with the FD-NLE is superior to that with the FD-LE even for the DMT transmission with bit loading. The BER performance of the SI-POF link for the bit-loaded DMT with mild clipping is marginally better than that without clipping. With extreme clipping, the BER performance is slightly worse than that of the DMT signal without clipping. For instance, a bit rate of ∼11 Gbps is achieved at a BER of $10^{-3}$ without clipping. But at the same BER, the bit rate becomes ∼10.7 Gbps and ∼11.1 Gbps for clipping levels of 10 dB and 13 dB, respectively.

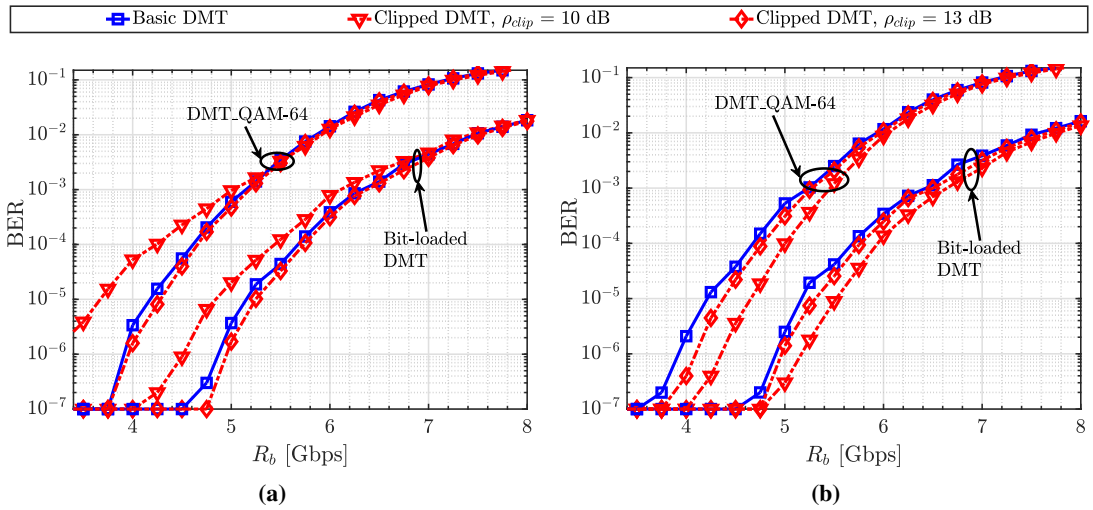


**Figure 5.8:** *The measured BER versus bit rate for DMT with and without clipping using: (a) FD-LE ($\alpha_2 = 0$) (b) FD-NLE ($\alpha_2 = 2$). Transmission is with the LD over a 30 m SI-POF at $\eta_{mod} = 0.85$.*

Figure 5.8a shows the BER results for a 30 m SI-POF with the LD setup using the FD-LE. With the DMT_QAM-64 format and the FD-LE, bit rates of 4 Gbps and 5.5 Gbps are achieved at a BER of $\sim 3 \times 10^{-6}$ and $\sim 3 \times 10^{-3}$, respectively. If the DMT signal is slightly clipped, the

BER performance of the SI-POF link is marginally better than that of the DMT signal without clipping. But with more severe clipping, the BER performance becomes significantly worse than that of the DMT signal without clipping. This pattern is exemplified in Fig. 5.8a where it shows an achievable bit rate of ∼4.3 Gbps at a BER of $2 \times 10^{-5}$ for DMT without clipping. But the bit rate becomes ∼3.8 Gbps and ∼4.4 Gbps for clipping levels of 10 dB and 13 dB, respectively, at the same BER. For the different clipping levels, the pattern of the BER results with the DMT_QAM-64 format is similar to those with the bit-loaded DMT: except that the latter offers a superior BER performance than the former. This similarity is because the size of the QAM formats at the sub-carriers for the prior DMT scheme is comparable to that used for the latter DMT scheme as Fig. 5.4 shows. For the bit-loaded DMT, a bit rate of ∼5.2 Gbps is achieved at a BER of $2 \times 10^{-5}$. However, the bit rate becomes ∼5 Gbps and ∼5.4 Gbps for clipping levels of 10 dB and 13 dB, respectively.

The BER results are shown in Fig. 5.8b to assess the performance of the FD-NLE for the 30 m SI-POF link using the same setup for Fig. 5.8a. With the DMT_QAM-64 format and the FD-NLE, the bit rate achieved at the BER of $\sim 3 \times 10^{-6}$ and $\sim 3 \times 10^{-3}$ is 4 Gbps to 5.5 Gbps, respectively. This result is similar to that from the FD-LE, which suggests that the non-linearities are negligible for the 30 m SI-POF link with DMT_QAM-64. The non-linearities are also negligible for the 30 m SI-POF link with the bit-loaded DMT since the FD-NLE offers the same BER performance as the FD-LE. With mild clipping, the BER performance of the SI-POF link is marginally better than that of the DMT signal without clipping. And with extreme clipping, the BER performance becomes significantly better than that of the DMT signal without clipping. Moreover, the BER performance of the FD-NLE from extreme clipping is significantly better than that of the FD-LE. At a BER of $2 \times 10^{-5}$ for instance, a bit rate of ∼4.3 Gbps is attained with the DMT_QAM-64 format that uses no clipping. The bit rate becomes ∼4.7 Gbps and ∼4.3 Gbps when the DMT signal is clipped at levels of 10 dB and 13 dB, respectively. With the bit-loaded DMT at the same BER, a bit rate of ∼5.2 Gbps, ∼5.6 Gbps and ∼5.4 Gbps is attained for the DMT scheme without clipping, with 10 dB clipping and with 13 dB clipping, respectively.

The BER results for a 60 m SI-POF with the LD setup are depicted in Fig. 5.9a for the FD-LE. Using the FD-LE for the DMT_QAM-16 format without clipping, the BER increases monotonously from $\sim 3 \times 10^{-6}$ to $\sim 3 \times 10^{-3}$ as the bit rate increases from 1.25 Gbps to 1.75 Gbps. If the DMT signal is marginally clipped at the 13 dB level, the BER performance

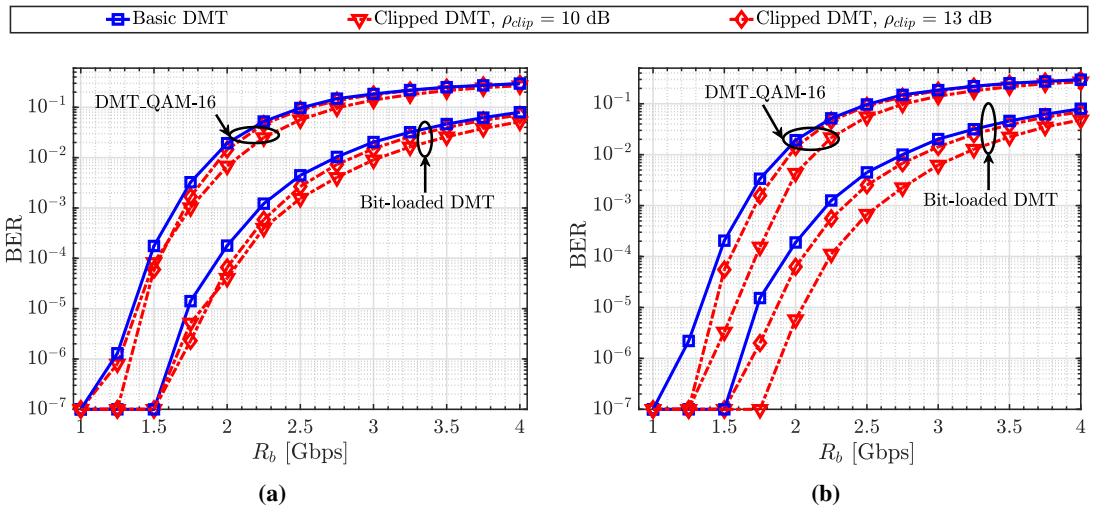


**Figure 5.9:** *The measured BER versus bit rate for DMT with and without clipping using: (a) FD-LE ($\alpha_2 = 0$) (b) FD-NLE ($\alpha_2 = 2$). Transmission is with the LD over a 60 m SI-POF at $\eta_{mod} = 0.85$.*

of the SI-POF link is marginally better than that of the DMT signal without clipping. With more severe clipping of 10 dB, the BER performance is also slightly better than that of the DMT signal without clipping. This pattern is demonstrated in Fig. 5.9a where it shows that a bit rate of ∼1.65 Gbps is achieved at a BER of $10^{-3}$ for DMT without clipping. But the bit rate becomes ∼1.75 Gbps and ∼1.7 Gbps for DMT transmission at clipping levels of 10 dB and 13 dB, respectively, at the same BER. For the different clipping levels, the pattern of the BER results with the DMT_QAM-16 format is similar to those with the bit-loaded DMT: and the latter offers a superior BER performance than the former. This similarity is because the size of the QAM formats at the sub-carriers for the prior DMT scheme is less than that used for the latter DMT scheme as Fig. 5.4 shows. For the bit-loaded DMT, a bit rate of ∼2.2 Gbps is achieved at a BER of $10^{-3}$. However, the bit rate becomes ∼2.4 Gbps and ∼2.35 Gbps for clipping levels of 10 dB and 13 dB, respectively. The bit rate values with clipping correspondingly translate to an increase of that without clipping by 9.1% and 6.8%.

Figure 5.9b depicts the BER plots used to assess the performance of the FD-NLE for the 60 m SI-POF link. The BER results are obtained with the same setup used in Fig. 5.9a. With the DMT_QAM-16 format and the FD-NLE, the bit rate achieved at the BER of $\sim 3 \times 10^{-6}$ and $\sim 3 \times 10^{-3}$ is 1.25 Gbps to 1.75 Gbps, respectively. This result is similar to that from the FD-LE, which suggests that the non-linearities are negligible for the 60 m SI-POF link with DMT_QAM-16. The non-linearities are also negligible for the 60 m SI-POF link with the bit-loaded DMT since the FD-NLE offers the same BER performance that the FD-LE presents.

With mild clipping, the BER performance of the SI-POF link is marginally better than that of the DMT signal without clipping. And with extreme clipping, the BER performance becomes significantly better than that of the DMT signal without clipping. The BER performance of the FD-NLE from extreme clipping is significantly better than that of the FD-LE at the same clipping level. At a BER of $10^{-3}$, for instance, a bit rate of ∼1.65 Gbps is attained with the DMT_QAM-16 format that uses no clipping. The bit rate becomes ∼1.9 Gbps and ∼1.7 Gbps when the DMT signal is clipped at levels of 10 dB and 13 dB, respectively. At the same BER, a bit rate of ∼2.2 Gbps is attained with bit-loaded DMT without clipping. The bit rate becomes ∼2.6 Gbps and ∼2.35 Gbps when the DMT signal is clipped at levels of 10 dB and 13 dB, respectively. The values with clipping correspondingly translate to an increase in the bit rate by 18.2% and 6.8%, which indicates that the FD-NLE significantly improves the performance of DMT signals with extreme clipping.

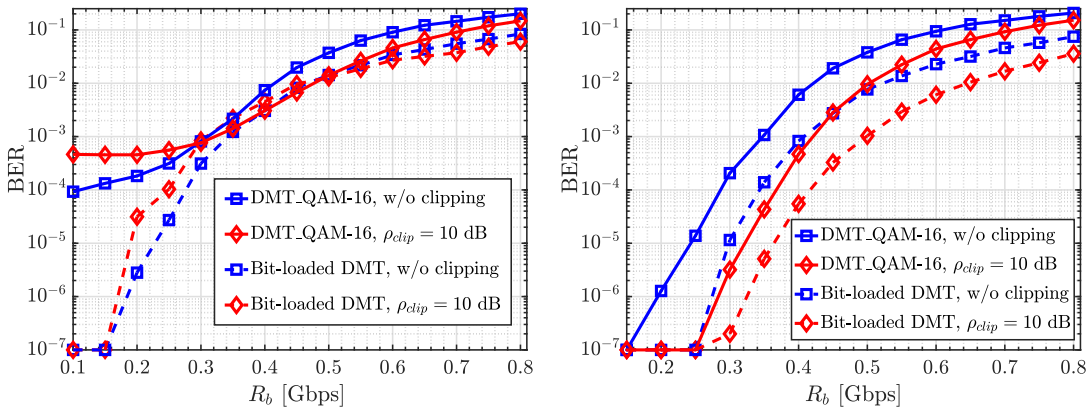


**(a)** **(b)**

**Figure 5.10:** *The measured BER versus bit rate for DMT with and without clipping using: (a) FD-LE ($\alpha_2 = 0$) (b) FD-NLE ($\alpha_2 = 3$). Transmission is with the RC-LED over a 60 m SI-POF at $\eta_{mod} = 0.85$.*

The BER results for a 60 m SI-POF with the RC-LED setup is depicted in Fig. 5.10a for the FD-LE. Henceforth, only the performance of the DMT signal with extreme clipping $\rho_{clip}$ =10 dB is considered as it is shown to offer either a similar or the best performance for the 60 m SI-POF link with the LD setup. With the FD-LE and the DMT_QAM-16 format without clipping, bit rates of 0.25 Gbps and 0.35 Gbps are achieved at a BER of $\sim 3 \times 10^{-4}$ and $\sim 3 \times 10^{-3}$, respectively. With the extreme clipping of the DMT signal, the BER performance becomes significantly worse than that of the DMT signal without clipping. Moreover, the BER does not go below an error floor of $\sim 4 \times 10^{-4}$ with clipping. With the bit-loaded DMT, a bit rate of ∼0.3 Gbps is achieved at a BER of $3 \times 10^{-4}$. However, the bit rate reduces to ∼0.28 Gbps with

clipping. The FD-NLE significantly improves the BER performance of the SI-POF link with the RC-LED setup as depicted in Fig. 5.10b. Using the FD-NLE without clipping the DMT_-QAM-16 signal, the bit rates of 0.31 Gbps and 0.38 Gbps are achieved at a BER of $\sim 3 \times 10^{-4}$ and $\sim 3 \times 10^{-3}$, respectively. Clipping the DMT signal while using the FD-NLE improves the BER performance of the system. At a BER of $10^{-3}$, for instance, a bit rate of ∼0.35 Gbps is attained with the DMT_QAM-16 format without clipping. The bit rate increases to ∼0.42 Gbps when the DMT signal is clipped. At the same BER, a bit rate of ∼0.41 Gbps is attained with bit-loaded DMT without clipping. And the bit rate increases to ∼0.5 Gbps when the DMT signal is clipped.

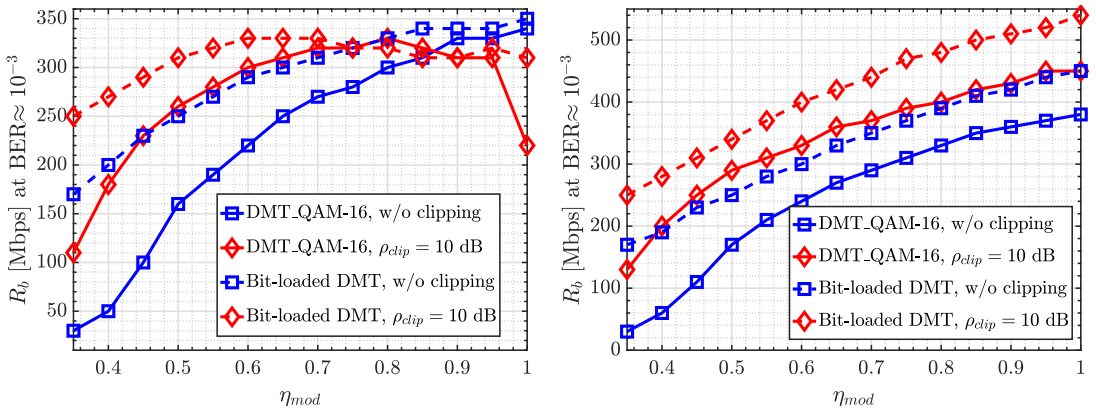


**Figure 5.11:** *The achievable bit-rate at a BER≈ $10^{-3}$ versus the modulation index ($\eta_{mod}$) for DMT with and without clipping using: (a) FD-LE ($\alpha_2 = 0$) (b) FD-NLE ($\alpha_2 = 3$). Transmission is with the RC-LED over a 60 m SI-POF.*

To evaluate the impact of the LED non-linearities for the 60 m SI-POF link, we evaluate the achievable bit rates for the FD-LE and the FD-NLE at a BER of $\sim 10^{-3}$ for the different modulation indices $\eta_{mod}$. This is because increasing $\eta_{mod}$ increases the non-linearities of the SI-POF link, as shown in Fig. 3.15a. The result of this evaluation is depicted in Fig. 5.11a and Fig. 5.11b for the FD-LE and the FD-NLE, respectively. With the FD-LE and the DMT_QAM-16 format without clipping, the bit rate increases continuously from ∼25 Mbps to ∼337.5 Mbps as the modulation index increases from 0.35 to 1. When the DMT signal is clipped, the bit rate at $\eta_{mod} = 0.35$ increases to ∼112.5 Mbps. The bit rate increases to ∼325 Mbps $\eta_{mod} = 0.8$, but then reduces at higher values of $\eta_{mod}$. At this modulation index, the SNR of the SI-POF system is cancelled out by the LED non-linearities, which cannot be mitigated with the FD-LE. A similar pattern is observed with bit-loaded DMT. Without clipping, the bit rate increases from ∼175 Mbps to ∼350 Mbps as the modulation index increases from 0.35 to 1. But with clipping,

the bit rate increases from ∼250 Mbps to ∼325 Mbps as the modulation index increases from 0.35 to 0.7. The bit rate then diminishes for values of $\eta_{mod}$ that are beyond 0.7.

The system performance significantly improves with the FD-NLE as Fig. 5.11b illustrates. Since the FD-NLE mitigates the non-linearities that increase with $\eta_{mod}$, the bit rate is observed to increase continuously for the DMT signal as the modulation index increases from 0.35 to 1. And it does not matter if the DMT signal is clipped or not. Hence, the maximum bit rates are achieved with the highest modulation index of 1. With the DMT_QAM-16 signal, this is ∼380 Mbps and ∼450 Mbps for the DMT signal without and with clipping, respectively. With the bit-loaded DMT signal, it is ∼450 Mbps and ∼540 Mbps for the signal without and with clipping, respectively.

The results from the experiments on DMT transmission over the SI-POF shows that with high-level QAM format ($M > 64$) in the DMT sub-carriers, clipping the DMT signal at the 10 dB level does not necessarily improve the BER performance of the SI-POF system. But with low-level QAM format in the DMT sub-carriers, the FD-NLE offers a significant improvement in the BER performance when compared to the FD-LE. In this section, the FD-NLE is shown to be relevant for DMT transmission with clipping over a non-linear system.

## 5.3 BER results for PAM and CAP transmission with FD-NLE

In Fig. 5.12, the BER results are used to compare the performances of the NLE when it is implemented in both the TD and the FD. The experiment setup for this comparison is similar to what was executed in section. 4.5. Figure 5.12a shows the measured BER versus the bit rate for a 30 m SI-POF using the LD setup. And Fig. 5.12b is for a 60 m SI-POF using the RC-LED setup. The truncation factor is equal to the number of feedforward taps for the VOLT2DFE, while the number of hidden layer neurons is six for the MLPDFE: like the equaliser parameters used in section. 4.5. Generally, the TD-NLE and the FD-NLE offer a similar BER performance for both PAM and CAP transmission over the SI-POF channel. This statement applies to both the VOLT2DFE and the MLPDFE. Moreover, the FD-NLE may offer a marginally better BER result than that from the TD-NLE.

The comparison study of the TD-NLEs (from Section 4.4) suggests that the Volterra DFE requires more computational complexity than the MLPDFE. This proposition is for a VOLT2DFE with full-memory length (i.e. $\alpha_2 = N_{ft}$), and for an MLPDFE, whose number of hidden layer

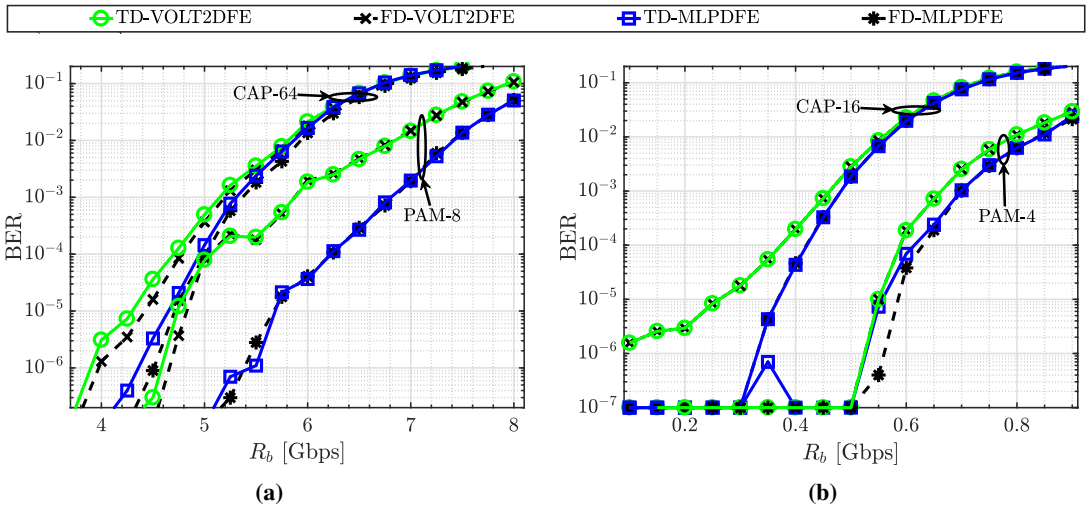


**Figure 5.12:** *BER performance comparison between TD-NLE and FD-NLE for: (a) PAM-8 and CAP-64 transmission over a 30 m SI-POF with LD (b) PAM-4 and CAP-16 transmission over a 60 m SI-POF with RC-LED.*

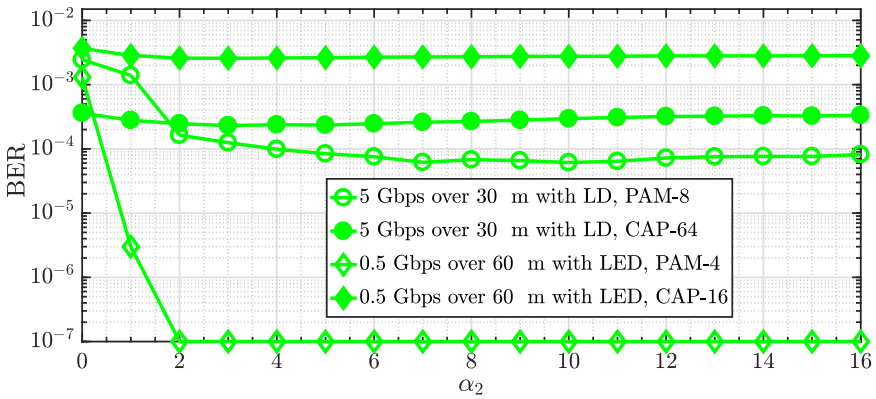


**Figure 5.13:** *BER performance comparison of FD-VOLT2DFE for values of the truncation factors $\alpha_2$*

neurons is less than the number of feedforward taps. However, the results from Fig. 5.13 indicate that a truncation factor ($\alpha_2$) of two is optimum to give the best BER performance. This truncation factor reduces the number of Volterra input taps by a factor of about $0.25N_{ft}$. Hence, the computational requirement of the VOLT2DFE reduces more significantly as the number of feedforward taps increases. The truncated VOLT2DFE offers about the same computational complexity as that of the MLPDFE if $\alpha_2 \approx N_{hn} - 1$.

## 5.4 Complexity comparison of TD-NLE and FD-NLE

The computational complexity of the proposed FD-NLE is evaluated with the required number of real-valued multiplications (RNRM), which is summarised in Table 5.2 and Table 5.3 for VOLT2DFE and MLPDFE, respectively. The RNRM is selected because the multiplier demands the highest computational cost compared to the other DSP operations [151]. For a fair comparison, Table 5.2 and Table 5.3 include the RNRM for the TD representation of the NLEs by using similar parameters from their respective FD-NLEs except for the FFT and other frequency-domain operations. The RNRM of the equalisers are also compared for when their inputs are real-valued and complex-valued: corresponding to PAM and CAP/QAM modulation, respectively.

Both the TD-NLE and the FD-NLE comprise of two stages, namely the training stage and the equalisation stage. The complexity analysis will not include the cost of the training stage because it depends on the training overhead. The channel state for the SI-POF slowly changes in comparison to the communication speed of the system. Thus, the training overhead is usually small (e.g., $\leq 4\%$) to the point that its effect on the overall complexity is negligible.

Table 5.2 demonstrates the RNRM required for each step with the TD-VOLT2DFE, which involves computing the Volterra inputs and filtering the input-taps. Each procedure is conducted $N_{spb}$ times for fair comparison with its FD counterpart that uses the FFT operation for a block set of the Volterra and the feedforward inputs. The FD-VOLT2DFE uses $\alpha_2 + 1$ FFT operations and implements non-linear equalisation using $\alpha_2 + 1$ complex-valued multiplications in the FD. It should be mentioned that the FFT and FD operations for complex-valued inputs are about twice of those for the real-valued inputs. For the FFT has the complex-conjugate symmetrical property for the real-valued input sequence. The resulting FFT outputs are summed up (as illustrated in Fig. 5.1 and stated in Eq. (5.18)), and the total is converted to the TD with one

| Equaliser | Operation Category | RNRM Size of Operation | Number of Operations per Block | RNRM |
|---|---|---|---|---|
| TD-VOLT2DFE (Real-valued) | Volterra input computation | $\alpha_2$ | $N_{spb} + N_{ft} - 1$ | $\alpha_2(N_{spb} + N_{ft} - 1)$ |
| | Feedforward filtering | $N_{ft}$ | $N_{spb}$ | $N_{spb}N_{ft}$ |
| | Volterra input filtering | $\alpha_2[N_{ft}+ 0.5(1-\alpha_2)]$ | | $N_{spb}\alpha_2[N_{ft}+ 0.5(1-\alpha_2)]$ |
| | Feedback filtering | $N_{bt}$ | | $N_{spb}N_{bt}$ |
| | Total | $N_{spb}[N_{ft} + N_{bt} + \alpha_2(N_{ft} + 0.5(3-\alpha_2))] + \alpha_2(N_{ft}-1)$ | | |
| TD-VOLT2DFE (Complex-valued) | Total | $4N_{spb}[N_{ft} + N_{bt} + \alpha_2(N_{ft} + 0.5(3-\alpha_2))] + 4\alpha_2(N_{ft}-1)$ | | |
| FD-VOLT2DFE (Real-valued) | Volterra input computation | $\alpha_2$ | $N_{FFT}$ | $\alpha_2 N_{FFT}$ |
| | FFT (split-radix) | $0.5N_{FFT}[\log_2(N_{FFT}) -3] + 2$ | $\alpha_2 + 1$ | $[0.5N_{FFT}(\log_2(N_{FFT}) -3) + 2](\alpha_2 + 1)$ |
| | FD multiplication | $2(N_{FFT} - 1)$ | $\alpha_2 + 1$ | $2(N_{FFT} - 1)(\alpha_2 + 1)$ |
| | IFFT | $0.5N_{FFT}[\log_2(N_{FFT}) -3] + 2$ | 1 | $0.5N_{FFT}[\log_2(N_{FFT}) -3] + 2$ |
| | Feedback filtering | $N_{bt}$ | $N_{spb}$ | $N_{spb}N_{bt}$ |
| | Total | $0.5N_{FFT}[(\alpha_2+2)\log_2(N_{FFT}) + (3\alpha_2 - 2)] + (N_{spb}N_{bt} + 2)$ | | |
| FD-VOLT2DFE (Complex-valued) | Volterra input Computation | $4\alpha_2$ | $N_{FFT}$ | $4\alpha_2 N_{FFT}$ |
| | FFT | $N_{FFT}[\log_2(N_{FFT}) -3] + 4$ | $\alpha_2 + 1$ | $[N_{FFT}(\log_2(N_{FFT}) -3) + 4](\alpha_2 + 1)$ |
| | FD multiplication | $4N_{FFT}$ | $\alpha_2 + 1$ | $4N_{FFT}(\alpha_2 + 1)$ |
| | IFFT | $N_{FFT}[\log_2(N_{FFT}) -3] + 4$ | 1 | $N_{FFT}[\log_2(N_{FFT}) -3] + 4$ |
| | Feedback filtering | $4N_{bt}$ | $N_{spb}$ | $4N_{spb}N_{bt}$ |
| | Total | $(N_{FFT}\log_2 N_{FFT} + 4)(\alpha_2+2) + N_{FFT}(5\alpha_2 - 2) + 4N_{spb}N_{bt}$ | | |

**Table 5.2:** *Complexity analysis of the TD and FD representation of VOLT2DFE*

| Equaliser | Operation Category | RNRM Size of Operation | Number of Operations per Block | RNRM |
|---|---|---|---|---|
| TD-MLPDFE (Real-valued) | Feedforward filtering | $N_{ft}N_{hn}$ | $N_{spb}$ | $N_{spb}N_{ft}N_{hn}$ |
| | Feedback filtering | $N_{bt}N_{hn}$ | | $N_{spb}N_{bt}N_{hn}$ |
| | Hidden layer computation | $N_{hn}$ | | $N_{spb}N_{hn}$ |
| | Total | $N_{spb}N_{hn}(N_{ft}+N_{bt}+1)$ | | |
| TD-MLPDFE (Split-complex) | Total | $2N_{spb}N_{hn}(N_{ft}+N_{bt}+1)$ | | |
| FD-MLPDFE (Real-valued) | FFT | $0.5N_{FFT}[\log_2(N_{FFT})-3]+2$ | 1 | $0.5N_{FFT}[\log_2(N_{FFT})-3]+2$ |
| | FD multiplication | $2(N_{FFT}-1)$ | $N_{hn}$ | $2N_{hn}(N_{FFT}-1)$ |
| | IFFT | $0.5N_{FFT}[\log_2(N_{FFT})-3]+2$ | $N_{hn}$ | $N_{hn}[0.5N_{FFT}(\log_2(N_{FFT})-3)+2]$ |
| | Feedback filtering | $N_{bt}N_{hn}$ | $N_{spb}$ | $N_{spb}N_{bt}N_{hn}$ |
| | Hidden layer computation | $N_{hn}$ | $N_{spb}$ | $N_{spb}N_{hn}$ |
| | Total | $0.5N_{FFT}[(N_{hn}+1)\log_2(N_{FFT})+(N_{hn}-3)]+N_{spb}N_{hn}(N_{bt}+1)+2$ | | |
| FD-MLPDFE (Split-complex) | FFT | $N_{FFT}[\log_2(N_{FFT})-3]+4$ | 1 | $N_{FFT}[\log_2(N_{FFT})-3]+4$ |
| | FD multiplication | $4(N_{FFT}-1)$ | $N_{hn}$ | $4N_{hn}(N_{FFT}-1)$ |
| | IFFT | $0.5N_{FFT}[\log_2(N_{FFT})-3]+2$ | $N_{hn}$ | $N_{hn}[0.5N_{FFT}(\log_2(N_{FFT})-3)+2]$ |
| | Feedback filtering | $2N_{bt}N_{hn}$ | $N_{spb}$ | $2N_{spb}N_{bt}N_{hn}$ |
| | Hidden layer computation | $2N_{hn}$ | $N_{spb}$ | $2N_{spb}N_{hn}$ |
| | Total | $0.5N_{FFT}[(N_{hn}+2)\log_2(N_{FFT})+(5N_{hn}-6)]+2N_{spb}N_{hn}(N_{bt}+1)+2(2-N_{hn})$ | | |

**Table 5.3:** *Complexity analysis of the TD and FD representation of MLPDFE*

IFFT operation.

Table 5.3 shows the RNRM required for each step with the TD-MLPDFE and the FD-MLPDFE. The first step requires filtering the input-taps to each neuron in the hidden layer. The outputs of these neurons are then processed via the output-layer neurons. This process is conducted for $N_{spb}$ times for fair comparison with its FD counterpart, which uses a single FFT operation for a block set of the feedforward inputs. The FD-MLPDFE realises equalisation with $N_{hn}$ complex-valued multiplications in the FD: according to the number of the hidden layer neurons. The IFFT algorithm converts the resulting outputs in the TD just before they are inputted to the hidden-layer neurons (as illustrated in Fig. 5.2). Hence, the FD-MLPDFE requires $N_{hn}$ IFFT operations. The RNRM of the MLPDFE with split-complex valued inputs is twice of that with the real-valued inputs, as the earlier case deals with two sets of inputs (i.e. real and imaginary).

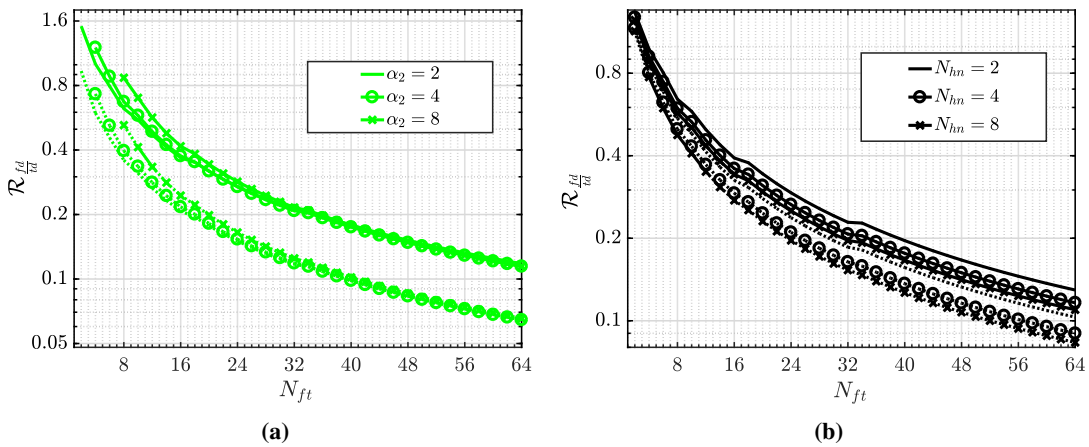


**Figure 5.14:** *The ratio of the RNRM of the TD-NLE and the FD-NLE for values of the feedforward taps ($N_{ft}$) using: (a) the Volterra equaliser with different truncation factors $\alpha_2$ and (b) the MLP equaliser with varying number of hidden-layer neurons ($N_{hn}$). The dashed and straight lines represent the equalisers with real-valued inputs and complex-valued inputs, respectively.*

By taking advantage of an efficient FFT algorithm, such as the split-radix algorithm, the FD-NLE can be used to achieve a lower complexity than the TD-NLE. To examine this complexity reduction of FD-NLE over TD-NLE, Fig. 5.14 shows the ratio of the RNRM of FD-NLE over that of TD-NLE. The ratio is denoted as $\mathcal{R}_{\frac{fd}{td}}$, and is computed in Fig. 5.14 for a varying number of feedforward taps without any feedback tap. To evaluate this ratio, the FD-NLEs are assumed to use an FFT size that is equal to at least eight times the feedforward taps with the expression:

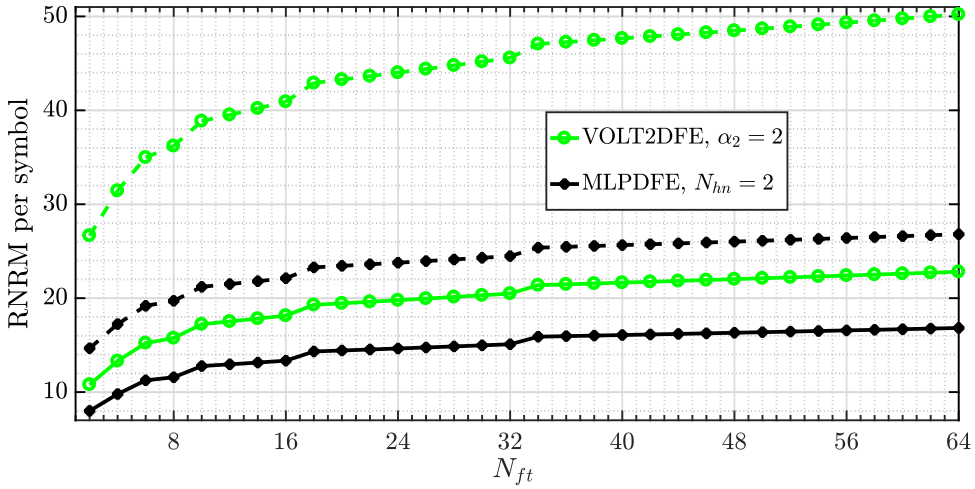


**Figure 5.15:** *The RNRM per symbol for values of the feedforward taps ($N_{ft}$) using the Volterra equaliser and the MLP equaliser. The dashed and straight lines represent the equalisers with real-valued inputs and complex-valued inputs, respectively.*

$$N_{FFT} = 2^{\lceil \log_2 N_{ft} \rceil + 3}. \tag{5.29}$$

Figure. 5.14a shows the values of $\mathcal{R}_{\frac{fd}{td}}$ for the Volterra equaliser with truncation factors of 2, 4 and 8. The values of $\mathcal{R}_{\frac{fd}{td}}$ are depicted for when the inputs are either real-valued or complex-valued. For values of $N_{ft}$ less than 30, $\mathcal{R}_{\frac{fd}{td}}$ increases slightly for higher values of $\alpha_2$. Otherwise, $\mathcal{R}_{\frac{fd}{td}}$ becomes marginal for the truncation factors with increasing $N_{ft}$. Furthermore, $\mathcal{R}_{\frac{fd}{td}}$ reduces exponentially as $N_{ft}$ increases. The complexity reduces even much more when the inputs are complex-valued compared to when they are real-valued. For instance, at $N_{ft} = 16$, $\mathcal{R}_{\frac{fd}{td}}$ is ∼0.38 at $\alpha_2 = 2$ if the inputs are real-valued. But, it slightly increases to ∼0.4 at $\alpha_2 = 8$. If the equaliser inputs are complex-valued, then $\mathcal{R}_{\frac{fd}{td}}$ reduces to ∼0.22. When $N_{ft}$ increases four-fold from 16 to 64, $\mathcal{R}_{\frac{fd}{td}}$ reduces from to ∼0.38 to ∼0.12 at $\alpha_2 = 2$. But, when $N_{ft}$ is reduced to 4, $\mathcal{R}_{\frac{fd}{td}}$ increases to ∼1.5.

Figure. 5.14b shows the values of $\mathcal{R}_{\frac{fd}{td}}$ for the MLP equaliser with hidden layer neurons of 2, 4 and 8. The values of $\mathcal{R}_{\frac{fd}{td}}$ are shown for when the inputs are either real-valued or split-complex valued. As the value of $N_{ft}$ increases, $\mathcal{R}_{\frac{fd}{td}}$ reduces slightly for higher values of $N_{hn}$. Like with the VOLT2DFE, $\mathcal{R}_{\frac{fd}{td}}$ reduces exponentially for the MLPDFE as $N_{ft}$ increases. However, the complexity reduces marginally for the MLPDFE when the inputs are split-complex valued compared to when they are real-valued. For instance, at $N_{ft} = 16$, $\mathcal{R}_{\frac{fd}{td}}$ is ∼0.4 at $\alpha_2 = 2$ if the inputs are real-valued. But, it slightly reduces to ∼0.35 at $\alpha_2 = 8$. If the equaliser inputs

are split-complex valued, then $\mathcal{R}_{\frac{fd}{td}}$ reduces to ∼0.33. When $N_{ft}$ increases four-fold from 16 to 64, $\mathcal{R}_{\frac{fd}{td}}$ reduces from to ∼0.4 to ∼0.14 at $\alpha_2 = 2$. But, when $N_{ft}$ is reduced to 4, $\mathcal{R}_{\frac{fd}{td}}$ increases to ∼0.9.

The computed RNRM per data symbol for the FD-MLPDFE is compared with that of the FD-VOLT2DFE in Fig. 5.15. The value of both $\alpha_2$ (for the FD-VOLT2DFE) and $N_{hn}$ (for the MLPDFE) is set as two for this comparison. The RNRM per symbol rises drastically as $N_{ft}$ increases from 1 to 10. Then, it rises more gently for the values of $N_{ft}$ that are above 10. Thus, the RNRM is proportionate to $\log_2 N_{ft}$. For $N_{ft} = 16$, the RNRM per symbol of the MLPDFE is 12 with real-valued inputs. While it is 22 with complex-valued inputs. For the same value of $N_{ft}$, the RNRM per symbol of the VOLT2DFE is 18 with real-valued inputs. And it is 42 with complex-valued inputs. Thus, the MLPDFE has lower computational complexity than the VOLT2DFE for $\alpha_2 = N_{hn}$. The computational requirement of the FD equalisers with complex-valued inputs is about twice of that of the FD equalisers with real-valued inputs.

While Fig. 5.14 investigates the complexity reduction for the number of feedforward taps, Fig. 5.16a considers the complexity reduction with respect to $\alpha_2$ and $N_{hn}$ for the VOLT2DFE and MLPDFE, respectively. The number of feedforward and feedback taps are kept constant as 24 and 3, respectively. For the VOLT2DFE with real-valued inputs, the value of $\mathcal{R}_{\frac{fd}{td}}$ initially decreases from ∼0.4 to ∼0.29 as $\alpha_2$ increases from 0 to 4. However, $\mathcal{R}_{\frac{fd}{td}}$ increases steadily with higher values of $\alpha_2$. A similar pattern is observed with the VOLT2DFE, when its inputs are complex-valued. This pattern can be attributed to the RNRM used to compute the Volterra inputs before filtering. And this RNRM varies proportionally with $\alpha_2$ as Table 5.2 shows. The minimum points for $\mathcal{R}_{\frac{fd}{td}}$ is at values of $\alpha_2$ ranging from 2 to 4. Fig. 5.13 already shows that these values are optimal for the best BER performance in an SI-POF channel. In contrast to the VOLT2DFE, $\mathcal{R}_{\frac{fd}{td}}$ for the MLPDFE reduces from ∼0.42 at $N_{hn} = 0$ to ∼0.32 at $N_{hn} = 16$.

Figure 5.16b depicts the RNRM per data symbol for both FD-MLPDFE and FD-VOLT2DFE: with $N_{ft} = 24$ and $N_{bt} = 3$. It is observed that the RNRM per symbol varies linearly with $\alpha_2$ for the FD-VOLT2DFE and $N_{hn}$ for the FD-MLPDFE. Furthermore, the FD-VOLT2DFE with real-valued inputs has the least computational requirement of the FD equalisers at high values of $\alpha_2$. The FD-MLPDFE follows this equaliser at high values of $N_{hn}$, and the FD-VOLT2DFE with complex-valued inputs follows the FD-MLPDFE. The slope of the plots in Fig. 5.16b for FD-MLPDFE is observed to be greater than that for FD-VOLT2DFE. This is because of the additional feedback inputs are filtered $N_{hn}$ times for the former equaliser. But they are filtered

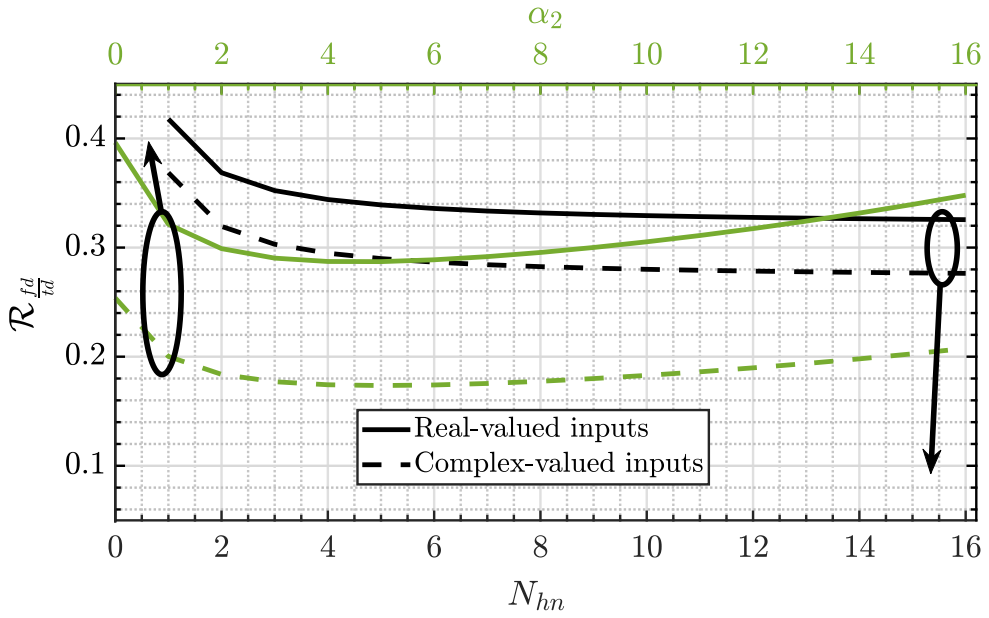


**(a)**

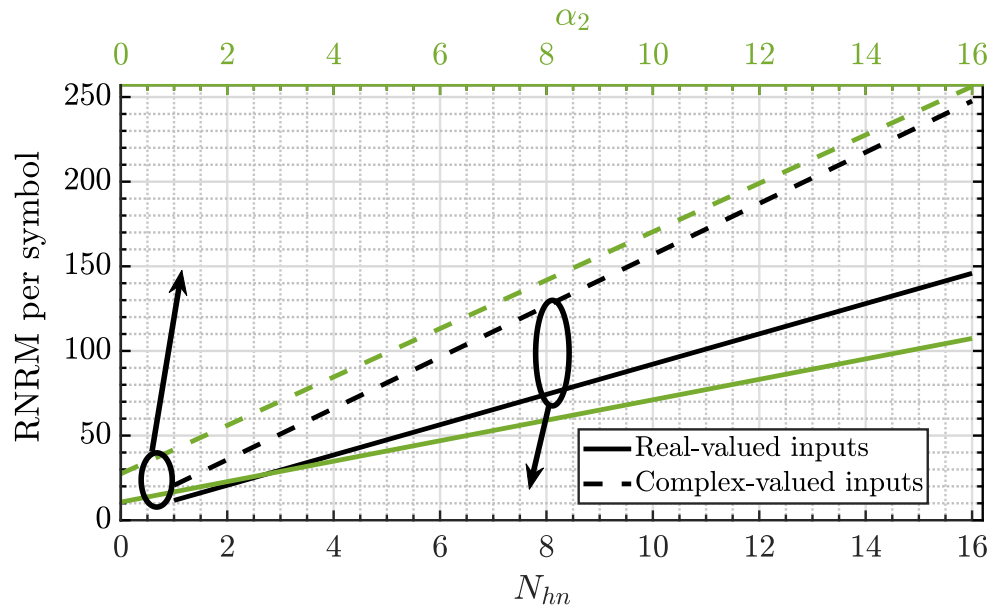


**(b)**

**Figure 5.16:** *(a) The ratio of the RNRM of the TD-NLE and the FD-NLE, and (b) the RNRM per symbol for values of $N_{hn}$ from the MLPDFE and for values of $\alpha_2$ from VOLT2DFE. $N_{ft} = 24$ and $N_{bt} = 3$.*

once for the latter equaliser as Table 5.2 and Table 5.3 shows. Therefore, the FD-MLPDFE requires lesser RNRM than the FD-VOLT2DFE for all values of $\alpha_2$ and $N_{hn}$ if $N_{bt} = 0$.

No feedback taps are considered for the equalisers in Fig. 5.14 because with the RNRM analysis in Table 5.2 and Table 5.3, $\mathcal{R}_{\frac{fd}{td}}$ can easily be expressed in terms of $N_{bt}$ as

$$\mathcal{R}_{\frac{fd}{td}} = \frac{\mathcal{R}_{\frac{fd}{td},0} + \mathcal{R}_{\frac{nbt}{nft}}}{1 + \mathcal{R}_{\frac{nbt}{nft}}}, \tag{5.30}$$

where $\mathcal{R}_{\frac{fd}{td},0}$ denotes the ratio of the RNRM of FD-NLE over that of TD-NLE for $N_{bt} = 0$. For VOLT2DFE, $\mathcal{R}_{\frac{nbt}{nft}} \approx \frac{N_{bt}}{N_{ft}(\alpha_2+1)}$ if $\alpha_2 \leq 3$, and for MLPDFE, $\mathcal{R}_{\frac{nbt}{nft}} = \frac{N_{bt}}{N_{ft}+1}$. The expression in Eq. (5.30) indicates that the number of feedback taps $N_{bt}$ increases the ratio $\mathcal{R}_{\frac{fd}{td},0}$ by a certain factor $\delta_r$ $\left(1 < \delta_r < \frac{1}{\mathcal{R}_{\frac{fd}{td},0}}\right)$. To ensure that $\mathcal{R}_{\frac{fd}{td}} \leq \delta_r \mathcal{R}_{\frac{fd}{td},0}$, then:

$$\mathcal{R}_{\frac{nbt}{nft}} \leq \frac{\mathcal{R}_{\frac{fd}{td},0}(\delta_r - 1)}{1 - \mathcal{R}_{\frac{fd}{td},0}\delta_r}. \tag{5.31}$$

It follows from Eq. (5.30) that with increasing values of $\alpha_2$, the effect of adding feedback taps on the RNRM ratio $\mathcal{R}_{\frac{fd}{td}}$ is less for the VOLT2DFE compared to the MLPDFE. This is further verified from the plots in Fig. 5.14 and Fig. 5.16a for $N_{ft} = 24$. For VOLT2DFE, Fig. 5.14 shows the value of $\mathcal{R}_{\frac{fd}{td},0}$ to be ∼0.3 with real-valued inputs at $\alpha_2 = 2$. While Fig. 5.16a depicts $\mathcal{R}_{\frac{fd}{td}}$ as ∼0.3 for $N_{bt} = 3$. The MLPDFE shows a similar value of $\mathcal{R}_{\frac{fd}{td},0}$ as ∼0.3 for real-valued inputs, but $\mathcal{R}_{\frac{fd}{td}}$ increases to ∼0.37 when $N_{bt} = 3$.

## 5.5 Summary

In this section, we have explored the representation of the NLEs (i.e. Volterra and MLP equaliser) in the FD. The FD-NLEs require a block transmission of the received signal with the cyclic prefix for DMT transmission, and with the overlap-save sectioning for PAM and CAP transmission over the SI-POF. The BER performance of the FD-NLE was compared with that of the conventional single-tap equaliser for DMT modulation with clipping. The results from the experiments on DMT transmission over the SI-POF shows that the FD-NLE offers a significant improvement in the BER performance when compared to the FD-LE when the DMT sub-carriers are mapped with low-level QAM format ($M \leq 64$).

The BER performance and the computational complexity of the FD-NLE were evaluated for PAM and CAP transmission. It is observed that the BER results from the FD-NLE were similar to those from the TD-NLE. The FD-VOLT2DFE can be realised with a tunable truncation factor of $\alpha_2$ to balance the performance and complexity: the optimal value for $\alpha_2$ is two. The complexity analysis shows that the FD-NLE requires less real-valued multiplications than the TD-NLE. For example, the FD-NLE requires at most 40% of the real-valued multiplications required from the TD-NLE if the number of feedforward tap is more than 16. The reduction of computational complexity becomes more significant as the number of feedforward taps for the NLEs increases.

# Chapter 6
# An Experimental Comparison on PAM, CAP and DMT with Non-linear Equalisers for SI-POF Communication

In the earlier chapters, we explored the performance of the NLEs with the modulation formats that are popular in an IM/DD SI-POF link, and they are PAM, CAP and DMT. The question arises: which modulation scheme provides the highest data rate for a given transmission setup that vary with regards to the transmitter, receiver, and the length of the SI-POF? This question has been typically answered, as several experiments that compare the performance of PAM, CAP and DMT have been reported for high-speed communication over SI-POF [113, 152, 153]. One of these experiments shows that PAM offers the highest throughput for longer SI-POF lengths ($\geq$ 50m) while DMT (with bit/power loading) is the optimal modulation format for short SI-POF lengths [152]. Another suggests that CAP-$M^2$ offers slightly higher data rates than PAM-$M$ for longer lengths with limited bandwidth when the SNR is high enough ($>$ 22 dB for CAP-16) [113].

However, the comparison experiments use the conventional TRDFE for PAM and CAP, and the FD-LE for DMT. These equalisers are not optimal for systems with high non-linearity. Hence, this chapter tries to answer a new question: using the NLEs discussed in the preceding chapters, which of these modulation schemes is the best option, especially for a highly non-linear SI-POF system? Therefore, the chapter reports the experimental performance of the modulation formats with their NLEs. The modulation formats considered in this study are PAM-$M$, CAP-$M^2$, DMT_QAM-$M^2$ with power loading and DMT with both bit and power loading. The modulation schemes and the NLEs are gauged from their achievable bit-rates (for their spectral efficiencies), their required transmitted electrical powers (as a measure of power efficiency), and their computational complexities. The LD and the RC-LED setups, described in Section 3.3, are used to evaluate the performances of the modulation formats with their NLEs. Furthermore, a description of the modulation formats can be found in Section 3.1. And the parameters of the modulation schemes and their NLEs can be found in Section 4.5 and Section 5.2.1.

## 6.1 Bit-rate performance

In Fig. 6.1, we present the computed BER for the various bit rates without any equalisation of the SI-POF link with lengths of 60 m, 30 m and 10 m. It should be noted that there is no bit and energy allocation for the DMT scheme. The reason for neglecting the equaliser and bit loading is to assess the performance of the modulation schemes without any additional signal processing technique. Figure 6.1 shows that for all the SI-POF lengths, the three modulation formats offer comparable BER result. The minimal difference in result from PAM, CAP and DMT is due to their PAPR and their different resilience to ISI. For instance, DMT modulation is the most resilient to ISI among the three schemes. But it has the highest PAPR, which limits the SNR of the modulated bit. CAP, being a bandpass signal, makes it more robust than PAM in terms of ISI. However, CAP has considerably higher PAPR ($\gtrapprox$ 2.5 dB) than PAM [131]. PAM is the most susceptible to ISI and system non-linearities, but it benefits having the least PAPR.

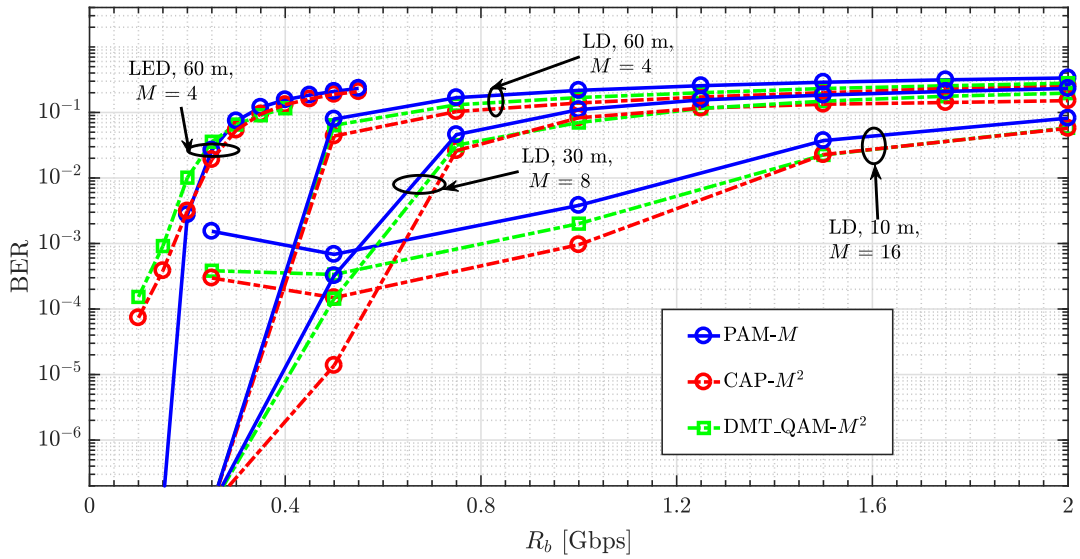


**Figure 6.1:** *BER results of the modulation formats for $\eta_{mod}$ = 0.85 without equalisation*

With the LD setup, CAP-$M^2$ offers the best BER performance while PAM-$M$ offers the worst BER result for all the SI-POF lengths. But with the RC-LED setup, PAM-$M$ offers the best BER performance while the DMT_QAM-$M^2$ offers the worst BER result for the 60 m SI-POF link. And CAP-$M^2$ format offers a marginally better BER result than that of PAM-$M$ at bit rates above 200 Mbps. These BER plots suggest that while PAM-$M$, CAP-$M^2$ and DMT_-QAM-$M^2$ have the same spectral efficiency of $\eta_b = 2\log_2 M$ bps/Hz without equalisation [124], CAP-$M^2$ shows more resilience to the channel ISI compared to the other two modulation

formats.

Based on the modulation order $M$ discussed in Section 4.5 and Section 5.2.1, the expected value of $\eta_b$ is 4, 6 and 8 bps/Hz for SI-POF of lengths 60 m, 30 m and 10 m, respectively. Considering the -3 dB bandwidth of the SI-POF link mentioned earlier in Section 4.1.2 for the LD setup, the theoretical bit rate ($R_b$) limit is 200 Mbps, 600 Mbps and 2 Gbps for the SI-POF lengths of 60 m, 30 m and 10 m, respectively. The measured bit rates corresponding to these SI-POF lengths at a BER of $\sim 10^{-3}$ is 400 Mbps, 600 Mbps and 1 Gbps as presented in Fig. 6.1. The measured bit rates of the SI-POF at both 60 m and 30 m SI-POF lengths are equal to or even more than their respective theoretical values at BERs below the 7% overhead FEC limit of $\sim 3.8 \times 10^{-3}$. And this suggests for the LD setup that the SNR for the SI-POFs is more than sufficient for the different lengths at their respective constellation sizes. However, the BER at the peak theoretical data rate of 2 Gbps over the 10 m SI-POF is $\sim$0.04. This irregularity is due to the effect of the system non-linearities that become significant with the high constellation size of $M$ = 16. The theoretical bit-rate limit of the RC-LED setup with a -3 dB bandwidth of $\sim$40 MHz (see Section 4.5.2) is 160 Mbps. The measured BER at this bit rate is $\sim 2 \times 10^{-3}$, which is below the 7% FEC limit. Consequently, the BER plots without equalisation confirm that the right constellation size is assigned to the SI-POF links of different lengths, transmitters and receivers.

In this section, the bit-rate performance of the SI-POF systems is gauged by obtaining the achievable rate at a BER of $10^{-3}$. Furthermore, the bit-rate performance of the modulation schemes is compared for the three NLEs considered in this thesis: which are the transversal equaliser, the Volterra equaliser and the ANN/MLP equaliser. The transversal equaliser is the TRDFE for PAM and CAP modulation, while it is the FD-LE for DMT modulation. The Volterra equaliser is the VOLT2DFE for PAM and CAP modulation, while for DMT modulation, it is the FD Volterra equaliser that is expressed in Eq. (5.4). The MLP equaliser is the MLPDFE for PAM, and it is the SC-MLPDFE for CAP. No form of this equaliser will be used for DMT in this thesis, but instead, the FD Volterra equaliser will be considered for DMT with clipping.

For the various modulation schemes and their NLEs, Fig. 6.2a depicts the maximal bit-rates that is attained for a 10 m SI-POF with the LD setup. With the conventional transversal equalisers, DMT with bit/power loading (or bit-loaded DMT) offers the highest bit rate of 10.7 Gbps. The modulation schemes that follow are DMT with QAM-256 and power loading (DMT_-

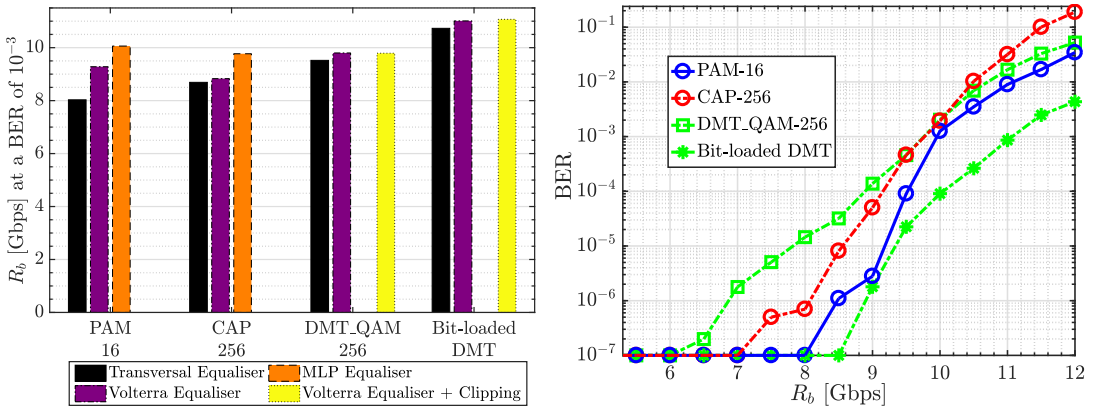


**(a)** **(b)**

**Figure 6.2:** *Bit-rate performance comparison of the modulation schemes for a 10 m SI-POF using the: (a) maximal bit-rates achieved at BER of* $10^{-3}$ *for the various NLEs (b) measured BER versus bit-rate with the best NLE. The results are obtained by using the LD setup with a fibre-coupled power of 6.5 mW and with* $\eta_{mod} = 0.85$.

QAM-256), CAP-256 and PAM-16, successively. With the Volterra equalisers, the bit-loaded DMT offers the highest bit rate of 11 Gbps and the bit rate increases to 11.1 Gbps with 13 dB clipping. The modulation scheme that follows is DMT_QAM-256, then PAM-16 and CAP-256. PAM offers a higher bit-rate than CAP with the Volterra equaliser, but unlike with the transversal equaliser, the opposite is the case. With the MLP equaliser, PAM-16 offers a bit-rate of 10.1 Gbps, which is higher than that presented from CAP-256. In Fig. 6.2b, the BER result for the modulation format is measured for values of the bit-rate with NLEs that present the best bit-rate performance for each modulation scheme. As illustrated in Fig. 6.2a, the MLP equalisers are these NLEs for PAM and CAP modulation, while the Volterra equalisers are for DMT modulation with clipping. Thus, the NLEs are used with their corresponding modulation formats for Fig. 6.2b. The bit-rates obtained at a BER of $\simeq 10^{-6}\{10^{-3}\}$ are $\sim$8.5$\{$10.1$\}$ Gbps, $\sim$8.1$\{$9.8$\}$ Gbps, $\sim$6.9$\{$9.8$\}$ Gbps and $\sim$8.9$\{$11.1$\}$ Gbps with PAM-16, CAP-256, DMT_-QAM-256 and bit-loaded DMT, respectively. The BER plots in Fig. 6.2b confirms that the bit-loaded DMT with the FD Volterra equaliser offers the best BER performance for all the bit-rates. PAM-16 with the MLPDFE, CAP-256 with the SC-MLPDFE and DMT_QAM-256 with the FD Volterra equaliser follows this.

Figure 6.3a shows the maximal bit-rates achieved at a BER of $\sim 10^{-3}$ for a 30 m SI-POF with the LD setup. With the transversal equalisers, the bit-loaded DMT offers the highest bit rate of 6.3 Gbps. DMT_QAM-64 and CAP-64 equally follow the bit-loaded DMT as they both

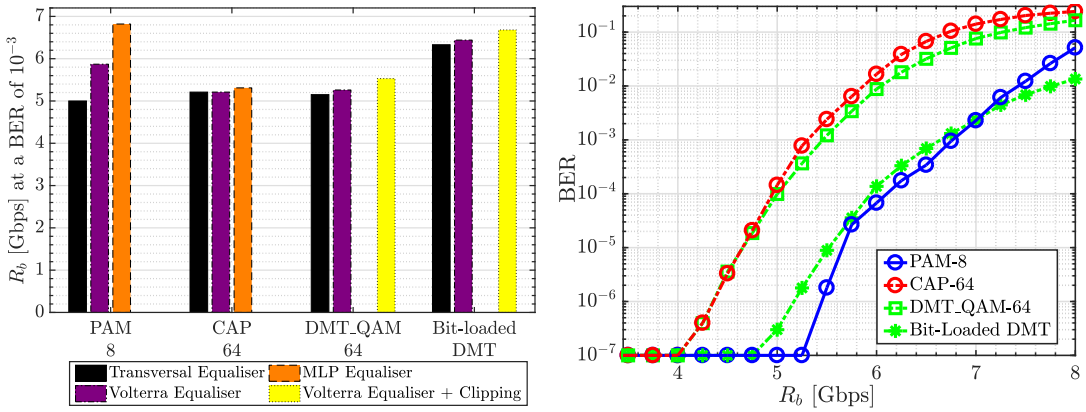


**(a)** **(b)**

**Figure 6.3:** *Bit-rate performance comparison of the modulation schemes for a 30 m SI-POF using the: (a) maximal bit-rates achieved at BER of* $10^{-3}$ *for the various NLEs (b) measured BER versus bit-rate with the best NLE. The results are obtained by using the LD setup with a fibre-coupled power of 6.5 mW and with* $\eta_{mod} = 0.85$.

offer the bit-rate of 5.2 Gbps. PAM-8 offers the least bit-rate of 5 Gbps. With the Volterra equaliser, the bit-loaded DMT offers the highest bit rate of 6.4 Gbps and the bit rate increases to 6.7 Gbps for the DMT with 10 dB clipping. The modulation scheme that follows is PAM-8, then DMT_QAM-64 and CAP-64. With the Volterra equaliser, PAM now offers a higher bit-rate than both DMT (without bit loading) and CAP. But unlike with the transversal equaliser, the opposite is the case. With the MLP equaliser, PAM-8 offers a bit-rate of 6.8 Gbps, which is significantly higher than 5.3 Gbps that is obtained with CAP-64. In Fig. 6.3b, the BER result for the modulation format is evaluated for values of the bit-rate with NLEs that offer the best bit-rate performance for each modulation scheme. As illustrated in Fig. 6.3a, the same NLEs employed for the 10 m SI-POF in Fig. 6.2b are also the best NLEs for the 30 m SI-POF. Similarly, they are used with their corresponding modulation formats for Fig. 6.3b. The bit rates achieved for the 30 m SI-POF at a BER of $\simeq 10^{-6}\{10^{-3}\}$ are $\sim$5.4$\{$6.8$\}$ Gbps, $\sim$4.4$\{$5.3$\}$ Gbps, $\sim$4.4$\{$5.5$\}$ Gbps and $\sim$5.2$\{$6.7$\}$ Gbps with PAM-8, CAP-64, DMT_QAM-64 and bit-loaded DMT, respectively. The BER plots in Fig. 6.3b confirms that the PAM-8 with the MLPDFE offers the best BER performance for the 30 m SI-POF. The modulation schemes that follow are the DMT schemes with the FD Volterra equaliser and CAP-64 with the SC-MLPDFE. It is also observed that CAP-64 and DMT_QAM-64 offer a similar BER performance at bit-rates less than $\sim$4.8 Gbps. But DMT_QAM-64 offers a superior BER result than CAP-64 at bit-rates above this value.

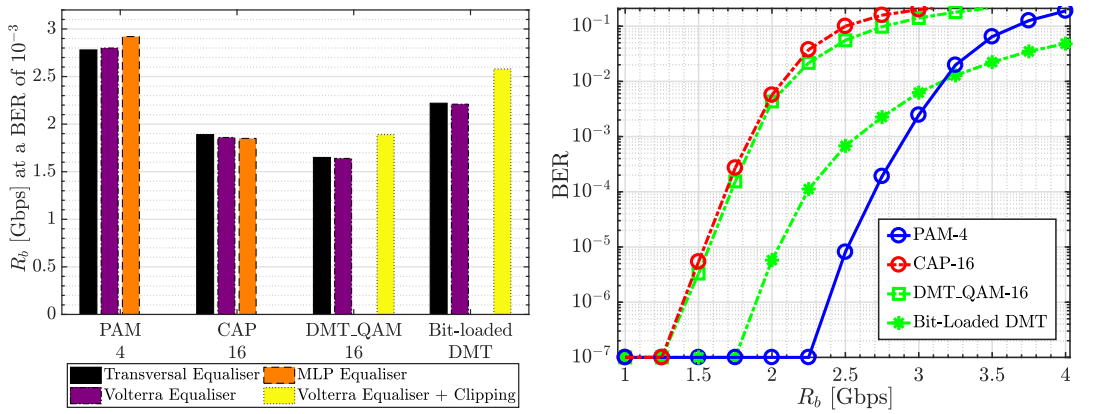


**(a)** **(b)**

**Figure 6.4:** *Bit-rate performance comparison of the modulation schemes for a 60 m SI-POF using the: (a) maximal bit-rates achieved at BER of* $10^{-3}$ *for the various NLEs (b) measured BER versus bit-rate with the best NLE. The results are obtained by using the RC-LED setup with a fibre-coupled power of 1 mW and with* $\eta_{mod} = 0.85$.

Figure 6.4a presents the maximal bit-rates achieved for a 60 m SI-POF using the LD setup with the modulation schemes and their NLEs. With the transversal equalisers, PAM-4 offers the highest bit rate of 2.8 Gbps. The modulation schemes that follow are bit-loaded DMT, CAP-16 and DMT_QAM-16, successively. With the Volterra equaliser, PAM-4 also offers the highest bit rate of 2.8 Gbps. The modulation scheme that follows is the bit-loaded DMT with the bit rate of 2.2 Gbps, and this increases to 2.6 Gbps for the DMT with 10 dB clipping. CAP-16 follows the bit-loaded DMT with a bit-rate of 1.9 Gbps. And DMT_QAM-16 offers the least bit-rate of 1.7 Gbps, which is increased to 1.9 Gbps with clipping. Unlike for the SI-POF of 10 m and 30 m lengths, the Volterra equalisers marginally improve the bit-rate performance of the transversal equalisers for the 60 m SI-POF. And both equalisers show PAM offers the highest bit rate followed by bit-loaded DMT, CAP-16 and DMT_QAM-16. This shows that the effect of non-linearity is negligible for the 60 m SI-POF with the LD setup. To further confirm the negligible non-linearity of the POF system, PAM-4 offers a bit-rate of 2.9 Gbps with the MLP equaliser, and the bit-rate is slightly higher than 2.8 Gbps from the transversal equaliser: which is a $\sim$3.6% bit-rate increase. CAP-16 with the MLP equaliser follows PAM-4; also with a bit-rate of 1.9 Gbps. In Fig. 6.4b, the BER result for the modulation format is evaluated for values of the bit-rate with NLEs that offer the best bit-rate performance for each modulation scheme. As illustrated in Fig. 6.4a, the same NLEs employed for both 10 m and 30 m SI-POF in Fig. 6.2b are also the best NLEs for the 60 m SI-POF. So, these NLEs are used

with their corresponding modulation formats for Fig. 6.4b. The bit rates achieved for the 60 m SI-POF at a BER of $\simeq 10^{-6}\{10^{-3}\}$ are $\sim$2.4$\{$2.9$\}$ Gbps, $\sim$1.4$\{$1.9$\}$ Gbps, $\sim$1.4$\{$1.9$\}$ Gbps and $\sim$2.1$\{$2.6$\}$ Gbps with PAM-4, CAP-16, DMT_QAM-16 and bit-loaded DMT respectively. The BER plots in Fig. 6.4b confirms that the PAM-4 with the MLPDFE offers the best BER performance for the 60 m SI-POF. The modulation schemes that follow this successively are the bit-loaded DMT with the FD Volterra equaliser, DMT_QAM-16 with the FD Volterra equaliser and CAP-16 with the SC-MLPDFE. It is also observed from Fig. 6.4b that the DMT_QAM-16 format marginally outperforms CAP-16 in terms of BER performance for all values of the bit-rates.

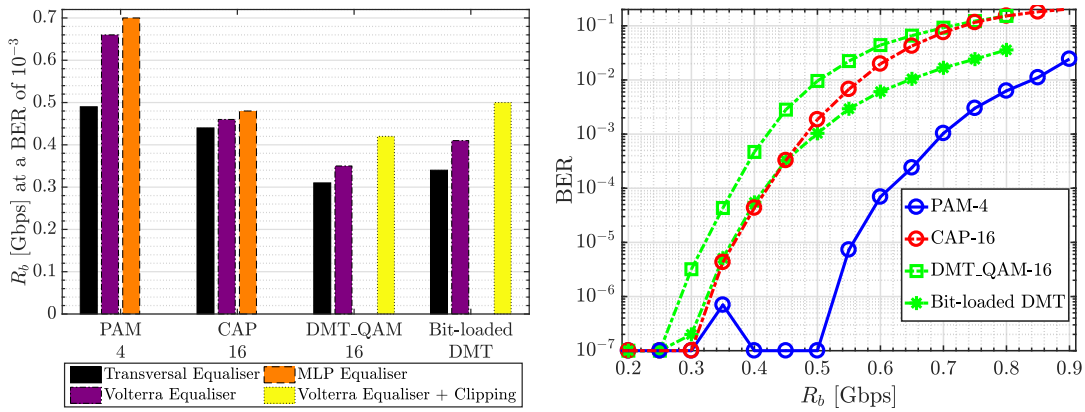


**(a)** **(b)**

**Figure 6.5:** *Bit-rate performance comparison of the modulation schemes for a 60 m SI-POF using the: (a) maximal bit-rates achieved at BER of* $10^{-3}$ *for the various NLEs (b) measured BER versus bit-rate with the best NLE. The results are obtained by using the RC-LED setup with a fibre-coupled power of 1 mW and with* $\eta_{mod} = 0.85$.

Figure 6.5a depicts the maximal bit-rates that is attained at a BER of $10^{-3}$ for the 60 m SI-POF with the RC-LED setup. PAM-4 offers the highest bit rate of 490 Mbps with the transversal equalisers. The modulation schemes that follow are CAP-16, bit-loaded DMT and DMT_QAM-16, successively: with the bit-rate of 440 Mbps, 340 Mbps and 310 Mbps, respectively. With the Volterra equaliser, PAM-4 also offers the highest bit rate of 660 Mbps. The modulation scheme that follows is CAP-16 with a bit-rate of 460 Mbps. The bit-loaded DMT follows CAP-16 with its bit rate of 410 Mbps, which increases to 500 Mbps for the DMT with 10 dB clipping. DMT_QAM-16 offers the least bit-rate of 350 Mbps, which with clipping, increases to 420 Mbps. Unlike for the 60 m SI-POF with the LD setup, the Volterra equalisers significantly improves the bit-rate performance of the transversal equalisers with the RC-LED setup for the

SI-POF of the same length. And both equalisers show PAM offers the highest bit rate followed by CAP-16, bit-loaded DMT and DMT_QAM-16. This shows that the effect of non-linearity is very significant for the 60 m SI-POF with the RC-LED setup. To further confirm the non-linearity of the POF system, PAM-4 offers a bit-rate of 700 Mbps with the MLP equaliser, and the bit-rate is much higher than 490 Mbps from the transversal equaliser: which translates to a $\sim$43% bit-rate increase. CAP-16 with the MLP equaliser follows PAM-4 offering a bit-rate of 480 Mbps. The same NLEs employed for the 60 m SI-POF in Fig. 6.4b are also the best NLEs for the 60 m SI-POF. Thus, the NLEs are used with their corresponding modulation formats for Fig. 6.5b. The bit rates achieved for the 60 m SI-POF at a BER of $\simeq 10^{-6}\{10^{-3}\}$ are $\sim$530$\{$700$\}$ Mbps, $\sim$330$\{$480$\}$ Mbps, $\sim$290$\{$420$\}$ Mbps and $\sim$320$\{$480$\}$ Mbps with PAM-4, CAP-16, DMT_QAM-16 and bit-loaded DMT respectively. The BER plots in Fig. 6.5b confirms that the PAM-4 with the MLPDFE offers the best BER performance for the 60 m SI-POF. The modulation schemes that follow this successively are the bit-loaded DMT with the FD Volterra equaliser, CAP-16 with the SC-MLPDFE and DMT_QAM-16 with the FD Volterra equaliser. It is noticed that CAP-16 and the bit-loaded DMT offer a similar BER performance at bit-rates below $\sim$450 Mbps. But at bit-rates above this value, the bit-loaded DMT offers a superior BER performance than CAP-16.

| **Modulation** | **RC-LED setup** | **LD setup** | | |
|---|---|---|---|---|
| | **60 m** | **60 m** | **30 m** | **10 m** |
| PAM-$M$ | 0.77 | 3.1 | 7.2 | 10.5 |
| CAP-$M^2$ | 0.53 | 2 | 5.6 | 10.2 |
| DMT_QAM-$M^2$ | 0.46 | 2 | 5.7 | 10.3 |
| Bit-loaded DMT | 0.58 | 2.9 | 7.3 | 12 |

**Table 6.1:** *Maximum data rates (in Gbps) obtained at 7% FEC limit (BER $\approx 3.8 \times 10^{-3}$) for the various modulation schemes for different SI-POF lengths with the NLEs. The results are obtained by using the RC-LED setup and the LD setup with a fibre-coupled power of 1 mW and 6.5 mW, respectively: $\eta_{mod} = 0.85$.*

The highest bit rate achieved at the 7% FEC limit is summarized in Table 6.1 for the different POF lengths. With the LD setup, the maximum bit rates for 60 m, 30 m and 10 m are 3.1 Gbps, 7.2 Gbps and 12 Gbps, respectively. This is obtained with the PAM-4, bit-loaded DMT and bit-loaded DMT, respectively. Consequently, $\eta_b$ for this FEC limit becomes 62, 72 and 48 bps/Hz for 60 m, 30 m and 10 m SI-POF, respectively.

The SI-POF with lengths shorter than 30 m has considerable SNR, and they also have a fre-

quency response profile that depicts the channel has benign conditions, as illustrated in Fig. 5.3. So, high-level modulation formats are used at these lengths of SI-POF. In this scenario, the bit-loaded DMT offers the highest bit rate compared to the other modulation schemes; the bit-loaded DMT is followed with the PAM-$M$, CAP-$M^2$ and DMT_QAM-$M^2$. At longer SI-POF lengths, the SNR is much lower, and the channel has malignant conditions. Thus, low-level modulation formats are selected for these lengths of SI-POF. With this setting, PAM-$M$ offers the highest bit rate compared to the other modulation schemes; this is followed with the bit-loaded DMT, CAP-$M^2$ and DMT_QAM-$M^2$. For 10 m and 30 m SI-POF lengths. It is observed that the bit-loaded DMT competes with PAM-$M$ as they have comparable bit rates, while CAP-$M^2$ competes with DMT_QAM-$M^2$.

## 6.2 Transmitted Electrical Power

The electrical power consumption is another metric used to gauge the performance SI-POF system with the NLEs. As mentioned in Section 1.4, the significant components that consume power in the SI-POF are the optical transmitter, the optical receiver and the digital signal processor (DSP). The DSP comprise the NLE and the modulation process, but it has been shown that an NLE algorithm takes most of the power from the DSP with PAM transmission due to its high complexity [84]. The power consumed by the NLE is related to its complexity, and it can be measured with an FPGA [50, 84]. Thus, the computational complexity of the NLE is a good measure of DSP power consumption. The power consumed by the receiver depends mostly on its circuit design.

The electrical power consumed by the optical source is from the DC-bias current ($I'_{bias}$) and the modulation index ($\eta_{mod}$) of the signal. We can relate $\eta_{mod}$ more closely to the mean transmitted electrical power as [84]:

$$P_{txelect} = \frac{(\eta_{mod} I'_{bias})^2 R_{txeq}}{\rho_{papr}}, \tag{6.1}$$

where $\rho_{papr}$ denotes the PAPR of the signal (see Eq. (3.2)), while $R_{txeq}$ denotes the equivalent impedance of the transmitter circuit and it is assumed as 50 $\Omega$ in this study.

The measured values of $\rho_{papr}$ (in dB) for the three modulation formats are shown in Table 6.2. The values of $\rho_{papr}$ for the modulation schemes are obtained with the parameters higlighted in Table 6.2 for $N_{sps} = 4$. Also, $\rho_{papr}$ is measured at a complementary cumulative distribution function (CCDF) of $10^{-5}$. The values obtained here are similar to those specified in [131]

| $M$ | 2 | 4 | 8 | 16 |
|---|---|---|---|---|
| $\rho_{papr}$ [dB] for PAM-$M$ | 3.62 | 6.14 | 7.20 | 7.70 |
| $\rho_{papr}$ [dB] for CAP-$M^2$ | 6.32 | 8.78 | 9.78 | 10.19 |
| $\rho_{papr}$ [dB] for DMT | 15.61 | | | |
| $P_{txelect}$ [dBm] for PAM-$M$ | 0.02 | -2.50 | -3.56 | -4.06 |
| $P_{txelect}$ [dBm] for CAP-$M^2$ | -2.68 | -5.14 | -6.14 | -6.55 |
| $P_{txelect}$ [dBm] for DMT | -11.97 | | | |

**Table 6.2:** *$P_{txelect}$ and $\rho_{papr}$ of the modulation formats at $\eta_{mod}$ = 0.85 for the LD.*

and they show that the PAPR of CAP-$M^2$ is about 2.5 dB more than that of PAM-$M$. It is also shown in Table 6.2 that the PAPR for DMT is constant at $\sim$15.61 dB irrespective of the constellation size $M$. The value of $P_{txelect}$ reduces for increasing values of $M$ as shown in Table 6.2. It should be noted that for similar values of $\eta_{mod}$ and $M$, the value of $P_{txelect}$ for PAM is greater than that of CAP by $\sim$2.5 dB.

In Fig. 6.6, the BER result for the modulation formats is measured as a function of the average transmitted electrical power $P_{txelect}$ for different SI-POF lengths. The results are obtained with the NLEs that offer the best bit-rate performance, as discussed in the previous section. Notably, the mean optical power $P_{oavg}$ is kept constant at 6.5 mW for the LD setup irrespective of the value of $P_{txelect}$. Likewise, $P_{oavg}$ is 1 mW for the RC-LED setup. Also, the non-linearity of the system is dependent on $P_{txelect}$ because it depends on $\eta_{mod}$, which in turn depends on $THD$ as Fig. 3.15a shows. For all the SI-POF lengths, it is observed that DMT with bit/power loading is the most power-efficient approach. With equalisation, DMT_QAM-$M^2$ and PAM-$M$ require identical electrical power while CAP-$M^2$ is the least power-efficient method.

The results in Fig. 6.6a are obtained for 8 Gbps transmission via the 10 m SI-POF with the LD setup. The values of $P_{txelect}$ obtained at a BER $\simeq 10^{-3}$ are $\sim$-17.5 dBm, $\sim$-13 dBm, $\sim$-19 dBm and $\sim$-23.5 dBm with PAM-16, CAP-256, DMT_QAM-256 and bit-loaded DMT, respectively. This implies that while CAP-256 requires the highest electrical power, PAM-16 needs 4.5 dB less power than CAP-256, DMT_QAM-256 requires 1.5 dB less electrical power than PAM-16, and the bit-loaded DMT requires 4.5 dB less power than DMT_QAM-256. A similar pattern is observed for the 30 m SI-POF with 4 Gbps transmission as shown in Fig. 6.6b. The values of $P_{txelect}$ obtained at a BER $\simeq 10^{-3}$ are $\sim$-16.5 dBm, $\sim$-12 dBm, $\sim$-17.5 dBm and $\sim$-22 dBm with PAM-8, CAP-64, DMT_QAM-64 and bit-loaded DMT, respectively. It is noticed that $P_{txelect}$ for PAM, CAP and DMT increases by less than 1.5 dB for 30 m length compared to the 10 m.

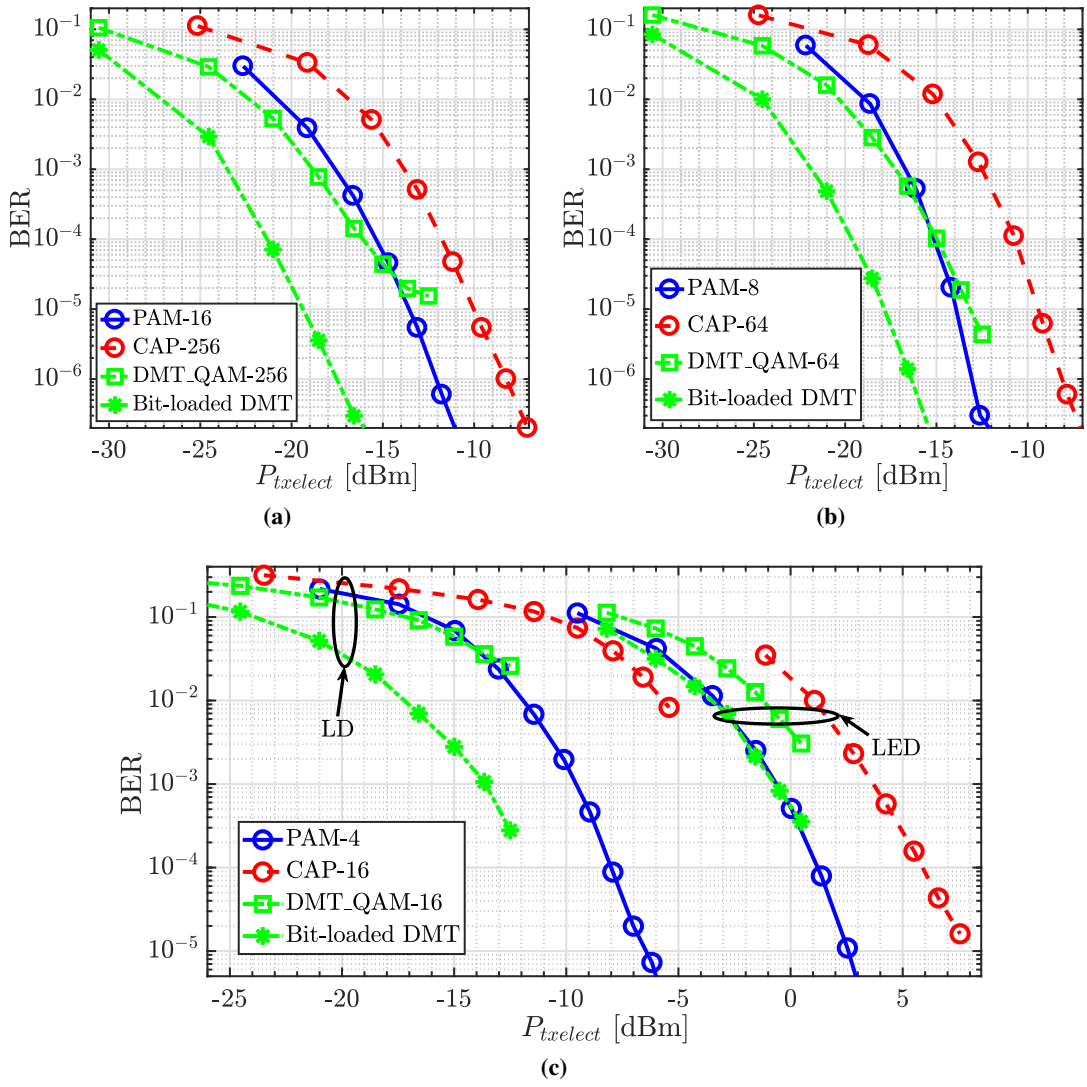


**Figure 6.6:** *The measured BER versus the mean transmitted electrical power ($P_{txelect}$) for comparing the performance of the modulation schemes at: (a) 8 Gbps over 10 m SI-POF with LD (b) 4 Gbps over 30 m SI-POF with LD (c) 2 Gbps with LD and 400 Mbps with RC-LED over 60 m SI-POF. The expression for $P_{txelect}$ can be found in (6.1).*

The BER plots for the 60 m SI-POF are depicted in Fig. 6.6c for the modulation schemes using the LD setup. A set of the BER plots is from the LD setup, where the plots are obtained at a bit rate of 2 Gbps. The values of $P_{txelect}$ at a BER $\simeq 10^{-3}$ for PAM-4 and the bit-loaded DMT are $\sim$-9.5 dBm and $\sim$-13.5 dBm, respectively. This translates to a 4 dB gain with the bit-loaded DMT compared to PAM-4 for the 60 m SI-POF. The other set is from the RC-LED setup, and the plots are obtained at a bit rate of 400 Mbps. Compared to the LD setup, whose values of $P_{txelect}$ are less than -6 dBm with PAM, the values of $P_{txelect}$ are more than -5 dBm. The RC-LED setup requires more transmit power than that of the LD setup because the former has its $I'_{bias}$ as $\sim$30 mA, which is above the value of $I'_{bias}$ of $\sim$8 mA from the LD setup. The values of $P_{txelect}$ obtained at a BER $\simeq 10^{-3}$ are $\sim$-0.5 dBm, $\sim$3.5 dBm, $\sim$1.5 dBm and $\sim$-0.5 dBm with PAM-4, CAP-16, DMT_QAM-16 and bit-loaded DMT, respectively. The results suggest that CAP-16 requires the highest electrical power, both PAM-4 and the bit-loaded DMT requires 4 dB less power than CAP-16, and DMT_QAM-16 requires 2 dB less electrical power than PAM-4.

## 6.3 Computational Complexity

The computational complexity of the modulation formats with their respective NLEs (that offer the best bit-rate performance) are evaluated with the RNRM per bit that is denoted as $\mathfrak{R}_{bit}$: which is the ratio of the RNRM per symbol/block/frames to the number of bits per symbol/block/frames. The RNRM per bit comprises of the RNRM for modulation as well as that for equalisation. Furthermore, we will not consider the contribution of the equaliser training algorithm to the RNRM per bit for the NLEs since the overhead data is used for this. Another reason is that the process of the LMBP (and RBP) training algorithm for MLPDFE (and SCMLP-DFE) is different from the RLS training algorithm for the FD Volterra equaliser.

For PAM-$M$, the RNRM required for both modulate and demodulate a symbol comes from the pulse-shape filtering and the matched filtering, respectively. The RNRM for a PAM symbol that uses the RRC pulse-shape filter with span $G_s$ and upsampling factor $N_{sps}$ is $N_{sps}G_s$. It is much simpler PAM modulation with rectangular pulse-shape filter (NRZ or RZ) requires no multiplications but a repetition of the PAM symbol $N_{sps}$ times. However, the RRC pulse-shape filter is more resilient to channel ISI than the rectangular pulse-shape filter. If the received signal is downsampled from the matched filter to get one sample per symbol, then the RNRM required per PAM symbol from the RRC matched filter is also $N_{sps}G_s$. The total RNRM

per PAM symbol for both modulation and demodulation is $2N_{sps}G_s$. As a PAM-$M$ symbol contains $\log_2(M)$ bits, $\mathfrak{R}_{bit} = \frac{2N_{sps}G_s}{\log_2(M)}$. The RNRM required to implement the MLPDFE (with three layers) for a PAM symbol is approximately equal to the number of synaptic weights of the equaliser, and it is $W_{mlp} = N_{hn}(N_{ft} + N_{bt} + 1)$. For high values of $N_{ft}$ ($> 8$), the equaliser can be efficiently implemented in the FD with FFT by the factor $\mathcal{R}_{\frac{fd}{td}} < 1$, which was discussed and obtained in Section 5.4. Hence, the RNRM per bit for the equaliser is $\frac{\mathcal{R}_{\frac{fd}{td}} W_{mlp}}{\log_2(M)}$.

For CAP-$M^2$, the RNRM required for both modulate and demodulate a symbol comes from the pulse-shape filtering and the matched filtering, respectively. CAP requires four FIR filters in its transceiver, a pair for pulse-shaping at the transmitter and another pair for matched filtering at the receiver [143]. If the same sampling rate $F_s$ and bit-rate $R_b$ for PAM-$M$ is used for CAP-$M^2$, the upsampling factor for the latter modulation format becomes $2N_{sps}$. Hence, the total RNRM per CAP symbol for both modulation and demodulation is $8N_{sps}G_s$. As a CAP-$M^2$ symbol contains $2\log_2(M)$ bits, $\mathfrak{R}_{bit} = \frac{4N_{sps}G_s}{\log_2(M)}$. The RNRM required to implement the SC-MLPDFE (with three layers) for a CAP symbol is twice that of the MLPDFE for the PAM symbol (i.e. $2W_{mlp}$ ). The SC-MLPDFE can also be efficiently implemented in the FD with FFT by $\mathcal{R}_{\frac{fd}{td}}$, which was discussed and obtained in Section 5.4. Hence, the RNRM per bit for the equaliser is also $\frac{\mathcal{R}_{\frac{fd}{td}} W_{mlp}}{\log_2(M)}$.

For DMT, an IFFT/ FFT operation is used to modulate/demodulate a block of bits. An FFT (or an IFFT) of size $N_{FFT}$ requires $0.5N_{FFT}(\log_2 N_{FFT} - 3) + 2$ real-valued multiplications, if the inputs to or the outputs of the FFT/IFFT operation are real-valued. And this is the case for DMT transmission over the SI-POF. The FFT operation is realised with the split-radix algorithm to obtain this number of multiplications. Hence, the total RNRM per DMT symbol for both modulation and demodulation is $N_{FFT}(\log_2 N_{FFT} - 3) + 4$. We also need to consider the number of real-valued multiplications used for the FD Volterra equaliser. As mentioned in Section 5.4, the equaliser requires $\alpha_2 N_{FFT}$ multiplications in TD to calculate $\alpha_2$ Volterra inputs. Each of the Volterra inputs is converted to the FD with an FFT operation, and this implies $0.5\alpha_2 N_{FFT}(\log_2 N_{FFT} - 3) + 2$ real-valued multiplications. For each sub-carriers in the FD, there is one tap from the linear input and $\alpha_2$ taps from the Volterra inputs; this translates to $\alpha_2 + 1$ complex-valued multiplications per sub-carrier. Assuming that the complex-valued multiplications are implemented with four real-valued multiplications, the FD operation will require $4N_{dsub}(\alpha_2 + 1)$. In total, the FD Volterra equaliser uses $0.5\alpha_2 \left[N_{FFT}(\log_2 N_{FFT} - 1) + 4\right] + 4N_{dsub}(\alpha_2 + 1)$. To obtain the RNRM per bit for the

DMT modulation and the FD Volterra equaliser, we use the number of bits in a DMT symbol $N_{bdmt}$ expressed in Eq. (5.24) for a given $F_s$ and $R_b$.

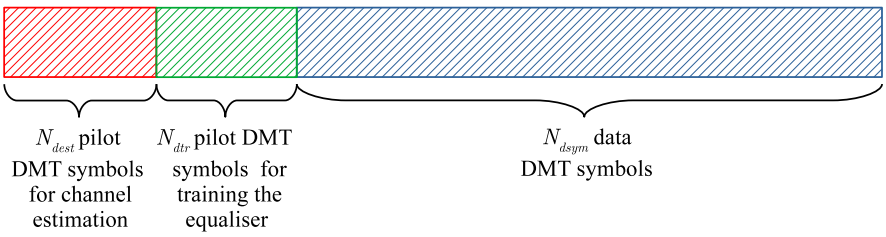


**Figure 6.7:** *An illustration of the DMT signal frame*

Unlike PAM and CAP, DMT modulation includes channel estimation, power-loading and bit-loading, and these have some computational requirement. The channel estimation process requires the use of overhead pilot DMT symbols. Hence, let us define a DMT frame as a cluster of $N_{dsym}$ data DMT symbols, $N_{dtr}$ pilot symbols for training the equaliser and $N_{dest}$ pilot symbols for channel estimation, as illustrated in Fig. 6.7. Since the SI-POF slowly changes, the ratio of the pilot symbols to the data symbols is usually negligible ($< 4\%$), which implies an insignificant reduction in bit-rate. The RNRM per bit, in this case, is defined as the ratio of the RNRM per DMT frame to the number of data bits in the DMT frame. For channel estimation, power-loading and bit-loading, the RNRM is presented in Table. 6.3 for a DMT frame. The number of bits in the DMT frame is denoted as $N_{dbit}$ and $N_{dsym} = \lceil \frac{N_{dbit}}{N_{bdmt}} \rceil$.

The RNRM per bit of the modulation formats and their NLEs are summarised and compared in Table 6.4 for similar values of $F_s$ and $R_b$. It shows that though the CAP-$M^2$ format demands twice as much RNRM compared to PAM-$M$, their equalisers offer the same RNRM. The RNRM that is presented in Table 6.4 is used to fairly evaluate the computational complexity of the modulation formats with their NLEs. The analysis is done for 8 Gbps over 10 m SI-POF and 4 Gbps over 30 m SI-POF for the LD setup, while for the RC-LED setup, it is considered for 0.3 Gbps over 60 m SI-POF. These bit-rates are selected for their corresponding SI-POF setups as error-free transmission (BER$\simeq 10^{-6}$) is achieved at these bit rates with the modulation formats and their NLES. Table 6.4 shows that the RNRM for PAM and CAP is dependent on the upsampling factor $N_{sps}$. By using Eq. (4.6) for the LD setup at $F_s$ = 4 Gsa/s, the $N_{sps}$ at 8 Gbps over the 10 m SI-POF with $M$ = 16 is two. Similarly, $N_{sps}$ at 4 Gbps over the 30 m SI-POF with $M$ = 8 is three. For the RC-LED setup at $F_s$ = 1 Gsa/s , the $N_{sps}$ at 0.3 Gbps over the 60 m SI-POF with $M$ = 4 is about seven.

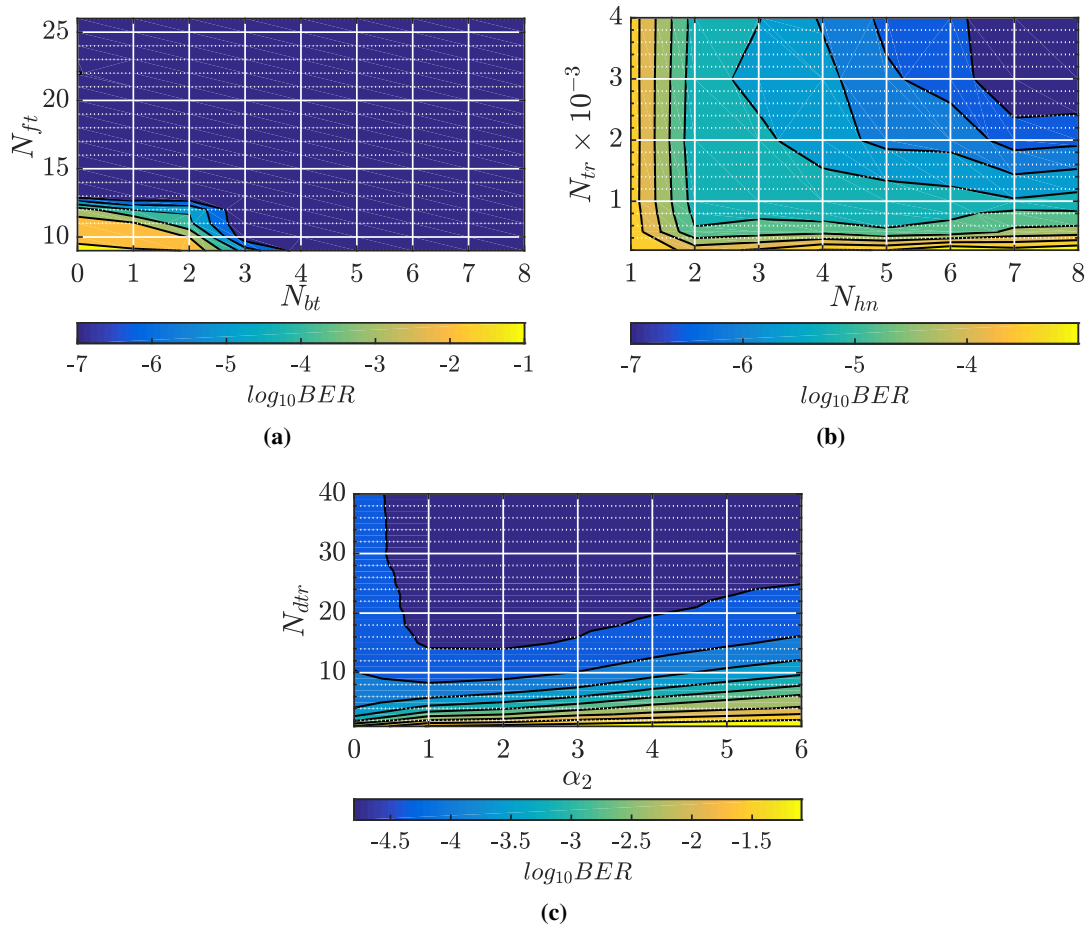


**Figure 6.8:** *BER contour plots at a bit rate of 8 Gbps over 10 m SI-POF to derive the optimal: (a) $N_{ft}$ and $N_{bt}$ for PAM-16 with MLPDFE ($N_{hn}$ = 8, $N_{tr}$ = 4000) (b) $N_{hn}$ and $N_{tr}$ for PAM-16 with MLPDFE ($N_{ft}$ = 14, $N_{bt}$ = 0) (c) $\alpha_2$ and $N_{dtr}$ for DMT_QAM-256 with FD-NLE*

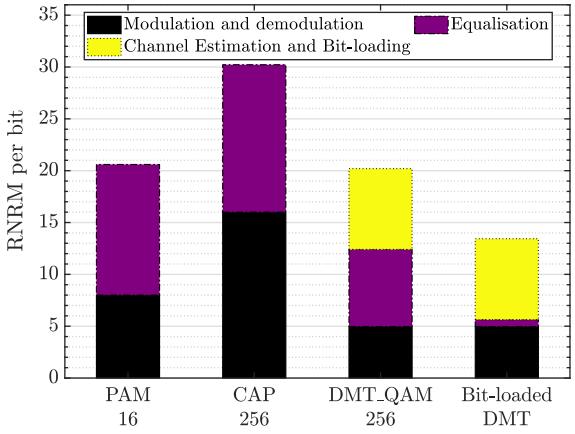


**(a)**

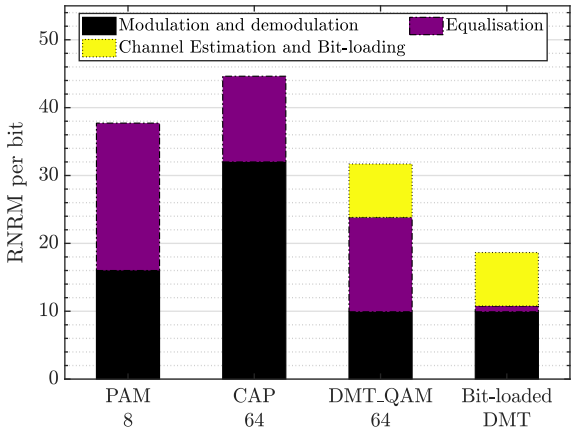


**(b)**

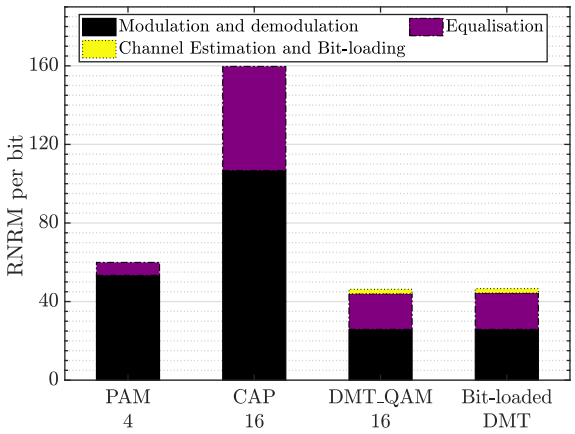


**(c)**

**Figure 6.9:** *RNRM per bit of the modulation schemes with their NLEs at a bit rate of: (a) 8 Gbps over 10 m SI-POF with LD (b) 4 Gbps over 30 m SI-POF with LD (b) 0.3 Gbps over 60 m SI-POF with RC-LED.*

| **Operation Category** | **RNRM Size of Operation** | **Number of Operations per DMT Frame** | **RNRM per DMT Frame** |
|---|---|---|---|
| FFT/IFFT modulation and demodulation of the pilot QPSK symbols | $N_{FFT}(\log_2 N_{FFT} -3)+4$ | $N_{dest}$ | $N_{dest}\,[N_{FFT}(\log_2 N_{FFT} -3)+4]$ |
| Magnitude and phase estimation of the received QPSK symbols with the RLS algorithm | $10(N_{FFT}-2)$ | | $10N_{dest}(N_{FFT}-2)$ |
| Normalisation of the received QPSK symbols | $2(N_{FFT}-2)$ | | $2N_{dest}(N_{FFT}-2)$ |
| Calculation of EVM/SNR per sub-carrier using the received QPSK symbols | $2N_{dest}$ | $0.5N_{FFT}-1$ | $N_{dest}(N_{FFT}-2)$ |
| Total RNRM per DMT frame for channel estimation | $N_{dest}\,[N_{FFT}(\log_2 N_{FFT}+10)-22]$ | | |
| Bit-loading | 1 | $N_{bdmt}$ | $N_{bdmt}$ |
| Power-loading | $2N_{dsub}$ | $N_{dsym}$ | $2N_{dsub}N_{dsym}$ |

**Table 6.3:** *RNRM required for channel state estimation, bit-loading and power-loading*

For a fair comparison of the RNRM of the NLEs, it is important to determine their optimum parameters. For MLPDFE and SCMLP-DFE, these are $N_{ft}$, $N_{bt}$, $N_{hn}$ and $N_{tr}$. For FD-NLE, they are $\alpha_2$ and $N_{dtr}$. The optimal values are obtained by an extensive search of the minimum parameters that offers a comparable BER result to those shown in Section. 6.1. An illustration of this for 8 Gbps over 10 m SI-POF is shown in Fig. 6.8 that displays the BER contour plots for the parameters of the equaliser that require optimisation.

The result of the contour plots is summarised in Table 6.5. For 4 Gbps over 30 m with the LD setup, it is observed that the optimum equaliser parameters for PAM-8 and CAP-64 are comparable. But for 8 Gbps over 10 m, the SCMLP-DFE for CAP-256 requires about 1.5 times as much taps than MLPDFE for PAM-16. This can be attributed to the lower upsampling factor of $2N_{sps} = 4$ for CAP-256 at 10 m – which is lower than the upsampling factor of 6 for CAP-64 at 30 m. To confirm this prediction, the RC-LED setup of 0.3 Gbps over 60 m with CAP-16 has an upsampling factor of about 13: and the number of taps for PAM-4 and CAP-16 are comparable as well. Also, the SCMLP-DFE requires 1000 more training symbols than MLPDFE, which shows the advantage of the convergence of the LMBP training algorithm for the second equaliser. There is a little prediction on how the optimal number of hidden layer neurons is related to the modulation formats since it depends on the training algorithm used and

| **Modulation Format** | **Operation Category** | **RNRM per bit** |
|---|---|---|
| PAM-$M$ | Modulation and demodulation with the RRC filter | $\frac{2N_{sps}G_s}{\log_2 M}$ |
| | Equalisation with MLPDFE (in FD) | $\frac{\mathcal{R}_{\frac{fd}{td}} W_{mlp}}{\log_2 M}$ |
| CAP-$M^2$ | Modulation and demodulation with the I/Q RRC filter | $\frac{4N_{sps}G_s}{\log_2 M}$ |
| | Equalisation with SCMLP-DFE (in FD) | $\frac{\mathcal{R}_{\frac{fd}{td}} W_{mlp}}{\log_2 M}$ |
| DMT | Modulation and demodulation with FFT (split-radix) | $\frac{N_{FFT}(\log_2 N_{FFT}-3)+4}{N_{bdmt}}$ |
| | Channel Estimation | $\frac{N_{dest}[N_{FFT}(\log_2 N_{FFT}+10)-22]}{N_{dbit}}$ |
| | Bit and power loading | $\frac{N_{bdmt}}{N_{dbit}} + \frac{2N_{dsub}}{N_{bdmt}}$ |
| | Equalisation with FD-NLE | $\frac{0.5\alpha_2[N_{FFT}(\log_2 N_{FFT}-1)+4]+4N_{dsub}(\alpha_2+1)}{N_{bdmt}}$ |

– Only the number of multiplications are considered here. Other DSP and arithmetic operations are ignored.
– The RNRM parameters for PAM-$M$ and CAP-$M^2$ are derived from [43, 95, 143]. $N_{sps}$ is defined in Eq. (4.6).
– The RNRM parameters for DMT are derived from [56], [154], and [147]. $N_{bdmt}$ is defined in Eq. (5.24).
– The RNRM per frame is highlighted in Table 6.3 for channel estimation, bit-loading and power-loading.
– $N_{dbit}$ denotes the number of data bits per DMT frame. It is assumed here to be $10^6$: $N_{dsym} = \lceil \frac{N_{dbit}}{N_{bdmt}} \rceil$.

**Table 6.4:** *RNRM per bit of the modulation formats with their non-linear equalisers.*

| **MLP-DFE Parameters** | **0.3 Gbps over 60 m using the RC-LED setup with:** | | **4 Gbps over 30 m using the LD setup with:** | | **8 Gbps over 10 m using the LD setup with:** | |
|---|---|---|---|---|---|---|
| | **PAM-4** | **CAP-16** | **PAM-8** | **CAP-64** | **PAM-16** | **CAP-256** |
| $N_{ft}$ | 10 | 10 | 13 | 12 | 14 | 21 |
| $N_{bt}$ | 0 | 1 | 2 | 1 | 0 | 1 |
| $N_{hn}$ | 1 | 9 | 5 | 4 | 7 | 7 |
| $N_{tr}$ | 500 | 2000 | 3000 | 3000 | 3000 | 4000 |
| **FD-NLE Parameters** | **DMT_ QAM-16** | **Bit-loaded DMT** | **DMT_ QAM-64** | **Bit-loaded DMT** | **DMT_ QAM-256** | **Bit-loaded DMT** |
| $\alpha_2$ | 1 | 1 | 2 | 0 | 2 | 0 |
| $N_{dtr}$ | 32 | 32 | 36 | 4 | 30 | 5 |
| $N_{dsub}$ | 159 | 188 | 1376 | 1756 | 2064 | 2800 |

**Table 6.5:** *Equaliser's optimum parameters for the modulation formats*

the magnitude of the system non-linearities.

With the LD setup, the FD-NLE parameters in Table 6.5 show a higher value of $\alpha_2 = 2$ for DMT_QAM-$M^2$ compared to the value of $\alpha_2 = 0$ for bit-loaded DMT. Correspondingly, the value of $N_{dtr}$ for DMT_QAM-$M^2$ is significantly more than that of the bit-loaded DMT. This is because compared to the first DMT scheme, the latter one has a smaller constellation size per sub-carrier as Fig. 5.4 shows. This makes it more resilient to the system non-linearity. The RC-LED setup, with much higher non-linearity than the LD setup, presents a similar value of $\alpha_2 = 1$ for both DMT_QAM-$M^2$ and bit-loaded DMT.

With the values from Table 6.5 and the RNRM equations from Table 6.4, the RNRM per bit for 8 Gbps over 10 m SI-POF and 4 Gbps over 30 m SI-POF (with the LD setup) are depicted in Fig. 6.9a and Fig. 6.9b, respectively. The RNRM per bit is also depicted for 0.3 Gbps over 60 m SI-POF with the RC-LED setup in Fig. 6.9c. Generally, they show that the bit-loaded DMT requires the least computational complexity for the highly non-linear SI-POF system. The bit-loaded DMT is in turn followed by DMT_QAM-$M^2$, PAM-$M$ and CAP-$M^2$.

## 6.4 Summary

We have experimentally presented and compared the performance of the advanced modulation formats and their respective NLEs for high-speed communication through an SI-POF. Particularly, PAM-$M$ with the MLPDFE is compared to CAP-$M^2$ with the SCMLP-DFE and DMT with the FD Volterra equaliser. The experimental results show that for a transmission distance less than 30 m over SI-POF, DMT with bit-loading offers higher data rates than PAM, especially for a highly non-linear system. However, for SI-POF transmission over lengths longer than 30 m, where the bandwidth is limited to less than 100 MHz, PAM can achieve more bit rates than DMT due to the advantage of its lower PAPR. At the same POF length and bit rate, DMT with bit-loading requires the least electrical transmit power and computational complexity (per bit) of the techniques considered. Therefore, this study has shown that bit-loaded DMT and PAM are viable for high-speed transmission over a non-linear IM/DD SI-POF system. Using the LD setup, this chapter reports at the 7% FEC limit bit-rates of 12 Gbps (with bit-loaded DMT), 7.3 Gbps (with bit-loaded DMT) and 3.1 Gbps (with PAM-4) at SI-POF of lengths 10 m, 30 m and 60 m, respectively. Similarly, with the LD setup, the chapter reports a bit-rate of 770 Mbps transmission over a 60 m SI-POF.

# Chapter 7
# Conclusion and Future Works

In this thesis, three non-linear equalisers (NLEs) used with advanced modulation formats have been investigated for high-speed SI-POF systems. The NLEs considered in this study are the transversal decision feedback equalisers (TRDFE), Volterra DFE, and the multilayer perceptron based equaliser/DFE (MLPDFE). The concepts of Volterra DFE and the MLPDFE have been studied in more detail compared to what is already available in the literature. Some of the existing issues with these NLE schemes have been identified, and suitable solutions have been suggested. The work has led to improved high-speed communication over an SI-POF system for which suitable theoretical, simulation and experimental analysis has been presented. The non-linear distortion in the optical system has been analysed from a new point of view, and the existing analytical concepts have been further extended. The work concludes with experimental comparisons of modulation format with their best NLEs for SI-POF systems.

## 7.1 Summary and Achievements

The first chapter goes through the background knowledge about the need for SI-POF links in applications like SOHO, automotive and industrial networks. Many thesis objectives were defined in this chapter, but the main one was to implement the three NLEs for an SI-POF link in order to achieve these following minimum target criteria that can satisfy a typical SOHO network within the next decade:

- A bit-rate of 500 Mbps
- An SI-POF length of 50 m
- Maximum BER of $3.8 \times 10^{-3}$
- An optical transmit power of 1 mW as it is the eye-safety and consumer-friendly power level [34]

The study presents a bit-rate of 780 Mbps over a 60 m SI-POF link with an eye-safe RC-LED to achieve the objectives mentioned above. To the best of the author's knowledge, the link is the first to be implemented with pulse amplitude modulation scheme and a machine learning equaliser. With additional work on real-time implementation, this can become a low-cost SI-POF link for the next-generation SOHO or automotive network. Hence, the aim of the thesis has been achieved based on implementing a high-speed SI-POF system with an NLE.

In the second chapter, the history of POF communication since the past six decades has been discussed, and the two different materials have used for POFs' fabrication are polymethylacrylate and fluorinated polymers. The POF from the first material is cheaper but has higher attenuation and lower bandwidth than that from the latter material. Polymethylacrylate is the vital material in the fabrication of SI-POF due to its low cost. The features of SI-POF systems, which include the optical sources and receivers, are discussed. Also, the linear and non-linear distortions in these systems are briefly mentioned. The chapter then presents a background of the three the NLEs, which are the TRDFE, the Volterra-based equaliser/DFE and the ANN-based equaliser/DFE. The state-of-the-art for high-speed communication over SI-POF systems since the past decade has been highlighted in this chapter. An analysis of the state-of-the-art indicates the use of the advanced modulation formats (like PAM, CAP and DMT) with equalisation schemes for high-speed SI-POF communication. The common NLEs for SI-POF systems is the TRDFE for PAM and CAP schemes and the conventional single-tap FD equaliser for DMT. However, there has been little to no work on the other NLEs for SI-POF systems. The review of the state-of-the-art reports a maximum bit-rate length product of 125 Gbps.m for real-time systems with PAM-2 and an analogue equaliser, 500 Gbps.m for offline systems with CAP-16 and the TRDFE, and 1089 Gbps.m for WDM systems with DMT and bit-loading.

The IM/DD scheme is commonly used for short-range optical communication systems (like SI-POF) because it is less costly than coherent detection. In the third chapter, the IM/DD model for the SI-POF was developed based on the studies done in [50, 84]. The model comprises the different estimations of the frequency response of the SI-POF, and they are the Gaussian, the first-order Butterworth and the power-flow models. The SNR of the IM/DD systems is also presented in this chapter. With the SNR and the frequency response models, the capacity of an SI-POF system was derived. The capacity results not only confirm the observations from studies in [50] and [84], but also adds to them by considering the bit-rate length product of the SI-POF system. The results prove that the bit-rate length product of the SI-POF channel

can be maximised by selecting an optimum length, provided there is a band-limitation from the optical source and receiver. The chapter also presents two experimental SI-POF systems: one uses an LD transmitter with a 1 GHz receiver, while the other uses an RC-LED transmitter with a 150 MHz receiver. Using the IM/DD model, the optimum fibre length {and maximum bit-rate length product } of the SI-POF channel is 30 m {$\sim$270 Gbps.m} and 60 m {$\sim$96 Gbps.m} from the LD setup and the RC-LED setup, respectively. The total harmonic distortion (THD) is used to measure the non-linearities of these setups based on their DC bias current and their modulation index. For the LD setup, there is an optimal bias current that minimises the non-linearity of the SI-POF system. For the RC-LED setup, the non-linearity is slightly constant irrespective of the bias current. The THD from the RC-LED setup is $\sim$8 dB higher than that from the LD setup at a fundamental frequency of 5 MHz. For the RC-LED setup, the second-order harmonic distortion significantly dominates the system non-linearities compared to the third-order harmonic distortion by at least a gain of $\sim$20 dB.

The fourth chapter presented the performance of the NLEs the SI-POF systems. The NLEs are implemented in the time-domain (TD), and they are compared with the use of single-carrier modulation (SCM) schemes (like PAM and CAP). The LD setup is estimated with a non-linear model, which is validated in the experiment. With the non-linear model, a set of extensive simulations is used to evaluate the performance of the NLEs. From all investigated scenarios, the MLP equalisers offer the best performance, especially for systems with high non-linear distortion and with high-level modulation formats. The Volterra equaliser and the transversal equaliser follows this. A complexity comparison of the NLEs was also explored in this chapter, and it suggests that The MLP equaliser require lesser computational order than the second-order Volterra equaliser if the number of hidden-layer neurons from the first equaliser is less than its number of taps. Both the LD and RC-LED setups are used to evaluate the performance of the NLEs. At a BER of $10^{-3}$, the bit-rate achieved for the LD setup is 10 Gbps, 6.8 Gbps and 2.92 Gbps for SI-POFs of 10 m, 30 m and 60 m length, respectively. Thus, the maximum bit-rate length product with the LD setup is 204 Gbps.m with a 30 m SI-POF. The RS-FEC code is used to achieve an error-free transmission for the 30 m SI-POF at a bit rate of 6.21 Gbps. For the RC-LED setup, a maximum bit rate of 780 Mbps was obtained via a 60 m SI-POF. The MLP equaliser was used to get the highest bit-rates for all the experimental setups.

The fifth chapter presented an efficient implementation of the NLEs by their conversion from TD to FD to reduce their computational complexities. The FD based NLEs involve the use of

efficient FFT algorithms. The cyclic-prefix method is employed for the FD-NLE with DMT. And the overlap-save method is used for the FD equaliser with both PAM and CAP. A comparison study between the FD-NLE and the conventional FD equaliser is presented for DMT signals with clipping. The comparison shows that the first equaliser offers a superior BER performance than the later for DMT signals with 10 dB clipping and with low-level modulation format ($M < 64$). The FD-NLE and the TD-NLE offer a similar BER performance for PAM and CAP transmission over the SI-POF. And the FD-NLE requires at most 40% of the real-valued multiplications required from the TD-NLE if the number of feedforward taps is more than 16.

The sixth chapter showed an experimental demonstration of high-speed SI-POF communication with the advanced modulation formats and their respective NLEs. The modulation formats considered in this study are PAM, CAP, DMT with only energy loading and DMT with both bit and energy loading. The modulation schemes with their NLEs were compared from their achievable bit-rates, their required transmitted electrical powers, and their computational complexities. The comparisons show that or a transmission distance less than 30 m over SI-POF, DMT with bit-loading offers higher data rates than PAM, mainly when the FD-NLE is used for a highly non-linear SI-POF system. However, for SI-POF transmission over lengths longer than 30 m, where the bandwidth is limited to less than 100 MHz, PAM can achieve more bit rates than DMT due to the advantage of its lower PAPR. At the same POF length and bit rate, DMT with bit-loading requires the least electrical transmit power and computational complexity (per bit) of the techniques considered. The chapter has therefore shown the viability of bit-loaded DMT and PAM for high-speed transmission over a non-linear IM/DD SI-POF system.

## 7.2 Limitations and Recommendations for Future Research

In this thesis, the use of NLEs with the advanced modulation formats have achieved outstanding results in terms of bit-rate and bit-rate length product. But the channel capacity calculations show that there is still enough space for performance improvement in terms of bit-rate-length product. The following presents the limitations and some ideas, with which the bit-rates can be improved.

- **Extensive investigation of ANN-based equalisers**: The MLP is one of the fundamental ANN structures for non-linear equalisation in digital systems. But other ANN equalisers

can be considered for equalisation, and they include the radial basis function and the functional link ANN [90,95]. For CAP/QAM schemes, there is also to need to investigate the performance of fully-complex valued ANN equaliser instead of the split-complex ANN equaliser employed in this study. This is because the first equaliser considers both the magnitude and phase of the complex-valued inputs, while the latter considers only the magnitude [97].

- **Improve the adaptivity or tracking feature of the NLEs**: In this work, the equalisers cannot adapt or track changes in the channel as it was assumed that the channel is entirely static. While this is mostly true for SI-POF links in SOHO environments, it is partly true for vehicular and industrial ones due to changes in temperature and vibration [34]. Future works can consider equalisers that do not just have the best convergence during training but also have the best tracking feature in those non-static channels.

- **Efficient implementation of the third-order Volterra equalisers**: This work suggests that the LD setup has a comparable second and third-order non-linearities. However, only the second-order Volterra equaliser was considered in this study. Extension of these equalisers to the third-order is an essential area of consideration for the LD-based SI-POF systems. Future works should also include an implementation of the third-order Volterra equalisers in the FD.

- **Variants of the advanced modulation formats**: There are variations of PAM, CAP and DMT schemes that can achieve even higher speeds in SI-POF systems. For instance, for PAM-2, it is the duo-binary PAM scheme [75]. There is an enhanced version of the CAP format, which was presented by Akande et al. in [155]. For DMT, it is the augmented spectrally-efficient (ASE) DMT presented by Islim et al. in [156]. These improved modulation formats can be used with the NLEs to achieved higher communication speeds.

- **Pre-coding schemes with the NLEs**: For the LED-based SI-POF systems, the feedback part of a DFEs at the receiver could be transferred as a pre-equaliser in the transmitter. A well-known implementation of the pre-equaliser for SCM schemes is the Tomlinson-Harashima precoding. It would be interesting to investigate the use of this pre-coder combined with either an ANN-based equaliser or a Volterra equaliser at the receiver.

- **Real-time implementation of SI-POF systems with the NLEs using an FPGA**: Field programmable gate array (FPGA) development is a promising area of research, and it has

been used as a means of achieving real-time implementation (RTI) of high-speed SI-POF systems. There have several works in the literature on the FPGA implementation of SI-POF systems [70–72] but these involve the use of the transversal DFE (TRDFE). This is because both Volterra and ANN equalisers demand more computational resources than the TRDFE, as discussed in this study. However, the FD implementation of the first two equalisers would make them more realisable with the FPGA. Using an FPGA will enable a thorough analysis of the various issues concerning the RTI of an SI-POF system with an NLE. It will also define the required hardware resources and the electrical power needed for this RTI. The electrical power measured from the FPGA will give a new perspective on the comparison of the modulation formats with their NLEs for an SI-POF system.

# References


[1] Cisco, *Cisco Visual Networking Index: Global Mobile Data Traffic Forecast Update, 2017–2022. URL: https://www.cisco.com/c/dam/m/en_us/solutions/service-provider/vni-forecast-highlights/pdf/Global_Network_Connections.pdf* , 2019 (accessed September 30, 2019).

[2] W. Lemstra, "Wi-Fi the Next Decade," *Available at SSRN 2585420*, 2015.

[3] P. A. Meshram, A. A. Deshmukh, and S. A. Khandekar, "Smart city with wi-max technology," *International Journal of Engineering, Economics and Management*, p. 1, 2015.

[4] M. Elkhodr, S. Shahrestani, and H. Cheung, "Emerging wireless technologies in the internet of things: a comparative study," *International Journal of Wireless and Mobile Networks*, 2016.

[5] M. Maier and M. Lévesque, "Dependable fibre-wireless (FiWi) access networks and their role in a sustainable third industrial revolution economy," *IEEE Transactions on Reliability*, vol. 63, no. 2, pp. 386–400, 2014.

[6] C. Lin, *Broadband Optical Access Networks and Fibre-to-the-Home*. Wiley Online Library, 2006.

[7] L. G. Kazovsky, N. Cheng, W.-T. Shaw, D. Gutierrez, and S.-W. Wong, *Broadband optical access networks*. Wiley Online Library, 2011.

[8] Smarthome news, *The Future and History of Smart Home - What Will Our Homes Be like in 2040. URL: https://www.smarthome.news/news/other - systems/the - future - of - smart - homes*, 2019 (accessed October 26, 2020).

[9] Futurithmic, *Future trends in the connected home. URL: https://www.futurithmic.com/2019/05/31/future - trends - in - connected - home/*, 2019 (accessed October 26, 2020).

[10] M. Boussard, D. Thai Bui, R. Douville, P. Justen, N. Le Sauze, P. Peloso, F. Vandeputte, and V. Verdot, "Future spaces: Reinventing the home network for better security and automation in the IoT era," *Sensors*, vol. 18, no. 9, p. 2986, 2018.

[11] Netflix, *Internet Connection Speed Recommendations. URL: https://help.netflix.com/en/*, (accessed October 26, 2020).

[12] Sky News, *Coronavirus: Working from home is here to stay - and it might do us all good. URL: https://news.sky.com/story/coronavirus - working - from - home - is - here - to - stay - and - it - might - do - us - all - good*, 2020 (accessed October 26, 2020).

[13] M. S. Ahsan, M. S. Lee, S. S. Newaz, and S. M. Asif, "Migration to the next generation optical access networks using hybrid WDM/TDM-PON," *Journal of Networks*, vol. 6, no. 1, p. 18, 2011.

[14] S. Bindhaiq, A. S. M. Supa, N. Zulkifli, A. B. Mohammad, R. Q. Shaddad, M. A. Elmagzoub, A. Faisal, *et al.*, "Recent development on time and wavelength-division multiplexed passive optical network (TWDM-PON) for next-generation passive optical network stage 2 (NG-PON2)," *Optical Switching and Networking*, vol. 15, pp. 53–66, 2015.

[15] A. Srivastava, "Next generation PON evolution," in *Broadband Access Communication Technologies VII*, vol. 8645, p. 864509, International Society for Optics and Photonics, 2013.

[16] Y. Luo, X. Zhou, F. Effenberger, X. Yan, G. Peng, Y. Qian, and Y. Ma, "Time- and wavelength-division multiplexed passive optical network (TWDM-PON) for next-generation PON stage 2 (NG-PON2)," *Journal of lightwave technology*, vol. 31, no. 4, pp. 587–593, 2012.

[17] Y. Luo, X. Yan, and F. Effenberger, "Next generation passive optical network offering 40Gb/s or more bandwidth," in *2012 Asia Communications and Photonics Conference (ACP)*, pp. 1–3, IEEE, 2012.

[18] R. A. Kumar, R. Murano, M. J. Cahill, J. M. Aufiero, and G. D. Bartolini, "Crosstalk performance analysis of low cost 8× 10 Gb/s tunable receiver for TWDM-PON," in *2013 Optical Fibre Communication Conference and Exposition and the National Fibre Optic Engineers Conference (OFC/NFOEC)*, pp. 1–3, IEEE, 2013.

[19] E. Wong, M. Mueller, and M. Amann, "Colourless operation of short-cavity VCSELs in C-minus band for TWDM-PONs," *Electronics Letters*, vol. 49, no. 4, pp. 282–284, 2013.

[20] Z. Xu, Y.-K. Yeo, X. Cheng, L. Zhou, and X. Shao, "Investigation of wavelength-tunable directly-modulated laser for 100-Gb/s EPON," in *National Fibre Optic Engineers Conference*, pp. NTh4F–4, Optical Society of America, 2013.

[21] Z. Li, L. Yi, Y. Zhang, Y. Dong, S. Xiao, and W. Hu, "Compatible TDM/WDM PON using a single tunable optical filter for both downstream wavelength selection and upstream wavelength generation," *IEEE Photonics Technology Letters*, vol. 24, no. 10, pp. 797–799, 2012.

[22] Z. Li, L. Yi, H. Ji, and W. Hu, "100-Gb/s TWDM-PON based on 10G optical devices," *Optics express*, vol. 24, no. 12, pp. 12941–12948, 2016.

[23] L. Yi, Z. Li, M. Bi, H. He, W. Wei, S. Xiao, and W. Hu, "Experimental demonstrations of symmetric 40-Gb/s TWDM-PON," in *2013 9th International Conference on Information, Communications & Signal Processing*, pp. 1–3, IEEE, 2013.

[24] L. Yi, Z. Li, M. Bi, W. Wei, and W. Hu, "Symmetric 40-Gb/s TWDM-PON with 39-dB power budget," *IEEE Photonics Technology Letters*, vol. 25, no. 7, pp. 644–647, 2013.

[25] M. Bi, S. Xiao, H. He, L. Yi, Z. Li, J. Li, X. Yang, and W. Hu, "Simultaneous DPSK demodulation and chirp management using delay interferometer in symmetric 40-Gb/s capability TWDM-PON system," *Optics express*, vol. 21, no. 14, pp. 16528–16535, 2013.

[26] M. Bi, S. Xiao, L. Yi, H. He, J. Li, X. Yang, and W. Hu, "Power budget improvement of symmetric 40-Gb/s DML-based TWDM-PON system," *Optics express*, vol. 22, no. 6, pp. 6925–6933, 2014.

[27] M. Fujiwara, R. Koma, K.-I. Suzuki, and A. Otaka, "Bidirectional EDFAs that support E2-class power budget of TWDM-PON without using gain-clamped light source," *Journal of Lightwave Technology*, vol. 34, no. 8, pp. 1997–2004, 2016.

[28] S. Yin, L. B. Du, C. DaSanti, X. Zhao, T. Zhang, A. Barratt, J. Jiang, and C. F. Lam, "Experimental Demonstration of Redundant Long-Reach PON," in *2018 European Conference on Optical Communication (ECOC)*, pp. 1–3, IEEE, 2018.

[29] S. Bindhaiq, N. Zulkifli, A. M. Supa'at, S. M. Idrus, and M. Salleh, "128 Gb/s TWDM PON system using dispersion-supported transmission method," *Optical Fibre Technology*, vol. 38, pp. 87–97, 2017.

[30] FTTH Council, *FTTH/B Global Ranking Sep 2018. URL: https://www.ftthcouncil.eu/documents/Reports/2019/FTTHB%20Ranking%20Sep%20 - 2018%20v2.pdf*, 2018 (accessed September 30, 2019).

[31] FTTH Council Middle East and North Africa, *FTTH MENA Fibreview 2018. URL: https://www.ftthcouncilmena.org/uploads/FTTH - MENA - Fibreview - 2018.pdf*, 2018 (accessed January 11, 2020).

[32] A. Koonen and E. Tangdiongga, "Photonic home area networks," *Journal of Lightwave Technology*, vol. 32, no. 4, pp. 591–604, 2014.

[33] O. Ziemann, J. Krauser, P. E. Zamzow, and W. Daum, *POF-polymer optical fibres for data communication*. Springer Science & Business Media, 2002.

[34] M. Atef and H. Zimmermann, *Optical Communication over Plastic Optical Fibres: Integrated Optical Receiver Technology*, vol. 172. Springer, 2012.

[35] O. Ciordia, C. Esteban, C. Pardo, and R. P. de Aranda, "Commercial silicon for gigabit communication over SI-POF," in *Proceedings of the 22nd International Conference on Plastic Optical Fibres, POF*, pp. 109–116, 2013.

[36] P. Kröplin, C. Dieling, M. Beckers, V. Schrank, M. Beer, T. Gries, G. Seide, and C.-A. Bunge, "Overview of the pof market," in *Polymer Optical Fibres*, pp. 349–400, Elsevier, 2017.

[37] AMSTechnologies, *Optical fibres broad range of waveguides for every application. URL: http://www.amstechnologies.com/fileadmin/amsmedia/AMS_Brochures_2018/Optical_Fibers_48-18-02.pdf*, 2018 (accessed September 01, 2020).

[38] Industrial Fibre Optics, *Optical Fibre and Cable. URL: https://i - fiberoptics.com/optical - fiber - selection.php*, (accessed September 01, 2020).

[39] Newport, *Single Mode Optical Fibres. URL: https://www.newport.com/c/optical - fibers*, (accessed September 01, 2020).

[40] Knowledge development for POF (KDPOF), *POF – Plastic Optical Fibre. URL: https://www.kdpof.com/plastic - optical - fiber - pof/* , (accessed October 27, 2020).

[41] Telefónica, *Telefónica revolutionizes the connectivity market with plastic fibre and 60GHz Wi-Fi. URL: https://www.telefonica.com/en/web/press-office/ - /telefonica - revolutionizes - the - connectivity - market - with - plastic - fibre - and - 60ghz - wi-fi*, 2017 (accessed January 11, 2020).

[42] CSI, *Nitto bullish as it enters plastic optical fibre business. URL: https://www.csimagazine.com/csi/Nitto - bullish - as - it - enters - plastic - optical -fibre - business.php*, 2017 (accessed January 11, 2020).

[43] J. G. Proakis and M. Salehi, *Digital communications*. McGraw-Hill, 2008.

[44] P. S. Diniz, *Adaptive Filtering: Algorithms and Practical Implementation, 4th Ed.* Springer, 2012.

[45] D. Falconer, S. L. Ariyavisitakul, A. Benyamin-Seeyar, and B. Eidson, "Frequency domain equalisation for single-carrier broadband wireless systems," *IEEE Communications Magazine*, vol. 40, no. 4, pp. 58–66, 2002.

[46] I. N. Osahon, S. Rajbhandari, and W. O. Popoola, "Performance comparison of equalisation techniques for SI-POF multi-gigabit communication with PAM-*M* and device non-linearities," *Journal of Lightwave Technology*, vol. 36, no. 11, pp. 2301–2308, 2018.

[47] I. N. Osahon, S. Rajbhandari, and W. O. Popoola, "SI-POF Transmission with CAP Modulation and Split-Complex MLP Equaliser," in *2018 IEEE International Conference on Communications (ICC)*, pp. 1–6, IEEE, 2018.

[48] I. N. Osahon, M. Safari, and W. O. Popoola, "10-Gb/s Transmission Over 10-m SI-POF With $M$-PAM and Multilayer Perceptron Equaliser," *IEEE Photonics Technology Letters*, vol. 30, no. 10, pp. 911–914, 2018.

[49] S. Randel and C.-A. Bunge, "Spectrally efficient polymer optical fibre transmission," in *Coherent Optical Communication: Components, Subsystems, and Systems*, vol. 7960, p. 79600M, International Society for Optics and Photonics, 2011.

[50] S. Lee, F. Breyer, D. Cardenas, S. Randel, and A. Koonen, "Real-time gigabit DMT transmission over plastic optical fibre," *Electronics letters*, vol. 45, no. 25, pp. 1342–1343, 2009.

[51] S. A. Cheema, M. Wolf, Ö. Tolay, and M. Haardt, "Efficient techniques for multi-gigabits/s transmission over plastic optical fibre," in *2015 17th International Conference on Transparent Optical Networks (ICTON)*, pp. 1–5, IEEE, 2015.

[52] D. Gloge, "Optical power flow in multimode fibres," *Bell System Technical Journal*, vol. 51, no. 8, pp. 1767–1783, 1972.

[53] J. Mateo, M. A. Losada, I. Garcés, and J. Zubia, "Global characterization of optical power propagation in step-index plastic optical fibres," *Optics express*, vol. 14, no. 20, pp. 9028–9035, 2006.

[54] J. Mateo, M. Losada, and J. Zubia, "Frequency response in step index plastic optical fibres obtained from the generalized power flow equation," *Optics Express*, vol. 17, no. 4, pp. 2850–2860, 2009.

[55] G. Stepniak, "Numerical modeling of transmission in step index polymer optical fibres using matrix exponential method," in *Photonics Applications in Astronomy, Communications, Industry, and High-Energy Physics Experiments 2018*, vol. 10808, p. 108080E, International Society for Optics and Photonics, 2018.

[56] G. Zhang, J. Zhang, X. Hong, and S. He, "Low-complexity frequency domain nonlinear compensation for OFDM based high-speed visible light communication systems with light emitting diodes," *Optics express*, vol. 25, no. 4, pp. 3780–3794, 2017.

[57] W. Daum, J. Krauser, P. Zamzow, and O. Ziemann, "POF Handbook: Optical short range transmission systems," 2008.

[58] Y. Koike, "High-bandwidth graded-index polymer optical fibre," *Polymer*, vol. 32, no. 10, pp. 1737–1745, 1991.

[59] Y. Koike, T. Ishigure, and E. Nihei, "High-bandwidth graded-index polymer optical fibre," *Journal of lightwave technology*, vol. 13, no. 7, pp. 1475–1489, 1995.

[60] Y. Koike and T. Ishigure, "Progress of low-loss GI polymer optical fibre from visible to 1.5-$\mu$m wavelength," in *IOOC-ECOC97. 11th International Conference on Integrated Optics and Optical Fibre Communications. 23rd European Conference on Optical Communications*, IET, 1997.

[61] G. Giaretta, M. Wegmueller, and R. Yelamarty, "11 Gb/sec data transmission through 100 m of perfluorinated graded-index polymer optical fibre," in *OFC/IOOC. Technical Digest. Optical Fibre Communication Conference, 1999, and the International Conference on Integrated Optics and Optical Fibre Communication*, pp. PD14–1, IEEE, 1999.

[62] M. A. Van Eijkelenborg, M. C. Large, A. Argyros, J. Zagari, S. Manos, N. A. Issa, I. Bassett, S. Fleming, R. C. McPhedran, C. M. de Sterke, *et al.*, "Microstructured polymer optical fibre," *Optics express*, vol. 9, no. 7, pp. 319–327, 2001.

[63] G. Surkova, R. Kruglov, R. Lwin, S. G. Leon-Saval, A. Argyros, H. Poisel, and A. Zadorin, "Multigigabit short-reach communication over microstructured polymer optical fibre," *Optical Fiber Technology*, vol. 34, pp. 65–69, 2017.

[64] H. Nakayama, T. Nakamura, M. Funada, Y. Ohashi, and M. Kato, "780nm VCSELs for home networks and printers," in *2004 Proceedings. 54th Electronic Components and Technology Conference (IEEE Cat. No. 04CH37546)*, vol. 2, pp. 1371–1375, IEEE, 2004.

[65] C. Pardo and R. P. de Aranda, "Demonstration of 1Gbps over 50m of low cost SI-POF with KDPOF technology," *Knowledge Development for POF*, 2010.

[66] R. P. de Aranda, O. Ciordia, and C. Pardo, "A standard for gigabit ethernet over POF. Product implementation," *POF'2011*, pp. 75–80, 2011.

[67] O. Sugihara, "Gigabit and Multi-Gigabit Data Transmission for Next-Generation Automotive Optical Network," in *2019 24th OptoElectronics and Communications Conference (OECC) and 2019 International Conference on Photonics in Switching and Computing (PSC)*, pp. 1–3, IEEE, 2019.

[68] G. Keiser, *Optical fibre communications*. McGraw-Hill, 2013.

[69] P. Polishuk, "Plastic optical fibres branch out," *IEEE communications Magazine*, vol. 44, no. 9, pp. 140–148, 2006.

[70] F. Breyer, S. J. Lee, D. Cardenas, S. Randel, and N. Hanik, "Real-time gigabit ethernet transmission over up to 25 m step-index polymer optical fibre using LEDs and FPGA-based signal processing," in *2009 35th European Conference on Optical Communication*, pp. 1–2, IEEE, 2009.

[71] C. Zerna, J. Sundermeyer, A. Fiederer, N. Verwaal, B. Offenbeck, and N. Weber, "Integrated PAM2 decision feedback equalizer for Gigabit Ethernet over standard SI-POF using red LED," in *36th European Conference and Exhibition on Optical Communication*, pp. 1–3, IEEE, 2010.

[72] A. Nespola, S. Straullu, P. Savio, D. Zeolla, J. C. R. Molina, S. Abrate, and R. Gaudino, "A new physical layer capable of record gigabit transmission over 1 mm step index polymer optical fibre," *Journal of Lightwave Technology*, vol. 28, no. 20, pp. 2944–2950, 2010.

[73] C. Gimeno, C. Sánchez-Azqueta, E. Guerrero, J. Aguirre, C. Aldea, and S. Celma, "Single-chip receiver for 1.25 Gb/s over 50-m SI-POF," *IEEE Photonics Technology Letters*, vol. 27, no. 11, pp. 1220–1223, 2015.

[74] D. Zeolla, A. Nespola, and R. Gaudino, "Comparison of different modulation formats for 1-Gb/s SI-POF transmission systems," *IEEE Photonics Technology Letters*, vol. 23, no. 14, pp. 950–952, 2011.

[75] D. Zeolla, A. Antonino, G. Bosco, and R. Gaudino, "DFE versus MLSE electronic equalisation for gigabit/s SI-POF transmission systems," *IEEE Photonics Technology Letters*, vol. 23, no. 8, pp. 510–512, 2011.

[76] S. Straullu, A. Nespola, P. Savio, S. Abrate, and R. Gaudino, "Different modulation formats for gigabit-over-POF," in *Access Networks and In-house Communications*, pp. AW3A–5, Optical Society of America, 2012.

[77] J. Vinogradov, R. Kruglov, K.-L. Chi, J.-W. Shi, M. Bloos, S. Loquai, and O. Ziemann, "GaN light-emitting diodes for up to 5.5-Gb/s short-reach data transmission over SI-POF," *IEEE Photonics Technology Letters*, vol. 26, no. 24, pp. 2473–2475, 2014.

[78] J. Vinogradov, R. Kruglov, R. Engelbrecht, O. Ziemann, J.-K. Sheu, K.-L. Chi, J.-M. Wun, and J.-W. Shi, "GaN-based cyan light-emitting diode with up to 1-GHz bandwidth for high-speed transmission over SI-POF," *IEEE Photonics Journal*, vol. 9, no. 3, pp. 1–7, 2017.

[79] G. Keiser, *Optical fibre communications*. Wiley Online Library, 2003.

[80] E. F. Schubert, Y.-H. Wang, A. Cho, L.-W. Tu, and G. Zydzik, "Resonant cavity light-emitting diode," *Applied physics letters*, vol. 60, no. 8, pp. 921–923, 1992.

[81] S.-Y. Huang, R.-H. Horng, J.-W. Shi, H.-C. Kuo, and D.-S. Wuu, "High-Performance InGaN-Based Green Resonant-Cavity Light-Emitting Diodes for Plastic Optical Fiber Applications," *Journal of Lightwave Technology*, vol. 27, 09 2009.

[82] Y. . Song, M. Diagne, H. Zhou, A. V. Nurmikko, and R. P. Schneider, "A blue resonant cavity light-emitting diode," in *Conference on Lasers and Electro-Optics (CLEO 2000). Technical Digest. Postconference Edition. TOPS Vol.39 (IEEE Cat. No.00CH37088)*, pp. 37–, 2000.

[83] O. Ziemann and L. Bartkiv, "POF-WDM, the truth," in *Proc. Int. Conf. Plastic Opt. Fibre*, pp. 525–530, 2011.

[84] F. Breyer, *Multilevel transmission and equalization for polymer optical fibre systems*. Verlag Dr. Hut, 2010.

[85] H. Elgala, R. Mesleh, and H. Haas, "Non-linearity effects and predistortion in optical OFDM wireless transmission using LEDs," *International Journal of Ultra Wideband Communications and Systems*, vol. 1, no. 2, pp. 143–150, 2009.

[86] S. Abrate, R. Gaudino, and G. Perrone, "Step-index PMMA fibers and their applications," *Current Developments in Optical Fiber Technology*, pp. 177–202, 2013.

[87] D. Falconer, "Adaptive equalization of channel non-linearities in QAM data transmission systems," *The Bell System Technical Journal*, vol. 57, no. 7, pp. 2589–2611, 1978.

[88] M. Schueppert, R. Kruglov, S. Loquai, and C.-A. Bunge, "Nonlinearities originated in a red RC-LED and Their impact on spectrally efficient modulation," *IEEE Photonics Technology Letters*, vol. 27, no. 19, pp. 2007–2010, 2015.

[89] M. Schüppert and C.-A. Bunge, "5Gb/s Eye-Safe LED-Based SI-POF Transmission With Equalisation of Transmitter Nonlinearities," *IEEE Photonics Technology Letters*, vol. 28, no. 23, pp. 2732–2735, 2016.

[90] K. Burse, R. Yadav, and S. Shrivastava, "Channel equalisation using neural networks: a review," *IEEE Transactions on Systems, Man, and Cybernetics, Part C (Applications and Reviews)*, vol. 40, no. 3, pp. 352–357, 2010.

[91] P. A. Haigh, Z. Ghassemlooy, S. Rajbhandari, I. Papakonstantinou, and W. Popoola, "Visible light communications: 170 Mb/s using an artificial neural network equaliser in a low bandwidth white light configuration," *Journal of Lightwave Technology*, vol. 32, no. 9, pp. 1807–1813, 2014.

[92] P. A. Haigh, F. Bausi, T. Kanesan, S. T. Le, S. Rajbhandari, Z. Ghassemlooy, I. Papakonstantinou, W. Popoola, A. Burton, H. Le Minh, *et al.*, "A 20-Mb/s VLC link with a polymer LED and a multilayer perceptron equalizer," *IEEE Photonics Technology Letters*, vol. 26, no. 19, pp. 1975–1978, 2014.

[93] P. A. Haigh, F. Bausi, H. Le Minh, I. Papakonstantinou, W. O. Popoola, A. Burton, and F. Cacialli, "Wavelength-multiplexed polymer LEDs: Towards 55 Mb/s organic visible light communications," *IEEE Journal on Selected Areas in Communications*, vol. 33, no. 9, pp. 1819–1828, 2015.

[94] Z. Ghassemlooy, P. A. Haigh, F. Arca, S. F. Tedde, O. Hayden, I. Papakonstantinou, and S. Rajbhandari, "Visible light communications: 3.75 Mbits/s data rate with a 160 kHz bandwidth organic photodetector and artificial neural network equalization," *Photonics Research*, vol. 1, no. 2, pp. 65–68, 2013.

[95] S. O. Haykin, *Neural networks and learning machines*, vol. 3. Pearson Upper Saddle River, NJ, USA:, 2009.

[96] Z. Ghassemlooy, W. Popoola, and S. Rajbhandari, *Optical Wireless Communications: System and Channel Modelling with Matlab®*. CRC Press, 2012.

[97] T. Kim and T. Adali, "Fully complex multi-layer perceptron network for nonlinear signal processing," *Journal of VLSI signal processing systems for signal, image and video technology*, vol. 32, no. 1-2, pp. 29–43, 2002.

[98] S.-S. Yang, C.-L. Ho, and S. Siu, "Sensitivity analysis of the split-complex valued multilayer perceptron due to the errors of the iid inputs and weights," *IEEE transactions on neural networks*, vol. 18, no. 5, pp. 1280–1293, 2007.

[99] E. Giacoumidis, S. T. Le, I. Aldaya, J. Wei, M. McCarthy, N. Doran, and B. Eggleton, "Experimental comparison of artificial neural network and Volterra based nonlinear equalisation for CO-OFDM," in *Optical Fibre Communications Conference and Exhibition (OFC), 2016*, pp. 1–3, IEEE, 2016.

[100] E. Giacoumidis, S. T. Le, M. Ghanbarisabagh, M. McCarthy, I. Aldaya, S. Mhatli, M. A. Jarajreh, P. A. Haigh, N. J. Doran, A. D. Ellis, *et al.*, "Fibre nonlinearity-induced penalty reduction in co-ofdm by ann-based nonlinear equalization," *Optics letters*, vol. 40, no. 21, pp. 5113–5116, 2015.

[101] A. Kantsila, M. Lehtokangas, and J. Saarinen, "Complex RPROP-algorithm for neural network equalization of GSM data bursts," *Neurocomputing*, vol. 61, pp. 339–360, 2004.

[102] D. D. Falconer and S. L. Ariyavisitakul, "Broadband wireless using single carrier and frequency domain equalisation," *Invited Overview Paper for WPMC*, vol. 2, pp. 58–66, 2002.

[103] J. J. Shynk *et al.*, "Frequency-domain and multirate adaptive filtering," *IEEE Signal processing magazine*, vol. 9, no. 1, pp. 14–37, 1992.

[104] A. Antonino, S. Straullu, S. Abrate, A. Nespola, P. Savio, D. Zeolla, J. R. Molina, R. Gaudino, S. Loquai, and J. Vinogradov, "Real-time Gigabit Ethernet bidirectional transmission over a single SI-POF up to 75 meters," in *2011 Optical Fibre Communication Conference and Exposition and the National Fibre Optic Engineers Conference*, pp. 1–3, IEEE, 2011.

[105] S. Loquai, T. Noelscher, C.-A. Bunge, T. Kupfer, F. Winkler, E. Hartl, and B. Schmauss, "10.7-Gb/s Real-Time Transmission Over 1-mm Large-Core Polymer Optical Fibre Using Maximum Likelihood Sequence Estimation," *IEEE Photonics Technology Letters*, vol. 24, no. 24, pp. 2229–2231, 2012.

[106] C. Gimeno, C. Sánchez-Azqueta, E. Guerrero, J. Aguirre, C. Aldea, and S. Celma, "A 2.5-Gb/s multi-rate continuous-time adaptive equalizer for short reach optical links," in *ESSCIRC Conference 2015-41st European Solid-State Circuits Conference (ESSCIRC)*, pp. 44–47, IEEE, 2015.

[107] C. Gimeno, E. Guerrero, C. Sanchez-Azqueta, J. Aguirre, C. Aldea, and S. Celma, "Multi-rate adaptive equalizer for transmission over up to 50-m SI-POF," *IEEE Photonics Technology Letters*, vol. 29, no. 7, pp. 587–590, 2017.

[108] X. Li, J. Wei, N. Bamiedakis, R. Penty, and I. White, "Avalanche photodiode enhanced PAM-32 5 Gb/s LED-POF link," in *2014 The European Conference on Optical Communication (ECOC)*, pp. 1–3, IEEE, 2014.

[109] X. Li, N. Bamiedakis, J. Wei, J. J. McKendry, E. Xie, R. Ferreira, E. Gu, M. D. Dawson, R. V. Penty, and I. H. White, "$\mu$LED-based Single-Wavelength Bi-directional POF Link with 10 Gb/s Aggregate Data Rate," *Journal of Lightwave Technology*, vol. 33, no. 17, pp. 3571–3576, 2015.

[110] R. Kruglov, J. Vinogradov, O. Ziemann, S. Loquai, J. Muller, U. Strauss, and C.-A. Bunge, "Eye-safe data transmission of 1.25 Gbit/s over 100-m SI-POF using green laser diode," *IEEE Photonics Technology Letters*, vol. 24, no. 3, pp. 167–169, 2011.

[111] G. Stepniak and J. Siuzdak, "Transmission beyond 2 Gbit/s in a 100 m SI POF with multilevel CAP modulation and digital equalisation," in *2013 Optical Fibre Communication Conference and Exposition and the National Fibre Optic Engineers Conference (OFC/NFOEC)*, pp. 1–3, IEEE, 2013.

[112] E. Pikasis, S. Karabetsos, T. Nikas, and D. Syvridis, "Rate-adaptive DFT-spread DMT and CDMA-DMT for 1-mm SI-POF short-range links," *IEEE Photonics Technology Letters*, vol. 25, no. 16, pp. 1574–1577, 2013.

[113] R. Kruglov, S. Loquai, C.-A. Bunge, M. Schueppert, J. Vinogradov, and O. Ziemann, "Comparison of PAM and CAP modulation schemes for data transmission over SI-POF," *IEEE Photonics Technology Letters*, vol. 25, no. 23, pp. 2293–2296, 2013.

[114] S. Loquai, R. Kruglov, B. Schmauss, C.-A. Bunge, F. Winkler, O. Ziemann, E. Hartl, and T. Kupfer, "Comparison of modulation schemes for 10.7 Gb/s transmission over large-core 1 mm PMMA polymer optical fibre," *Journal of Lightwave Technology*, vol. 31, no. 13, pp. 2170–2176, 2013.

[115] R. Kruglov, J. Vinogradov, O. Ziemann, S. Loquai, and C.-A. Bunge, "10.7-Gb/s discrete multitone transmission over 50-m SI-POF based on WDM technology," *IEEE Photonics Technology Letters*, vol. 24, no. 18, pp. 1632–1634, 2012.

[116] R. Kruglov, J. Vinogradov, O. Ziemann, S. Loquai, C. Bunge, and L. Bartkiv, "Potential of CWDM technology for 10 Gbit/s data transmission over SI-POF," in *Intern. POF Conference POF*, pp. 290–295, 2012.

[117] M. Jončić, R. Kruglov, M. Haupt, R. Caspary, J. Vinogradov, and U. H. Fischer, "Four-channel WDM transmission over 50-m SI-POF at 14.77 Gb/s using DMT modulation," *IEEE Photonics Technology Letters*, vol. 26, no. 13, pp. 1328–1331, 2014.

[118] R. Kruglov, J. Vinogradov, S. Loquai, O. Ziemann, C.-A. Bunge, T. Hager, and U. Strauss, "21.4 Gb/s discrete multitone transmission over 50-m SI-POF employing 6-channel WDM," in *Optical Fibre Communication Conference*, pp. Th2A–2, Optical Society of America, 2014.

[119] R. Kruglov, S. Loquai, J. Vinogradov, O. Ziemann, C.-A. Bunge, G. Bruederl, and U. Strauss, "10.7 Gb/s WDM Transmission over 100-m SI-POF with Discrete Multitone," in *Optical Fibre Communication Conference*, pp. W4J–5, Optical Society of America, 2016.

[120] P. Pinzón, I. Perez, and C. Vazquez, "Visible WDM system for real-time multi-Gb/s bidirectional transmission over 50-m SI-POF," *IEEE Photonics Technology Letters*, vol. 28, no. 15, pp. 1696–1699, 2016.

[121] X. Li, N. Bamiedakis, J. McKendry, E. Xie, R. Ferreira, E. Gu, M. Dawson, R. Penty, and I. White, "11 Gb/s WDM transmission over SI-POF using violet, blue and green $\mu$LEDs," in *2016 Optical Fibre Communications Conference and Exhibition (OFC)*, pp. 1–3, IEEE, 2016.

[122] P. J. Pinzón, I. P. Garcilópez, and C. Vázquez, "Efficient multiplexer/demultiplexer for visible WDM transmission over SI-POF technology," *Journal of Lightwave Technology*, vol. 33, no. 17, pp. 3711–3718, 2015.

[123] G.-H. Im, D. Harman, G. Huang, A. Mandzik, M.-H. Nguyen, and J.-J. Werner, "51.84 mb/s 16-cap atm lan standard," *IEEE Journal on Selected Areas in Communications*, vol. 13, no. 4, pp. 620–632, 1995.

[124] P. Golden, H. Dedieu, and K. S. Jacobsen, *Fundamentals of DSL technology*. CRC Press, 2005.

[125] S. Randel, F. Breyer, S. C. Lee, and J. W. Walewski, "Advanced modulation schemes for short-range optical communications," *IEEE Journal of Selected Topics in Quantum Electronics*, vol. 16, no. 5, pp. 1280–1289, 2010.

[126] L. Peng, M. Hélard, and S. Haese, "Optimization of multi-band DFT-spread DMT system for polymer optical fibre communications," in *IEEE International Conference on Communications (ICC)*, pp. 3862–3867, IEEE, 2013.

[127] W. O. Popoola, Z. Ghassemlooy, and B. G. Stewart, "Pilot-assisted PAPR reduction technique for optical OFDM communication systems," *Journal of Lightwave Technology*, vol. 32, no. 7, pp. 1374–1382, 2014.

[128] J. Campello, "Optimal discrete bit loading for multicarrier modulation systems," in *Information Theory, 1998. Proceedings. 1998 IEEE International Symposium on*, p. 193, IEEE, 1998.

[129] J. Campello, "Practical bit loading for DMT," in *1999 IEEE International Conference on Communications (Cat. No. 99CH36311)*, vol. 2, pp. 801–805, IEEE, 1999.

[130] P. S. Chow, J. M. Cioffi, and J. A. Bingham, "A practical discrete multitone transceiver loading algorithm for data transmission over spectrally shaped channels," *IEEE Transactions on communications*, vol. 43, no. 2/3/4, pp. 773–775, 1995.

[131] G. Stepniak, M. Schüppert, and C.-A. Bunge, "Advanced modulation formats in phosphorous LED VLC links and the impact of blue filtering," *Journal of Lightwave Technology*, vol. 33, no. 21, pp. 4413–4423, 2015.

[132] B. Drljača, S. Savović, and A. Djordjevich, "Calculation of the frequency response in step-index plastic optical fibres using the time-dependent power flow equation," *Optics and Lasers in Engineering*, vol. 49, no. 5, pp. 618–622, 2011.

[133] B. Drljača, A. Djordjevich, and S. Savović, "Frequency response in step-index plastic optical fibres obtained by numerical solution of the time-dependent power flow equation," *Optics & Laser Technology*, vol. 44, no. 6, pp. 1808–1812, 2012.

[134] D. Cárdenas, A. Nespola, P. Spalla, S. Abrate, and R. Gaudino, "A media converter prototype for 10-Mb/s ethernet transmission over 425 m of large-core step-index polymer optical fibre," *Journal of lightwave technology*, vol. 24, no. 12, pp. 4946–4952, 2006.

[135] R. Gaudino, G. Bosco, A. Bluschke, O. Hofmann, N. Kiss, M. Matthews, P. Rietzsch, S. Randel, J. Lee, and F. Breyer, "On the ultimate capacity of SI-POF links and the use of OFDM: Recent results from the POF-ALL project," *Fibre OpticsWeekly Update*, pp. 283–288, 2007.

[136] R. G. Gallager, *Information theory and reliable communication*, vol. 2. Springer, 1968.

[137] Thorlabs, *Thorlabs Product Specification Sheet, Laser Diode L650P007. URL: https://www.thorlabs.com/drawings/L650P007-SpecSheet.pdf*, 2010 (accessed October 26, 2020).

[138] Thorlabs, *Thorlabs PDA10A(-EC) Si Amplified Fixed Gain Detector User Guide. URL: https://www.thorlabs.com/drawings/PDA10A-EC-Manual.pdf*, 2017 (accessed October 26, 2020).

[139] Hamamatsu, *L10762: Resonant Cavity LED for POF data communication. URL: https://www.hamamatsu.com/resources/pdf/ssd/l10762_kled1054e.pdf*, 2016 (accessed October 26, 2020).

[140] Newport/New Focus, *Models 1601 and 1611 User's Manual: High-Speed Photoreceivers. URL: https://www.newport.com/medias/1601-1611-User-Manual-RevF.pdf*, 2018 (accessed October 26, 2020).

[141] T. Komuro, S. Sobukawa, H. Sakayori, M. Kono, and H. Kobayashi, "Total Harmonic Distortion Measurement System of Electronic Devices up to 100 MHz With Remarkable Sensitivity," *IEEE Transactions on Instrumentation and Measurement*, vol. 56, no. 6, pp. 2360–2368, 2007.

[142] M. C. Jeruchim, P. Balaban, and K. S. Shanmugan, *Simulation of communication systems: modeling, methodology and techniques*. Springer Science & Business Media, 2006.

[143] K. O. Akande, P. A. Haigh, and W. O. Popoola, "On the Implementation of Carrierless Amplitude and Phase Modulation in Visible Light Communication," *IEEE Access*, vol. 6, pp. 60532–60546, 2018.

[144] J. Lee and V. J. Mathews, "A fast recursive least squares adaptive second order Volterra filter and its performance analysis," *IEEE transactions on signal processing*, vol. 41, no. 3, pp. 1087–1102, 1993.

[145] S. B. Wicker and V. K. Bhargava, *Reed-Solomon codes and their applications*. John Wiley & Sons, 1999.

[146] A. V. Oppenheim and R. W. Schafer, *Digital Signal Processing [by] Alan V. Oppenheim [and] Ronald W. Schafer*. Prentice-Hall, 1975.

[147] J. G. Proakis, *Digital signal processing: principles algorithms and applications*. Pearson Education India, 2001.

[148] K. Ying, *Nonlinear distortion mitigation in dynamic-range-limited optical wireless communication systems*. PhD thesis, Georgia Institute of Technology, 2016.

[149] S. Dimitrov, S. Sinanovic, and H. Haas, "Clipping noise in OFDM-based optical wireless communication systems," *IEEE Transactions on Communications*, vol. 60, no. 4, pp. 1072–1081, 2012.

[150] D. J. Mestdagh, P. Spruyt, and B. Biran, "Analysis of clipping effect in DMT-based ADSL systems," in *Proceedings of ICC/SUPERCOMM'94-1994 International Conference on Communications*, pp. 293–300, IEEE, 1994.

[151] D. J. Barros, S. K. Wilson, and J. M. Kahn, "Comparison of orthogonal frequency-division multiplexing and pulse-amplitude modulation in indoor optical wireless links," *IEEE Transactions on Communications*, vol. 60, no. 1, pp. 153–163, 2012.

[152] G. Stepniak and J. Siuzdak, "Experimental investigation of PAM, CAP and DMT modulations efficiency over a double-step-index polymer optical fibre," *Optical Fibre Technology*, vol. 20, no. 4, pp. 369–373, 2014.

[153] S. Loquai, R. Kruglov, C.-A. Bunge, O. Ziemann, and B. Schmauss, "10-Gb/s pulse-amplitude modulated transmission over 1-mm large-core polymer optical fibre," *IEEE Photonics Technology Letters*, vol. 24, no. 10, pp. 851–853, 2012.

[154] J. Zhang, C. Guo, J. Liu, X. Wu, A. P. T. Lau, C. Lu, and S. Yu, "Low Complexity Frequency-Domain Nonlinear Equalisation for 40-Gb/s/wavelength Long-Reach PON," in *2018 Optical Fibre Communications Conference and Exposition (OFC)*, pp. 1–3, IEEE, 2018.

[155] K. O. Akande and W. O. Popoola, "Subband index carrierless amplitude and phase modulation for optical communications," *Journal of Lightwave Technology*, vol. 36, no. 18, pp. 4190–4197, 2018.

[156] M. S. Islim, *Spectrum and energy efficient digital modulation techniques for practical visible light communication systems*. PhD thesis, The University of Edinburgh, 2019.